Università degli Studi di Torino
Doctoral School of the University of Turin
PhD Programme in Chemical and Materials Sciences XXXIV Cycle

HCN reactivity at solid surfaces: possible implications of heterogeneous catalysis in prebiotic chemistry

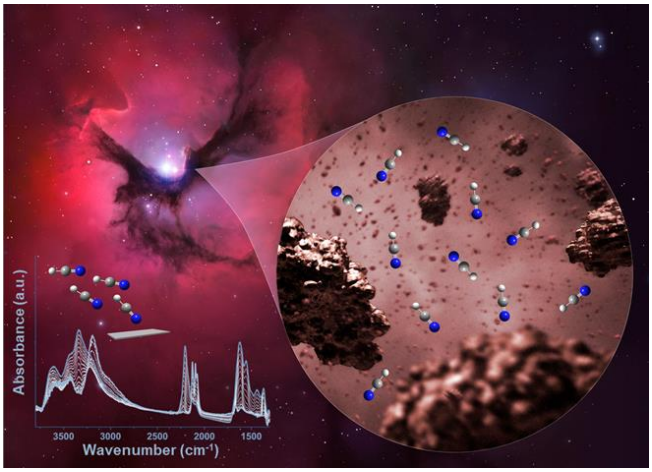

Rosangela Santalucia

Supervisors:
Prof. Giuseppe Spoto
Prof.ssa Domenica Scarano

Università degli Studi di Torino

Doctoral School of the University of Turin

PhD Programme in Chemical and Materials Sciences XXXIV cycle

HCN reactivity at solid surfaces: possible implications of heterogeneous catalysis in prebiotic chemistry

Candidate: **Rosangela Santalucia**

Supervisors: Prof. **Giuseppe Spoto**
Prof.ssa **Domenica Scarano**

Jury Members: Prof. **Piero Ugliengo**
Università di Torino
Department of Chemistry

Prof. **Raffaele Saladino**
Università della Tuscia
Department of Ecological and Biological Sciences

Prof.ssa **Barbara Onida**
Politecnico di Torino
Department of Applied Science and Technology

Head of the Doctoral School: Prof. Alberto Rizzuti
PhD Programme Coordinator: Prof. Bartolomeo Civalleri

Torino, 2022

A Gianmario

"The cosmos is within us. We are made of star stuff.

We are a way for the universe to know itself."

Carl Sagan

Table of Contents

Abstract

Hydrogen cyanide is a fascinating molecule, especially when its contrasting role concerning life is considered. On one side, it is a very powerful poison often used for murders, suicides and as a chemical weapon, while also being a harmful air pollutant. On the other side, it is the simplest molecule containing carbon and nitrogen and is so widely diffused in the Universe that it is thought to have played a crucial role in terrestrial and/or extra-terrestrial environments for the synthesis of some of the main molecular building blocks of living matter, including amino acids and nucleobases.

HCN also deserves attention in the contest of materials science, as possible precursor for the synthesis of C/N-containing materials like graphitic carbon nitride (g-C_3N_4) which indeed can be in principle considered as an HCN polymerization products. Bidimensional materials like g-C_3N_4 are of interest for the preparation of hybrid solids (especially TiO_2/g-C_3N_4 composites) with worthful physical and chemical properties which include semiconductivity, ferroelectricity, catalytic and photocatalytic activity. Finally, HCN derived chemicals also of interest for the preparation of coatings and adhesives for biomedical applications.

The chemistry of HCN has been extensively investigated in the past mainly in homogeneous conditions, while only a few studies have been on the contrary devoted to the interaction of gaseous HCN with solid surfaces.

The conviction that prompted this thesis is that a systematic investigation of heterogeneous (gas/solid) HCN reactivity could be beneficial for many research areas, like:

i. environmental science, in view of the removal by adsorption of HCN traces released by industrial processes, combustion of fossil fuels and some plastics, vehicle exhaust emissions, and biomass burning;
ii. prebiotic chemistry, as the interaction of HCN in gas or condensed phases with solid mineral surfaces in terrestrial (rocks, powders, etc.) and extra-terrestrial (cosmic dust, meteorites, comets, etc.) atmosphere may have contributed significantly to the development of prebiotic molecules;
iii. materials science, where the development of systems functionalized with C/N polymers like those mentioned above could benefit from heterogeneous synthetic procedures like those developed for C/C analogues.

Among the reasons for the lack in the literature of data concerning the HCN chemistry in heterogeneous conditions, a gap which this work aims to contribute to fill, there are certainly the safety issues associated with the production and use of pure gaseous HCN in standard laboratories. After a survey of the literature concerning the HCN chemical and spectroscopic properties, the first part of this Ph.D. work was therefore devoted to the setup of an innovative methods for the laboratory scale production of high purity HCN gas in controlled and safe conditions and for its direct dosage at the surface of some selected solids.

The investigated solids where first the SiO_2, TiO_2, Al_2O_3 and MgO pure oxides, then followed by an Mg_2SiO_4 magnesium-silicate in amorphous and crystalline (forsterite) form. Their interaction with HCN was studied in the range 150-300 K by *in situ* infrared spectroscopy.

The choice of the SiO_2, TiO_2, Al_2O_3 and MgO pure oxides as substrates was made for several reasons:

i. they are by themselves of interest in all the aforementioned research and application areas, although our attention rapidly focussed on the prebiotic implications of their surface chemistry with HCN;
ii. their surface structure and properties are quite satisfactory described in the literature, as extensively studied in the past with the methods of surface science;
iii. they have some different surface properties in terms of Brønsted acidity and/or Lewis acidity and basicity, which allows to investigate the HCN chemistry in different conditions;
iv. some of them (SiO_2 and MgO) can been assumed as model solids for the structurally more complex, and less characterized, Mg-Silicates.

The choice of Mg-silicates as substrates for studying the HCN surface chemistry is then justified by the special attention they have attracted in the prebiotic and astrochemistry research fields. Minerals with this composition are in fact present on Earth since its formation in igneous and metamorphic rocks as well as in extra-terrestrial bodies like comets and meteorites, and also contribute to the composition of in interstellar

dust particles. In this thesis a dispersed Mg_2SiO_4 sample prepared in amorphous and crystalline (namely forsterite) forms was actually investigated as a laboratory model for the interstellar dust grains.

In all the cases, the *in situ* FTIR investigation at variable temperature of the HCN/solid interaction allowed to separate two main steps: one occurring at lower temperature, when physical, and in some cases chemical, adsorptions are the prevailing phenomena and a second one, namely in the 150-300 K temperature range, where HCN undergoes complex chemical transformations initiated by its oligomerization. For sake of clarity, in the following these two steps will be illustrated and discussed separately.

IR spectroscopy resulted to be a powerful technique to investigate the two adsorption and reaction steps and to individuate the "chemical classes" of formed products but did not allow to establish their exact nature. For this reason, the products formed on some of the investigated solid surfaces were further examined by high-resolution mass spectrometry.

As it will be shown, most of the obtained results are of some relevance when framed in the prebiotic research field. Products formed from HCN/solids interaction include glycine, imidazoles, purines and pyrimidines, a result which supports the hypothesis that prebiotic molecular building blocks can be easily formed through surface catalytic processes in the absence of high-energy supply.

Chapter 1

Hydrogen cyanide and its chemistry

1.1 HCN in the human history

Already at the time of ancient Egyptians and Romans, plants, and substances of vegetable origin such as cassava, bitter almonds, cherry bay leaves, peach seeds, etc. were used as poisons for murders and suicides, and sometimes as a military weapon (for instance the Roman emperor Nero used cherry laurel water to poison the enemies wells). However, it took centuries to identify and isolate the lethal substance contained in these natural products, that is cyanide and its derivatives. Hydrogen cyanide was first obtained in 1752 by the French chemist P. Macquer from ferric ferrocyanide ($Fe_4^{III}[Fe^{II}(CN)_6]_3$), a blue pigment synthesized in Berlin around 1704 known as Prussian or Berlin blue (*Figure 1*), and for this reason initially called Prussic acid. Only in 1815 Gay-Lussac established its chemical formula (*Figure 1*) and coined the term "*cyanide*", from the Greek word *kyanos* (κὐανος, dark blue).[1, 2]

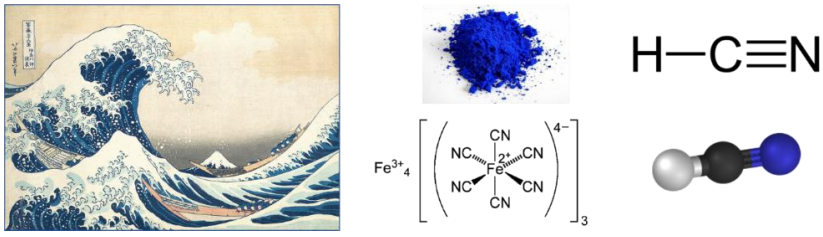

Figure 1. From the left side: "The Great Wave off Kanagawa" by K. Hokusai (1831), a masterpiece where the pigment Prussian blue (powdered form and chemical structure of Ferric

Ferrocyanide in the centre) has been extensively used; chemical structure and model of Hydrogen Cyanide molecule (on the right side).

Hydrogen cyanide exists as a highly volatile, colourless, and flammable liquid between -13.4 °C (melting point) and 25.6 °C (boiling point), and as gas with almond-like odour at higher temperature (*Table 1*).[3]

Table 1. Chemical-physical properties of hydrogen cyanide. Adapted from ref. [3]

Agent properties	
Chemical formula	HCN
Specific gravity	0.69
Boiling point	78 °F (25.6 °C)
Density	Liquid: 0.687
Vapor density (gas)	0.94
Flammability	Flammable at temperatures greater than 0 °F (−18 °C)
Flashpoint	0 °F (−18 °C)
Ionization potential	13.60 eV
Melting point	7.9 °F (−13.4 °C)
Molecular mass	27.03
Soluble in	Ether, glycerin, chloroform, and benzene.
Aqueous solubility	Miscible
Vapor pressure	630 mmHg at 68 °F (20 °C)
Volatility	1,080,000 mg, in 3 at 77 °F (25 °C)

It is a highly toxic, fast-acting substance that causes eye and respiratory irritation, along with systemic toxicity due to inhibitor effect of the CN^- cyanide ion on the cytochrome c oxidase enzyme, which stops the cellular respiration. Exposure to HCN gas in concentration of the order of 100-150 ppm can results in unconsciousness in seconds and coma and death in minutes (*Table 2*).[4]

Table 2. Toxicity of hydrogen cyanide by inhalation. Adapted from ref. [4]

Concentration		Effects
mg/m^3	ppm	
20–40	18–36	Slight symptoms after several hours
50–60	45–54	Endurable for 20–60 min without effect
120–150	110–135	Very dangerous (fatal) after 30–60 min
150	135	Lethal after 30 min
200	181	Lethal after 10 min
300	270	Immediately lethal

The darkest chapter in human history related to HCN is certainly the use of the Zyklon B pesticide during the Holocaust (*Figure 2*, left side). Zyklon B consists of HCN adsorbed into an inert and porous absorbent material (calcium sulphate or diatomaceous) and indeed some blue spots visible on the walls of the gas chambers of some Nazi champs still testify its lethal use (*Figure 2*, right side). Such stains are in fact due to the formation of ferric ferrocyanide (Prussian blue) by reaction between HCN released by Zyklon B and iron oxide present on the walls in form of rust.[4]

Figure 2. Canisters of Zyklon B found in the Dachau concentration camp from United Stated Holocaust Memorial Museum (on the left side); interior view of a gas chamber at the Majdanek extermination camp in Poland, from Panstwowe Muzeum na Majdanku (on the right side). Adapted from ref. [4]

Finally, it is worth recalling the use of HCN for capital executions, a practice that seemed abandoned but could be resumed by some US states (like Arizona).[5]

Today, HCN is considered a dangerous pollutant and poses a significant risk not only to human health but also to the environment.

1.2 HCN and environmental science

Although little known, risks exist in the everyday life of accidental or systematic exposure to cyanides of natural or anthropogenic origins like those summarized in *Table 3* and discussed in the following.[4] For this reason, the problem of HCN pollution has attracted the attention of academic and industrial researchers and prompted studies to prevent its release and develop strategies for its capture and neutralization.

Table 3. Various possible sources of cyanide poisoning. Adapted from ref. [4]

Fire smoke	Smoke generated after combustion of silk, polyurethanes, polyacrylonitriles, nylon, melamine resins, plastics, etc., in accidents including industrial, residential, car, aircraft, ship fires
Industrial exposure	Plastics production, dyeing, printing and photography, fumigation of pesticides/rodenticides, synthetic rubber production, fertilizer production, metal polish, tanning in leather industry, electroplating, metallurgy, paper and textile manufacture
Drugs	Sodium nitroprusside, laetrile, succinonitrile
Dietary	Cassava, lima beans, linseed, bamboo sprout, macadamia nuts, hydrangea, Rosaceae family (plum, peach, pear, apple, bitter almond, cherry), *Sorghum* species (Johnson grass, sorghum, Sudan grass, arrow grass), *Linum* species (flax, yellow pine flax)
Others	Cigarette smoking, phencyclidine synthesis, ingestion of nail polish remover, suicide, homicide, terrorist attack, chemical warfare, capital punishment

1.2.1 Sources of HCN

Besides volcanic activity and related phenomena, the main natural sources of HCN are the biological activity of some higher plants, bacteria, algae, and fungi, and biomass burning.

Indeed, over 2000 species of plants contain cyanogenic glycosides (like amygdalin) which can release HCN if biodegraded or ingested, while vegetation burning because of shifting agriculture, permanent deforestation, savannah fires and disposal of agricultural wastes is estimated to contribute to the global release of HCN into the

environment with a significant amount, ranging between 0.2 and 6.13 Mt/yr.[6]

However, there is no doubt that the main sources of HCN pollution and exposure risks are anthropogenic activities related to industrial processes, combustion of some synthetic plastics and fibres, and even cigarette smoke.

The industrial processes involved in using HCN (*ca.* 1.5 Mt/yr) include fumigation, mining (mainly gold and silver), chemical synthesis (of polymers, pharmaceuticals, dyes, pesticides), electroplating, tanning and metallurgy.[4] As far as the exposure risks related to these activities are concerned, the Occupational Safety and Health Administration (OSHA) has fixed the exposure limit to 10 ppm (11 mg/m^3) of HCN for an 8-hour workday and established the application of rigid standard procedures together with the use of safety devices like individual gas masks and industrial filters.[3] These devices contain adsorbent materials capable to capture HCN, such as activated carbons impregnated with Cr, Cu, Ag, Zn Mo, or Co inorganic salts or with organic compounds like pyridine and triethylenediamine.[7]

HCN (along with CO) poisoning is a common cause of death in house fires, as it can be released by combustion of synthetic, carbon- and nitrogen-containing materials such as polyurethane, acrylate plastics and synthetic fibres (nylon).[6]

Even tobacco smoke contains HCN. Its content in inhaled smoke ranges from 10 to 400 µg per cigarette (US Brands); 0.6 to 27 % of this amount is then released into the surrounding. The global emissions of HCN in the environment due to cigarette smoke can be estimated between 56 and 2240 t/yr. In this respect, research has recently been

devoted to the development of new techniques for reducing the HCN yield of smoke.[6] Cigarette filters generally contain a variety of HCN adsorbents (activated carbons, molecular sieves, silica gel, porous alumina, ion exchange resins, metal and metal oxides, alkaline and transition metal salts) which however suffer from problems, like limited efficiency, poor safety, and high cost of materials (see ref.[8] and references therein).

Finally, one other HCN anthropogenic source is the exhausts of motor vehicles and fossil fuel combustion. Several studies have demonstrated that HCN plays a key role as an intermediate in NO_x (such as N_2O, NO_2, NO) chemistry, including formation and elimination processes. As regards the latter, HCN is a by-product of NO_x reduction reactions, both in the selective catalytic reduction (SCR) process and in the three-way catalyst (TWC) system.[9-11]

1.2.2 Strategies to remove HCN from the environment

Strategies developed to the date for HCN removal include adsorption, combustion, catalytic oxidation, and catalytic hydrolysis (refs.[9, 12, 13] and references therein).

Disadvantages of sorption and combustion methods are due to the fact that they are rarely quantitative and may generate secondary pollution. Catalytic oxidation and catalytic hydrolysis can efficiently decompose low concentrations of HCN to NH_3, N_2, and H_2O at relatively low temperatures, according to the reaction schemes:

$$4HCN + 5O_2 \rightarrow 4CO_2 + 2N_2 + 2H_2O$$

$$HCN + H_2O \rightarrow NH_3 + CO$$

One of the first catalysts investigated for HCN hydrolysis has been γ-Al_2O_3 [14] which allows 80% conversion at 300 °C.

Supporting Pt or Pd metal over Al_2O_3 [12, 15] improves the HCN conversion by oxidation but at the expense of a higher cost. Supporting other non-noble metals (Cu, Co, Fe, Cr, Ni, and Zn) over γ-Al_2O_3 has been also attempted and among these Cu-Ni/γ-Al_2O_3 at 400°C has shown excellent hydrolysis performances.[16]

Concerning the oxides, TiO_2-anatase showed activity toward HCN hydrolysis twice than Al_2O_3 at 300 and 450°C, but poorer oxidation properties and thermal stability.[12] The use of pure or modified Al_2O_3/TiO_2 mixed catalysts has been also attempted, the best performances (*ca*. 100% HCN conversion at 200 °C) being reported for the $Mn/MnO_x/TiO_2/Al_2O_3$ system. This is due to synergistic effects from combining HCN catalytic hydrolysis and oxidation.[17] TiO_2-supported Pt, Pd, Rh, Ag, V_2O_5, WO_3 and, especially $CuSO_4$ catalysts have shown good HCN oxidation performances, but at the expense of significant N_2O emissions.[18] *Ca*. 100% HCN conversion rates in the 100 – 400 °C temperature range without NO_x by-production have been recently reported for the La_xCu_y/TiO_2 combined oxidation and hydrolysis catalyst.[19]

Along the series of metal/TiO_x catalysts, it has been also found that HCN hydrolysis over Nb/La–TiO_x occurs with conversion efficiencies of *ca*. 97.6% at 250 °C and *ca*. 100% above 300 °C.[20]

Fe-Ti-O_x HCN hydrolysis catalysts have recently attracted attention because of their peculiar properties in terms of both high surface areas and redox properties.[21, 22] Very promising results have been also reported for the activity in the 30-150°C temperature range of porous

CeO_2 flower-like spheres loaded with bimetal (Cu–Ag, Cu–Mn, Cu–Zn, Cu– Ni, Cu–Co, Cu–Fe) oxides. Among these systems, the Cu_8Mn_2/CeO_2 composition showed a conversion rate near 100% at 90 °C.[23]

The removal of HCN has been also attempted by using zeolites as catalysts. HCN conversion up to 80% to NH_3 and CO has been reported to occur by means of hydrolysis at 500°C over H-ferrierite,[24] whereas the acid parent H-ZSM-5 was found nearly inactive. One of the advantages of the zeolites is due to the beneficial incorporation (by ionic exchange) of transition metals into the porous framework, which occurs at the atomic level, with dispersion degrees not achievable on external surfaces.[12, 25, 26]

Concerning this research area, Hu *et al.*[13] reported that metal oxides (Fe, Cu) modified HZSM-5 prepared by incipient wetness impregnation allow 100% HCN conversion at about 250 °C. This high catalytic activity is due either to the high dispersion of the Fe and Cu containing active phase, and to their excellent redox properties, together with the acidity control ensured by the zeolitic matrix.

Despite the already obtained promising results, the investigation of catalysts for HCN abatement is still ongoing, aiming to find more active and more stable systems operating at lower temperatures.

1.3 Prebiotic chemistry: the role of HCN in the Origin of Life

Nowadays, the hypothesis is quite widespread that HCN may have been a key ingredient for the formation of the first biomolecules or of their precursors. This in both, the scenario that places the synthesis of the first biomolecules on primordial earth as well in that, which hypothesizes an extra-terrestrial origin of the molecules at the basis of life. The last one is gaining more and more credit.
In the next sections a summary based on the specialized literature is given of the possible HCN formation routes according the two scenarios and in general of the possible role of HCN in prebiotic chemistry.

1.3.1 HCN in the early Earth's atmosphere

The first evidence of a contribution of HCN to the synthesis of pre-biological molecules came from the pioneering experiment (1952) of Urey and Miller,[27] rightfully considered as the founding of the "prebiotic chemistry" research field. This experiment aimed to verify the Oparin-Haldane theory (Oparin-Haldane, 1938)[28, 29] according to which simple prebiotic organic molecules were first formed under the effect of external energy sources (lightning or UV solar photons) in a primordial reduced (oxygen free) atmosphere, where CH_4, H_2 and NH_3 were the prevailing gases, and then accumulated in the warm primitive ocean to form a "primordial soup". Following random chemical processes occurring in this soup, self-replicating molecules (proteins or nucleic acids) would have formed, thus opening the road to life.

To verify their hypotheses, Urey and Miller subjected a gas mixture containing CH_4, NH_3, H_2O and H_2 to spark discharges and then condensed the reaction products, which indeed consisted of hydrogen cyanide together formaldehyde and formic acid, in warm water (*Figure 3*).

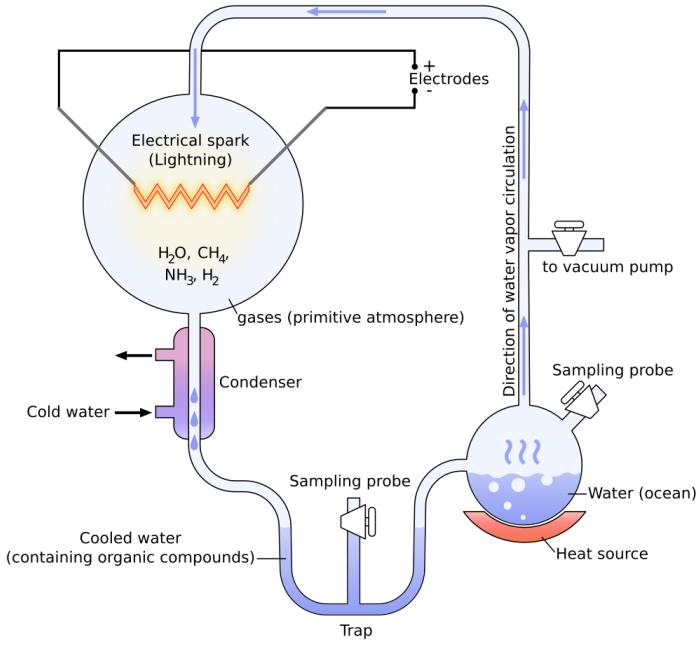

Figure 3. Schematic description of the Urey and Miller experiment. Adapted from ref. [30]

Actually, the analysis of the "soup" after a week evidenced the presence some amino acids like glycine, alanine and aspartic acid, which are supposed to have formed via the Strecker synthesis. More in detail HCN and aldehydes (formed in the discharge) react to form α-aminonitriles. Then, these α-aminonitriles are hydrolyzed to form the corresponding amino acids, as reported in the following for glycine amino acid (*Figure 4*).[31]

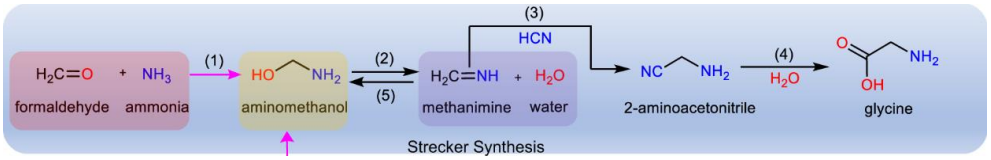

Figure 4. Strecker synthesis of glycine. Adapted from ref. [31]

A prebiotic role was attributed to HCN also in the later hypothesis of an oxidized atmosphere dominated by gases (prevalently H_2O, CO_2 and N_2) released by the surface volcanic activity and with reducing conditions confined to limited regions like hydrothermal vents.[32]

A list of the possible gas mixtures, all leading to HCN in the above conditions, is given in *Table 4.*

Table 4. Gas phase synthesis of cyano compounds. From ref. [33]

Gas Mixture	Energy Source	Products
CH_4-NH_3-H_2-H_2O	Spark Discharge	HCN
CH_4-N_2	Spark Discharge	HCN, HC≡C-CN
CO-N_2-H_2	Spark Discharge	HCN
CO_2-N_2-H_2	Spark Discharge	NCO^-
N_2-C_2H_2	Spark Discharge	HCN, NC-CN
CH_4-NH_3	High Frequency Electrical Discharge	HCN
CO_2-N_2-H_2	Shock Waves	HCN
CO_2-N_2-H_2O	Shock Waves	HCN
CH_4-N_2	Shock Waves	HCN
CH_4-NH_3	Shock Waves	HCN
CO_2-N_2	Shock Waves	·CN
CH_4-NH_3-H_2-H_2O	5 MeV e^- Bombardment	HCN
CH_4-NH_3	UV	HCN
CO-NH_3	UV	NH_4CNO, HCN
CH_4-NH_3	Heat (1200°C)	HCN

In all cases an external energy input is needed to activate the gaseous molecules. For instance, photolysis of CH_4 by the 121.567 nm

(Lyman-α line) and of N_2 by the 10-120 nm solar light components to form methylene fragments in triplet state ($^3CH_2$) together with methyl radicals ($CH_3^\bullet$) and N atoms are thought to be at the basis of HCN production following the reactions:[34]

$$^3CH_2 + N \rightarrow HCN + H$$

$$CH_3^\bullet + N \rightarrow H_2CN + H \rightarrow HCN + H_2$$

An alternative model still considers $CH_3^\bullet$ radicals as carbon source and the naturally occurring NO radical molecule (formed by volcanism or by chemical or photochemical routes) as nitrogen source instead of N_2.[35]

1.3.2 HCN in extra-terrestrial environments

HCN has been found in the solar system in the atmosphere of Jupiter[36], Neptune, Uranus,[37] Pluto[38] and abundantly on Titan (the largest moon of Saturn).[39]

As graphically illustrated in *Figure 5*, whether or not HCN can accumulate in a planetary atmosphere (given the presence of N_2) depends on its composition in terms of the C/O ratio.[40] For instance, in the nitrogen-rich atmosphere of Titan, which is characterized by a very high C/O ratio, as well as by the abundance of CH_4, HCN is efficiently produced by photochemical reactions in its mesosphere and thermosphere.[41-43]

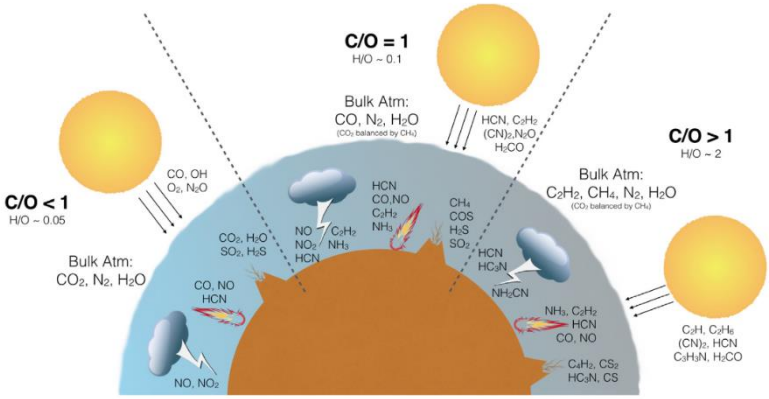

Figure 5. Effect of the C/O ratio on the atmospheric composition under the effect of lightning, impacts, volcanism, ultraviolet photons. Adapted from ref. [40]

In the Titan atmosphere, HCN reaction products including polymers are among the components of the so called *tholins*,[44-46] *i.e.* the complex mixture of aliphatic and aromatic hydrocarbons, highly unsymmetrical polycyclic aromatic nitrogenated hydrocarbons (PANHs), conjugated imines, nitriles, etc. which form dense, orange-coloured aerosol, detected by the Cassini Huygens mission.[47-49] Tholins are also the major constituents of the dark crust of some comets and HCN itself has been detected in their comas,[50-52] as well as in meteorites and asteroids.[53]

After the first observation in 1971 of the presence of HCN in interstellar regions,[54, 55] it then became clear that this molecule is ubiquitous in the whole Universe[56-60] and the question obviously arose as to whether HCN could play a role in the formation of prebiotic molecules also in extra-terrestrial and extrasolar environments.

HCN has been detected even in the rarefied ($<10^{-6}$ molecules/cm^3) InterStellar Medium (ISM),[61-67] *i.e.* in the mixture of ions, atoms,

molecules, dust particles and radiation filling the space between the stars of galaxies; it is therefore considered as a major source of nitrogen for the formation of nitrogen containing COMs (complex organic molecules containing 6-13 atoms) (*Table 5*).[68-70]

Table 5. Molecules in the interstellar medium or circumstellar shells. From ref.[70]

2 Atoms		3 Atoms		4 Atoms	5 Atoms	6 Atoms	7 Atoms
CH	CP	H_2O	N_2O	NH_3	HC_3N	CH_3OH	CH_3CHO
CN	NH	HCO^+	MgCN	H_2CO	HCOOH	CH_3CN	CH_3CCH
CH^+	SiN	HCN	$H3^+$	HNCO	CH_2NH	NH_2CHO	CH_3NH_2
OH	SO^+	OCS	SiCN	H_2CS	NH_2CN	CH_3SH	CH_2CHCN
CO	CO^+	HNC	AlNC	C_2H_2	H_2CCO	C_2H_4	HC_5N
H_2	HF	H_2S	SiNC	C_3N	C_4H	C_5H	C_6H
SiO	N_2	N_2H^+	HCP	HNCS	SiH_4	CH_3NC	c-C_2H_4O
CS	CF^+	C_2H	CCP	$HOCO^+$	c-C_3H_2	HC_2CHO	CH_2CHOH
SO	PO	SO_2	AlOH	C_3O	CH_2CN	H_2C_6	C_6H^-
SiS	O_2	HCO	H_2O^+	l-C_3H	C_5	C_5S	CH_3NCO
NS	AlO	HNO	H_2Cl^+	$HCNH^+$	SiC_4	HC_3NH^+	HC_3O
C_2	CN^-	HCS^+	KCN	H_3O^+	H_2CCC	C_5N	
NO	OH^+	HOC^+	FeCN	C_3S	CH_4	HC_4H	
HCl	SH^+	SiC_2	HO_2	c-C_3H	HCCNC	HC_4N	
NaCl	HCl^+	C_2S	TiO_2	HC_2N	HNCCC	c-H_2C_3O	
AlCl	SH	C_3	CCN	H_2CN	H_2COH^+	CH_2CNH	
KCl	TiO	CO_2	SiCSi	SiC_3	C_4H^-	C_6N^-	
AlF	ArH^+	CH_2	S_2H	CH_3	CNCHO	HNCHCN	
PN	NS^+	C_2O	HCS	C_3N^-	HNCNH	SiH_3CN	
SiC		MgNC	HSC	PH_3	CH_3O		
		NH_2	NCO	HCNO	NH_3D^+		
		NaCN		HOCN	H_2NCO^+		
				HSCN	$NCCNH^+$		
				HOOH	CH_3Cl		
				l-C_3H^+			
				HMgNC			
				HCCO			
				CNCN			

8 Atoms	9 Atoms	10 Atoms	11 Atoms	12 Atoms	13 Atoms	Fullerenes
$HCOOCH_3$	CH_3OCH_3	$(CH_3)_2CO$	HC_9N	C_6H_6	c-C_6H_5CN	C_{60}
CH_3C_3N	CH_3CH_2OH	$HO(CH_2)_2OH$	CH_3C_6H	n-C_3H_7CN		C_{60}^+
C_7H	CH_3CH_2CN	CH_2CH_2CHO	CH_3CH_2OCHO	i-C_3H_7CN		C_{70}
CH_3COOH	HC_7N	CH_3C_5N	CH_3COOCH_3			
H_2C_6	CH_3C_4H	CH_3CHCH_2O				
CH_2OHCHO	C_8H	CH_3OCH_2OH				
HC_6H	CH_3CONH_2					
CH_2CHCHO	C_8H^-					
CH_2CCHCN	CH_2CHCH_3					
NH_2CH_2CN	CH_3CH_2SH					
CH_3CHNH	HC_7O					
CH_3SiH_3						

The presence of organic compounds in the dense ISM, especially in the "hot corinos" regions (warm and dense inner regions surrounding Sun-like protostars) is the foundation of theories that hypothesize an exogenous origin of the molecules which have initiated the road to life on Earth.[71, 72]

Without entering into details, the cycle of matter in space and the delivery of exogenous materials to primitive Earth by means of dust

particles, comets, and asteroids[73, 74] is effectively represented by the following image:

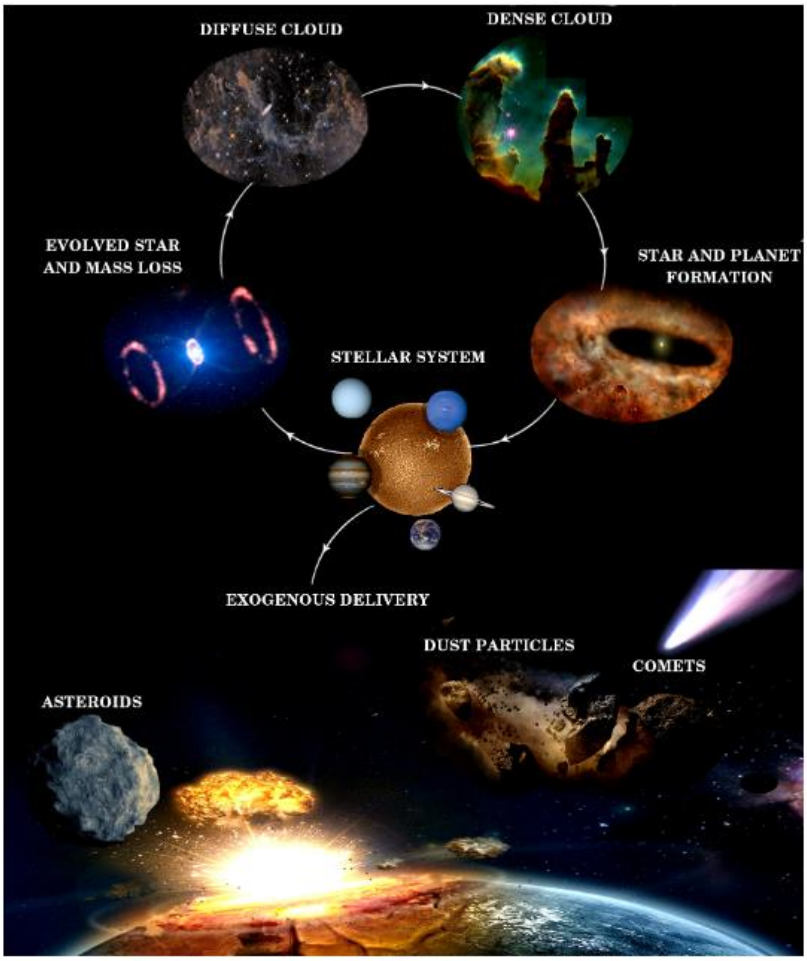

Figure 6. The cycle of matter in space and the delivery of exogenous material to the primitive Earth. Adapted from ref. [75].

Similar mechanisms of formation and distribution of the seeds of life can of course have operated (or still operate at the present) also on the extrasolar planetary systems, which are continuously discovered, leading to the panspermic theory that the life could be distributed throughout the Universe.

To give an idea of the possible role of HCN in this context, in the next paragraphs the reactivity of HCN in homogeneous (in gas phases and solutions) and in heterogeneous conditions will be shortly described with special attention to reactions of prebiotic or biotic interest.

1.3.3 The homogeneous chemistry of HCN

HCN due to the presence of a carbon-nitrile triple bond has a high energy content and thus is a very reactive molecule. Being a crucial molecule in the birth of life, over the years, the HCN polymerization mechanisms have been extensively investigated, in particular under homogeneous conditions (i.e., in a gas phase or in an aqueous solution) in order to simulate the HCN behaviour in the early Earth atmosphere (or in some astrophysical environments) and in the primordial oceans.

1.3.3.1 HCN chemistry in gas phase

A number of experimental and theoretical studies indicate that gaseous HCN (and HNC isomer[60, 62]) can react through a variety of neutral, radical and ionic reaction paths, like those listed in *Table 6* which are hypothesized to occur in dark molecular clouds.

Table 6. Summary of gas-phase reactions involving HCN and HNC in dark molecular clouds. Adapted from. [60] (see references therein).

	Reaction	ΔE (kJ/mol)
1.	$H^+ + HCN \rightarrow HNC^+ + H$	-219
2.	$H^+ + HNC \rightarrow HNC^+ + H$ $\rightarrow HCN + H^+$	-219 -53
3.	$C + HNC \rightarrow HCN + C$ $\rightarrow H + CNC$	-53 -20

4.	$C^+ + HCN$	$\rightarrow$	$H + CNC^+$ $H + C_2N^+$	-100 +6
5.	$C^+ + HNC$	$\rightarrow$	$H + CNC^+$ $H + CCN^+$	-155 -49
6.	$CH + HCN$	$\rightarrow$	$CCN + H_2$ $HCCN + H$	-42 -23
7.	$CH + HNC$	$\rightarrow$	$CCN + H_2$ $HCCN + H$	-97 -76
8.	$CH_3^+ + HCN$	$\rightarrow$	$CH_3CNH^+ + h\nu$	-
9.	$CH_3^+ + HNC$	$\rightarrow$	$CH_3CNH^+ + h\nu$	-
10.	$C_2 + HCN$	$\rightarrow$	$C_3N + H$	-148
11.	$C_2 + HNC$	$\rightarrow$	$C_3N + H$	-201
12.	$C_2H + HNC$	$\rightarrow$	$HC_3N + H$	-182
13.	$C_3N + HNC$	$\rightarrow$	$NC_4N + H$	-127

The HCN reaction patways in a planetary oxygen rich atmosphere and in presence of energetic photons are on the contrary schematized in *Figure 7* .[40]

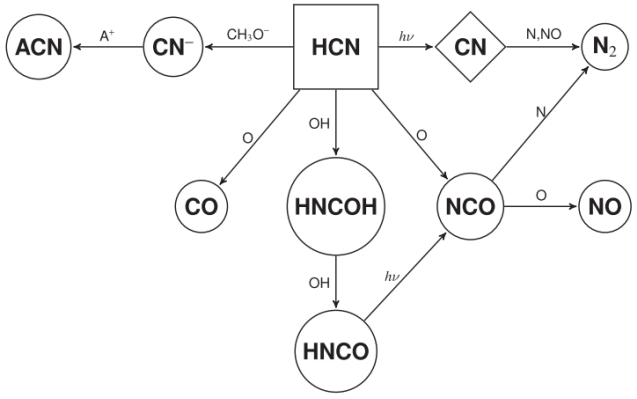

Figure 7. Collection of known pathways to destroy HCN on rocky planets. Destruction is primarily via atomic oxygen, the hydroxyl radical, anion chemistry, or photodissociation of HCN followed by reaction with atomic nitrogen or NO. Adapted from ref. [40]

Lastly, in nearly oxygen free atmospheres, like on Titan, HCN can be consumed by reaction with $N(^2D)$ or C_3N radicals or by photodissociation:[76]

$$N(^2D) + HCN \rightarrow CH + N_2$$

$$HCN + hv \rightarrow CN + H$$

$$HCN + C_3N \rightarrow C_4N_4 + H$$

A number of studies (mostly theoretical) have been then devoted to the HCN oligomerization mechanisms in gas phase, often in conditions simulating the interstellar environment (refs.[77-80] and references therein). The simplest possible products are dimers, in form of van der Waals complexes (HCN···HCN, HCN···HNC, HNC···HCN, and HNC···HNC) and covalently bound species like iminoacetonitrile (HN=CH-CN), N-cyano-methanimine (CH_2=NCN), aminocyanocarbene (NH_2-C-CN), and ethenediimine (HN=C=C=NH). Among them, iminoacetonitrile (IAN) has been detected recently in the interstellar molecular clouds. Its gas phase synthesis through neutral, radical, and ionic pathways seems to be prevented in interstellar environments (with typical temperatures in the range 10–100 K) by prohibitively high activation barriers. Therefore, the hypothesis has been advanced that its formation could have occurred on planetary bodies close to stars through geological heating, catalytic pathways, plasma discharges (lightning), or from other precursors besides HCN such as cyanide radical and methylene imine (H_2C=NH).[81] Whatever the origin, iminoacetonitrile (HN=CH-CN) is of considerable interest in the prebiotic contest as represents the first steps of chemistry which can lead through HCN oligomerization to purines and pyrimidines formation, as well as to complex polymers (*Figure 8*).[82]

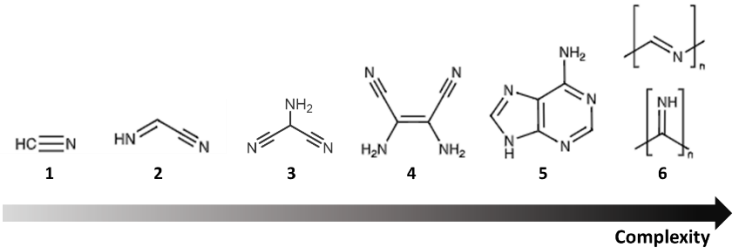

Figure 8. Selection of compounds proposed to form HCN reaction mixtures. HCN (1) can react to form its dimer iminoacetonitrile (IAN) (2), trimer aminomalonitrile (AMN) (3) and tetramer diaminomaleonitrile (DAMN) (4) which are considered key intermediates in the formation of more complex molecules, such as biologically relevant molecules including adenine (5), and various polymers (e.g., 6). Adapted from ref. [81]

1.3.3.2 HCN chemistry in solution

As already discussed in Section *1.3.1*, Miller and Urey were the first to assign a role to HCN in the synthesis of amino acids via the Strecker mechanism. Eight years after, J. Oró claimed the synthesis of the adenine nucleobase in aqueous solution of NH_3 and HCN[83] so opening the way to a great number of reactions in solution involving HCN.

Hydrogen cyanide polymerizes spontaneously in solution in the 8-10 pH range or through radicals pathways under the effect of ionising radiation to give coloured (from yellow to black) insoluble solids.[84]

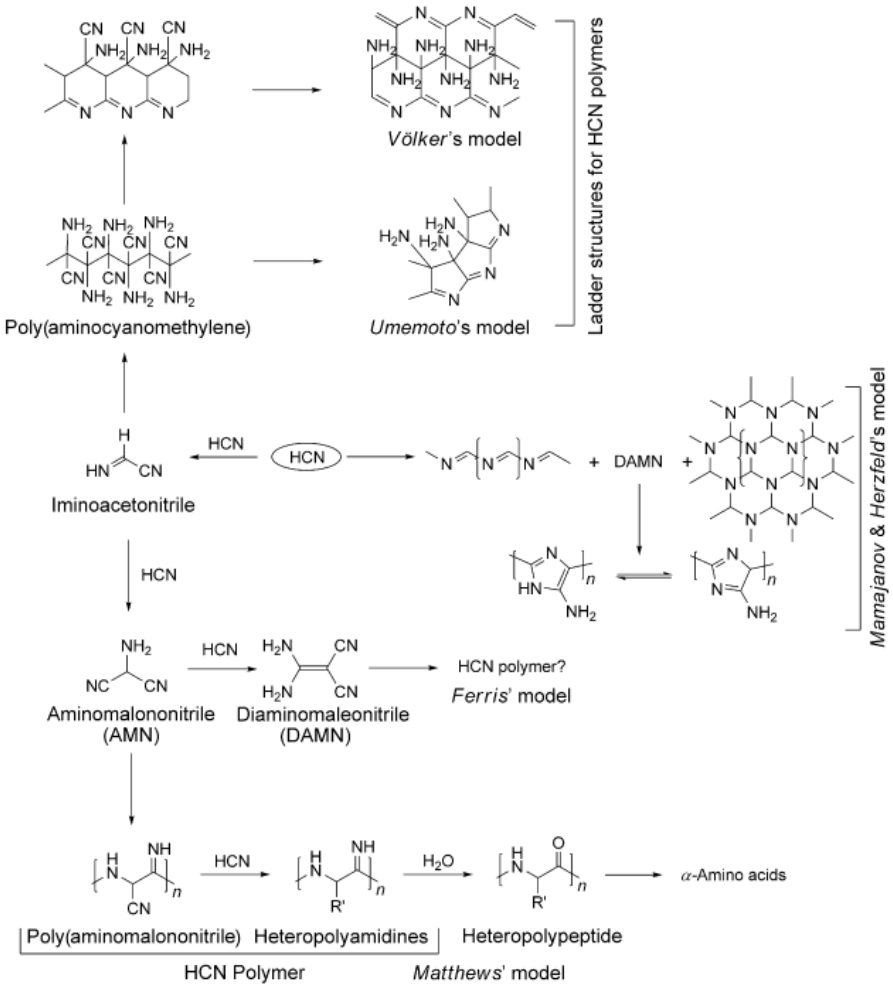

Figure 9. Different models proposed in the literature for HCN polymers. Adapted from ref. [84]

Different models, summarized in *Figure 9*, have been proposed to account for the large variety of products, assuming the iminoacetonitrile (IAN) dimer,[85, 86] the aminomalononitrile (AMN) trimer[87] or the diaminomaleonitrile (DAMN) tetramer[88, 89] are the oligomeric precursors, formed by the initial action of CN^- nucleophilic species present in basic solutions, as in the following figure.[90, 91]

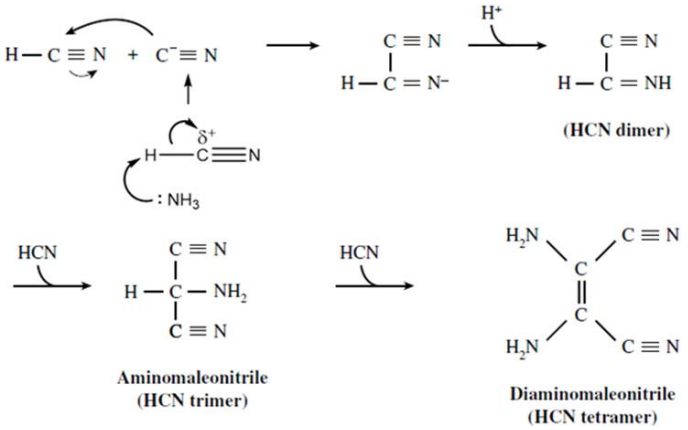

Figure 10. HCN oligomerization reaction catalyzed by ammonia. Adapted from ref.[91]

In addition, depending on the polymerization and reactions conditions, on the analytical tools, besides purines and pyrimidines, also a great variety of other compounds of biological interests, including amino acids, carboxylic acids, aldehydes, and ketones, pteridines, hydantoins, urea etc. have been identified. The main biomolecules identified in HCN polymers are listed in *Figure 11*, taken from the comprehensive review published by Ruiz Bermejo *et al.*[92]

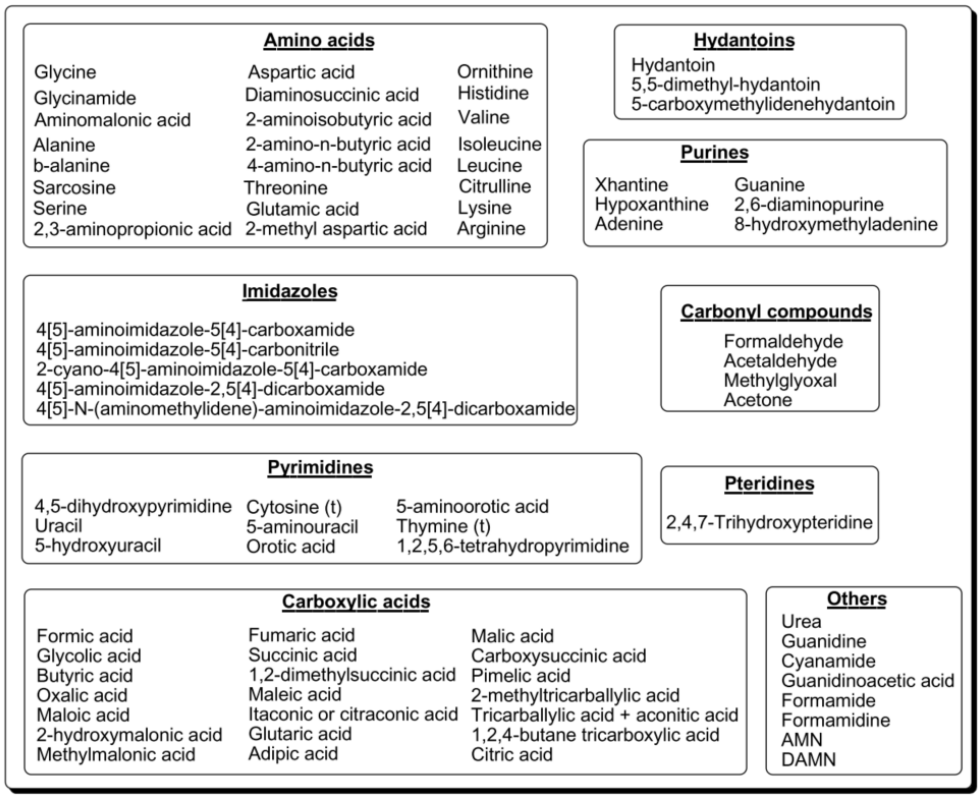

Figure 11. Summary of the simple organics and biomonomers identified in HCN polymers. Adapted from ref. [92]

Many of these organic compounds are building blocks of current proteins and nucleic acids or are active participants in metabolism. On the basis of this short resume, the central role attributed nowadays to HCN in the chemical evolution processes (*Figure 12*) appears fully justified.

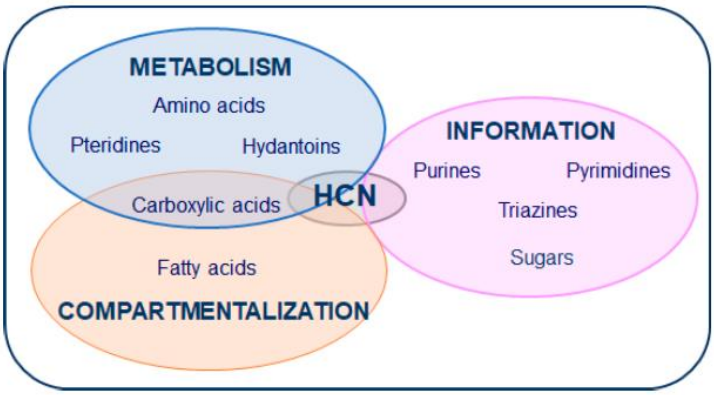

Figure 12. HCN is a key molecule in the simultaneous development of primaeval protometabolic, informational and compartmentalization systems. Adapted from ref. [93]

Nevertheless, some problems arise when considering the possibility that the chemistry described above may have actually operated under the conditions existing on the early Earth. The most critical one is that polymerization in water/NH_3 requires HCN concentrations larger than 0.01 M to overcome the competing hydrolysis to formamide and ammonium formate occurring in diluted conditions. Taking into account the production rate of HCN in the primitive atmosphere and the hydrolysis rate in solution, the steady state concentration of HCN in the primitive ocean can be estimated to be in the 10^{-8}–10^{-6} M range (at pH=8 and $0 \leq T \leq 25$°C).[94] Considering, however, that formamide itself is considered a prebiotic precursor,[95] some HCN concentration mechanisms can be imagined allowing to overcame the diluition problem, *i.e.*: (i) cooling at the eutectic point; (ii) solvent evaporation in local environments ensuring high pH values; (iii) precipitation and/or concentration in form of ferrocyanides; (iv) formation of floating patches at the water surface; and (v) concentration by adsorption at mineral surfaces.[93]

1.3.4 The heterogeneous chemistry of HCN

As mentioned above, the adsorption of the reactants on solids (minerals) can represent a way to overcome problems related to concentration in homogeneous prebiotic chemistry. Of course, mineral surfaces can also act as catalysts, as is common in heterogeneous chemistry. Based on this, the gas/solid or liquid/solid interactions have been extensively investigated aiming to elucidate the catalytic role of minerals in the origin of life.

1.3.4.1 Role of mineral surfaces in chemical evolution

The physicist J.D. Bernal was the first to propose in 1951 that clay minerals might have an important role in prebiotic synthesis.[96] According to the Bernal theory, the naturally occurring clays were able to: (i) concentrate organic matter by adsorption; (ii) catalyse the polymerization of adsorbed molecules; (iii) protect organic molecules from photolytic degradation; (iv) select specific molecules capable to act as potential enantioselective substrates. Some years later, the chemist and biologist A.G. Cairns-Smith (1966) suggested that lattice imperfections replicated during the growth of some crystals can store and replicate chemical information during surface synthetic processes. Therefore, they could have acted as a sort of primitive genetic code.[97] Clays (a class of hydrous aluminium phyllosilicates) were formed very early on the primordial Earth by alteration produced by water of silicate minerals but could not have represented the unique substrates for the development of a prebiotic chemistry;[98] other candidates are silicates

(olivine, quartz, feldspar, serpentine, zeolites, etc.), metal oxides and hydroxides, carbonates, phosphates, sulfides, borates, and molybdates and more.[99-102]

Many experimental and theoretical studies have been devoted to the interaction of biomolecules with mineral surfaces, aiming to investigate the adsorption and polymerization of organic monomers like amino acids, sugars, and nucleobases[102-104] and the catalytic properties of a variety of minerals toward the peptide bond formation have been proven beyond doubt.[105] The capability of minerals' surfaces to catalyse oligonucleotide formation from RNA monomers has been also explored.[106-108] Noteworthy are the studies by Ferris and co-workers, mainly focused on montmorillonite clay,[109] but further studies have been performed on other clays[110, 111] as well as non-clay minerals including goethite,[112] rutile,[113] olivine, calcite, pyrite[114] and mica.[115] Among all, montmorillonite has proven to be the better candidate for the concentration and polymerization of nucleic acids.[109]

A number of studies have concerned the HCN chemistry at the liquid/solid interface, as this molecule is considered by many authors the main precursor of the bases of nucleic acids. Among them notable are those devoted to montmorillonite,[116] to layered double hydroxides (LDH)[117] and to other minerals including periclase, magnesite,[118, 119] olivine, dolomite, serpentine, and zeolite.[120, 121]

The studies involving the Mg-containing minerals are of special significance for this thesis, as they proved that their surfaces are effective toward the condensation of HCN and play the same catalytic

function of ammonia in homogeneous conditions in the formation of diaminomaleonitrile, heterocyclic compounds and amino acids.[118, 119] Great attention has been also paid to the surface chemistry of formamide ($HCONH_2$) and formic acids, which are compounds closely to hydrogen cyanide (HCN) as shown in the following scheme:

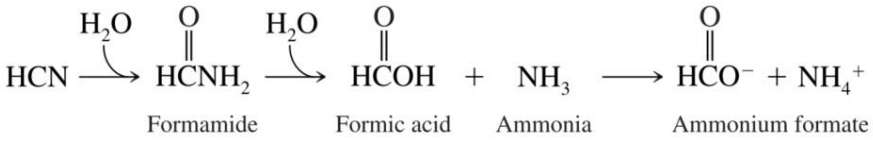

Figure 13. HCN hydrolysis to form formamide and then formic acid and ammonia, which readily convert into the very soluble salt ammonium formate. Adapted from ref. [91]

Concerning the chemistry of formamide, the reader is referred to the remarkable papers of Saladino and co-workers, which have shown that by heating neat formamide between 100 and 160°C in presence of a variety of minerals (zeolites, clays, olivines, and iron-sulfur-, phosphates-, borate- and zirconium- minerals) and metal oxides (SiO_2, Al_2O_3, TiO_2, ZrO_2), it is possible to obtain a number of biomolecules, including nucleobases, amino acids, and related compounds.[95]

Despite the number of papers devoted to the HCN chemistry at the liquid/solid interface, it quite surprising the lack of studies on the gas/solid interface (except for some studies concerning the interaction of gaseous HCN with some oxides[122-127] and other solids[128, 129] but none in relation with prebiotic concerns). Among several reasons, the safety problems related to the use of high purity gaseous HCN in standard chemical labs, must be considered.

1.3.4.2 Extraterrestrial minerals

The formation of minerals, from the first elements released by the supernova explosions of the early giant stars existing in the young Universe to the variety of mineral species we know today (more than 4400 only on Earth), is a long and fascinating story that authors like R.M. Hazen have masterfully narrated.[130] This is resumed, as far our solar system is concerned, in *Table 7*.

Table 7. Eras and stages of mineral evolution in our solar system. Adapted from ref.[131]

Era/Stage	Age (Ga)	Cumulative no. of species
Prenebular "Ur-Minerals"	>4.6	12
Era of Planetary Accretion (>4.55 Ga)		
1. Primary chondrite minerals	>4.56 Ga	60
2. Achondrite and planetesimal alteration	>4.56 to 4.55 Ga	250
Era of Crust and Mantle Reworking (4.55 to 2.5 Ga)		
3. Igneous rock evolution	4.55 to 4.0 Ga	350 to 500*
4. Granite and pegmatite formation	4.0 to 3.5 Ga	1000
5. Plate tectonics	>3.0 Ga	1500
Era of Biologically Mediated Mineralogy (>2.5 Ga to Present)		
6. Anoxic biological world	3.9 to 2.5 Ga	1500
7. Great Oxidation Event	2.5 to 1.9 Ga	>4000
8. Intermediate ocean	1.9 to 1.0 Ga	>4000
9. Snowball Earth events	1.0 to 0.542 Ga	>4000
10. Phanerozoic era of biomineralization	0.542 Ga to present	4400+

* Depending on the volatile content of the planet or moon

To date, the number of minerals found in extraterrestrial environments exceeds 500, but many others are not found on Earth as they were formed under conditions that do not exist on our planet, like low gravity or complete absence of liquid water or even biological life.

In the previous paragraph it was shortly reviewed the literature concerning the role that some terrestrial minerals could have played in the synthesis of prebiotic molecules, in the present one we will focus on minerals (and in general solids) which are present in exotic environments like even interstellar clouds.

The study of primitive cosmic materials, as bodies that have not (or little) been altered since their formation, is important because they allow shedding light on the physicochemical and dynamical processes that underlie the extraterrestrial (and also terrestrial) chemical evolution. Among these, there are asteroids and comets, small enough to have escaped geological processes that transformed primitive planetesimals into planets, as well as interplanetary dust particles (IDPs) and carbonaceous chondrites meteorites deriving from them.[132, 133] The reason for this interest resides in the hypothesis, advanced on the basis of recent astronomical observations, that some so-called interstellar complex organic molecules (iCOMs) and other prebiotic species may be produced during the early phases of formation of planetary systems (included our Solar System) and then transported to planetary bodies (included our early Earth) by impact of cosmic dust, meteorites, and comets.[74] Notice that the iCOMs synthesis occurs at the surface of the dust grains surrounding stars and protostars, which allow concentration of the otherwise rarefied in the void space chemical species, facilitate their mutual interaction, and even catalyse their reactions.

Cosmic dusts are classified on the basis of their origin and astronomical location. An *interstellar dust* means a mix of stardust, re-processed stardust and dust formed *in situ* in the ISM (InterStellar Medium).

Pre-solar dust grains are intended to precede the formation of the planetary system of a star and are subsequently incorporated into meteorites and comets. Lastly, the term *circumstellar dust* means the newly formed particles in the ejected shells of gases that surround stars during the final stages of their life. The grain composition of the different dust families is *Table 8.*[134]

Table 8. Grain composition of interstellar, circumstellar and pre-solar dust (from ref. [134]).

Interstellar	Circumstellar	Pre-solar
Hydrocarbons		
aromatic	aromatic	aromatic
aliphatic	aliphatic	—
—	—	graphite
—	[*nano*]diamond	nanodiamond
Silicates		
amorphous	amorphous	amorphous
—	Mg-rich crystalline (forsterite, Mg_2SiO_4; clinoenstatite, $MgSiO_3$; diopside, $CaMgSi_2O_6$)	Mg-rich crystalline (forsterite, Mg_2SiO_4; olivine; pyroxene)
Oxides		
[*MgO & FeO*]	crystalline oxides ($Fe_{0.9}Mg_{0.1}O$; spinel, $MgAl_2O_4$; corundum, Al_2O_3)	crystalline oxides (spinel, $MgAl_2O_4$; hibonite, $CaAl_{12}O_{19}$; corundum, Al_2O_3)
Carbides		
—	β-SiC	β-SiC
—	—	TiC & FeC (as graphite inclusions)
Nitrides		
—	—	Si_3N_4

On the contrary, the classified *interplanetary dust particles* (IDPs) are related to the grain fragments released by comets and asteroids. Cometary and asteroidal dusts differ for the composition: *i.e.*, the first one resembles that of interstellar grains (which can include silicates, polycyclic aromatic hydrocarbons, and water ice), while the last one resembles carbonaceous chondritic meteorites.[135]

Considering the materials listed in *Table 8*, which compose the different families of dusts, silicates are the most abundant and common to all the cosmic environments (interstellar, circumstellar, and pre-solar), although their chemical composition and their crystal structure can vary.

It is finally noteworthy that in the cold and dense regions of the interstellar medium, the dust grains become covered by icy mantles composed of frozen CO_2, CO, NH_3, H_2O, CH_3OH, HCN, etc..[136] The formation of the grain mantles has two important consequences: it concentrates species from the gas phase and, as depicted in *Figure 14*, under the energy supply due to bombardment by cosmic rays, ultra-violet and infra-red photons present in the ISM, it promotes the synthesis at the grain surfaces of new molecules, including iCOMs and even prebiotic or biotic molecules.[74]

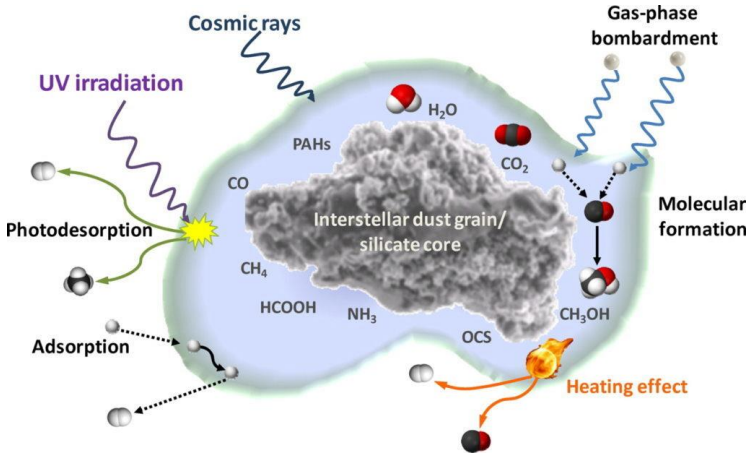

Figure 14. Pictorial representation of the events involving the icy mantle of interstellar dust grains and energetic photons. Adapted from ref.[137]

1.4 Material science: systems functionalized with C/N polymers

HCN polymers have recently gained increasing attention in materials science[138] because of the possible applications recently reviewed[93] and summarized in *Figure 15*.

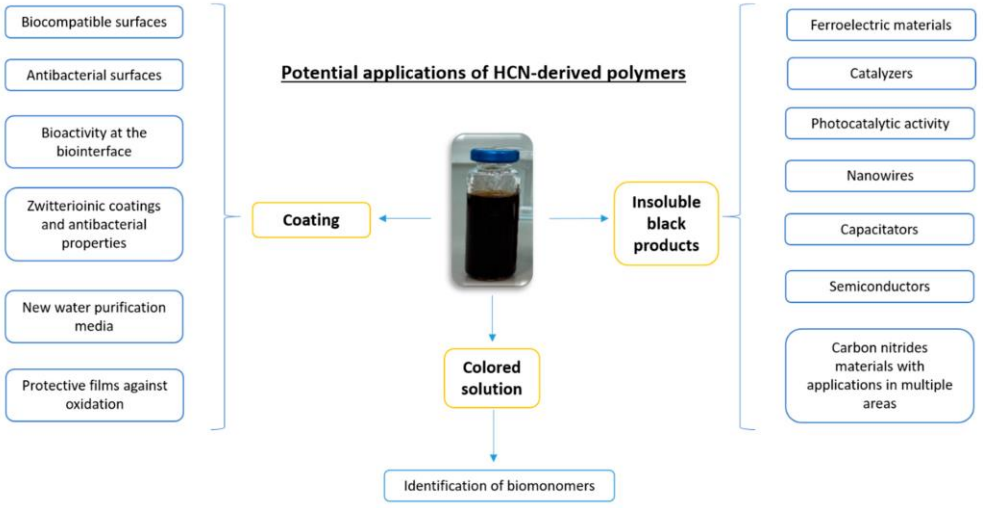

Figure 15. Current stage of the potential applications of HCN-derived polymers. Adapted from ref. [93]

Despite the interest, the relationships between their structure and properties, as well the polymerization mechanisms and their dependence on the conditions of synthesis *(i.e.* nature and concentration of the precursors, temperature, presence of oxygen, reaction time) have not been fully elucidated yet.

HCN-polymers form a heterogeneous group of complex substances (*Figure 9*) with colours variable from yellow/orange to brown/black depending on the degree of polymerization and/or cross-linking.

As shown in *Figure 15*, they can be produced through various synthetic routes starting from a variety of precursors: pure HCN or soluble cyanide salts (e.g., NaCN, KCN or NH_4CN), the HCN trimer (aminomalononitrile, AMN) or tetramer (diaminomaleonitrile DAMN), or formamide ($HCONH_2$) (*Figure 16*).

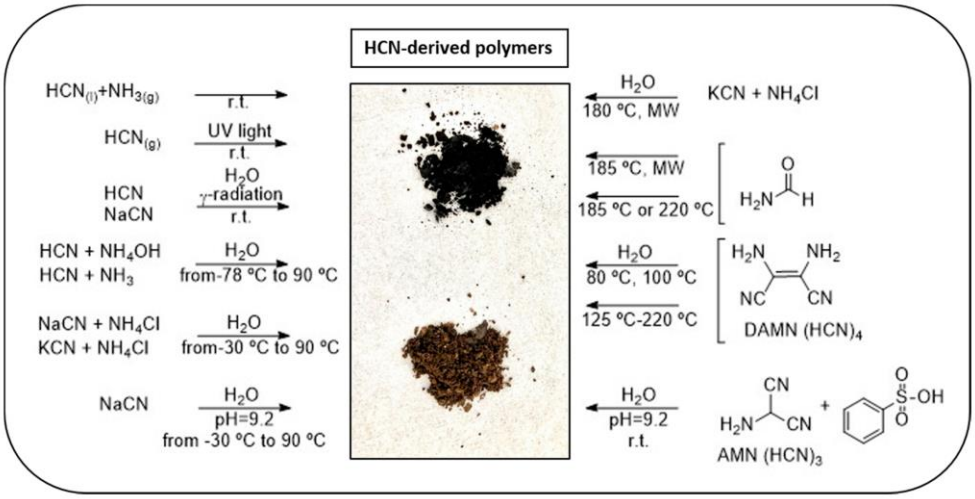

Figure 16. Summary of the main routes for the production of HCN-derived polymers. Adapted from ref. [93]

Recently graphitic carbon nitride (g-C_3N_4), a two-dimensional (2D) polymer containing networks of conjugated -C=N- groups, has attracted special attention because of its optoelectronic properties with applications in photovoltaics, biosensing and photocatalysis.[139] Several methods have been developed for the production of this material, although some of them require precursors, which are unstable or difficult to handle because explosive (for instance azines and cyanamide).[140]

Among them, urea and nucleobases have been used as precursors, *i.e.* known molecules in the field of the prebiotic chemistry of HCN and derivates:[141]

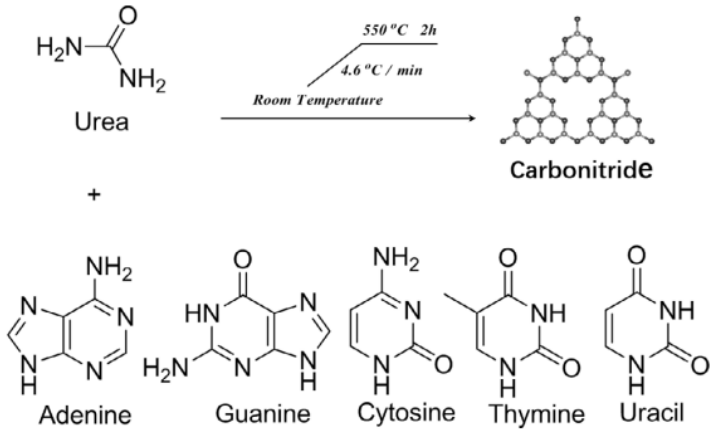

Figure 17. The chemical production of polymeric carbon nitride semi-conductors from nucleobases and urea. Adapted from ref. [141]

It is also known that 2D systems containing extended networks of conjugated -C=N- groups, such as g-C_3N_4, can be prepared by polymerization of DAMN HCN tetramer (*Figure 9*). Like g-C_3N_4 these polymers show good properties as electrocatalysts and biosensors.[142]

Films of polymeric chains containing conjugated -C=N- groups can be also prepared at the surface of a variety of solids starting from the AMN HCN trimer (*Figure 18*)[143] to obtain hybrid materials with antibacterial[144] and antioxidant[145] properties or, by copolymerization with suitable molecules, antifouling films.[146]

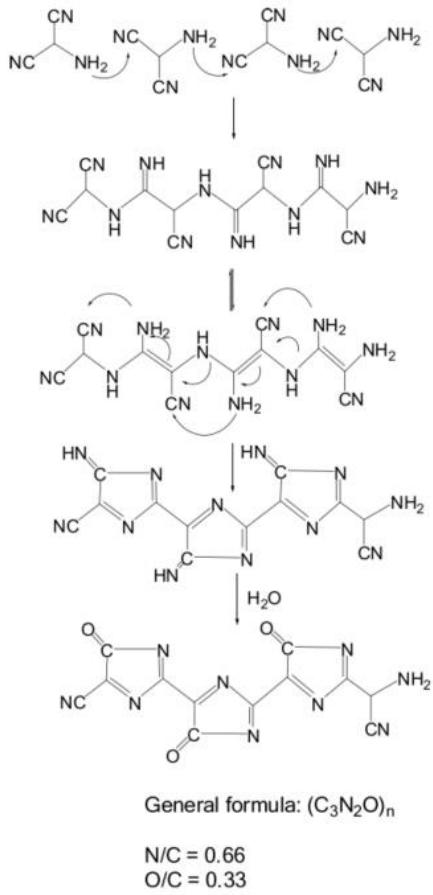

Figure 18. Proposed structure of the polymeric material obtained at the solid-liquid interface an AMN-based solution at pH=8. Adapted from ref. [147]

It is known that -C=N- containing polymers, like g-C_3N_4, could be combined with TiO_2 surfaces to give rise to hybrid composites, aiming to improve the photochemical properties of the TiO_2 semiconductor.[148] By the way, the *in situ* synthesis of a 2D polymeric layer could produce better materials with respect to other deposition methods. An example of an *in situ* synthesis of g-C_3N_4 at the surface of hydroxylated TiO_2, starting from urea as precursor is given in *Figure 19* .[149]

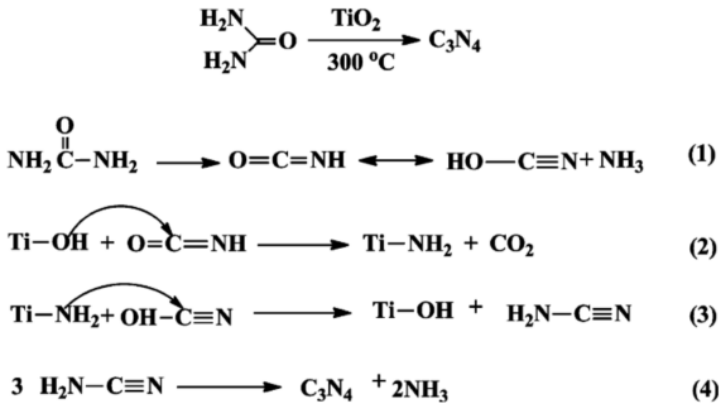

Figure 19. Mechanism for the in situ formation of a g-C_3N_4 film at the TiO_2 surface from urea.

As already mentioned elsewhere, based on the shortly above-reviewed literature data, one of the aims of this thesis is also to explore the possibility of directly using HCN as precursor for the growth of conjugated -C=N- containing polymers at the TiO_2 surface by gas/solid interaction in mild conditions (low HCN pressures and temperature close to 300 K).

1.5 Research objectives and organization of the work

In this sections (*Chapter 1*) it is shown how over the years HCN chemistry has been the subject of numerous studies in different research areas spanning from materials and environmental sciences to prebiotic- and astrochemistry. It is however a matter of facts that a number of questions concerning the real nature and the pathways of formation of the HCN-derived compounds still remain unresolved.

In this context, the objective of this work is to contribute to the knowledge of the gas-surface interaction mechanisms between HCN and solid surfaces, paying special attention to the prebiotic issues.

Most of the literature data concerning this research field are based on experiments performed in condensed phase and/or under harsh energetic conditions (temperatures far beyond 300 K or under UV/proton irradiation) supposed to simulate prebiotic/astrophysical contexts. On the contrary, this work aims to explore the potential catalytic role of solids surfaces toward HCN gas already in milder conditions (low pressure, temperatures in the 77-300 K and in absence of external energetic inputs).

In this perspective, as described in *Chapter* 2 the first step of the experimental work was devoted to the development of a new safe and effective synthetic route for the production of high purity gaseous HCN.

Afterward, the interaction of HCN gas with well characterized solids having different surface structure and properties (SiO_2, TiO_2,

Al_2O_3, MgO) and with solids of astrochemical interest (Mg-silicates in amorphous and crystallin form) was studied by in situ IR spectroscopy at variable temperature. *Chapter 3* and

Chapter 4 are devoted to the investigation of the HCN/solid interaction at ca. 150 K, where surface HCN adsorption/chemisorption is the main observed phenomenon.

Chapter 5 deals with the complex evolution of the systems at temperature higher than 150 K and up to 300 K, in conditions where on some of the investigated solids HCN undergoes a series of surface reactions ending with products which include molecules as complex as adenine.

Finally, in *Chapter 6* the results of the compositional analysis of the reaction products by high-resolution mass spectrometry are reported.

The adopted experimental workflow, which is reflected in the organization of this manuscript as far the experimental data illustration and discussion are concerned, is schematized in the following figure:

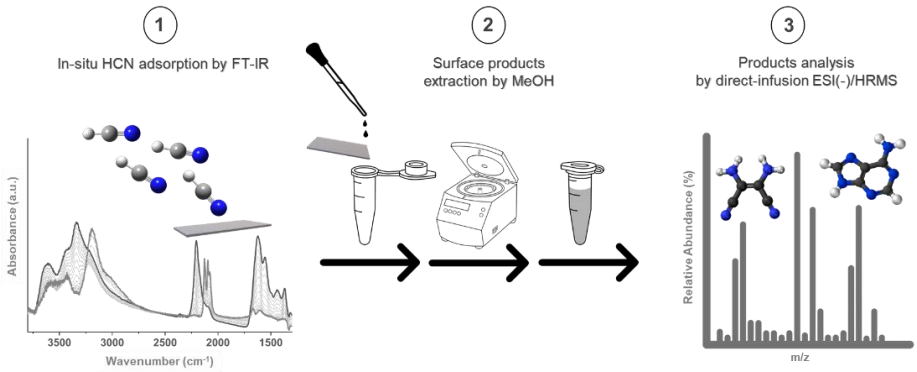

Figure 20. Schematic workflow: (1) in situ FT-IR investigation of HCN adsorption and reactivity, (2) product extraction using methanol, and (3) product identification by direct-infusion ESI (-)/HRMS. From ref.[150]

1. Macquer, P.-J., "*Éxamen chymique de bleu de Prusse" [Chemical examination of Prussian blue]*. In Mémoires de l'Académie royale des Sciences **1756**; pp 60-77.
2. Gay-Lussac, "*Recherche sur l'acide prussique" [Prussic acid research]*. Annales de chimie **1815,** 95, 136-231.
3. Dutch Expert Committee on Occupational Standards ; *Hydrogen cyanide, sodium cyanide, and potassium cyanide; Health-based recommended occupational exposure limits*. The Hague: Health Council of the Netherlands, **2002**; publication no. 2002/15OSH.
4. Cope, R. B., Chapter 25 - *Acute cyanide toxicity and its treatment: the body is dead and may be red but does not stay red for long*. In Handbook of Toxicology of Chemical Warfare Agents (Third Edition), Gupta, R. C., Ed. Academic Press: Boston, **2020**; pp 373-388.
5. Steven I. Baskin, J. B. K., Beverly I. Maliner, Gary A. Rockwood, and Csaba K. Zoltani, *Cyanide Poisoning*. In Medical Aspects of Chemical Warfare, Office of the Surgeon General, U.S. Army: **2008**.
6. European Centre for Ecotoxicology Toxicology of Chemicals; *Cyanides of Hydrogen, Sodium and Potassium, and Acetone Cyanohydrin*: (CAS No. 74-90-8, 143-33-9, 151-50-8 and 75-86-5). ECETOC: **2007**.
7. Nickolov, R. N.; Mehandjiev, D. R., *Comparative study on removal efficiency of impregnated carbons for hydrogen cyanide vapors in air depending on their phase composition and porous textures*. J Colloid Interface Sci **2004,** 273 (1), 87-94.
8. Wang, Y. P.; Yang, S.; Jia, Y. Z.; Sun, P. J.; Sun, X. H.; Wang, H. B.; Guo, J. W.; Zhang, X. B.; Liu, H. M.; Nie, C., *Application of Peanut Shell-Based Porous Materials for the Effective Removal of HCN in Cigarette Mainstream Smoke*. Key Engineering Materials **2020,** 842, 127-134.
9. Dagaut, P.; Glarborg, P.; Alzueta, M. U., *The oxidation of hydrogen cyanide and related chemistry*. Progress in Energy and Combustion Science **2008,** 34 (1), 1-46.
10. Wren, S. N.; Liggio, J.; Han, Y.; Hayden, K.; Lu, G.; Mihele, C. M.; Mittermeier, R. L.; Stroud, C.; Wentzell, J. J. B.; Brook, J. R., *Elucidating real-world vehicle emission factors from mobile measurements over a large metropolitan region: a focus on isocyanic acid, hydrogen cyanide, and black carbon.* Atmos. Chem. Phys. **2018,** 18 (23), 16979-17001.
11. Zengel, D.; Koch, P.; Torkashvand, B.; Grunwaldt, J. D.; Casapu, M.; Deutschmann, O., *Emission of Toxic HCN During NO_x Removal by Ammonia SCR in the Exhaust of Lean-Burn Natural Gas Engines*. Angew Chem Int Ed Engl **2020,** 59 (34), 14423-14428.
12. Kröcher, O.; Elsener, M., *Hydrolysis and oxidation of gaseous HCN over heterogeneous catalysts.* Applied Catalysis B: Environmental **2009,** 92 (1-2), 75-89.
13. Hu, Y.; Liu, J.; Cheng, J.; Wang, L.; Tao, L.; Wang, Q.; Wang, X.; Ning, P., *Coupling catalytic hydrolysis and oxidation of HCN over HZSM-5 modified by metal (Fe,Cu) oxides.* Applied Surface Science **2018,** 427, 843-850.

14. Marsh, J. D. F.; Newling, W. B. S.; Rich, J., *The catalytic hydrolysis of hydrogen cyanide to ammonia.* Journal of Applied Chemistry **1952,** 2 (12), 681-684.

15. Zhao, H.; Tonkyn, R. G.; Barlow, S. E.; Koel, B. E.; Peden, C. H. F., *Catalytic oxidation of HCN over a 0.5% Pt/Al_2O_3 catalyst*. Applied Catalysis B: Environmental **2006,** 65 (3-4), 282-290.

16. Yan, L.; Tian, S.; Zhou, J.; Yuan, X., *Catalytic hydrolysis of gaseous HCN over Cu–Ni/γ-Al_2O_3 catalyst: parameters and conditions.* Frontiers of Environmental Science & Engineering **2016,** 10 (6).

17. Wang, L.; Wang, X.; Cheng, J.; Ning, P.; Lin, Y., *Coupling catalytic hydrolysis and oxidation on Mn/TiO_2-Al_2O_3 for HCN removal*. Applied Surface Science **2018,** 439, 213-221.

18. Miyadera, T., *Selective reduction of NOx by ethanol on catalysts composed of Ag/Al_2O_3 and Cu/TiO_2 without formation of harmful by-products*. Applied Catalysis B: Environmental **1998,** 16 (2), 155-164.

19. Wang, Q.; Wang, X.; Wang, L.; Hu, Y.; Ning, P.; Ma, Y.; Tan, L., *Catalytic oxidation and hydrolysis of HCN over LaxCuy/TiO_2 catalysts at low temperatures.* Microporous and Mesoporous Materials **2019,** 282, 260-268.

20. Ma, Y.; Wang, F.; Wang, X.; Ning, P.; Jing, X.; Cheng, J., *The hydrolysis of hydrogen cyanide over Nb/La–TiO_x catalyst*. Journal of the Taiwan Institute of Chemical Engineers **2017,** 70, 141-149.

21. Song, Z.; Huang, Z.; Liu, B.; Liu, H.; Zhu, X.; Xia, F.; Kang, H.; Mao, Y.; Liu, X.; Zhao, B.; Zhang, Q., *Catalytic hydrolysis of HCN over Fe–Ti-O catalysts prepared by different calcination temperatures: Effect of Fe chemical valence and Ti phase*. Microporous and Mesoporous Materials **2020,** 292.

22. Yin, L.; Song, Z.; Chang, M.; Zhang, Q.; Zhao, B.; Ning, P., *Synergetic effect between Fe and Ti species on Fe-Ti-O_x for hydrogen cyanide purification*. Environ Technol **2021**, 1-7.

23. Yi, Z.; Sun, J.; Li, J.; Yang, Y.; Zhou, T.; Wei, S.; Zhu, A., *The highly efficient removal of HCN over Cu_8Mn_2/CeO_2 catalytic material*. RSC Advances **2021,** 11 (15), 8886-8896.

24. Nanba, T.; Obuchi, A.; Akaratiwa, S.; Liu, S.; Uchisawa, J.; Kushiyama, S., *Catalytic Hydrolysis of HCN over H-Ferrierite.* Chemistry Letters - CHEM LETT **2000**, 29, 986-987.

25. Song, Z.; Zhang, Q.; Ning, P.; Wang, Y.; Duan, Y.; Wang, J.; Huang, Z., *Catalytic hydrolysis of HCN on ZSM-5 modified by Fe or Nb for HCN removal: surface species and performance*. RSC Advances **2016,** 6 (112), 111389-111397.

26. Liu, N.; Yuan, X.; Chen, B.; Li, Y.; Zhang, R., *Selective catalytic combustion of hydrogen cyanide over metal modified zeolite catalysts: From experiment to theory*. Catalysis Today **2017,** 297, 201-210.

27. Miller, S. L., A *Production of Amino Acids Under Possible Primitive Earth Conditions*. Science **1953**, 117 (3046), 528-529.

28. Oparin, A. I. *The Origin of Life*, Moscow 1936, English translation: Oparin, A. I. The Origin of Life. New York: Dover (1952) (first translation published in **1938**).

29. Haldane, J.B.S. **1954**. *The Origin of Life*. Penguin Books, Harmondsworth.
30. Wikipedia contributors. *Miller–Urey experiment*. In Wikipedia, The Free Encyclopedia. https://en.wikipedia.org/w/index.php?title=Miller%E2%80%93Urey_experiment&oldid=1091351648.
31. Singh, S. K.; Zhu, C.; La Jeunesse, J.; Fortenberry, R. C.; Kaiser, R. I., *Experimental identification of aminomethanol (NH_2CH_2OH)—the key intermediate in the Strecker Synthesis*. Nature Communications **2022,** 13 (1), 375.
32. Zahnle, K.; Schaefer, L.; Fegley, B., *Earth's earliest atmospheres*. Cold Spring Harb Perspect Biol **2010,** 2 (10), a004895.
33. Ferris, J. P.; Hagan, W. J., *HCN and chemical evolution: The possible role of cyano compounds in prebiotic synthesis.* Tetrahedron **1984,** 40 (7), 1093-1120.
34. Zahnle, K., *Photochemistry of Methane and the Formation of Hydrocyanic Acid (HCN) in the Earth's Early Atmosphere*. **1986**.
35. Ghoshal, S.; Pramanik, A.; Sarkar, P., *Theoretical Investigations on the Possibility of Prebiotic HCN Formation via O-Addition Reactions*. J Phys Chem A **2020,** 124 (23), 4782-4792.
36. Tokunaga, A. T.; Beck, S. C.; Geballe, T. R.; Lacy, J. H.; Serabyn, E., *The detection of HCN on Jupiter.* Icarus **1981,** 48 (2), 283-289.
37. Marten, A.; Gautier, D.; Owen, T.; Sanders, D. B.; Matthews, H. E.; Atreya, S. K.; Tilanus, R. P. J.; Deane, J. R., *First Observations of CO and HCN on Neptune and Uranus at Millimeter Wavelengths and Their Implications for Atmospheric Chemistry*. Astrophys. J. **1993,** 406, 285.
38. Lellouch, E.; Gurwell, M.; Butler, B.; Fouchet, T.; Lavvas, P.; Strobel, D. F.; Sicardy, B.; Moullet, A.; Moreno, R.; Bockelée-Morvan, D.; Biver, N.; Young, L.; Lis, D.; Stansberry, J.; Stern, A.; Weaver, H.; Young, E.; Zhu, X.; Boissier, J., *Detection of CO and HCN in Pluto's atmosphere with ALMA.* Icarus **2017,** 286, 289-307.
39. Molter, E. M.; Nixon, C. A.; Cordiner, M. A.; Serigano, J.; Irwin, P. G. J.; Teanby, N. A.; Charnley, S. B.; Lindberg, J. E., *Alma Observations of Hcn and Its Isotopologues on Titan*. The Astronomical Journal **2016,** 152 (2).
40. Rimmer, P. B.; Rugheimer, S., *Hydrogen cyanide in nitrogen-rich atmospheres of rocky exoplanets*. Icarus **2019,** 329, 124-131.
41. Wilson, E. H.; Atreya, S. K., *Current state of modeling the photochemistry of Titan's mutually dependent atmosphere and ionosphere*. Journal of Geophysical Research: Planets **2004,** 109 (E6).
42. Gautier, T.; Carrasco, N.; Buch, A.; Szopa, C.; Sciamma-O'Brien, E.; Cernogora, G., *Nitrile gas chemistry in Titan's atmosphere*. Icarus **2011,** 213 (2), 625-635.
43. Gautier, T., *Mid- and far-infrared absorption spectroscopy of Titan's aerosols analogues*. **2013,** (April).
44. Sagan, C.; Khare, B. N., *Tholins: organic chemistry of interstellar grains and gas*. Nature **1979,** 277 (5692), 102-107.

45. Coll, P.; Coscia, D.; Smith, N.; Gazeau, M. C.; Ramírez, S. I.; Cernogora, G.; Israël, G.; Raulin, F., *Experimental laboratory simulation of Titan's atmosphere: aerosols and gas phase.* Planetary and Space Science **1999,** 47 (10), 1331-1340.

46. Imanaka, H.; Smith, M. A., *Formation of nitrogenated organic aerosols in the Titan upper atmosphere.* Proceedings of the National Academy of Sciences **2010,** 107 (28), 12423-12428.

47. Imanaka, H.; Khare, B. N.; Elsila, J. E.; Bakes, E. L. O.; McKay, C. P.; Cruikshank, D. P.; Sugita, S.; Matsui, T.; Zare, R. N., *Laboratory experiments of Titan tholin formed in cold plasma at various pressures: implications for nitrogen-containing polycyclic aromatic compounds in Titan haze*. Icarus **2004,** 168 (2), 344-366.

48. Israël, G.; Szopa, C.; Raulin, F.; Cabane, M.; Niemann, H. B.; Atreya, S. K.; Bauer, S. J.; Brun, J. F.; Chassefière, E.; Coll, P.; Condé, E.; Coscia, D.; Hauchecorne, A.; Millian, P.; Nguyen, M. J.; Owen, T.; Riedler, W.; Samuelson, R. E.; Siguier, J. M.; Steller, M.; Sternberg, R.; Vidal-Madjar, C., *Complex organic matter in Titan's atmospheric aerosols from in situ pyrolysis and analysis*. Nature **2005,** 438 (7069), 796-799.

49. Derenne, S.; Coelho, C.; Anquetil, C.; Szopa, C.; Rahman, A. S.; McMillan, P. F.; Corà, F.; Pickard, C. J.; Quirico, E.; Bonhomme, C., *New insights into the structure and chemistry of Titan's tholins via ^{13}C and ^{15}N solid state nuclear magnetic resonance spectroscopy.* Icarus **2012,** 221 (2), 844-853.

50. Ip, W. H.; Rosenbauer, H.; Schwenn, R.; Balsiger, H.; Geiss, J.; Meier, A.; Goldstein, B. E.; Lazarus, A. J.; Shelley, E.; Kettmann, G., *Giotto IMS measurements of the production rate of hydrogen cyanide in the coma of comet Halley*. Annales Geophysicae **1990,** 8, 319-325.

51. Matthews, C. N.; Minard, R. D., *Hydrogen cyanide polymers, comets and the origin of life*. Faraday Discussions **2006,** 133 (0), 393-401.

52. Mumma, M. J.; Charnley, S. B., *The Chemical Composition of Comets—Emerging Taxonomies and Natal Heritage.* Annual Review of Astronomy and Astrophysics **2011,** 49 (1), 471-524.

53. Pizzarello, S., *Hydrogen Cyanide in the Murchison Meteorite*. The Astrophysical Journal **2012,** 754 (2).

54. Buhl, D., *Chemical Constituents of Interstellar Clouds*. Nature **1971,** 234 (5328), 332-334.

55. Dalgarno, A.; Black, J. H., *Molecule formation in the interstellar gas*. Reports on Progress in Physics **1976,** 39 (6), 573-612.

56. Clark, F. O.; Buhl, D.; Snyder, L. E., *Observational Evidence for the Excitation of HCN and H_20 in Protostellar Molecular Clouds.* The Astrophysical Journal **1974,** 190, 545-556.

57. Bieging, J. H.; Chapman, B.; Welch, W. J. *In The Distribution of HCN in the Circumstellar Envelope of IRC+10216, Mass Loss from Red Giants*, Dordrecht, 1985//; Morris, M.; Zuckerman, B., Eds. Springer Netherlands: Dordrecht, **1985**; pp 155-156.

58. Jørgensen, J. K.; Schöier, F. L.; van Dishoeck, E. F., *Molecular inventories and chemical evolution of low-mass protostellar envelopes**. A&A **2004,** 416 (2), 603-622.

59. Godard, B.; Falgarone, E.; Gerin, M.; Hily-Blant, P.; De Luca, M., *Molecular absorption lines toward star-forming regions: a comparative study of HCO^+, HNC, HCN, and CN ***.* A&A **2010,** 520.

60. Loison, J.-C.; Wakelam, V.; Hickson, K. M., *The interstellar gas-phase chemistry of HCN and HNC.* Monthly Notices of the Royal Astronomical Society **2014,** 443 (1), 398-410.

61. Goldsmith, P. F.; Langer, W. D.; Ellder, J.; Irvine, W.; Kollberg, E., *Determination of the HNC to HCN abundance ratio in giant molecular clouds.* **1981,** 249:2.

62. Schilke, P.; Walmsley, C. M.; Pineau Des Forets, G.; Roueff, E.; Flower, D. R.; Guilloteau, S., *A study of HCN, HNC and their isotopometers in OMC-1. I. Abundances and chemistry*. Astronomy and Astrophysics **1992,** 256, 595-612.

63. Lahuis, F.; Dishoeck, E., *ISO-SWS spectroscopy of gas-phase C_2H_2 and HCN toward massive young stellar objects.* Astronomy and Astrophysics **2000,** 355, 699-712.

64. Boonman, A. M. S.; Stark, R.; van der Tak, F. F. S.; van Dishoeck, E. F.; van der Wal, P. B.; Schäfer, F.; de Lange, G.; Laauwen, W. M., *Highly Abundant HCN in the Inner Hot Envelope of GL 2591: Probing the Birth of a Hot Core?* The Astrophysical Journal **2001,** 553 (1), L63-L67.

65. Lahuis, F.; van Dishoeck, E. F.; Boogert, A. C. A.; Pontoppidan, K. M.; Blake, G. A.; Dullemond, C. P.; Evans Ii, N. J.; Hogerheijde, M. R.; Jørgensen, J. K.; Kessler-Silacci, J. E.; Knez, C., *Hot Organic Molecules toward a Young Low-Mass Star: A Look at Inner Disk Chemistry.* The Astrophysical Journal **2005,** 636 (2), L145-L148.

66. Knez, C.; Lacy, J. H.; Evans, N. J.; van Dishoeck, E. F.; Richter, M. J., *High-resolution mid-infrared spectroscopy of NGC 7538 IRS 1: probing chemistry in a massive young stellar object.* The Astrophysical Journal **2009,** 696 (1), 471-483.

67. Rolffs, R.; Schilke, P.; Wyrowski, F.; Dullemond, C.; Menten, K. M.; Thorwirth, S.; Belloche, A., Hot HCN around young massive stars at 0.1" resolution. A&A **2011,** 529.

68. Herbst, E.; van Dishoeck, E. F., *Complex Organic Interstellar Molecules. Annual Review of Astronomy and Astrophysics* **2009,** 47 (1), 427-480.

69. Ceccarelli, C.; Caselli, P.; Fontani, F.; Neri, R.; López-Sepulcre, A.; Codella, C.; Feng, S.; Jiménez-Serra, I.; Lefloch, B.; Pineda, J. E.; Vastel, C.; Alves, F.; Bachiller, R.; Balucani, N.; Bianchi, E.; Bizzocchi, L.; Bottinelli, S.; Caux, E.; Chacón-Tanarro, A.; Choudhury, R.; Coutens, A.; Dulieu, F.; Favre, C.; Hily-Blant, P.; Holdship, J.; Kahane, C.; Al-Edhari, A. J.; Laas, J.; Ospina, J.; Oya, Y.; Podio, L.; Pon, A.; Punanova, A.; Quenard, D.; Rimola, A.; Sakai, N.; Sims, I. R.; Spezzano, S.; Taquet, V.; Testi, L.; Theulé, P.; Ugliengo, P.; Vasyunin, A. I.; Viti, S.; Wiesenfeld, L.; Yamamoto, S., Seeds Of Life In Space (SOLIS): *The Organic Composition Diversity at 300–1000 au Scale in Solar-type Star-forming Regions.* The Astrophysical Journal **2017,** 850 (2), 176.

70. McGuire, B. A., 2018 *Census of Interstellar, Circumstellar, Extragalactic, Protoplanetary Disk, and Exoplanetary Molecules*. The Astrophysical Journal Supplement Series **2018,** 239 (2), 17.

71. Chyba, C.; Sagan, C., *Endogenous production, exogenous delivery and impact-shock synthesis of organic molecules: an inventory for the origins of life*. Nature **1992**, 355 (6356), 125-132.

72. Vazart, F.; Balucani, N.; Skouteris, D.; Ceccarelli, C.; Shalayel, I.; Vallée, Y., *The origin of organic chemistry on Earth: endogenous synthesis or exogenous delivery?* Memorie della Societa Astronomica Italiana **2019**, 90, 467.

73. Whittet, D. C. B., *Planetary and Interstellar Processes Relevant to the Origins of Life*. Springer Dordrecht: 1997.

74. Ehrenfreund, P.; Charnley, S. B., *Organic Molecules in the Interstellar Medium, Comets, and Meteorites: A Voyage from Dark Clouds to the Early Earth*. Annual Review of Astronomy and Astrophysics **2000,** 38 (1), 427-483.

75. Mateo-Marti, E.; Prieto-Ballesteros, O.; Muñoz Caro, G.; González-Díaz, C.; Muñoz-Iglesias, V.; Gálvez-Martínez, S., *Characterizing Interstellar Medium, Planetary Surface and Deep Environments by Spectroscopic Techniques Using Unique Simulation Chambers at Centro de Astrobiologia (CAB).* Life **2019,** 9 (3).

76. Hébrard, E.; Dobrijevic, M.; Loison, J. C.; Bergeat, A.; Hickson, K. M., *Neutral production of hydrogen isocyanide (HNC) and hydrogen cyanide (HCN) in Titan's upper atmosphere*. A&A **2012,** 541.

77. Evans, R. A.; Lorencak, P.; Ha, T. K.; Wentrup, C*., HCN Dimers: Iminoacetonitrile and N-Cyanomethanimine.* Journal of the American Chemical Society **1991,** 113 (19), 7261-7276.

78. Smith, I. W. M.; Talbi, D.; Herbst, E., *The production of HCN dimer and more complex oligomers in dense interstellar clouds.* A&A **2001,** 369 (2), 611-615.

79. Yim, M. K.; Choe, J. C., *Dimerization of HCN in the gas phase: A theoretical mechanistic study.* Chemical Physics Letters **2012,** 538, 24-28.

80. Jung, S. H.; Choe, J. C., *Mechanisms of Prebiotic Adenine Synthesis from HCN by Oligomerization in the Gas Phase.* Astrobiology **2013,** 13 (5), 465-475.

81. Sandstrom, H.; Rahm, M., *The Beginning of HCN Polymerization: Iminoacetonitrile Formation and Its Implications in Astrochemical Environments*. ACS Earth Space Chem **2021,** 5 (8), 2152-2159.

82. Kliss, R. M.; Matthews, C. N., Hydrogen cyanide dimer and chemical evolution. Proceedings of the National Academy of Sciences **1962**, 48 (8), 1300-1306.

83. Orò, J., *Synthesis of adenine from ammonium cyanide*. Biochem. Biophys. Res. Commun. **1960,** 2, 407-412.

84. Ruiz-Bermejo, M.; de la Fuente, J. L.; Rogero, C.; Menor-Salván, C.; Osuna-Esteban, S.; Martín-Gago, J. A., *New Insights into the Characterization of 'Insoluble Black HCN Polymers'.* Chemistry & Biodiversity **2012,** 9 (1), 25-40.

85. Volker, T. H., *Polymere Blausäure*. [Polymeric hydrocyanic acid] Angew. Chem. **1960,** 72 (11), 379-384.

86. Umemoto, K.; Takahasi, M.; Yokota, K., *Studies on the structure of HCN oligomers. Origins of life and evolution of the biosphere* **1987,** 17 (3), 283-293.

87. Matthews, C. N.; Moser, R. E., *Prebiological protein synthesis*. Proceedings of the National Academy of Sciences **1966**, 56 (4), 1087-1094.

88. Mamajanov, I.; Herzfeld, J., *HCN polymers characterized by solid state NMR: Chains and sheets formed in the neat liquid.* The Journal of Chemical Physics **2009,** 130 (13), 134503.

89. Ferris J.P. - Edelson, E. H.; Edelson Eh Fau - Auyeung, J. M.; Auyeung Jm Fau - Joshi, P. C.; Joshi, P. C., *Structural studies on HCN oligomers*. **1981,** (0022-2844 (Print)).

90. Ferris, J. P.; Wos, J. D.; Ryan, T. J.; Lobo, A. P.; Donner, D. B., *Biomolecules from HCN*. Origins of life **1974,** 5 (1), 153-157.

91. Zubay, G., Chapter 13 - *Similarities and Differences between the Biosynthesis of Nucleotides and the Prebiotic Synthesis of Nucleotides*. In Origins of Life on the Earth and in the Cosmos (Second Edition), Zubay, G., Ed. Academic Press: San Diego, **2000**; pp 223-250.

92. Ruiz-Bermejo, M.; Zorzano, M. P.; Osuna-Esteban, S., *Simple Organics and Biomonomers Identified in HCN Polymers: An Overview*. Life (Basel) **2013,** 3 (3), 421-48.

93. Ruiz-Bermejo, M.; de la Fuente, J. L.; Pérez-Fernández, C.; Mateo-Martí, E., *A Comprehensive Review of HCN-Derived Polymers.* Processes **2021,** 9 (4).

94. Miyakawa, S.; Cleaves, H.; Miller, S., *The cold origin of life: A. Implications based on the hydrolytic stabilities of hydrogen cyanide and formamide*. Origins of life and evolution of the biosphere : the journal of the International Society for the Study of the Origin of Life **2002**, 32, 195-208.

95. Saladino, R.; Crestini, C.; Pino, S.; Costanzo, G.; Di Mauro, E., *Formamide and the origin of life.* Phys Life Rev **2012,** 9 (1), 84-104.

96. Bernal, J. D., *The Physical Basis of Life*. Proceedings of the Physical Society. Section A **1949,** 62 (9), 537-537.

97. Cairns-Smith, A. G., *The origin of life and the nature of the primitive gene*. Journal of Theoretical Biology **1966,** 10 (1), 53-88.

98. Kloprogge, J. T. T.; Hartman, H., *Clays and the Origin of Life: The Experiments.* Life (Basel) **2022,** 12 (2).

99. Schoonen, M.; Smirnov, A.; Cohn, C., *A perspective on the role of minerals in prebiotic synthesis*. Ambio **2004,** 33 (8), 539-51.

100. Hazen, R. M., Presidential Address to the Mineralogical Society of America, Salt Lake City, October 18, 2005: *Mineral surfaces and the prebiotic selection and organization of biomolecules.* American Mineralogist **2006,** 91 (11-12), 1715-1729.

101. Hazen, R. M.; Sverjensky, D. A., *Mineral surfaces, geochemical complexities, and the origins of life.* Cold Spring Harb Perspect Biol **2010,** 2 (5), a002162.

102. Cleaves, H.; Michalkova, A.; Hill, F.; Leszczynski, J., *Mineral-organic interfacial processes : potential roles in the origin of life.* **2012,** (May 2014).

103. Ferris, J. P., *Catalysis and Prebiotic Synthesis. Reviews in Mineralogy and Geochemistry* **2005,** 59 (1), 187-210.

104. Rimola, A.; Sodupe, M.; Ugliengo, P., *Role of Mineral Surfaces in Prebiotic Chemical Evolution. In Silico Quantum Mechanical Studies*. Life (Basel) **2019,** 9 (1).

105. Lambert, J. F., *Adsorption and polymerization of amino acids on mineral surfaces: a review*. Orig Life Evol Biosph **2008,** 38 (3), 211-42.

106. Jheeta, S.; Joshi, P. C., *Prebiotic RNA Synthesis by Montmorillonite Catalysis*. Life **2014,** 4 (3).

107. Pedreira-Segade, U.; Hao, J.; Razafitianamaharavo, A.; Pelletier, M.; Marry, V.; Le Crom, S.; Michot, L. J.; Daniel, I., *How do Nucleotides Adsorb Onto Clays?* Life (Basel) **2018,** 8 (4).

108. Mignon, P.; Corbin, G.; Le Crom, S.; Marry, V.; Hao, J.; Daniel, I., *Adsorption of nucleotides on clay surfaces: Effects of mineral composition, pH and solution salts.* Applied Clay Science **2020,** 190.

109. Aldersley, M. F.; Joshi, P. C.; Price, J. D.; Ferris, J. P., *The role of montmorillonite in its catalysis of RNA synthesis.* Applied Clay Science **2011,** 54 (1), 1-14.

110. Franchi, M.; Ferris, J. P.; Gallori, E., *Cations as Mediators of the Adsorption of Nucleic Acids on Clay Surfaces in Prebiotic Environments.* Origins of life and evolution of the biosphere **2003,** 33 (1), 1-16.

111. Cai, P.; Huang, Q.; Zhang, X.; Chen, H., *Adsorption of DNA on clay minerals and various colloidal particles from an Alfisol.* Soil Biology and Biochemistry **2006,** 38 (3), 471-476.

112. Holm, N. G.; Ertem, G.; Ferris, J. P., *The binding and reactions of nucleotides and polynucleotides on iron oxide hydroxide polymorphs*. Origins of life and evolution of the biosphere **1993,** 23 (3), 195-215.

113. Cleaves, H. J., 2nd; Jonsson, C. M.; Jonsson, C. L.; Sverjensky, D. A.; Hazen, R. M., *Adsorption of nucleic acid components on rutile (TiO_2) surfaces*. Astrobiology **2010,** 10 (3), 311-23.

114. James Cleaves, H.; Crapster-Pregont, E.; Jonsson, C. M.; Jonsson, C. L.; Sverjensky, D. A.; Hazen, R. A., *The adsorption of short single-stranded DNA oligomers to mineral surfaces*. Chemosphere **2011,** 83 (11), 1560-1567.

115. Valdrè, G.; Antognozzi, M.; Wotherspoon, A.; Miles, M. J., *Influence of properties of layered silicate minerals on adsorbed DNA surface affinity, self-assembly and nanopatterning*. Philosophical Magazine Letters **2004,** 84 (9), 539-545.

116. Ferris, J. P.; Edelson, E. H.; Mount, N. M.; Sullivan, A. E., *The effect of clays on the oligomerization of HCN.* Journal of Molecular Evolution **1979**, 13 (4), 317-330.

117. Boclair, J. W.; Braterman, P. S.; Brister, B. D.; Jiang, J.; Lou, S.; Wang, Z.; Yarberry, F., *Cyanide Self-Addition, Controlled Adsorption, and Other Processes at Layered Double Hydroxides*. Origins of life and evolution of the biosphere **2001,** 31 (1), 53-69.

118. Yuasa S. ; Orò. J., *Role of weak bases on the prebiotic formation of heterocyclic compounds*. In Cosmochemical Evolution and the Origins of Life, Springer, D., Ed. **1974**; pp 295-299.

119. Yuasa, S.; Ishigami, M., *Geochemically possible condensation of hydrogen cyanide in the presence of divalent metal compounds*. GEOCHEMICAL JOURNAL 1977, 11 (4), 247-252.

120. Colín-García, M.; Ortega-Gutiérrez, F.; Ramos-Bernal, S.; Negrón-Mendoza, A., *Heterogeneous radiolysis of HCN adsorbed on a solid surface.* Nuclear Instruments and Methods in Physics Research Section A: Accelerators, Spectrometers, Detectors and Associated Equipment 2010, 619 (1), 83-85.

121. Villafane-Barajas, S. A.; Ruiz-Bermejo, M.; Rayo-Pizarroso, P.; Galvez-Martinez, S.; Mateo-Marti, E.; Colin-Garcia, M., *A Lizardite-HCN Interaction Leading the Increasing of Molecular Complexity in an Alkaline Hydrothermal Scenario: Implications for Origin of Life Studies.* Life (Basel) **2021,** 11 (7).

122. Morrow, B. A.; Cody, I. A., *Infra-red studies of reactions on oxide surfaces. Part 3.—HCN and C_2N_2 on silica.* Journal of the Chemical Society, Faraday Transactions 1: Physical Chemistry in Condensed Phases **1975**, 71 (0), 1021-1032.

123. Low, M. J. D.; Ramasubramanian, N.; Ramamurthy, P.; Deo, A. V., *Infrared spectrum, surface reaction, and polymerization of adsorbed hydrogen cyanide on porous glass*. The Journal of Physical Chemistry **1968,** 72 (7), 2371-2378.

124. Low, M. J. D.; Ramamurthy, P., *Infrared study of hcn polymer on alumina*. Journal of the research institute for catalysis Hokkaido University **1968,** 16 (2), 535-542.

125. Raskó, J.; Bánsági, T.; Solymosi, F., *HCN adsorption on silica and titania supported Rh catalysts studied by FTIR.* Physical Chemistry Chemical Physics **2002,** 4 (14), 3509-3513.

126. Kim, S.; Sorescu, D. C.; Yates, J. T., *Infrared Spectroscopic Study of the Adsorption of HCN by γ-Al_2O_3: Competition with Triethylenediamine for Adsorption Sites*. The Journal of Physical Chemistry C **2007,** 111 (14), 5416-5425.

127. Tsyganenko, A. A.; Chizhik, A. M.; Chizhik, A. I., A FTIR search for linkage isomerism of CN^- ions adsorbed on oxides and zeolites. Physical Chemistry Chemical Physics **2010**, 12 (24), 6387-6395.

128. Rudakova, A. V.; Belykh, R. A.; Tsyganenko, A. A., *FTIR study of HCN adsorption on magnesium fluoride.* Vestnik of Saint Petersburg University. Physics. Chemistry **2018,** 5(63) (2), 114-126.

129. Abdel-Rahman, M.; Feng, X.; Muir, M.; Ghale, K.; Xu, Y.; Trenary, M., *Reaction pathways for HCN on transition metal surfaces.* Physical Chemistry Chemical Physics **2019,** 21 (9), 5274-5284.

130. Hazen, R. M.; Papineau, D.; Bleeker, W.; Downs, R. T.; Ferry, J. M.; McCoy, T. J.; Sverjensky, D. A.; Yang, H., *Mineral evolution*. American Mineralogist **2008,** 93 (11-12), 1693-1720.

131. Hazen, R.; Ferry, J., *Mineral Evolution: Mineralogy in the Fourth Dimension*. Elements **2010,** 6, 9-12.

132. Grady, M.; Wright, I., *Types of extraterrestrial material available for study. Meteorites and the Early Solar System II,* **2006**.

133. Giraldo Ramírez, W.; Tobón, J., *Extraterrestrial minerals and future frontiers in mineral exploration.* Dyna (Medellin, Colombia) **2014,** 80, 83-87.

134. Jones, A. P., *The mineralogy of cosmic dust: astromineralogy*. European Journal of Mineralogy **2007,** 19 (6), 771-782.

135. Bradley, J. P., 1.26 - *Interplanetary Dust Particles.* In Treatise on Geochemistry, Holland, H. D.; Turekian, K. K., Eds. Pergamon: Oxford, **2007**; pp 1-24.

136. Gibb, E.; Whittet, D.; Boogert, A.; Tielens, a., *Interstellar Ice: The Infrared Space Observatory Legacy.* The Astrophysical Journal Supplement Series **2008,** 151, 35.

137. Meinert, C.; de Marcellus, P.; Le Sergeant d'Hendecourt, L.; Nahon, L.; Jones, N. C.; Hoffmann, S. V.; Bredehöft, J. H.; Meierhenrich, U. J., *Photochirogenesis: Photochemical models on the absolute asymmetric formation of amino acids in interstellar space*. Physics of Life Reviews **2011,** 8 (3), 307-330.

138. D'Ischia, M.; Manini, P.; Moracci, M.; Saladino, R.; Ball, V.; Thissen, H.; Evans, R. A.; Puzzarini, C.; Barone, V., *Astrochemistry and Astrobiology: Materials Sciencein Wonderland?* Int J Mol Sci **2019,** 20 (17).

139. Rono, N.; Kibet, J. K.; Martincigh, B. S.; Nyamori, V. O., *A review of the current status of graphitic carbon nitride. Critical Reviews in Solid State and Materials Sciences* **2021,** 46 (3), 189-217.

140. Zhu, J.; Xiao, P.; Li, H.; Carabineiro, S. A. C., *Graphitic Carbon Nitride: Synthesis, Properties, and Applications in Catalysis.* ACS Applied Materials & Interfaces **2014,** 6 (19), 16449-16465.

141. Yang, C.; Wang, B.; Zhang, L.; Yin, L.; Wang, X., Synthesis of Layered Carbonitrides from Biotic Molecules for Photoredox Transformations. Angewandte Chemie (International ed. in English) **2017**, 56.

142. Ruiz-Bermejo, M.; García-Armada, P.; Mateo-Martí, E.; de la Fuente, J. L., *HCN-derived polymers from thermally induced polymerization of diaminomaleonitrile: A non-enzymatic peroxide sensor based on prebiotic chemistry*. European Polymer Journal **2022,** 162.

143. Thissen, H.; Koegler, A.; Salwiczek, M.; Easton, C. D.; Qu, Y.; Lithgow, T.; Evans, R. A., *Prebiotic-chemistry inspired polymer coatings for biomedical and material science applications*. NPG Asia Materials **2015,** 7 (11), e225-e225.

144. Liao, T. Y.; Easton, C. D.; Thissen, H.; Tsai, W. B., *Aminomalononitrile-Assisted Multifunctional Antibacterial Coatings.* ACS Biomater Sci Eng **2020,** 6 (6), 3349-3360.

145. Ball, V., *Antioxidant activity of films inspired by prebiotic chemistry*. Materials Letters **2021,** 285.

146. Chen, W. H.; Liao, T. Y.; Thissen, H.; Tsai, W. B., *One-Step Aminomalononitrile-Based Coatings Containing Zwitterionic Copolymers for the Reduction of Biofouling and the Foreign Body Response.* ACS Biomater Sci Eng **2019,** 5 (12), 6454-6462.

147. Toh, R. J.; Evans, R.; Thissen, H.; Voelcker, N. H.; d'Ischia, M.; Ball, V., *Deposition of Aminomalononitrile-Based Films: Kinetics, Chemistry, and Morphology*. Langmuir **2019,** 35 (30), 9896-9903.

148. Mino, L.; Cesano, F.; Scarano, D.; Spoto, G.; Martra, G., *Molecules and heterostructures at TiO_2 surface: the cases of H_2O, CO_2, and organic and inorganic sensitizers*. Research on Chemical Intermediates **2019,** 45 (12), 5801-5829.

149. Zou, X.-X.; Li, G.-D.; Wang, Y.-N.; Zhao, J.; Yan, C.; Guo, M.-Y.; Li, L.; Chen, J.-S., *Direct conversion of urea into graphitic carbon nitride over mesoporous TiO_2 spheres under mild condition*. Chemical Communications **2011,** 47 (3), 1066-1068.

150. Santalucia, R.; Pazzi, M.; Bonino, F.; Signorile, M.; Scarano, D.; Ugliengo, P.; Spoto, G.; Mino, L., *From gaseous HCN to nucleobases at the cosmic silicate dust surface: an experimental insight into the onset of prebiotic chemistry in space.* Physical Chemistry Chemical Physics **2022**, 24 (12), 7224-7230.

Chapter 2

The production of HCN

2.1 "Conventional" methods

2.1.1 Industrial processes

HCN is mainly produced by the *Andrussow process* in which mixtures of methane and ammonia are combusted with oxygen (air) at 1000-1500°C in presence of Pt or Pt-Rh alloys as catalysts following the reaction:[1]

$$2CH_4 + 2NH_3 + 3O_2 \xrightarrow{Pt} 2HCN + 6H_2O \quad (1)$$

In this process, the energy for the reaction is mainly supplied by the exothermic partial oxidation reactions of methane and ammonia.
The reaction of methane and ammonia, in presence of noble metals catalysts, but in absence of oxygen is also at the basis of the *Degussa BMA process* (Blausäure-Methane-Ammoniak), which is preferred for a small-scale production of HCN:[1]

$$CH_4 + NH_3 \xrightarrow{Pt-Al-Ru} HCN + 3H_2 \quad (2)$$

In this process, energy must be supplied from the outside.

Finally, HCN can be also produced through the *Shawinigan* (or *Flouhmic*) *process*, based on the reaction between hydrocarbons (for instance propane) and ammonia over a coke bed at 1300−1600°C:[1]

$$C_3H_8 + 3NH_3 \rightarrow 3HCN + 3H_2 \quad (3)$$

2.1.2 Conventional laboratory-scale processes

On a laboratory scale, it is possible to produce HCN by hydrolysis of sodium or potassium cyanide, or potassium ferrocyanide with sulfuric acid.[2] For instance:

$$NaCN + H_2SO_4 \xrightarrow{H_2O} HCN + NaHSO_4 \quad (4)$$

These reactions are difficult to control, potentially dangerous and therefore require special precautions and highly qualified personnel. Furthermore, the obtained HCN is often contaminated by gaseous side products (H_2O, CO, CO_2, NH_3, SO_3, and SO_2) and needs complex purification stages to be obtained at the high purity grade, necessary for the adsorption experiments object of this work.

To avoid the severe risks associated with the use of industrial HCN cylinders or its production by acid hydrolysis (with the associated purity problems) a fair amount of time of this Ph.D. work was spent in order to design and to set up an innovative method for the *in situ* production of small amounts of high purity HCN, in very safe and controlled conditions, as described in the next paragraph.

2.2 An innovative laboratory-scale method developed in this thesis

Cyanides, including hydrogen cyanide (H-CN) and cyanogen (CN-CN), are sometimes classified as "pseudohalogens" because of some chemical analogies with true halogens.[3] For instance, HCl can be obtained by reaction of sulfuric acid and sodium chloride, in a way closely resembling that cited in the previous part to produce HCN by NaCN acid hydrolysis.

It is also well known that metal halides like AgCl, AuCl, and CuCl react with hydrogen at T ≥ 300°C to give the metal and HCl.[4] As an example:

$$2AgCl + H_2 \xrightarrow{\Delta} 2HCl + 2Ag \qquad (5)$$

On this ground, we decided to try to obtain HCN from noble metal cyanide by reduction with molecular hydrogen. To the scope, AuCN was chosen as a precursor because of its stability and chemical inertness, which allows to handle it without special safety precautions. From the literature, we became however aware that a possible drawback of this method, when applied to cyanides, could be represented by the side-production of cyanogen (NC-CN) *via* competitive thermolysis at temperatures higher than 350°C, as indeed reported for AuCN as well as for AgCN, CuCN, $HgCN_2$.[3, 5] In general:

$$2MCN_x \xrightarrow{\Delta} (CN)_2 + 2M \quad \text{M=Ag, Au, Cu, Hg and x=1, 2} \qquad (6)$$

To clarify this point, it was decided to compare the thermal behavior of AuCN in the absence and in presence of H_2 by using the same experimental conditions and the same analytical methods for the investigation of the gas-phase products.

To this scope, some milligrams of AuCN (in form of yellow powder) were first introduced in a quartz ampoule directly connected to a vacuum line and previously outgassed at room temperature (to eliminate traces of water and other adsorbed impurities). The sample was then progressively heated up to 500 °C (by means of an external furnace) under a static vacuum, then the developed gas-phase was analyzed by means of a quadrupole gas-mass spectrometer directly connected to the same line. In order to be sure to detect all the possible gaseous products, the analysis was first carried out in full scan mode to explore a wide m/z range (20-100), then it was focused on the masses of interest by operating in multiple ion detection (MID) mode. For sake of brevity, only the experimental results obtained in the MID mode for the m/z values typical of HCN and C_2N_2 are shown in *Figure 21.*

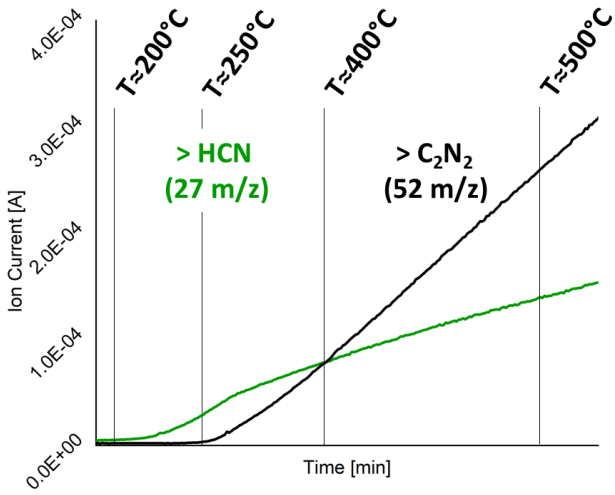

Figure 21. Mass spectrogram in MID (Multiple Ion Detection) mode of the gas phase evolved by thermal treatment of AuCN from 200°C up to 500°C. Selected peaks are those of HCN (27 m/z) and C_2N_2 (52 m/z).

The MS spectrograms in *Figure 21* show that the AuCN thermal decomposition starts at ca. 200°C and reaches the maximum rate at 500°C. Besides the expected C_2N_2 product, the simultaneous evolution of small amounts of HCN are also observed, possibly formed by AuCN hydrolysis in presence of traces of water not completely removed by the preventive outgassing stage at RT or released by the all-glass vacuum line. As it is shown from *Figure 21*, HCN, although produced in small amount, is the main product in the 200 – 400°C range, with a maximum at about 250°C, while above 400°C, C_2N_2 becomes largely predominant. These results are in full agreement with the literature data.[6]

Moving now to illustrate and discuss the results obtained by thermal treatment of AuCN in presence of H_2, several attempts (not illustrated here in detail for sake of brevity) were made to find the best

temperature conditions suitable to maximize the production of the evolution of HCN by minimizing that of cyanogen. In agreement with the data concerning the thermal decomposition of AuCN (*vide supra*), this temperature was individuated at *ca.* 250°C. It was also found that the reduction of AuCN by H_2 is favoured by the addition of small fragments of Pd metal to the AuCN powder.

The beneficial effect of palladium is not surprising, as this metal is well known to be able to homolitically dissociate the hydrogen molecule (while adsorbing H atoms to form an interstitial hydride phase) thus making hydrogen atoms easily available at the metal particle surface by the so-called *spill-over effect*.[7] As shown by the mass spectrogram in *Figure 22*, performing the AuCN reduction with H_2 in presence of Pd metal allows obtaining a significant yield of HCN already at 250 °C, without any trace of C_2N_2 contamination.

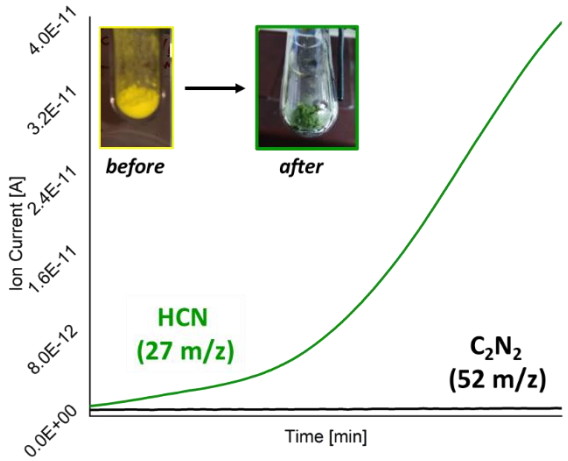

Figure 22. Mass spectrogram (obtained via MID mode) illustrating the composition of gaseous reaction products of AuCN/Pd with H_2 at 250°C as a function of the time. The green curve is the spectrogram at the m/z value of HCN, and the black curve at that of C_2N_2. The insert on

the top left shows the change in colour of the AuCN/Pd powder before and after the above thermal treatment.

Finally, it is worth noticing that after the above treatment the remaining mixture of unreacted AuCN and Pd particles, which shows the typical yellow colour of the gold cyanide, appears greenish (*Figure 22*). The colour is certainly in part due to the formation of small Au nanoparticles (as expected), but probably also to the formation of some polymerization product. In contrast, when the AuCN was treated at 400-500 °C in absence of H_2/Pd the final powder appears dark brown (*Figure 23*), typical of the paracyanogen species (as reported in literature).[8]

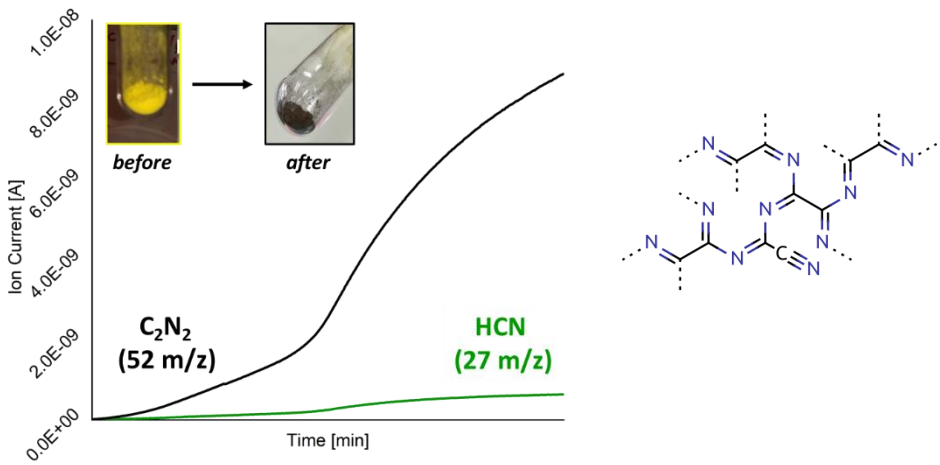

Figure 23. Left: mass spectrogram (obtained via MID mode) illustrating the composition of gaseous reaction products of AuCN at 500°C as a function of the temperature. The green curve is the spectrogram at the m/z value of HCN, and the black curve at that of C_2N_2. The insert on the top left shows the change in colour of the AuCN/Pd powder before and after the above thermal treatment. Right: a possible representation of paracyanogen from ref.[8]

The total absence of cyanogen in the reaction products obtained by reported method deserves some comment. It is known that H_2 can reduce cyanogen to HCN following the scheme:

$$(CN)_2 + H_2 \xrightarrow{\Delta} 2HCN \qquad (7)$$

However, the reaction requires temperatures as high as *ca.* 680 °C and long-time (a couple of days) to be completed.[5] Hence, the absence of cyanogen in our much milder temperature conditions (250 °C) cannot be due to its direct reduction whether formed.

It is however a matter of the fact that reaction (7) is supposed to proceed following the mechanism summarized below, which requires the activated form of $CN^{\cdot}$ and $H^{\cdot}$ (hydrogen atom) radicals to take place:[9]

$$(CN)_2 \rightarrow 2CN\bullet$$
$$CN\bullet + H_2 \rightarrow HCN + H\bullet$$
$$H\bullet + (CN)_2 \rightarrow HCN + CN\bullet$$
$$H\bullet + HCN \rightarrow CN\bullet + H_2$$
$$\bullet CN + \bullet CN \rightarrow (CN)_2$$

On this basis, it is conceivable that the easy conversion of C_2N_2 to HCN in our very mild conditions is advantaged by the Pd spillover effect, which makes available $H^{\cdot}$ species even at RT.

As it will be better shown in the following section, the gas produced with our method is further purified prior usage, by flowing it over solid

$CaCl_2$ as desiccant and by repeated freeze-thaw cycles to remove excess H_2.

2.2.1 Experimental details

Materials

- Gold (I) cyanide (AuCN) as precursor: commercial (Sigma Aldrich) in the form of yellow, high purity fine grain crystalline powder.
- H_2: certified gas cylinder (Siad Spa, Italy) ≥ 99.8%
- Small (< 1 mm) Pd metal crystals as hydrogenation catalyst
- Calcium chloride ($CaCl_2$) as desiccant agent: commercial (Sigma Aldrich) anhydrous, granular, ≤7.0 mm, ≥93.0%.

Methods

For the preliminary studies, aimed to find the best HCN synthesis conditions, small amounts of pure AuCN (when studying its thermal decomposition) or of AuCN together with 2-3 small Pd fragments (1 mm or less in linear dimensions) were placed in a quartz tube connected to a vacuum line and to a gas-mass spectrometer (Pfeiffer Omnistar) and eventually filled with H_2 (typically 20-30 mbar), when studying the AuCN reduction.

The quartz tube and its content were then heated by means of an external oven and the temperature monitored by a thermocouple in contact with the sample holder. The experimental setup is shown in the following *Figure 24*:

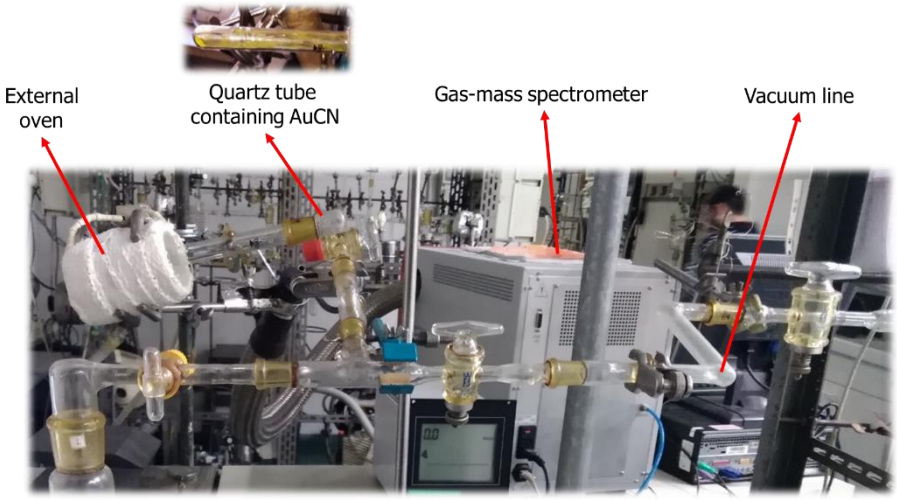

Figure 24. Experimental setup used to monitor the evolution of the gas-phase composition obtained during thermal treatment of AuCN powder.

Once the best conditions were identified, HCN was produced, purified, and stored by the standard procedure described in the following and by means of the setup illustrated in *Figure 25*. The same setup was also suitable to dose HCN on the solids of interest and to perform in situ IR experiments:

i. The AuCN/Pd powder was first outgassed at ca. 120 °C under vacuum up to a residual pressure of $5 \cdot 10^{-4}$ mbar.

ii. The portion of line including the quartz tube containing the AuCN/Pd, the HCN collection flask (equipped with a cold finger) and the trap containing $CaCl_2$ desiccant (previously outgassed at 150 °C) was isolated from the vacuum system and then H_2 (ca. 20-30 mbar) was admitted from a reservoir connected to the line.

iii. The AuCN/Pd mixture was heated at 250 °C for 2-3 hr in presence of H_2.

iv. The produced HCN was collected in the storage flask by cooling the cold finger with liquid nitrogen and finally purified by repeated freeze-thaw cycles to remove H_2 excess.

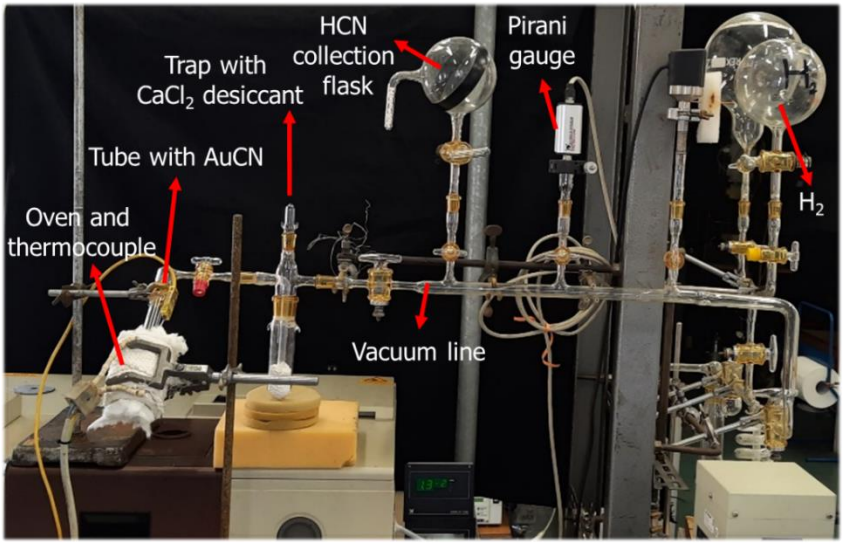

Figure 25. Experimental setup employed for HCN production.

1. European Centre for Ecotoxicology Toxicology of Chemicals; *Cyanides of Hydrogen, Sodium and Potassium, and Acetone Cyanohydrin*: (CAS No. 74-90-8, 143-33-9, 151-50-8 and 75-86-5). ECETOC: **2007**.
2. SECTION 11 - CARBON. In Handbook of Preparative Inorganic Chemistry (Second Edition), Brauer, G., Ed. Academic Press: **1963**; pp 630-675.
3. Holub, A. M.; Köhler, H.; Skopenko, V. V., *Chemistry of Pseudohalides*. Elsevier: 1986.
4. Pazé, C.; Bordiga, S.; Spoto, G.; Lamberti, C.; Zecchina, A., *IR spectroscopy of CH_3CN–HCl adducts in silicalite channels A model system for the study of acid–base reactions in zeolites.* Journal of the Chemical Society, Faraday Transactions **1998,** 94 (2), 309-314.
5. Brotherton, T. K.; Lynn, J. W., The Synthesis And Chemistry Of Cyanogen. Chemical Reviews **1959,** 59 (5), 841-883.
6. Beck, M. T.; Bertóti, I.; Mohai, M.; Németh, P.; Jakab, E.; Szabó, L.; Szépvölgyi, J., *Gold nano-particle formation from crystalline AuCN: Comparison of thermal, plasma- and ion-beam activated decomposition*. Journal of Solid State Chemistry **2017,** 246 (November 2016), 65-74.
7. Prins, R., *Hydrogen Spillover. Facts and Fiction*. Chemical Reviews **2012,** 112 (5), 2714-2738.
8. Maya, L., *Paracyanogen reexamined. Journal of Polymer Science Part A: Polymer Chemistry* **1993,** 31 (10), 2595-2600.
9. Robertson, N. C.; Pease, R. N., *The Kinetics of the Thermal Reaction between Hydrogen and Cyanogen.* Journal of the American Chemical Society **1942,** 64 (8), 1880-1886.

Chapter 3

IR investigation of the HCN interaction with SiO_2, TiO_2, Al_2O_3 and MgO at 150 K

In this Chapter the results of the IR spectroscopic investigation of the HCN interaction with SiO_2, TiO_2, Al_2O_3 and MgO are reported and discussed.

These oxides have been chosen because: (i) in the past their surface properties have been extensively investigated in surface science and catalysis; (ii) they have different surface structures and therefore possible different activities toward HCN and (iii) they can be considered as reference solids to study the role of heterogeneous chemistry in prebiotic issues.

As far as point (ii) is concerned, the surface properties of SiO_2 mainly depend on the presence of defective hydroxyl groups (Si-OH) which confer to the solid weak Brønsted acidity, while the surface properties of TiO_2, Al_2O_3 and MgO are mainly due to the presence of coordinatively unsaturated acid (M^{n+}) and base (O^{2-}) Lewis sites with different structures and chemical behaviour.

On all the materials the interaction with HCN from the gas phase was investigated by *in situ* IR spectroscopy at variable temperature in the 77-300 K range. The variable temperature methodology was adopted aiming to investigate the different surface steps (if any) related to the HCN/solid interaction (namely adsorption, activation, formation of

complex products). Moreover, the chosen range (77-300 K) is also compatible with the temperatures of some typical prebiotic environments (like interplanetary regions, meteorites, and comets' surfaces).

As it will be shown in the following, on all the investigated solids the predominant phenomenon at around 150 K is HCN adsorption (in molecular and/or dissociated form) while at higher temperature (except for the SiO_2 case) a complex surface chemistry occurs catalysed by the solid surface. For sake of clarity the two steps will be illustrated and discussed separately, the adsorption in this chapter and the reactivity in the *Chapter 5*.

Some background information on the IR spectroscopy of the HCN molecule itself are given in paragraph *3.1*, while paragraph *3.2* provides some basic information about the nature of the oxide samples and of the treatments they underwent before interaction with HCN, as well as a short description of the adopted experimental procedure.

Finally, for each investigated solid, more detailed information on the surface structure and properties, as described in the specialized literature, will be provided, before the discussion of the experimental results.

3.1 The IR spectrum of HCN

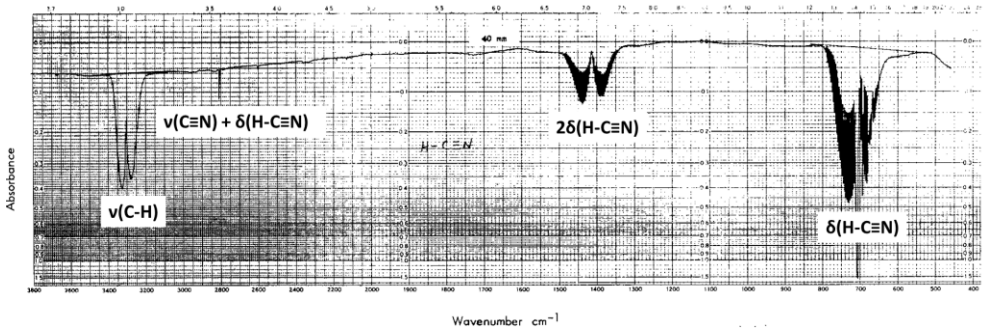

Observed frequency (cm^{-1})	Observed intensity	Observed band shape	Assignment
712	Very strong	PQR	**Fundamental** Bend (ν_2)
1412	Strong	PR	Combination of 2 Bends ($2\nu_2$)
2089	IR-inactive	PR	**Fundamental** HC-N stretch (ν_1)
2800	Strong	PQR	Combination of HC-N stretch and a bend ($\nu_1+\nu_2$)
3311	Strong	PR	**Fundamental** H-CN stretch (ν_3)

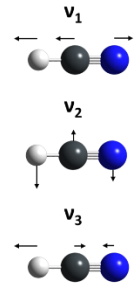

Figure 26. HCN Spectrum from NIST database and assignment from ref. [1]

The IR spectrum of gaseous HCN is reported in *Figure 26* together with the assignment of its roto-vibrational features. The most intense absorptions are due to the C-H stretching (3311 cm^{-1}) and H-C-N bending (712 cm^{-1}) modes, while it is noteworthy that the C≡N stretching (2089 cm^{-1}) is inactive in the gas phase.

3.2 Experimental details

Materials

- ✓ **SiO_2:** pyrogenic silica Aerosil AOX50 (EVONIK, formerly Degussa), Specific Surface Area (SSA) = 50 m^2/g. AOX50 samples differing for the surface hydration degree were used. They are labelled in the following according to the thermal pre-treatment in vacuo they underwent before HCN dosage:
  - **AOX50@rt**: *i.e.,* sample outgassed in vacuum at room temperature to remove physisorbed water.
  - **AOX50@973K**: *i.e.,* sample outgassed in vacuum at 973 K to obtain surface dehydroxylation.

- ✓ **TiO_2:** pure anatase samples were used differing for the particles morphology:
  - **a-TiO_2**: commercial anatase nano-powder (Sigma-Aldrich), SSA ≈ 140m^2/g.
  - **TiO_2 truncated bipyramid:** shape engineered anatase nanoparticles (SSA ≈ 37 m^2/g) prevalently exposing (001) terminations.
  - **TiO_2 nano-sheet**: shape engineered anatase nanoparticles (SSA ≈ 34 m^2/g) prevalently exposing (101) terminations.

    The shape engineered samples where synthesized[2] and kindly provided by Professor V. Maurino of our Department of Chemistry.

Before HCN dosage, all the TiO_2 samples were outgassed at 773 K for 2 hours under high vacuum (residual pressure $5x10^{-4}$ mbar) to remove adsorbed surface contaminants (H_2O, carbonates, and bicarbonates). Under these conditions titania undergoes partial reduction by oxygen release; to obtain fully stoichiometric Ti(IV)O_2 all the outgassed samples were treated with O_2 (20 mbar) at 773 K for 15 minutes (repeated two times), cooled down to 393 K in O_2 and finally outgassed at room temperature.

- ✓ **Al_2O_3:** nano-powder γ-Al_2O_3 (SSA ≈120 m^2/g; pore volume ca. 0.40 cm^3/g) samples were used (kindly provided by Chimet Laboratories) outgassed under vacuo at 1000 K and oxidized with O_2 at the same temperature before HCN dosage.

- ✓ **MgO:** two different MgO materials were used, differing for the SSA and the particles morphology:
  - **MgO hsa (high surface area)**: SSA≈200 m^2g^{-1}, prepared by slow thermal decomposition of magnesium hydroxide (Sigma-Aldrich) in vacuo at ca. 523 K, then outgassing at 1073 K in vacuo and treatment in O_2 at 773 K.
  - **MgO smoke**: SSA≈10 m^2g^{-1}, obtained by direct combustion of an Mg metal ribbon in air. To avoid surface contamination and surface reconstruction the obtained powder was stored

under inert atmosphere prior usage and outgassed at 1073 K before HCN dosage.

Methods

For the transmission IR spectroscopic measurements, the powder samples were pressed in form of thin self-supporting pellets and inserted in an all-quartz cell, equipped with IR transparent KBr windows and a valve for connection to a vacuum line (residual pressure $5 \cdot 10^{-4}$ mbar). This setup allows adsorption/desorption experiments to be carried out *in situ* under controlled atmosphere. The cell is also designed to carry out low temperature experiments by cooling the sample by means of a reservoir of liquid nitrogen (*Figure 27*).

Before HCN dosage, all samples were subjected to thermal treatments already described in paragraph 3.2. All the experiments with HCN were performed in the same conditions, namely by dosing HCN gas (typically 5 mbar equilibrium pressure) into the cell cooled with liquid N_2 (*i.e.* at a nominal temperature of 77 K). In this conditions the gas frozes on the walls of the liquid nitrogen reservoir, which are colder than the sample heated by the IR beam, without reaching it. The temperature of the system is then allowed to slowly increase. In this way HCN is gradually released and reaches the sample when its temperature is estimated to be ≈150 K. The first spectra sequence can be essentially described as the dosage of increasing amounts of HCN at constant temperature (150 K). As it will be shown, the main phenomenon occurring at this stage is HCN adsorption at the oxides surfaces. The temperature of the HCN/solid system is then allowed to freely rise up

to 300 K and kept constant, typically for 1 hr. As it will be clear later, in the 150-300 K range a chemical evolution of the HCN/solid systems takes place with formation of a variety of surface products.

For sake of clarity, in the following the two steps, *i.e.* (i) the adsorption of increasing doses of HCN at 150 K and (ii) the chemical evolution of the HCN/solid systems as a function of the temperature in the 150-300 K interval and of the contact time at 300 K, will be discussed separately (with the only exception of SiO_2 on which the second step does not take place). The adsorption and the system evolution were monitored *in situ* by continuously acquiring IR spectra by means of a Bruker EQUINOX 55 FTIR spectrometer, equipped with a DTGS detector. Typically, 128 interferograms (at 4 cm^{-1} resolution) were acquired for each spectrum to attain a good signal-to-noise ratio.

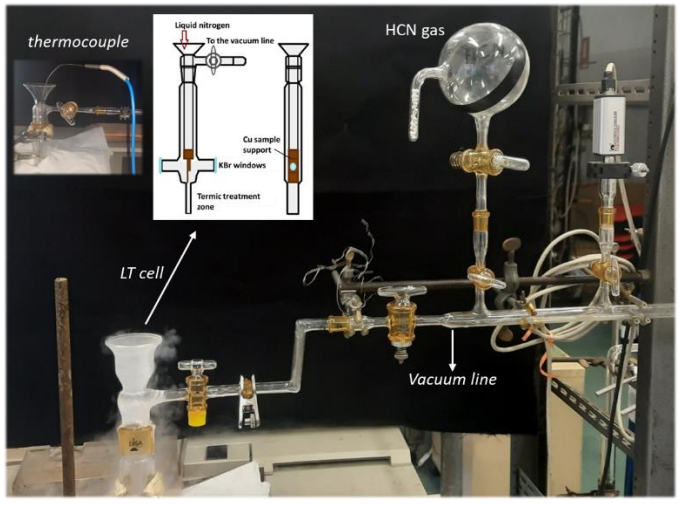

Figure 27. Experimental setup adopted for in-situ IR investigation of the HCN (gas)/solid (SiO_2, TiO_2, Al_2O_3 and MgO) interaction in the 77-300 K temperature range. The sample temperature during the experiments was estimated by means of an external thermocouple located as shown in the inset.

3.3 Amorphous silica (SiO_2)

3.3.1 SiO_2 surface structure and chemical properties

About 90% of the Earth crust is composed by silicates. The simplest member (and the most abundant) is silica (SiO_2), a covalent solid whose structure consists of tetrahedral $[SiO_4]^{4-}$ units connected through the corner oxygens to form a variety of ordered (crystalline) and disordered (amorphous) polymorphs (*Figure 28*).

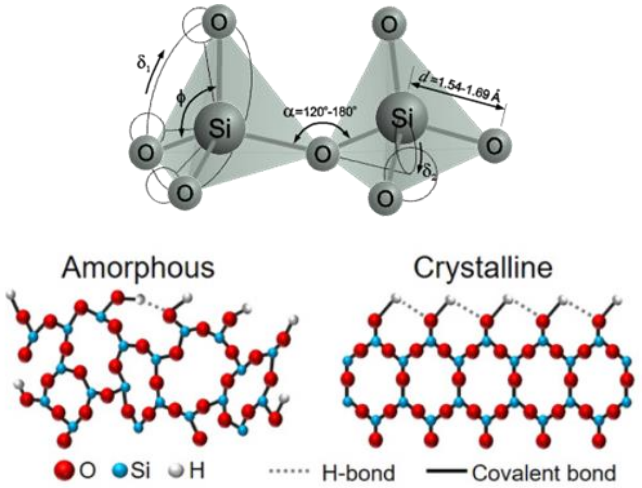

Figure 28. Typical Si-O-Si bond angles and lengths of interconnected $[SiO_4]^{4-}$ units with the schematic representation of the amorphous and crystalline SiO_2 structures. Adapted from ref. [3]

As mentioned above, the material used in this thesis is a commercial pyrogenic (or fumed) amorphous silica (AOX50) which is prepared by combustion at high temperature (1300 °C) of $SiCl_4$ following the reaction:

$$SiCl_4 + O_2 + 2H_2 \rightarrow SiO_2 + 4HCl$$

Most of the physical and chemical properties of this material, and in general of SiO_2, are related to the structure of the external surface, which is terminated by Si-O-Si (siloxane) bridges and Si-OH groups (silanols) in a relative amount which depends on the sample preparation procedure (*Figure 29*).

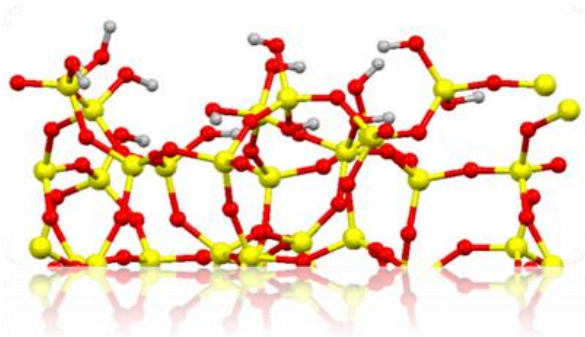

Figure 29. Computer simulation of the surface structure of dehydrated amorphous silica showing the coexistence of Si-O-Si (siloxane bridges) and SiOH (silanol groups or silanols) terminations. Si atoms are shown in yellow, O in red and H in grey. Model kindly provided by the Theoretical Chemistry Group of our Department of Chemistry.

Among other properties, silanols confer to silica a hydrophilic character as they can interact with polar molecules like H_2O through hydrogen bond (H-bond) interactions; siloxane groups are on the contrary moderately hydrophobic. Because of the hydrophilicity, when exposed to air or moisture the silica surface is fully hydrated, as shown on the left part of *Figure 30.*

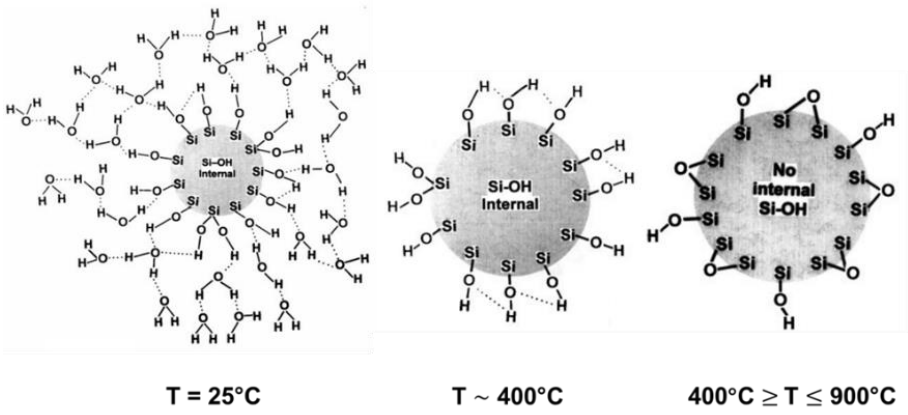

Figure 30. Schematic representation of the surface functionalization of a SiO_2 particle as a function of the temperature. Adapted from ref.[4]

Upon heating the surface gradually loses the adsorbed water leaving a hydroxylated surface manly populated by silanols groups (central part of *Figure 30*). For temperatures higher than 400°C, the silanols condensation process takes place following the scheme:[3]

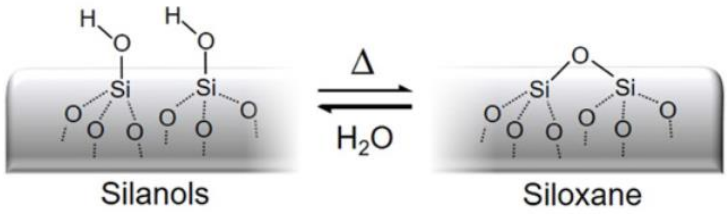

which finally results in a surface exposing siloxane bridges and residual, isolated silanols (right part of *Figure 30*).

As shown in the following scheme, in particular conditions (high-temperature treatments performed under dynamic vacuum), siloxane bridges can originate a variety of strained $(Si\text{-}O)_N$ rings.

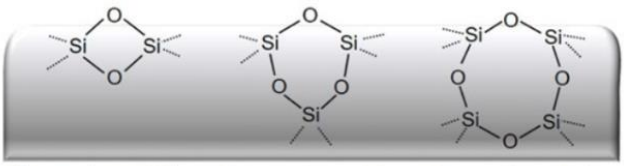

The strained structures are of particular interest as they can be opened through heterolytic or homolytic mechanisms by reaction with foreign molecules to give chemisorbed and/or reactive species, as schematized below for H_2O (see ref.[3] and references therein):

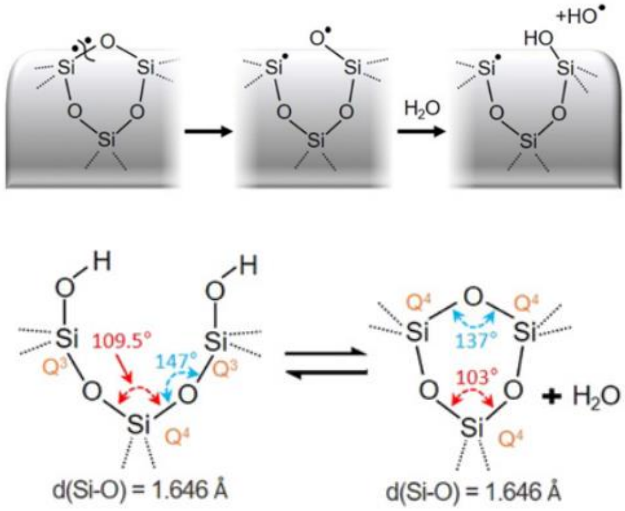

Similar mechanisms operate also in case of more complex molecules. For instance, methanol is heterolytically split on highly dehydroxylated silica with formation of Si-O-H and methoxy Si-O-CH_3 groups:[5]

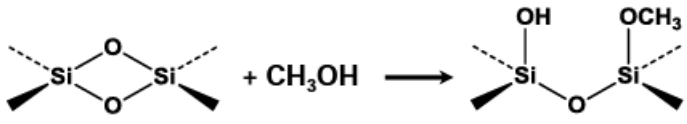

As far silanols are concerned, it is possible to distinguish different families according to number of OH groups *per* Si atom, to their reciprocal distance and, when at proper distance, to the strength of their reciprocal interaction by hydrogen bonding (*Figure 31*).[6]

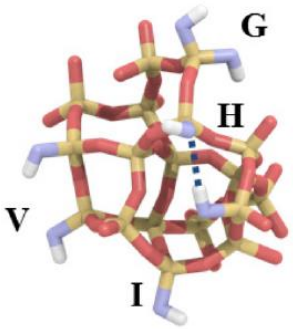

Figure 31. A cartoon of the possible silica surface sites: isolated SiOH (I, Q3), geminal SiOH (G, Q2), vicinal SiOH (V, Q3), and H-bonded SiOH (H, Q3). From ref.[12]

The relative concentration of the different families of silanols and of siloxane bridges depend on the outgassing temperature, as shown in *Figure 32*.

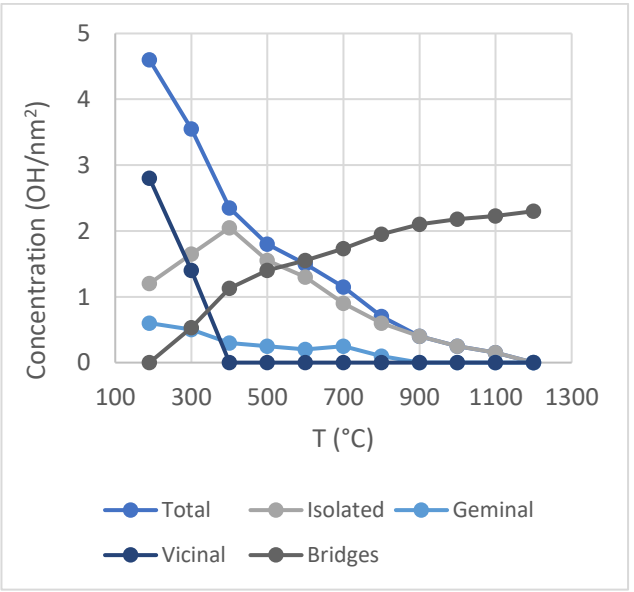

Figure 32. Concentration (number/nm^2) of the different silanol species and of siloxane bridges at the SiO_2 surface as a function of the outgassing temperature under vacuum (based on the data of ref. [4]

The silanol groups confer to silica weak Brønsted acidity. Fumed silica outgassed at high temperature (973 K) is for instance able to adsorb NH_3, by the (predominant) formation of -SiO-H···NH_3 hydrogen bonded adducts which involve isolated silanols.[7, 8] Some more due to CO adsorption, the formation of -SiO-H···CO and -SiO-H···OC species in a mutual equilibrium controlled by the adsorption temperature can be observed.[9]

They are also characterized by different IR manifestations[10] which are heavily and characteristically affected by the presence of adsorbates (see the next experimental part). For instance, the formation of Si-O-H···B complexes (where B = NH_3, CO, H_2O, etc.) results in the perturbation of the vibrational modes of both the Si-O-H groups and of the adsorbed B molecule. In particular, the bands due to O-H stretching modes shift to lower frequency while their bandwidth increases. Both the shift and the bandwidth are correlated with the adsorption energy.[11]

3.3.2 Silica and prebiotic chemistry

Silicates are abundant not only on Earth but also in extra-terrestrial environments like meteorites, comets, and interstellar dust particles. The relevance of silica as suitable reference material for studies in the field of prebiotic chemistry is therefore self-evident.[12] For this kind of investigations, amorphous silica has been usually preferred to

crystalline quartz, although the latter is more abundant in nature. This choice is justified by the fact that, while having identical composition and similar surface terminations, amorphous silica has a much higher specific surface area (50 m^2/g), and optical properties which make it more appropriate for spectroscopic and/or catalytic investigations.

To mention some literature studies concerning SiO_2 in prebiotic concerns, fumed silicas (AEROSIL) have been used as substrates for the investigation of the abiotic polymerization of amino acids and for the formation of the AMP (adenosine monophosphate) nucleoside.[13] Martra et al. have investigated the role played by silanols in amidation reactions,[14, 15] while Signorile et al.[16] have studied the reactivity of formamide (namely the HCN hydration product) in presence of amorphous silica samples with different surface silanols population.

3.3.3 The HCN/SiO_2 interaction in the 150-300 K temperature range: experimental results and discussion

Unlike the other investigated solids, the interaction of HCN with SiO_2 gives rise only to physisorption, without any evidence of surface reactivity; for this reason, the complete spectral series obtained in the whole 150-300 K will be illustrated and discussed here at once.

To evaluate the effect of different surface silanols populations, the HCN adsorption has been studied on two AOX50 samples pretreated under vacuum at 973 K (hereafter AOX50@973K) and at 300 K (AOX50@rt). The spectra of the two materials before HCN dosage are compared in *Figure 33*.

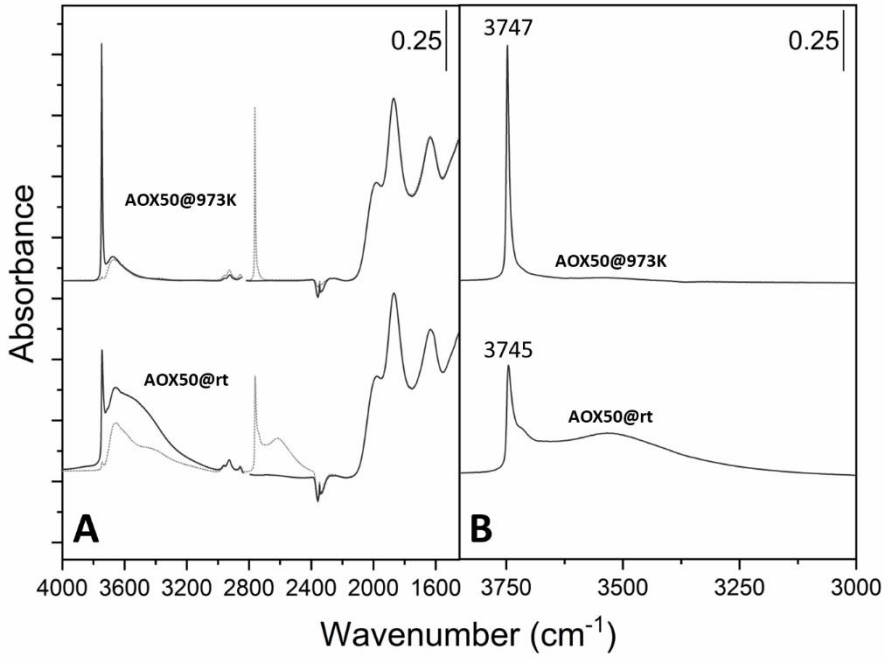

Figure 33. Part A: IR spectra of AOX50 samples outgassed at 973 K (AOX50@973K, solid line) and at 300 K (AOX50@rt, solid line). The dotted spectra were obtained after OH/OD exchange with D_2O. Part B: difference spectra in the OH stretching region obtained by subtraction of the D-exchanged spectrum from the H-exchanged one for the two samples.

From the spectra of both the AOX50@973K and AOX50@rt the absorptions in the 2000-1400 cm^{-1} region of part A are due to overtone and combination modes of the low frequency (< 700 cm^{-1}) SiO_2 framework vibrations[17] and will not be further discussed here; they are absent in the difference spectra of part B because fully compensated.
The sharp band at 3747 cm^{-1} in the spectrum of H-exchanged AOX50@973K is due to the $\nu_{(OH)}$ stretching vibration of the residual, isolated silanols (*Figure 34*). This absorption disappears when H is exchanged for D and it is replaced by the corresponding $\nu_{(OD)}$ manifestation isotopically shifted to 2762 cm^{-1} (dotted line in Part A of *Figure 33*). This behaviour indicates that the silanol groups responsible for the 3747 cm^{-1} band are fully accessible to external molecules. This is not the case for those responsible for the broad tail (centred at 3660 cm^{-1}) on the low frequency side of the main peak. Indeed, this feature has been assigned to inaccessible (in the present case to D_2O) OH groups which are entrapped in internal voids generated by aggregation of the first formed particles during the SiO_2 pyrogenic synthesis (intraglobular OHs).[18] Therefore, it can be concluded that the spectrum of the AOX50@973K sample reported in part B of *Figure 33* represent the spectroscopic fingerprint of the external, accessible to foreign molecules, isolated silanols. Concerning the IR manifestations of the sample outgassed at room temperature (AOX50@rt), together with the narrow peak at 3745 cm^{-1} due to isolated silanols, it is possible to recognize in part B of *Figure 33* a broad absorption centred at 3530 cm^{-1} due to the $\nu_{(OH)}$ stretching vibration of silanols engaged in strong hydrogen bonding interaction (*Figure 34*).[10]

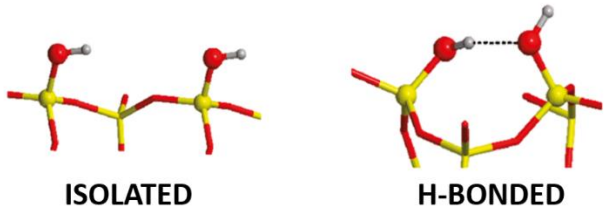

Figure 34. Models for the isolated and H-bonded silanol groups at the amorphous silica surface.

It is worth noticing that engaging the O-H groups in hydrogen bonding interactions results in the lowering of the $\nu_{(OH)}$ stretching frequency and in the increasing of the FWHM (Full Width at Half Maximum) of the corresponding band. Both the shift and the FWHM are depending on the strength of the interaction. Similar spectroscopic effects are observed when the Brønsted acid Si-O-H groups are engaged in hydrogen bonding interactions with basis to form Si-O-H···B surface adducts.[6, 19] Unlike the silanols groups, the siloxane bridges which are generated by the dehydroxylation process at high temperature do not give rise to any observable spectroscopic fingerprint, being their vibrational modes buried in the intense low frequency (<700 cm^{-1}) absorptions due to the SiO_2 framework modes (not shown for sake of brevity).

The effect of dosing increasing amounts of HCN at 150 K on the AOX50@973K sample is shown in the upper part of *Figure 35* (labelled as "ads LT"); the evolution of the spectra in the 150-300 K range is shown in the bottom part (LT→RT).

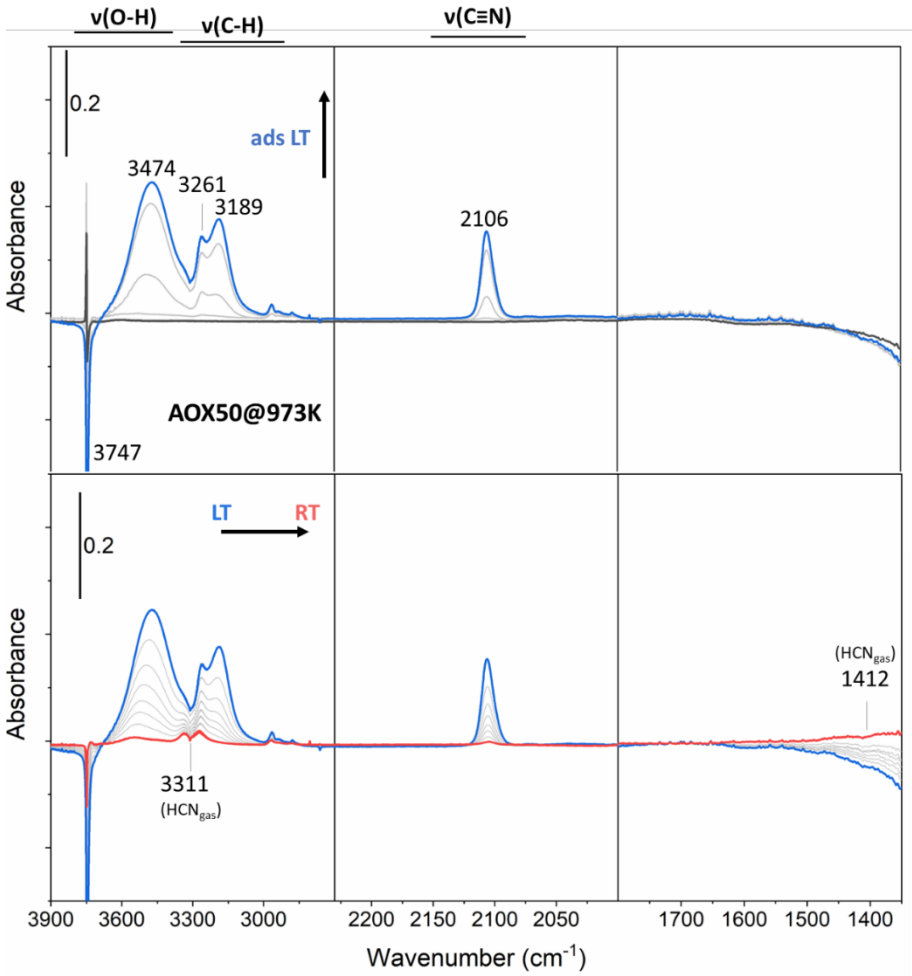

Figure 35. IR spectra obtained upon interaction of gaseous HCN with an AOX50 SiO_2 sample outgassed at 973 K (AOX50@973K). The series in the top panels was obtained at 150 K on increasing the HCN equilibrium pressure (from the dark grey to the blue curve); those in the bottom panels on increasing the temperature from 150 (blue curve) to 300 K (red curve). The red line in bottom panels is the spectrum recorded after 1 h of contact at 300 K. All the spectra are background subtracted, i.e., obtained after subtraction of the spectrum of pure SiO_2, and hence the negative peaks belong to species which are consumed following the HCN/solid interaction and the positive to species which are formed.

As evident in *Figure 35* (upper part) the interaction of HCN at 150 K with highly dehydroxylated AOX50@973K samples results in the gradual erosion with the HCN coverage of the $\nu_{(OH)}$ band at 3747 cm^{-1}

(due to isolated silanols) with parallel formation of a broader absorption (FWHM ≈ 250 cm^{-1}) centred at 3474 cm^{-1} ($\Delta\bar{\nu}_{(OH)}$ = -273 cm^{-1}). Based on the literature concerning the interaction of acid solids with basic molecules[6, 19] this behaviour is the clear evidence of the hydrogen bonding interaction between the SiO_2 isolated silanols and the hydrogen cyanide molecule to form SiOH···(HCN) acid/base adducts.

The interaction also causes (i) the perturbation of the $\nu_{(C-H)}$ mode of the engaged HCN molecules, as witnessed by the appearance of two absorptions at 3261 and 3189 cm^{-1} (downward shifted of 50 and 122 cm^{-1}, respectively, with respect to the 3311 cm^{-1} $\nu_{(C-H)}$ frequency of the gas molecule) and most noticeably (ii) the appearance of a medium-strong band at 2106 cm^{-1} undoubtedly associated with the C≡N stretching vibration. The $\nu_{(CN)}$ vibration is IR inactive in the free molecule but gain intensity in the adsorbed state because of a lowered symmetry and of polarization effects, the latter also responsible for its up-ward shift of *ca*. 17 cm^{-1}.

On increasing the temperature up to 300 K (bottom panels), all the above bands gradually decrease in intensity and finally disappear nearly completely at r.t. (from blue curve to red curve in *Figure 35*) when they are substituted by those of HCN gas (at 3311 and 1412 cm^{-1}). This indicates that the SiOH···(HCN) adducts are not stable at r.t. and that their formation is a fully reversible process. It is worth underlining the absence in *Figure 35* of any other spectroscopic manifestation which may be related to HCN chemisorption possibly involving the distorted Si-O-Si bridges (for instance by heterolytic

splitting mechanisms like that reported for H_2O and ROH[5] to form Si-CN and Si-OH species).

The spectral series (grey curves in bottom panels) of the AOX50@973/HCN system recorded while the temperature rises from 150 K (blue curve) to 300 K (red curve) deserve some further comments:

(i) it is evident that the intensities of the $\nu_{(OH)}$ band at 3474 cm^{-1} and of $\nu_{(CH)}$ at 3261 cm^{-1} change with the temperature in a parallel way and that the decrease in intensity of this doublet is parallel to the increase in intensity of the isolated silanols absorption at 3747 cm^{-1}. Together with the presence of a clear isosbestic point at ca. 3680 cm^{-1}, this behaviour suggests that the species responsible for the 3747 cm^{-1} band (isolated silanols) are transformed in a 1:1 ratio into those responsible for the 3474 and 3261 cm^{-1} doublet (*i.e.,* the Si-OH(HCN) hydrogen bonded adducts) and *vice versa* following the equilibrium reaction:

$$\text{Si-OH} + \text{HCN} \underset{\text{High T}}{\overset{\text{Low T}}{\rightleftarrows}} \text{Si-OH}\cdots\text{(HCN)}$$

For these adducts the structure schematized below can be reasonably hypothesised, being the wavenumbers of the OH, CN and CH functional groups reported in cm^{-1} together with their shift, with respect to free Si-O-H and HCN, in parenthesis:

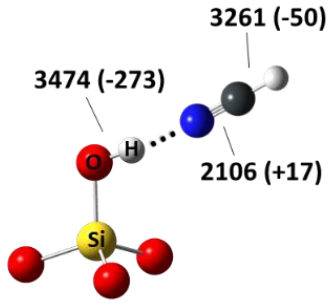

I

A similar structure has been proposed for the silanols interaction with CH_3CN, a bases which has a proton affinity (PA = 783 KJ/mol) comparable with that of HCN (PA = 713 KJ/mol), which causes a redshift of the silanol $\nu_{(OH)}$ frequency similar to that observed with HCN ($\Delta\nu_{(OH)} \approx 300$ cm^{-1}).[6]

(ii) It is evident that the $\nu_{(CH)}$ band at 3189 cm^{-1} behaves in a different way, as it disappears much faster than the 3474−3261 cm^{-1} doublet on increasing the temperature. This suggests that, due to HCN adsorption, the formation of different species can be highlighted. The remarkable download shift of the $\nu_{(CH)}$ frequency with respect to the gas (-122 cm^{-1}) suggests the possibility of an interaction of the HCN molecule through the C-H end. Possible candidates are: (a) the oxygen atoms of Si-O-Si siloxane bridges (especially those in distorted configurations); (b) the oxygen atoms of the Si-O-H groups and (c) the already adsorbed HCN molecules of the SiOH/HCN complexes, to give adsorbed HCN dimers, trimers, etc. The interaction of HCN with surface oxygens has been already hypothesized on solids like TiO_2[20] and Al_2O_3[21] where downward

shifts of the $\nu_{(CH)}$ mode of the order of 160-200 cm^{-1} are reported. Notice that these shifts, although larger, look still compatible with those observed on AOX50@973K (-122 cm^{-1}) when the stronger basic character of the oxygen centres in the more ionic TiO_2 and Al_2O_3 structures is taken into account. Structures II and III reported below schematically represent the results of possible adsorption mechanisms involving the oxygen of a silanol group (II) or an already adsorbed HCN molecule to form an adsorbed HCN dimer (III).

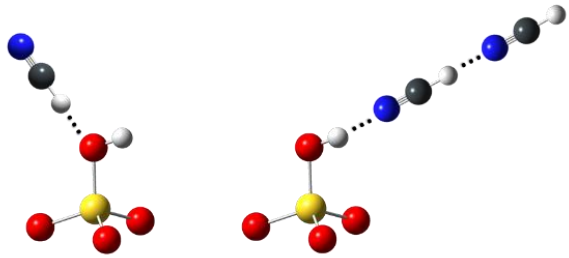

II III

Formation of $N(C\text{-}H)_{HB}\cdots N(C\text{-}H)_t$ dimers similar to that of structure II have been studied in very cold (20-8 K) Ar, N_2 and CO matrices and differences between the $\nu_{(CH)}$ frequencies of the hydrogen bonded $(C\text{-}H)_{HB}$ and of the terminal $(C\text{-}H)_t$ CH groups of the order of 40-100 cm^{-1} are reported.[1] The splitting (72 cm^{-1}) of the CH doublet in *Figure 35* falls in this interval. It is however a matter of facts that the formation of the dimer in cold matrices also results in coupling between the two C≡N oscillators with a splitting of the $\nu_{(CN)}$ frequencies of about 20-25 cm^{-1}. Similar splitting is not observed in *Figure 35*, where the

$\nu_{(CN)}$ band at 2106 cm^{-1} appears on the contrary highly symmetrical and without any trace of sub-components.

In conclusion the assignment of the 3189 cm^{-1} absorption in the spectra of the AOX50@973K/HCN system (*Figure 35*) looks troublesome based on the IR spectroscopic data alone and will hopefully benefit of the results of quantum mechanics calculations which are in progress.

Moving finally to illustrate and discuss the spectra obtained for the HCN adsorption on the hydroxylated AOX50@rt sample, it is evident from *Figure 36* (where only the spectral series recorded from 150 K to 300 K is shown, for sake of brevity) that they do not differ substantially from those of the sample dehydroxylated at 973 K (bottom part of *Figure 35*).

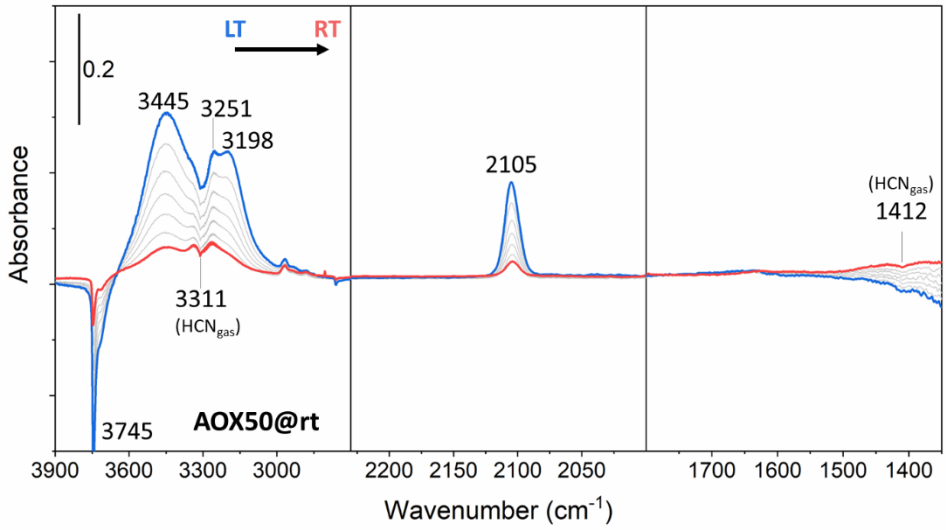

Figure 36. Background subtracted IR spectra obtained upon interaction of gaseous HCN with SiO_2 outgassed at room temperature (AOX50@rt), in the 150-300 K temperature range. i) The

blue curve is the spectrum after HCN dosage (5 mbar equilibrium pressure) at 150 K, (ii) the grey lines are the spectral sequence obtained by allowing the temperature to freely rise up from 150 to 300 K in presence of HCN gas. The red line is the spectrum recorded after 1 hr of contact at 300 K.

In general, the bands of the HCN/AOX50@rt system look less defined with respect to HCN/AOX50@973K: this is not unexpected as the surface of the hydroxylated sample is more heterogenous in terms of silanols population. The most relevant difference is however represented by the fact that, unlike on AOX50@973K, the manifestations associated with the 1:1 SiOH···(HCN) adducts (at 3445, 3251 and 2105 cm^{-1}) are still present in the spectrum at r.t. of the hydroxylated sample with not negligible intensity. It is thought that this behaviour is the consequence of the more acid character of terminal $(OH)_t$ silanols in ···O-H···O-H···O-H···$(O-H)_t$ chains of H-bonded SiOH groups (which of course are absent on the dehydroxylated sample), which makes their hydrogen bonded complexes more stable at r.t..

In conclusion, the detailed investigation of the HCN interaction with SiO_2 at variable temperature allows to conclude that HCN is reversibly adsorbed by hydrogen bonding mechanisms, involving the surface silanols (as already hypothesized in previous works. [20, 22, 23] Moreover, there are no evidence of HCN chemisorption products nor formation of large HCN polymeric species which could represent precursors for the formation of prebiotic molecules (paragraph *1.3.3.2*).

3.4 Titanium dioxide (TiO_2)

3.4.1 TiO_2 surface structure and chemical properties

The most common TiO_2 polymorphs are anatase, rutile and brookite. The crystal structures made by TiO_6 octahedra sharing corners, edges, and faces are shown in *Figure 37*.

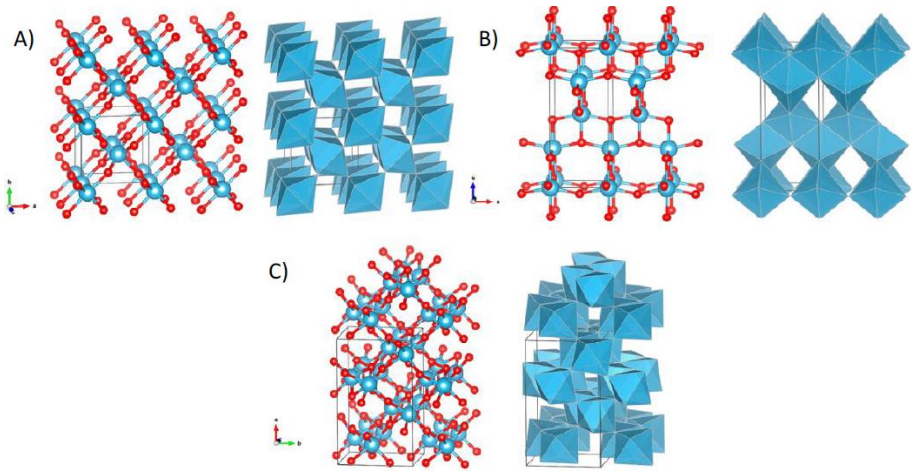

Figure 37. Structures of TiO_2 phases presented in the ball-and-stick models and in the polyhedron model. A) Rutile; B) Anatase; C) Brookite. Reproduced from ref. [24]

Rutile (the thermodynamically stable phase) and above all anatase have been extensively investigated in recent times because of their outstanding properties for applications in photocatalysis, solar energy conversion, environmental pollution remediation and as biomaterial.[24] They both crystallize in the tetragonal crystal system but differ for the dimension of their respective unit cells. Some more, the anatase structure is distorted along the crystallographic *c* direction (*Figure 38)*.

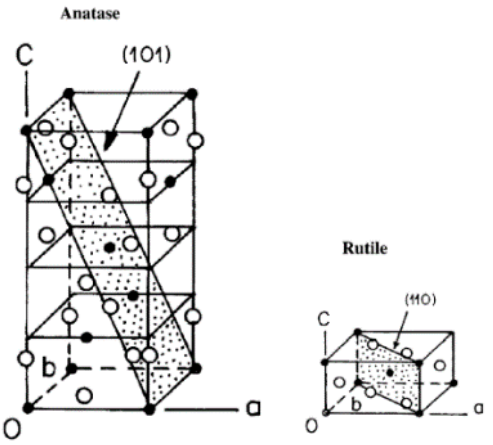

Phase	Rutile	Anatase
Cristal system	Tetragonal	Tetragonal
a (Å)	4.5941	3.7842
b (Å)	4.5941	3.7842
c (Å)	2.9589	9.5146

Figure 38. Structural characteristics of rutile and anatase crystalline phases. Adapted from ref. 24, 25

Most of the literature devoted to the TiO_2 photocatalytic properties concern TiO_2 P25, a commercial (Degussa/Evonik) material which is an intimate mixture of anatase (85%) and rutile (15%) obtained by combustion of Ti-alkoxides. Nevertheless, for the scopes of the thesis, pure anatase samples, having controlled shape, were used, as described in paragraph 3.4.4. This allows to correlate particles morphology and surface structure with the photocatalytic properties.[25] The most common morphology of the anatase nanoparticles is that of truncated bipyramid mainly exposing the (101) and (001) surfaces, and (110), (100) and (103) terminations at much less extent. The (101) is the thermodynamically most stable surface (*Table 9*) and, according to

the Wulff construction, it represents more than 90% of the total surface of the anatase particles (*Figure 39*).[26]

Table 9. Comparison of calculated surface formation energies (in J/m^2) for relaxed, unreconstructed TiO_2 surfaces. Two different structures for the (103) surfaces (a "faceted" and a "smooth" one) have been considered. From ref. [26]

Rutile (1 1 0)	0.31
Anatase (1 0 1)	0.44
(1 0 0)	0.53
(0 0 1)	0.90
$(1\,0\,3)_f$	0.83
$(1\,0\,3)_s$	0.93
(1 1 0)	1.09

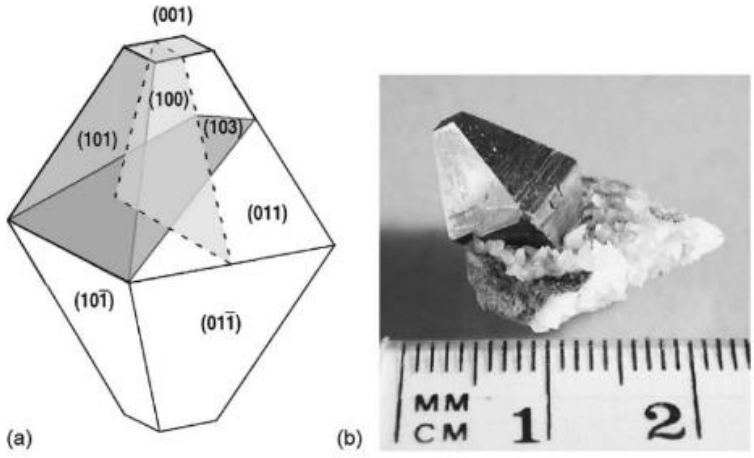

Figure 39. (a) The equilibrium shape of TiO_2 crystal in the anatase phase, according to the Wulff constructions and surface energies given in Table 10. (b) Photograph of an anatase mineral crystal.

The surface structure of the prevalent (101) and (001) terminations is schematized in *Figure 40*:

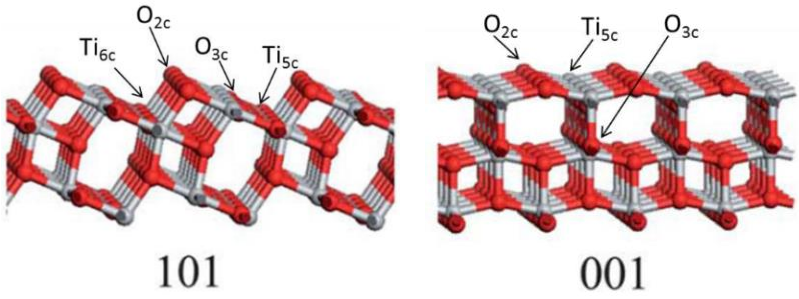

Figure 40. Computer simulation of the anatase (101) and (001) surfaces. The coordinative status of the exposed cations and anions is also indicated (from ref. [27]).

The (101) surface exposes Titanium atoms in 5-fold (Ti_{5C}) and 6-fold (Ti_{6C}) coordination, and Oxygen atoms in 2-fold (O_{2C}) and 3-fold (O_{3C}) coordination. The (001) surface exposes coordinatively unsaturated Ti_{5C} cations together with O_{2C} and O_{3C} anions (*Figure 40*). The surface density (sites per nm^2) of the ions exposed on (101) and (001) anatase terminations, as well as on less common faces, is listed in *Table 10*.[28]

Table 10. Surface density (sites per nm^2) of the atoms exposed by the various crystal surfaces of anatase. From ref. [28]

anatase crystal surface	Ti_{6C}	Ti_{5C}	Ti_{4C}	O_{3C}	O_{2C}
(101)	5.1 (5.2)	5.1 (5.2)		5.1 (10.4)	5.1 (5.2)
(100)	5.4 (5.6)	5.4 (5.6)		5.4 (11.2)	5.4 (5.6)
(001)		6.9 (7.0)		6.9 (7.0)	6.9 (7.0)
(110)	(7.9)		3.8 (4.0)	(7.9)	7.7 (7.9)
$(103)_f$	(3.6)	(7.2)		(10.7)	(7.2)

The exposed surfaces, under normal conditions, are covered by OH hydroxyl groups and molecularly adsorbed water, which are widely removed by thermal treatments in vacuum, although not completely as far as the OH groups. The number of residual OH groups is depending on the samples morphology as well as on the temperature and external pressure during the thermal treatments.[29, 30]

The properties of the Ti^{4+} and O^{2-} centres and of residual OH groups and their dependence on the sample morphology have been investigated in the past, mainly by means of IR spectroscopy of adsorbed molecular probes. Among them, it is worth mentioning CO and NH_3 as probes for the Ti^{4+} Lewis and Ti-OH Brønsted acidity, and CO_2 for the O^{2-} Lewis basicity. The use of more reactive molecules like alcohols has allowed to highlight synergic effects due to the presence of $\cdots Ti^{4+}O^{2-}\cdots$ acid/base pairs. Along this theme, it was found that the $Ti^{4+}O^{2-}$ pairs at the surface of rutile are very effective toward dissociative adsorption of alcohols to form OH groups and Ti-alcolates, whereas the anatase surface is much less active and alcohols are adsorbed preferentially in molecular form.[30]

IR spectroscopy has been used also to investigate the nature and the properties of the OH groups. In this respect, dehydroxylated anatase samples show many components in the 3750-3600 cm^{-1} OH stretching region (see *Table 11*) related to the presence of different families of surface OH groups whose properties have been tested by adsorption of probes like ammonia, pyridine, and benzene.[31]

Table 11. Behaviour of surface hydroxy-groups on TiO_2 anatase. From ref.[31]

Notation	ν/cm^{-1}	Presence on TiO_2				$\Delta\nu$ (C_6H_6)	NH_4^+ from NH_3	pyH^+ from py
		DA	TA	TS	BA			
A	3735	+	+	-	-	260	reversible	no
B	3725	+	+	-	-	160	reversible	no
C	3715	+	+	+	-	100	no	no
D	3690	-	-	+	-	200	irreversible	yes
E	3670	+	+	+	+	30	no	no
F	3640	+	+	+	-	n.o.	no	no

Tsyganenko and Filimonov[32] have proposed structural models of the different OH families to distinguish for instance between terminal (type I in the following scheme, absorbing at 3720 and 3715 cm^{-1}) and bridged hydroxyls (type II, absorbing at 3675 and 3640 cm^{-1}).

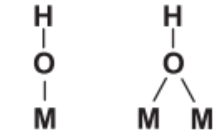

To account for the surface heterogeneity in terms of Lewis and Brønsted properties, as discussed above, different models of anatase TiO_2 crystal terminations have been proposed by many authors including.[30, 31, 33]

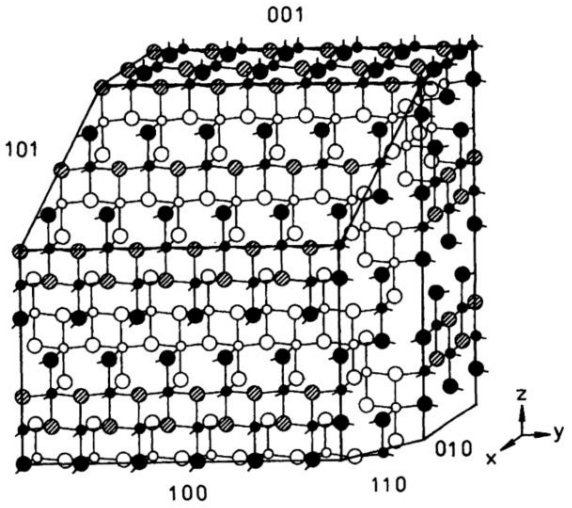

Figure 41. Scheme of an anatase crystal with different exposed faces. •, c.u.s. Ti^{4+} ions from the subsurface layers; ● c.u.s. O^{2-} ions; ◍ saturated O^{2-} ions from the surface layers, ○ saturated O^{2-} ions from the subsurface layers. From ref. [30]

According to model shown in *Figure 41*, the anatase surfaces expose three types of coordinatively unsaturated (*cus*) titanium cations:

i) *α* sites: 4C Ti^{4+} (where 4C stands for tetra-coordinated). These sites are located on the (110), (111) and (113) as well as on the edges of the (110) faces and are characterized by strong Lewis acidity;

ii) *β* sites: 5C Ti^{4+} belonging to $Ti^{4+}O^{2-}$ acidic-basic pairs. The *β* sites are less acidic than the *α* ones and are located on the most common and abundant (101), equivalent to the (011) and on the (100) ones, equivalent to the (010) faces.

iii) *γ* sites: 5C Ti^{4+} belonging to $\cdots Ti^{4+}$- O^{2-}- Ti^{4+}- $O^{2-}\cdots$ rows located on the (001) and (112) faces and at edges at the (101)x(011) intersections. These sites are less electrophilic (less acidic) than the isolated *β* sites because the Ti atom is actually engaged in bonds with two O atoms instead of one.

The Ti^{4+} centres are coupled with O^{2-} counter-anions of different Lewis basicity. Some of the O^{2-} ions as well as some families of OH^- sites show basic properties as they form carbonates and hydrogencarbonates by reaction with CO_2. However, they show a very moderate basicity, as the carbonates are decomposed already by outgassing at room temperature.

3.4.2 Titania in material science

Most of the studies devoted to the TiO_2 surface chemistry deal with photocatalysis, an application field which is outside the topic of this thesis (see [34] and reference therein). Studies concerning the H-C≡C-

H/TiO_2 system are mentioned below, as they are somehow related to the H-C≡N/TiO_2 one.[35, 36] As schematized in *Figure 42*, it was found that acetylene is chemisorbed at the surface of coordinatively unsaturated $Ti^{4+}O^{2-}$ acid/base pairs through an heterolytic splitting mechanism. The resulting C_2H- fragments initiate a chain of oligomerization reactions leading to *in situ* formation of polycyclic condensed hydrocarbons anchored to the TiO_2 surface. This surface chemistry is interesting because the products have a graphene-like structure, and TiO_2/graphene heterojunction has indeed been proposed as a route to improve the TiO_2 photocatalytic performances.

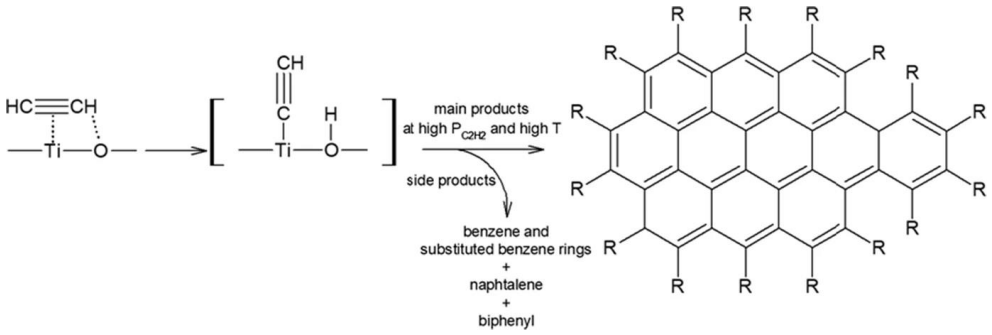

Figure 42. Schematic representation of the reactions chain leading to formation of graphene-like layers at the TiO_2 surface by reaction with acetylene. From ref.[37]

A polycyclic material which has also attracted much attention, on this matter, is graphitic carbon nitride (g-C_3N_4), whose idealized structure shown in the following figure and can be roughly imagined as derived from HCN oligomerization.[38]

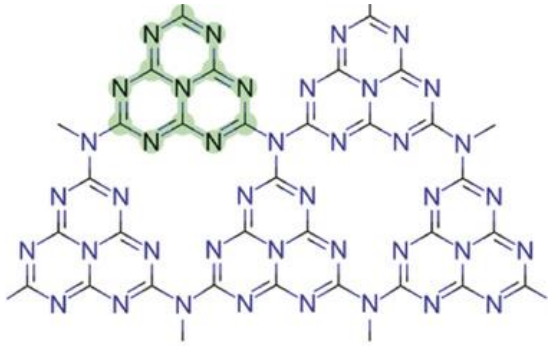

Figure 43. The structure of g-C_3N_4. From ref.[38]

The chemistry of the H-C≡C-H/TiO_2 system has therefore prompted to investigate the possibility to obtain g-C_3N_4-like structures anchored to the TiO_2 surface by H-C≡N oligomerization.

3.4.3 Titania and prebiotic chemistry

Although in small amount, TiO_2 minerals are supposed to be present on Earth, from its formation.[39] Among them, anatase is common in igneous and metamorphic rocks.

TiO_2 minerals are present as well in extra-terrestrial environments like the stardust nucleation/condensation regions forming interstellar pre-solar dust grains and in meteoritic materials.[40-42]

The hypothesis that, despite the low abundance, TiO_2 could have played a catalytic role in the terrestrial or extraterrestrial synthesis of molecules related to the origin of life is at the basis of many studies in the field of prebiotic chemistry.

Some papers have been devoted to the elucidation of the adsorption mechanisms of amino acids and nucleobases,[15, 43-45] while others are worthy of mention to have ascertained the role played by the surface

Lewis and Brønsted sites on the (101) anatase surface in the formation of peptide bonds between glycine monomers,[46-49] then in the formation of nucleobases and acyclonucleosides from formamide,[50] as well as of sugars.[51]

Two papers only (better discussed in the following) concern the interaction of HCN/TiO_2 but not in the prebiotic chemistry perspective.[20, 23]

In this thesis the HCN interaction with the anatase surface was investigated in the 150-300 K temperature range. For sake of clarity the data obtained at 150 K (adsorption stage) will be discussed in the next paragraph separately from those obtained on increasing the temperature from 150 to 300 K (reaction stage, discussed in *Chapter 5*).

3.4.4 The HCN/TiO_2 interaction at 150 K: experimental results and discussion

As already mentioned, nanoanatase TiO_2 was preferred to the much more investigated Evonik P25, in order to avoid the presence of rutile (contained in P25 in *ca.* 15% amount) and because of the high surface area (*ca.* 140 m^2g^{-1}), which makes the material ideal for surface catalysis studies.

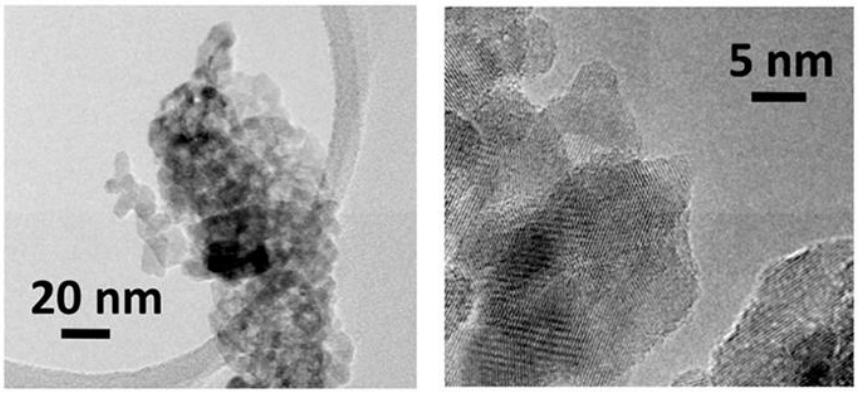

Figure 44. HRTEM images of the nanoanatase sample used in the experiments. Adapted from ref. [52]

As shown in *Figure 44*, nanoanatase TiO_2 consists of irregularly shaped nanoparticles with average linear dimension of *ca.* 16 nm and characterized by low abundance of extended facelets with a considerable amount of defects like edges, steps, and corners,[52] which are expected to show an enhanced activity toward adsorption and activation of gaseous molecules like HCN.

The IR spectra obtained at 150 K upon increasing doses of HCN (up to an equilibrium pressure of 5 mbar) on a nanoanatase sample,

previously outgassed at 773 K under high vacuum, are reported in the upper part of *Figure 45*.

In the background subtracted series of *Figure 45* (upper part) the two negative peaks at 3718 and 3672 cm^{-1} witness the gradual "consumption" of the TiO_2 residual surface OH groups (terminal and bridged, respectively, following Tsyganenko and Filimonov:[32] see paragraph *3.4.1.*). The formation of new species is revealed by the positive bands simultaneously growing in the 3600-2800 cm^{-1} (where OH and CH stretching vibrations are expected to fall), in the 2200-2000 cm^{-1} (typical of the C≡N vibrations) and in the 1800-1000 cm^{-1} regions (where double bonds stretching and low frequency modes of the adsorbed species can be expected).

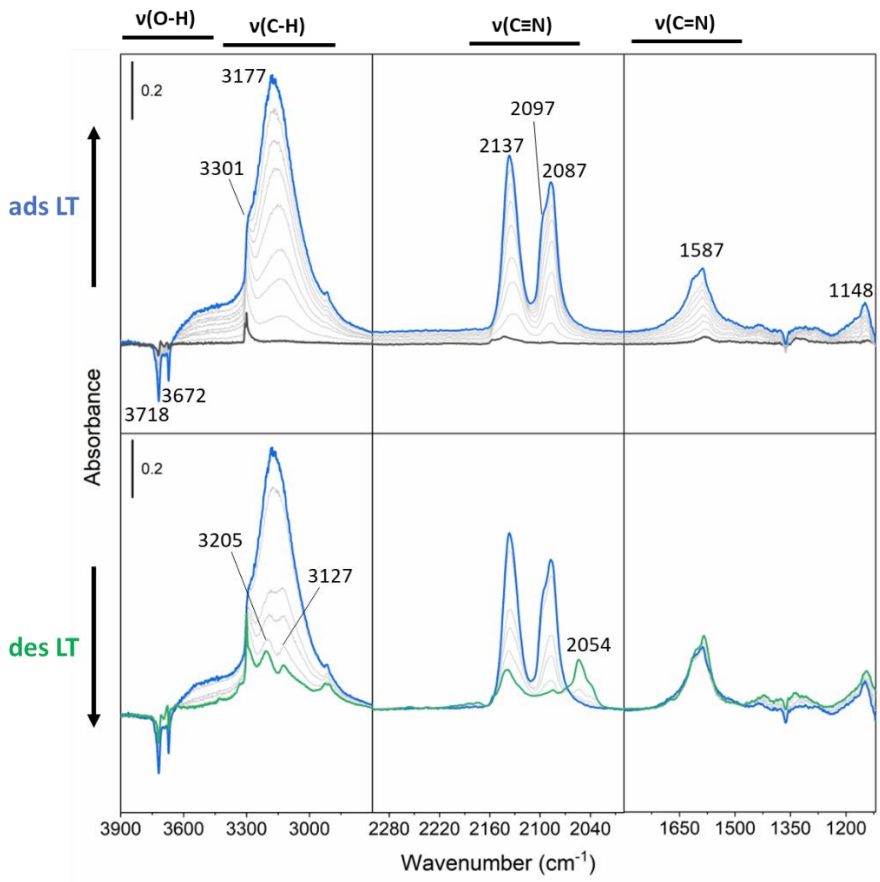

Figure 45. Upper part: background subtracted IR spectra of HCN adsorbed at 150 K on nanoanatase previously outgassed at 773 K. The series show the effect of gradually increasing the HCN equilibrium pressure up to 5 mbar (blue spectrum). In the lower part of the figure the effect is shown of the subsequent reduction of the HCN pressure (from the blue spectrum, corresponding as in the upper part to 5 mbar, to the green one).

More in detail, it is clear in *Figure 45* (upper part) that the erosion of the ν(OH) bands at 3718 and 3672 cm^{-1} is accompanied by the parallel formation of a broad, apparently structureless absorption covering 3600-3300 cm^{-1} interval. As already discussed in the part devoted to the HCN/SiO_2 system, this behavior is a clear indication of the occurrence of hydrogen bonding interaction between the HCN molecules and the residual Brønsted acidic Ti-OH groups.[52] Notice that

the simultaneous growth of a sharp band at 3301 cm^{-1}, rapidly submerged by a much broader and strong absorption growing at 3177 cm^{-1}, can be observed together with a triplet at 2137 cm^{-1}, 2097 cm^{-1} (shoulder) 2087 cm^{-1}, and of a couple of features at 1587 and 1148 cm^{-1}.

The bottom part of *Figure 45* shows the effect of cooling again the sample to the lowest temperature by adding liquid nitrogen in the cell reservoir; in this way HCN is frozen back on the coldest part of the cell with the net effect of reducing the HCN equilibrium pressure. The HCN desorption experiment reveals that:

i) the broad band at 3177 cm^{-1} is due to the superposition of two main components at 3205 and 3127 cm^{-1}, whose relative intensity slightly changes with the HCN coverage (the latter one being apparently favored at the highest coverages);
ii) the high frequency component (2137 cm^{-1}) of the triplet in the 2200-2000 cm^{-1} interval decreases in intensity, while the features at 2097 and 2087 cm^{-1} are disappearing with the parallel growth of a new signal at 2054 cm^{-1}, thus suggesting that at least one of the species responsible for the former doublet is not destroyed upon desorption but rather transformed into different ones;
iii) the couple of features at 1587 and 1148 cm^{-1} is very little affected by HCN desorption and hence due to strongly adsorbed species.

As far the assignment of the above spectral features is concerned, comparison with the literature data[20, 23] is not straightforward, because

obtained on different TiO_2 samples (in terms of composition, pretreatments, etc.) and in different experimental conditions (for instance upon heating in HCN atmosphere at high temperature). Nevertheless, in order to summarize the proposed HCN/TiO_2 interaction mechanisms, the following possibilities emerge (see also *Figure 46*):

I. weak hydrogen bond interaction of HCN with the residual Ti-OH Brønsted acid sites, as in structure I or I';

II. weak hydrogen bonding interaction with *cus* Lewis basic O^{2-}, as in structure II;

III. weak hydrogen bonding interaction between already adsorbed and gaseous HCN molecules to form dimeric (or larger) surface species, as in structures III and III';

IV. end-on (IV) HCN interaction with the Lewis acidic Ti^{4+} sites;

V. HCN dissociative adsorption on Ti^{4+}-O^{2-} pairs with formation of OH groups and Ti-cyanide (V) or isocyanide (V') species;

VI. η^2(C, N) binding on $Ti^{4+}O^{2-}$ centres, as in structure VI.

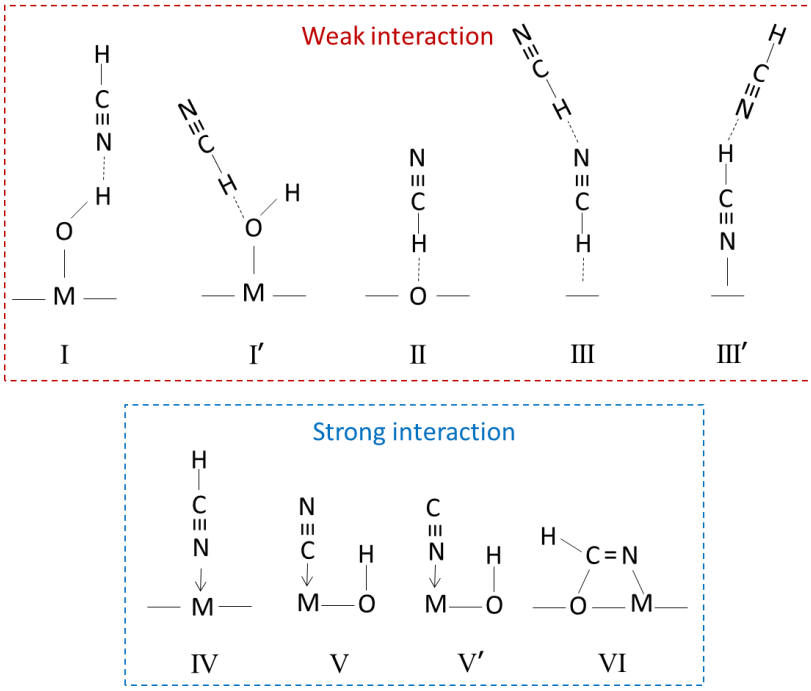

Figure 46. Summary of the possible interaction mechanisms of HCN with the TiO_2 surface. The term "weak" and "strong" are used here to distinguish between hydrogen bonded and otherwise adsorbed species.

In agreement with the conclusion drown for the SiO_2/HCN system (paragraph *3.3*) there is little doubt that the disappearance of the OH doublet at 3718 and 3672 cm^{-1} in favor of the broad absorption in the 3600-3300 cm^{-1} region is due to formation of complexes I (*Figure 46*). Although the high frequency component has been sometime attributed to less acidic terminal OHs and the low one to more acidic bridged OH groups, HCN does not seem able to distinguish them; they are in fact consumed (upon HCN dosage) and restored (upon HCN desorption) at the same time. Assuming an average value of about 3450 cm^{-1} for the $\nu_{(OH)}$ frequencies of the perturbed O-H groups, the $\Delta\bar{\nu}_{(OH)}$ shift for the

Ti-OH···NCH complexes result to be similar to that (*ca*. -300 cm^{-1}) observed for the Si-OH···NCH species. On this basis it is reasonable to hypothesize that also the perturbation of the $\nu_{(CH)}$ and $\nu_{(C\equiv N)}$ modes on the two solids should be similar. This in turn allows to conclude that the $\nu_{(CH)}$ vibration of the Ti-OH···NCH species may contribute with a component in the broad and composite absorption in the 3300-2800 cm^{-1} range (with maximum at 3177 cm-1), and that the $\nu_{(CN)}$ vibration (observed on SiO_2 at 2106 cm^{-1}) may be now responsible for the 2097 cm^{-1} component of the triplet in the 2200-2000 cm^{-1} interval of *Figure 45*. A similar assignment (2098 cm-1) of the CN component has been given by Tsyganenko and coworkers in a study of the HCN adsorption on TiO_2 P25, although the maximum of the broad component related to the $\nu_{(CH)}$ mode is located at lower frequencies (3133 cm^{-1}).

A doublet at 3294 (C-H stretching) and 2128 (C≡N stretching) was assigned by Tsyganenko *et al.* to HCN adsorbed on the Ti^{4+} Lewis acid sites as in structure IV of *Figure 46*. It is reasonable to hypothesize that the same assignment holds for the doublet at 3301 and 2137 cm^{-1} on our sample. Notice that H-C≡N end-on coordination to Ti^{4+} cations through the HCN 5σ MO, roughly speaking the "nitrogen lone pair", results in a positive shift of the CN stretching ($\Delta\nu_{(CN)}$ = +48). The slightly higher frequency of the CN mode observed here could be related the less regular (highly defective) structure of nanoanatase with respect to P25.

A band at 2082 cm^{-1} on P25 has been assigned to the C≡N vibration, with the CH stretching counterpart hypothesized at 3145 cm^{-1}, of HCN molecules adsorbed on O^{2-} Lewis basic sites to give complexes II in

Figure 46 . It is thought that the same explanation holds for the 2087 cm^{-1} component in *Figure 45*. Nevertheless, while it is reported that the 2082 cm^{-1} absorption on P25 simply decreases in intensity, the gradual disappearance of the 2087 cm^{-1} band in the desorption experiment of *Figure 45* is clearly accompanied by the parallelly growth of a new component at 2054 cm^{-1} (with a shoulder at 2037 cm^{-1}) and of two vCH signals at 3205 and 3127 cm^{-1} (bottom part of *Figure 45*). The presence of an isosbestic point at ca. 2070 cm^{-1} accompanying the 2087/2054-2037 cm^{-1} transformation is noteworthy, because it suggests a 1:1 interconversion of the involved species. It is thought that this behavior, typical of the highly defective nanoanatase sample but not observed on the more regular P25 particles, could be the consequence of a change with the HCN coverage of the geometry and/or of the lateral interactions of some $O^{2-}\cdots$H-C≡N species adsorbed on defects, not present on P25. The consequences of these structural changes of the adsorbed molecules are the reinforcement of the HCN interactions with the surface, the weakening of the CN bond and a consequent causes a larger downward shift of the CN stretching frequency.

Another feature observed on nanoanatase but not reported by Tsyganenko on P25 is the signal at 1587 cm^{-1}, a value compatible with a C=N double bond vibration. A band in similar position has been observed by Kim *et al.*[21] by HCN adsorption on Al_2O_3 and assigned to η^2(C,N)-HCN structures in which the HCN molecules interact with the surface in a bridged configuration through both the C and N atoms (as in structure VI in *Figure 46*). It is conceivable that a similar, very stable structure (as demonstrated by the fact that the manifestation at

1587 cm^{-1} appears immediately upon HCN dosage and is nearly unaffected by desorption) are formed as well on the highly defective nanoanatase surface. This structure can also account for the signal at 1148 cm^{-1} compatible with the stretching of the C-O bond formed between the C of η^2(C,N)-HCN species and surface oxygens.
As a further comment to the spectra of *Figure 45*, it is noteworthy that there is no evidence of HCN dissociative chemisorption to form OH and Ti(CN) species (structures V and V' in *Figure 46*).

To possibly evaluate the role of the different exposed crystalline faces on the HCN/nanoanatase chemistry, the adsorption of HCN was also investigated on shape engineered TiO_2 (anatase) nanoparticles. Two shape-controlled samples were used (whose morphology is schematized in *Figure 47)* consisting of nanosheets-like nanoparticles (with dominant (001) facets) and bipyramidal nanoparticles (mainly exposing (101) surfaces).
Without going into details, it is immediately evident from *Figure 47* that, despite the reduced overall intensity of the absorptions of the nano-sheet-TiO_2/HCN system, the spectra do not show substantial differences as far the position and the number of components is concerned. This suggests that the HCN adsorption involves mainly the stable (101) surfaces (which are the predominant ones on nano-anatase and truncated bipyramid samples) or defects located at their border. A lower activity of the (001) surfaces is not surprising, when their documented tendency to surface reconstruction is considered.[2]

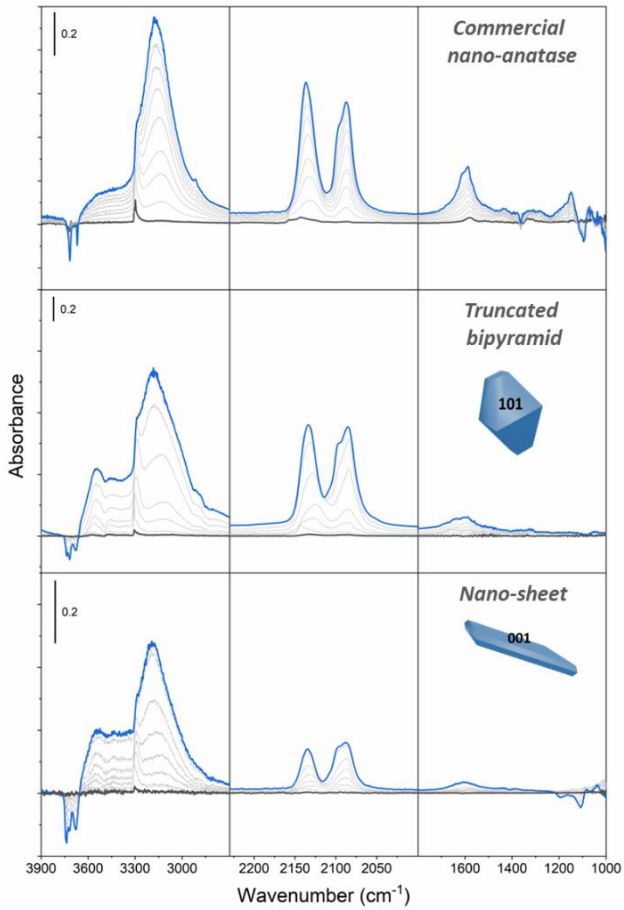

Figure 47. Comparison between the background subtracted IR spectra of HCN adsorbed at 150 K and increasing HCN equilibrium pressure on commercial nano-anatase and TiO_2 samples with controlled morphology (TiO_2-truncated bipyramid and TiO_2-nanosheet).

In conclusion, the FTIR results indicate that at 150 K HCN is adsorbed at the TiO_2 (anatase) surface mainly in molecular form, without any evidence of dissociative pathways. However, on the highly defective nano-anatase sample, some special, possibly highly unsaturated, centres able to activate the CN triple bond by formation of η^2(C,N)-HCN bridged species are evidenced.

3.5 Alumina (Al_2O_3)

3.5.1 Al_2O_3 surface structure and chemical properties

The surface properties of alumina are due to exposed *cus* M^{n+}-O^{2-} acid-base Lewis pairs and to residual hydroxyl groups, in a similar way to TiO_2.

The Al_2O_3 stoichiometry is common to several polymorphs (γ-, δ-, η-, θ-, κ- and χ-Al_2O_3) which can be obtained from the precursors (hydroxides or oxyhydroxides) and following the thermal treatments summarized in *Figure 48*.[54]

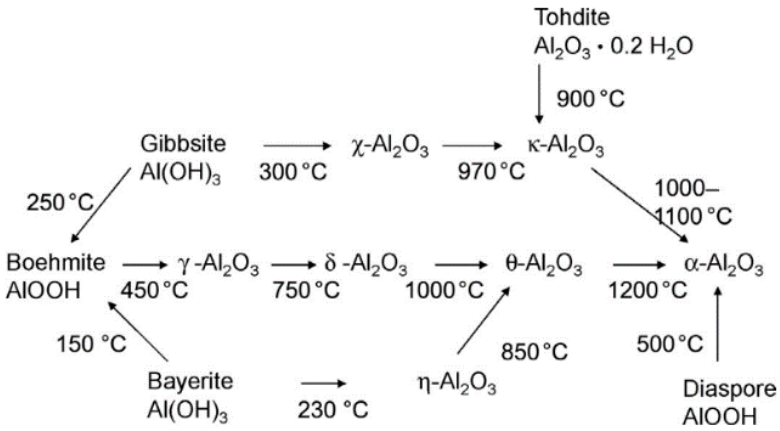

Figure 48. Most common evolution paths for phase transformations of aluminum hydroxides and oxides upon heat treatment. Adapted from ref. [54]

The ending phase of all the transformations schematized in *Figure 48* is the thermodynamically stable α-Al_2O_3 (corundum) polymorph. The intermediates phases (η, γ, χ, δ, κ, and θ) are referred to as *transition* or *metastable aluminas*. Among them, γ-alumina find several industrial applications because of the high specific surface area and defective structure. The physical-chemical properties of γ-Al_2O_3 have been

extensively studied with the methods of surface science (see and references therein), and also for this reason it was chosen in this thesis for studying the Al_2O_3 properties toward HCN.

From the structural point of view γ-Al_2O_3 is conventionally classified as a cubic defective, non-stoichiometric spinel. The normal spinel structure is typical of compounds with AB_2O_4 composition and can be described as a sequence of close-packed O^{2-} layers, stacked in an ABC order (cubic close packing, ccp) and intercalated by two different alternating layers of cations, one consisting of octahedrally-coordinated B^{3+} species and the second one of octahedrally-coordinated B^{3+} and tetrahedrally coordinated A^{2+} cations (*Figure 49*).[55]

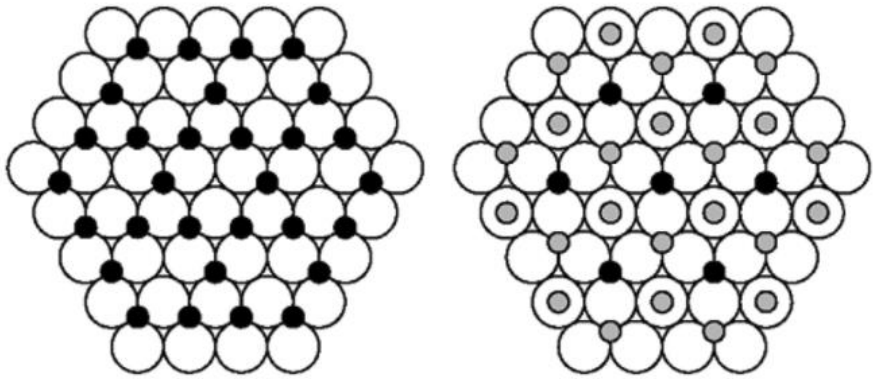

Figure 49. View perpendicular to two (111) planes of an AB_2O_4 normal spinel structure with closed-packed layers of O^{2-} anions (large white spheres) and tetrahedrally coordinated A^{2+} cations (small grey spheres) and octahedrally coordinated B^{3+} cations (small black spheres) in between the oxygen anion layers. From ref. [55]

In the γ-Al_2O_3 structure all the A^{2+} species are replaced by trivalent Al^{3+} cations and some of the positive sites must therefore remain

vacant to ensure charge balance. For this reason, γ-Al_2O_3 is usually considered as a *defective spinel*.

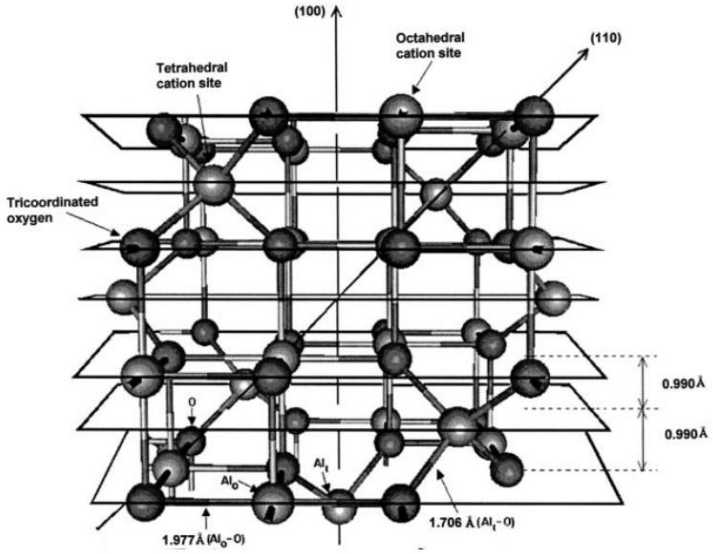

Figure 50. Experimental cubic γ-Al_2O_3 spinel-type unit cell. From ref. [56]

While the Al^{3+} ions are distributed among T_d and O_h sites (*Figure 50*), the question of whether the positive vacancies preferentially occupy the T_d or the O_h sites or if they are randomly distributed among the two positions is still debated.[54] As outlined in ref. [57]: "*the location of the vacancies is not a secondary problem, as it is related to the way the cations are arranged. In a spinel structure the Al^{3+} distribution can in fact vary between 62% [Al^{VI}] and 38% [Al^{IV}] when assuming that vacancies occupy exclusively O_h interstices, and 75% O_h and 25% T_d when vacancies are supposed to be exclusively located in T_d sites".*

To further complicate the picture, besides the "spinel model" other descriptions of the γ-Al_2O_3 structure have been proposed known as the

"non-spinel" and the "hydrogen spinel" models. The first hypothesizes supposes that some Al^{3+} cations occupy non-spinel sites, while according the second one the γ-Al_2O_3 cation deficiency with respect to the spinel stoichiometry is balanced by the presence of a certain number of protons distributed inside the bulk.

The distribution of the different cationic and anionic sites at the surface of γ-Al_2O_3 is of course also related to the sample morphology. This can be deduced from that of boehmite, because γ-Al_2O_3 is obtained from this solid by a topotactical phase transition at 450 °C.[54] Boehmite nanoparticles usually have rhombohedral shape and are terminated by predominant (010) basal planes and (100), (001), and (101) edge surfaces. During the topotactical phase transition the above surfaces are transformed into the (110), (100) and (111) planes of γ-Al_2O_3 (as shown in *Figure 51*), in 74, 16 and 10% relative abundance.

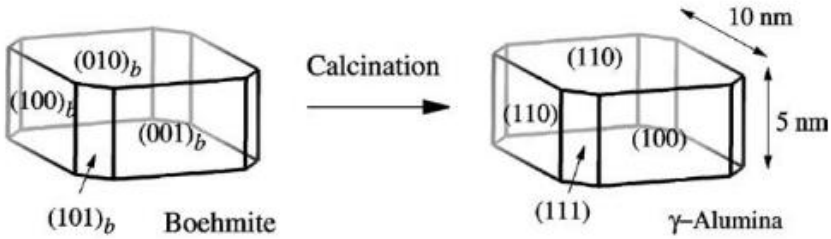

Figure 51. Transformation of boehmite into γ- alumina nanoparticles with the corresponding surface orientations. From ref. [58]

By the combined use of SEM and HRTEM electron microscopy techniques and of IR spectroscopy of CO and H_2 adsorbed at very low temperature (60 and 20 K respectively), it has been confirmed that at the surface of highly dehydrated γ-Al_2O_3, a variety of cationic sites is exposed which can be classified as $[Al^{VI}]_V$, $[Al^{VI}]_{IV}$, $[Al^{VI}]_{III}$ and $[Al^{IV}]_{III}$,

being the Roman numeral at the apex referred to O_h (VI) and T_d (IV) Al^{3+} sites and the subscript to the coordinative unsaturation of the ion (V for penta-, IV for tetra and III for tri-coordinated). It is also concluded that their polarizing power (essentially a measure of their relative Lewis acidity) is in the order $[Al^{VI}]_V < [Al^{VI}]_{IV} < [Al^{VI}]_{III}$, $[Al^{IV}]_{III}$.[57]

As far the surface distribution of these sites is concerned, III- and IV-coordinated Al^{3+} ions are exposed on the prevalent (110) surface, while the less abundant (100) surface exposes V-coordinated cations. The (111) surface is polar and for this reason remains completely hydroxylated up to 800 K.

Coming now to the surface properties related to the *cus* O^{2-} centers, although they do not possess any remarkable basicity, are able to react with CO_2 to give surface carbonates. Nevertheless, some of the catalytic properties of γ-Al_2O_3, and in general of transition aluminas, are due to the $Al^{3+}O^{2-}$ pairs working in synergy. They do for instance promote the dissociative adsorption of alcohols (an important step in their catalytic dehydration to ethers and olefins) as well as the extraction of hydrogen from acetonitrile or acetone to give Al-CH_2CN or Al-CH_2COCH_3 and O-H species, or from olefins to produce surface Al-allyl species.[54] Wischert et al.[59] have also shown that the highly *cus* tri-coordinated Al^{3+} sites (mainly present as metastable species on the dehydroxylated (110) surface) are by themselves capable of adsorbing N_2, while in combination with specific O^{2-} centres are able to chemisorb H_2 and CH_4 by heterolytically splitting the H-H and the C-H bonds,[60] as shown in *Figure 52.* This activity rapidly declines after thermal

treatments above 750 °C, when γ-Al_2O_3 is first transformed into the θ and finally to the α-phases with a significant loss of surface area.

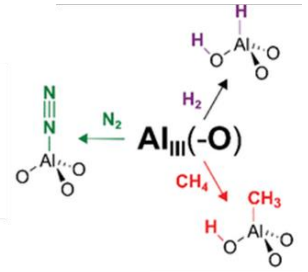

Figure 52. Schematic representation of the adsorption of N_2 and of the splitting of CH_4 and H_2 on Al_{III} defective sites. Adapted from ref. [59]

$Al^{3+}O^{2-}$ pairs are also responsible for rehydroxylation (or rehydration) in H_2O atmosphere of samples previously outgassed at high temperature. For γ-Al_2O_3 a two-step process has been proposed going through the non-dissociative adsorption of H_2O on *cus* Al^{3+} sites, followed by dissociative chemisorption, as in the scheme below:[56]

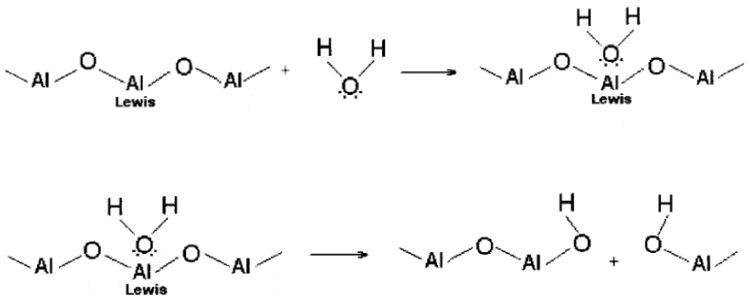

Dehydroxylation under vacuum at temperatures below the γ-Al_2O_3 phase transition to δ-Al_2O_3 (750°C) leaves residual OH groups in concentrations ranging from 12–16 OH/nm^2 at 100°C and to 0.7-2.6 OH/nm^2 after outgassing at 700–750°C. The OH groups give rise to

complex IR patterns in the 3800−3500 cm^{-1} region (*Figure 53*), so revealing their structural heterogeneity.

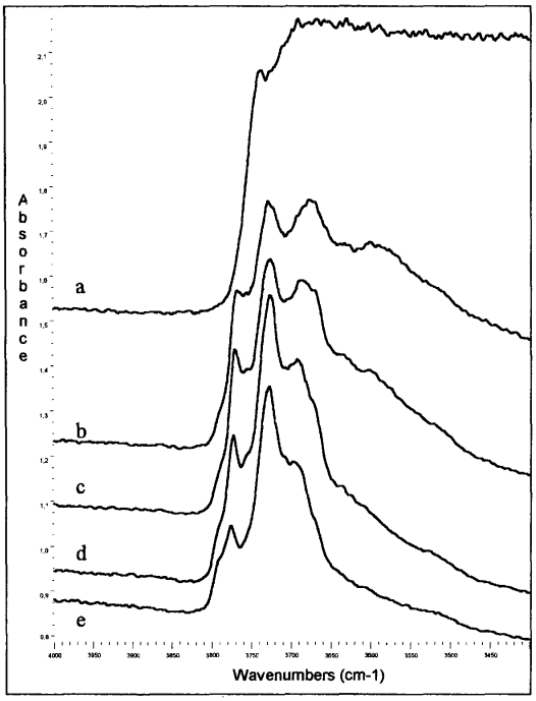

Figure 53. FTIR spectra of the OH stretching region of γ-Al2O3 after outgassing at 30°C (a), 450°C (b), 550°C (c), 650°C (d), and 730°C (e). From ref. [54]

As summarized in *Table 12* a number of structural models have been proposed for their assignment.[61] The most popular model for interpreting some of the chemical properties of alumina is that proposed by Knözinger and Ratnasamy.[62]

Table 12. Spectral position and assignments proposed for surface hydroxyl species on transitions aluminas. From ref.[61]

OH band	Average frequency	Peri's assignment [22]	Tsyganenko's assignment [21]	Knözinger's assignment [35]	Busca's assignment [23]
1	3800	A	I	Ib	Al^{IV}
2	3775	D	I	Ia	□-O-Al^{IV}
3	3745	B	II	IIb	Al^{VI}
4	3730	E	II	IIa	□-O-Al^{VI}
5	3710	C	III	III	bridged
6	3690	C	III	III	bridged
7	3590	H-bonded		H-bonded	tribridged

Following Knözinger and Ratnasamy, OH groups can be located on both tetrahedrally (Al^{IV}) and octahedrally coordinated (Al^{VI}) cations, and their spectroscopic features and chemical behaviour correlated to their "net electric charge" (σ), a parameter related to the number of aluminium neighbours and to the aluminium coordination, as shown in the following figure:

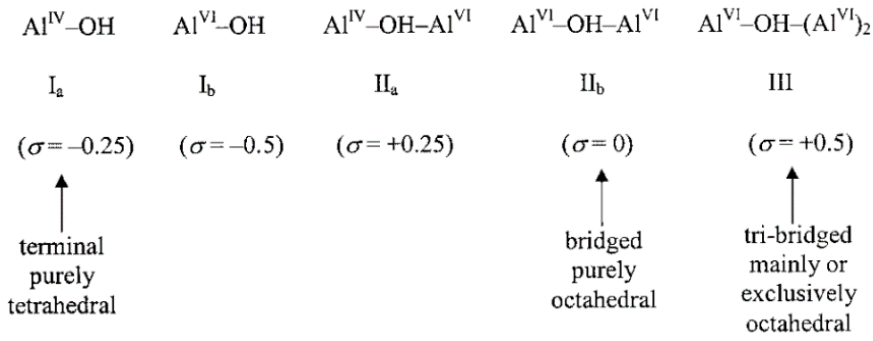

Figure 54. Knözinger and Ratnasamy's model. From ref. [56]

The lower the value of the parameter σ, the lower is the v(OH) stretching frequency and the higher the Brønsted acidity of the OH group. It is important to notice that in the case of terminal Al-OH hydroxyls σ assumes negative values, and in these circumstances the OH group assumes basic properties.

Due to the presence of stable surface OH groups, to its Lewis acidity, and to the polarity of the surface $Al^{3+}O^{2-}$ pairs, Al provides specific sites for anchoring cationic, anionic and metallic species.

3.5.2 Alumina and prebiotic chemistry

Considering that aluminium compounds and related minerals were probably among the major components of the primitive earth lithosphere and that aluminium oxide has been detected on Mars[63] and in pre-solar grains,[64, 65] it is not surprising that Al_2O_3 has inspired many investigations in the field of prebiotic chemistry. The efficiency of alumina to promote in mild conditions the formation of peptide bonds among amino acids has been for instance experimentally demonstrated.[66-69] Saladino and co-workers have shown that alumina catalyses the synthesis of purine, adenine, cytosine, and 4(3H)-pyrimidinone starting from formamide.[70]

By studying the interaction of ribonucleotides with α and γ-Al_2O_3, Arora et al.[63] have concluded that alumina may have played a role in selectively adsorbing and concentrating biomolecules during chemical evolution to life.

Concerning the HCN/Al_2O_3 interaction, only two studies are available in the literature,[21, 71] but none address prebiotic issues.

In this thesis, the HCN adsorption on Al_2O_3 was monitored in the 150-300 K interval in the same conditions already described for SiO_2 and TiO_2.

Although the natural occurring mineral on the earth crust is the corundum α-Al_2O_3, the γ- Al_2O_3 was used because of its high surface

area and better spectroscopic properties in the MIR region with the conviction that it can be a reference material for other aluminium-containing minerals of prebiotic interest like the aluminosilicates.

3.5.3 The HCN/Al_2O_3 interaction at 150 K: experimental results and discussion

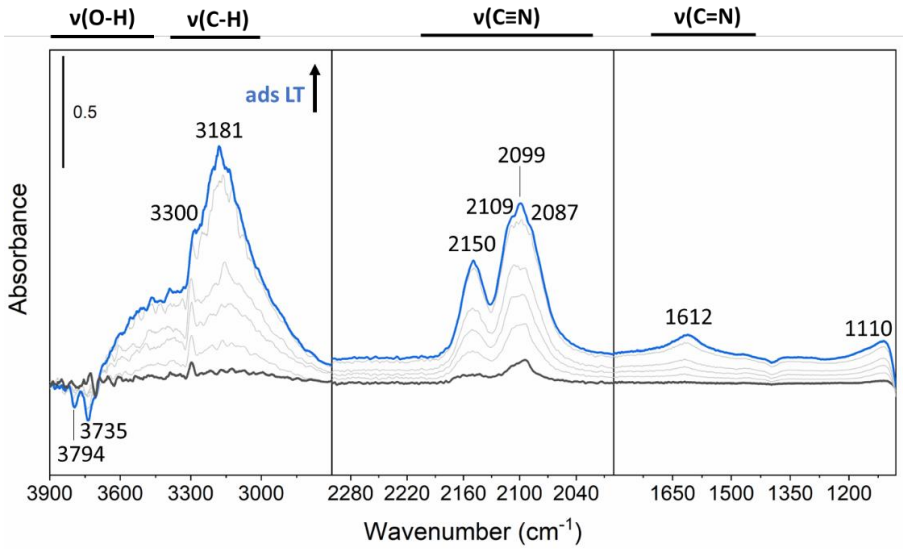

Figure 55. Background subtracted IR spectra of HCN adsorbed at 150 K on γ-Al_2O_3 previously outgassed at 1000 K. The series shows the effect of gradually increasing the HCN equilibrium up to 5 mbar (blue spectrum).

The spectra obtained at increasing equilibrium pressure by HCN dosage at 150 K on a γ-Al_2O_3 sample previously outgassed at 1000 K are shown in *Figure 55*. Already, at a first glance it is evident that they are not substantially different from those the HCN/TiO_2 system as far as the number and the positions of the main absorptions are concerned (see *Figure 45* in paragraph *3.4.4*). The main difference is that, especially in the $\nu_{(C\equiv N)}$ stretching region, the spectra on Al_2O_3 looks less resolved suggesting a more pronounced surface heterogeneity.

Also in this case the erosion of the $\nu_{(OH)}$ bands (at 3794 and 3735 cm^{-1}, associated to Al^{IV}-OH and Al^{VI}-OH species respectively following the assignment in *Table 12*) and the contemporary growth of a broad

absorption in the 3600-3300 cm^{-1} interval are the unequivocal symptoms of formation of OH···N≡C-H adducts.

Concerning the assignment of the other features in the spectra of *Figure 55*, the reader is referred to the work of Kim et al., who have investigated the HCN/Al_2O_3 by the combined use of experimental IR and computational methods.[21] The main results of the Kim's work are summarized in *Figure 56*, where the structure of the HCN surface adducts predicted by the theoretical calculations on the (100) and (110) γ-Al_2O_3 main terminations are shown (see paragraph *3.5.1*), and in *Figure 57*, where their calculated and experimental C≡N stretching frequencies are compared.

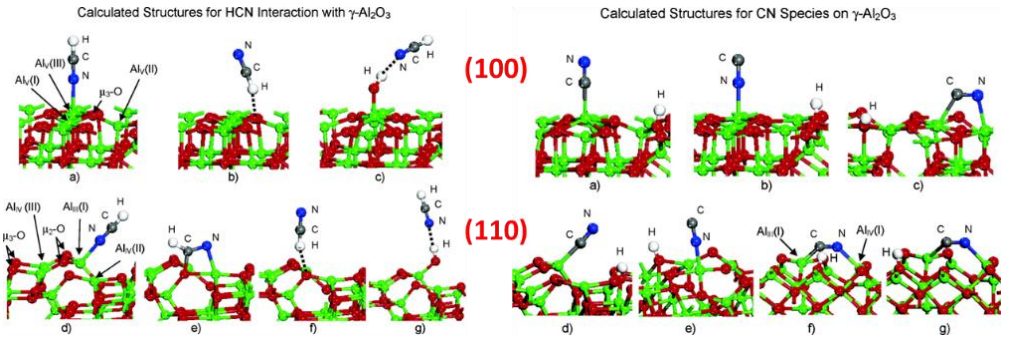

Figure 56. Calculated structures of the surface species formed by molecular (on the left) and dissociative (on the right) HCN adsorption at the main (100) (upper part) and (110) (on the bottom) terminations of γ-Al_2O_3. Adapted from ref.[21]

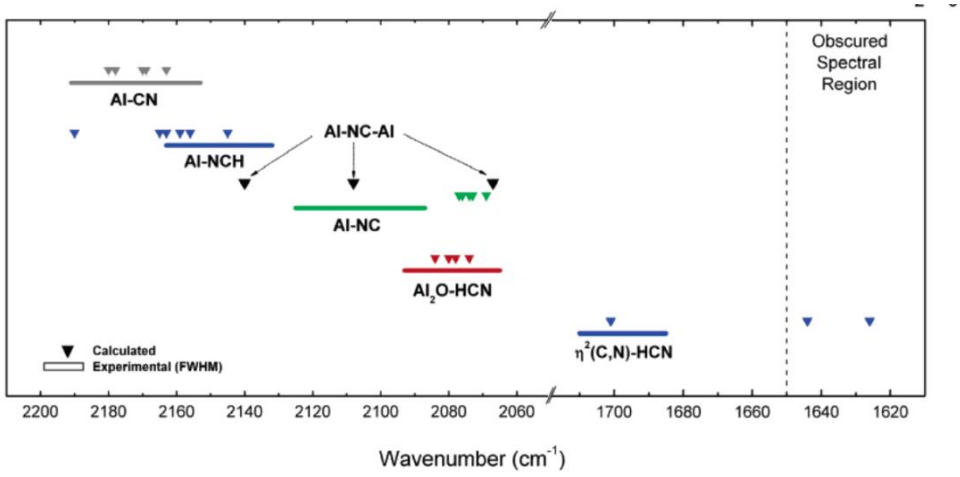

Figure 57. Correlation between the calculated and experimental C≡N stretching frequencies of the HCN/γ-Al_2O_3 adducts sketched in Figure 56. From ref. [21]

Based on the data of *Figure 56* and *Figure 57* and, in comparison with the experimental results reported in *Figure 55*, the following can be commented and concluded:

1. as on TiO_2, also on γ-Al_2O_3 HCN adsorption at 150 K gives rise to weak hydrogen bonded interaction between the undissociated molecule and (i) the surface OH acidic Brønsted sites (see structures *c* and *g* in *Figure 56*), (ii) the coordinatively unsaturated (*cus*) Al^{3+} Lewis acid sites (structures *a* and *d*) and (iii) the *cus* O^{2-} basic sites (structures *b* and *f*);
2. the species described at point (a) are responsible of the ν(C≡N) bands in the 2160-2140 cm^{-1} interval with frequencies in the order $Al^{3+}\cdots N{\equiv}CH$ > $OH\cdots N{\equiv}CH$ ≈ $Al_2O\cdots HC{\equiv}N$; based on the Kim's assignments, it is conceivable that these species are responsible of the features observed in the spectra (*Figure 55*) at 2150 and 2085 cm^{-1} and for ν(CH) counterparts at 3300 ($Al^{3+}\cdots N{\equiv}CH$ and $OH\cdots N{\equiv}CH$) and 3180 cm^{-1} ($Al_2O\cdots HC{\equiv}N$);

3. special $Al^{3+}O^{2-}$ *cus* acid base pairs, located on the (110) surfaces, following Kim and co-workers, are able to adsorb HCN more strongly to give η^2(C,N)-HCN bridged species (see structure *e* in *Figure 56*, also hypothesized on TiO_2) where the C-N bond order is greatly reduced, giving rise to the absorption at 1610 cm^{-1} with $\nu_{(C=N)}$ character. It is thought that the signal at 1110 cm^{-1} in *Figure 55* (region not shown in the Kim' paper) could be due to the stretching mode of the C-O bond involving the C atom of bridged HCN and the oxygen atom of the $Al^{3+}O^{2-}$ couple;
4. as a novelty with respect to TiO_2, in the Kim's work evidence was given of dissociative HCN chemisorption on $Al^{3+}O^{2-}$ acid base pairs which are more coordinatively unsaturated (and hence more reactive) than those discussed at point (c). The products of this surface reaction are Al^{3+}−CN (cyanide: structures *a* and *d* in *Figure 56*) and Al^{3+}−NC terminal species (isocyanide: structures *b* and *e*), Al^{3+}−CN−Al^{3+} bridged species (structures *c*, *f,* and *g*) and OH groups. Following the Kim's hypothesis, all these species have $\nu_{(CN)}$ frequencies covering a broad interval between 2140 and 2060 cm^{-1} (*Figure 57*). It is therefore conceivable that similar species are responsible for the 2110 cm^{-1} yet unassigned component in the spectra (*Figure 55*). It is noteworthy, that the presence of absorptions at CN frequencies as high 2200-2150 cm^{-1}, which are typical of Al^{3+}−CN cyanide species is not observed, while in the Kim work weak absorptions assigned to these complexes are reported at *ca*. 2180 cm^{-1}. It is however well known that the cyanides and

isocyanides isomers are often in a mutual equilibrium, which depends on the temperature (see ref.[20] and references therein); the different behaviour of here reported system with respect to that of Kim can therefore be due to slightly different thermal conditions. Finally, the OH groups created by the HCN heterolytic split contribute to the broad absorption in the 3600−3310 cm^{-1} range.

It can be concluded that although TiO_2 and Al_2O_3 have similar properties as far the adsorption of HCN in undissociated form is concerned, Al_2O_3 shows peculiar properties toward HCN dissociative chemisorption even at 150 K. This observation is in agreement with the fact that on Al_2O_3 special metal/oxygen pairs are able to heterolytically split the hard H_2 molecule too,[60] unlike what was reported for TiO_2.

3.6 Magnesium oxide (MgO)

3.6.1 MgO surface structure and chemical properties

MgO is an ionic oxide with typical rock salt structure in which the cations are distributed in a *fcc* arrangement and the anions occupy the octahedral interstices (and *vice versa*, see *Figure 58*). MgO has been widely used in the past as a model solid for experimental and theoretical studies in the fields of surface science and catalysis, and its surface structure and properties are therefore well characterized (ref.[72] and references therein). When prepared in dispersed (powdered) form, the MgO particles morphology and the surface structure can dramatically change depending on the preparation method, exposure to the atmosphere, thermal treatments, etc.

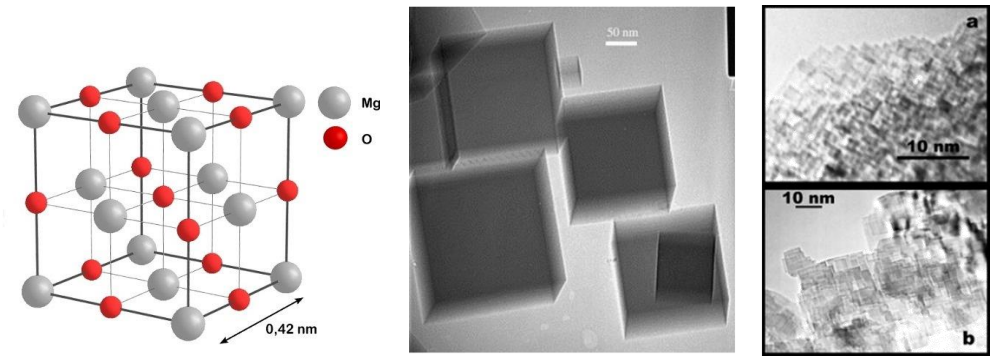

Figure 58. MgO crystalline structure (on the left) and HRTEM (High Resolution Transmission Electron Microscopy) images of MgO samples prepared by Mg metal combustion in air (in the centre) (from ref. [73]) and by decomposition in vacuum at 1073 K of $Mg(OH)_2$ (shown on the right at different magnifications and orientations) (from ref.[72]).

For instance, combustion of Mg metal in air produces isolated, nearly perfectly cubic MgO nanoparticles with linear dimension in the *ca.* 50-200 nm range and BET surface area of *ca*. 10 m^2g^{-1} (*smoke* MgO)

(*Figure 58*). Decomposition in vacuum at 1073 K of $Mg(OH)_2$ (brucite) results on the contrary in MgO samples where much smaller (10 nm or less) cubic nanostructures are still observed but interpenetrated and fused together to form large particles with a complex surface structure (*Figure 58* and *Figure 59*) and high surface area (*ca*. 230 m^2g^{-1}; *hsa* MgO).[72]

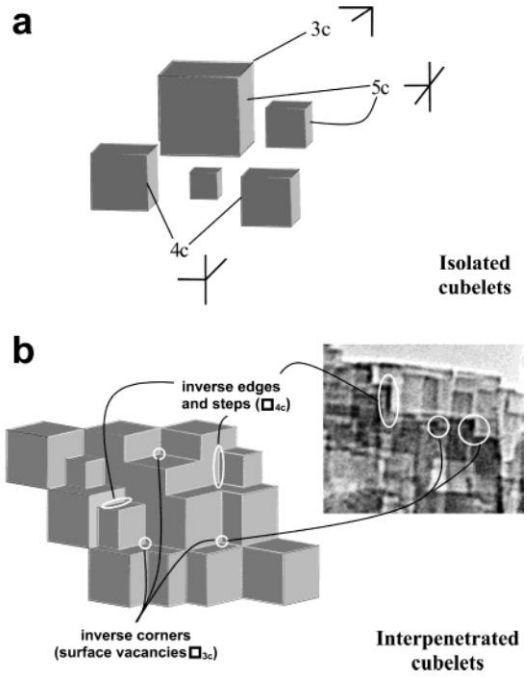

Figure 59. Schematic representation of the morphology and surface structure of smoke (a) and hsa MgO (b) (from ref. [74]). The coordinative status "nc" of the Mg^{2+} and O^{2-} species exposed on the surface at corners, edges and on extended faces is also indicated. Notice the presence on hsa MgO of "inverse" situations formed at the nano-cubelets junctions not found on smoke MgO.

The *smoke* MgO cubic particles are terminated by (i) extended (001) faces, where a large number of coordinatively unsaturated (*cus*) penta-coordinated (C5) Mg^{2+} and O^{2-} cations are exposed, (ii) edges exposing a relatively smaller number of *cus* Mg^{2+}(C4) and O^{2-}(C4) tetra-

coordinated cations and anions and (iii) regular corners where a very small percentage of tri-coordinated Mg^{2+}(C3) and O^{2-}(C3) sites are present.

On *hsa* MgO the following can be highlighted: (i) the relative number of C4 and C3 highly *cus* cations and anions enormously increases with respect to less defective C5 sites on the (001) facelets; (ii) together with "regular" edge and corners, "inverse" structures appear at the stepped portions of the surface which are absent on *smoke* MgO (*Figure 59* and *Figure 60*).

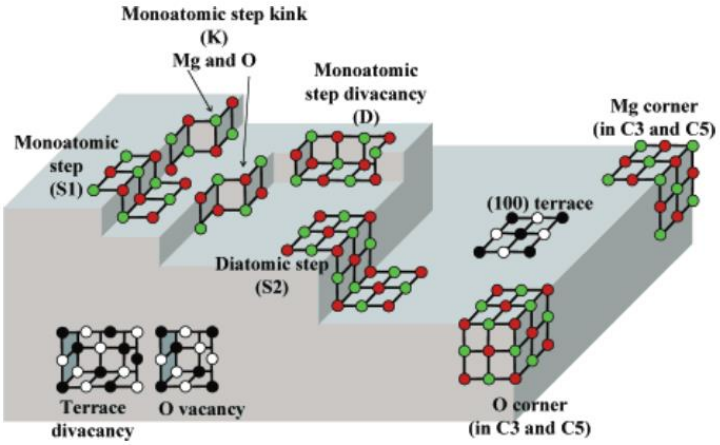

Figure 60. Schematic representation of the different defective structures including the cationic and anionic coordinative status at the surface of hsa MgO.[75]

Depending on the unsaturation degree and the local environment, the different surface *cus* species behave in different way when exposed to molecules from the gas phase. In the following the CO and H_2 interactions will be shortly discussed, as they can help to elucidate the HCN/MgO chemistry discussed later.

The IR spectra of CO adsorbed at 60 K, as a function of the gas pressure on *hsa* MgO, on *sintered* MgO (i.e., *hsa* sample thermally treaded to decrease the surface area), then on *smoke* MgO are reported, respectively, panels a, b, c in *Figure 61*.

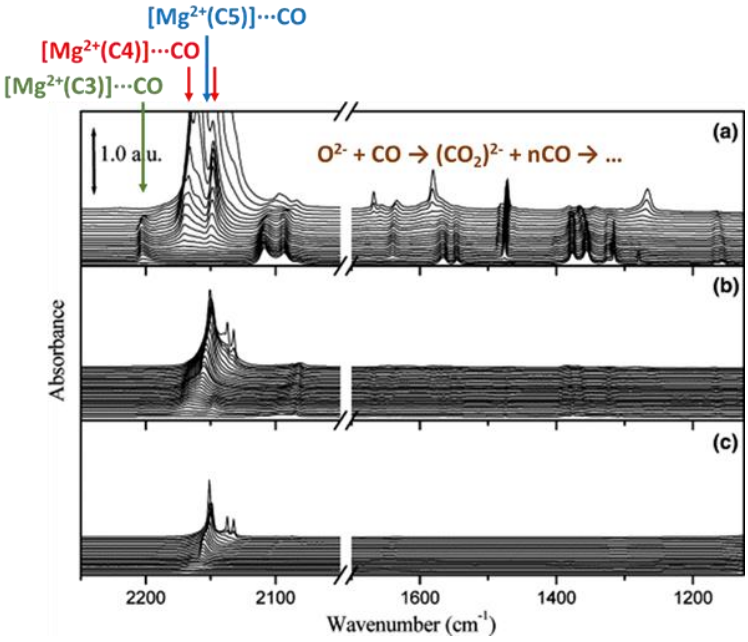

Figure 61. Spectra of CO adsorbed at 60 K on hsa (a), sintered (b) and smoke MgO as a function of the gas phase equilibrium pressure (decreasing in each series from 40 mbar for the most intense spectrum to 10^{-3} mbar for the less intense). The assignment of some of the spectral features is also reported. Adapted from ref.[72]

From the spectral series of *Figure 61*, it is possible to roughly distinguish two regions: (i) the 2250-2120 cm^{-1} region which contains features due to Mg^{2+}···CO adducts formed by reversible physisorption of CO on surface Mg^{2+} *cus* sites acting as Lewis acid centres, and (ii) the 2120-1150 cm^{-1} region where manifestations due to the reaction

between CO and surface *cus* O^{2-} sites acting as basic Lewis centres are observed.

A more detailed discussion of the spectra of *Figure 61* is outside the scope of this thesis and the reader is referred to refs.[72] and [76] for further details. However, it is important to mention that:

i) CO is adsorbed on the Mg^{2+} cationic sites to form linear $Mg^{2+}\cdots CO$ adducts where the CO adsorption energy as well as the CO stretching frequency (with respect to the gas) increase on increasing the coordinative unsaturation (C3 > C4 > C5);

ii) the CO molecules adsorbed on Mg^{2+}(C4) sites located on monoatomic steps (*Figure 60*) can suffer multiple interactions with the surface, as schematized below:

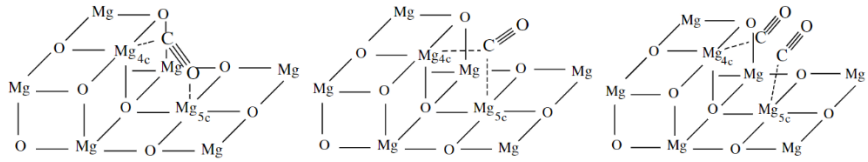

iii) the C5 and C4 *cus* anionic sites located on extended faces and edges positions are inert toward CO, whereas the O^{2-}(C3) species present on monoatomic step kinks (*Figure 60*) show an enhanced Lewis basicity, which makes them able to form $(CO_2)^{2-}$ species stabilized by multiple interaction with the surrounding Mg^{2+} centres, as in the following scheme:

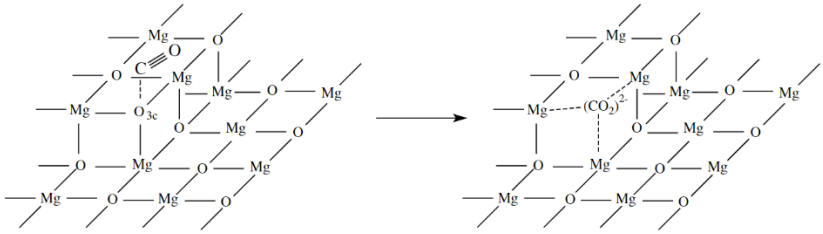

iv) the first formed $(CO_2)^{2-}$ species can further add CO molecules to give $(C_nO_{n+1})^{2-}$ polymeric and $(C_nO_n)^{2-}$ + $(CO_3)^{2-}$ disproportion products.

Similar IR spectroscopic studies performed with H_2 in the 20–300 K range have again allowed to distinguish less reactive sites, where H_2 is reversibly adsorbed (at 20 K) in molecular form, and highly reactive ones, able to heterolytically split the molecule to form irreversibly adsorbed surface species (Mg hydrides and OH groups).[72, 74]

The sites responsible for molecular adsorption following the equilibrium reaction $Mg^{2+} + H_2 \rightleftarrows Mg^{2+}\cdots H_2$ are supposed to be the *cus* Mg^{2+} cationic sites located at "regular" defective position like corners (C3), edges (C4) and extended (100) faces (C5). Upon adsorption the H_2 molecule (IR inactive in the gas phase) is polarized, thus giving rise to a number of separated components in the 4800 – 4000 cm^{-1} interval, each associated which a specific adsorbing site (*Figure 4*).

As far as the dissociative, heterolytic adsorption is concerned, the cooperative action of *cus* $Mg^{2+}O^{2-}$ Lewis acid/base pairs is required as shown in the scheme:

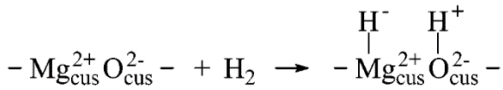

with formation of metal-hydride species absorbing in the 1500−1000 cm^{-1} region and of OH groups absorbing in the 3800−3200 cm^{-1} interval.

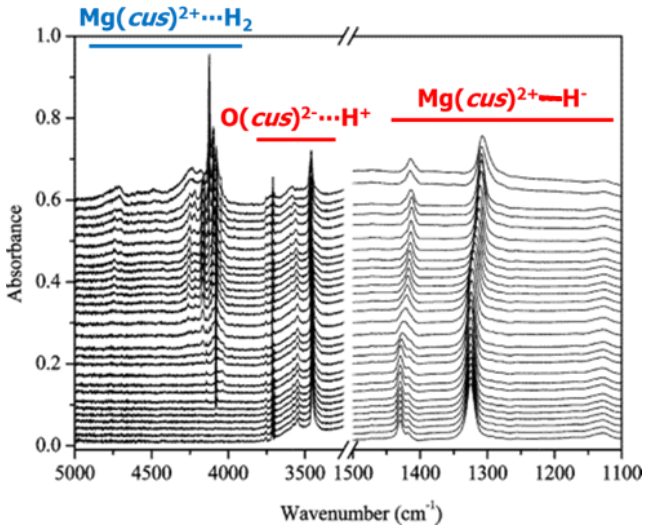

Figure 62. Spectra of H_2 adsorbed at 20 K on hsa MgO as a function of the gas phase equilibrium pressure (decreasing in each series from 10 mbar for the most intense spectrum to 10^{-3} mbar for the less intense). The assignment of some of the spectral features is also reported. Adapted from ref.[74]

The Mg/O pairs responsible for H_2 splitting are supposed to be exposed on "special" surface defects:

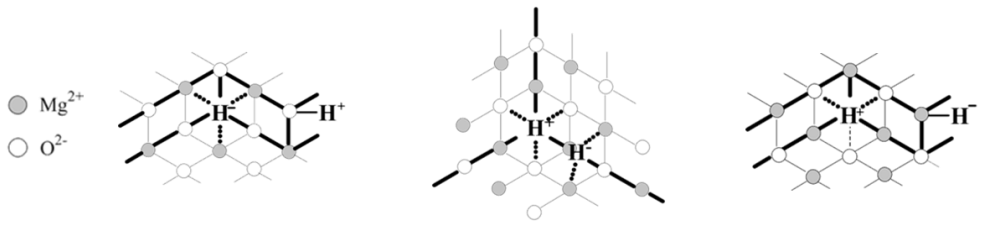

For instance, a defect like that in the left part of the following scheme (I), which combines an inverse corner generated by a O^{2-}(C3) vacancy and a nearby edge at a monoatomic step, has been proposed as

responsible for the OH absorption at *ca.* 3700 cm^{-1} and the Mg-H hydride counterpart at 1125 cm^{-1}, while the structure II would generate the 3454 (O-H) and 1325 (Mg-H) cm^{-1} pair. The manifestations in the 3576−3547 cm^{-1} (O-H) and in the 1430−1418 cm^{-1} (Mg-H) intervals, are finally supposed to belong to species formed on a surface structure analogous to the II one, the only difference being a positive (C3) pseudo-vacancy now located at the inverse corner (III).

3.6.2 MgO and prebiotic chemistry

Magnesium is the eighth most abundant element on Earth and is also common on other rocky planets. For this reason and because Mg^{2+} ions are involved in many physiological functions, including energy production, nucleic acid and protein synthesis, ion transport, cell signalling, etc.[77] it is believed that Mg-minerals could have played a central role in the biochemical evolution. Among them MgO (periclase), $MgCO_3$ (magnesite), $CaMg(CO_3)_2$ (dolomite) and Mg-silicates (like olivine and pyroxene groups) are abundant on Earth and some also in extraterrestrial environments.[39]

As far MgO is more specifically concerned, it has been found to be an efficient adsorber of nucleobases, which suggests a potential role in concentrating biomolecules in prebiotic conditions.[78] It has also been shown that suspensions of MgO (or $MgCO_3$) in HCN aqueous solution promote the condensation of HCN, so playing a catalytic role similar to that of ammonia (*Figure 10*).[79, 80]

Although MgO has been investigated as catalyst for HCN abatement,[81] a systematic study of the HCN_{gas}/MgO interaction has never been attempted before.

To contribute to fill this gap and with the aim of contribute to the studies of HCN chemistry in prebiotic environments, in this thesis the interaction of HCN at variable temperature (150–300 K) has been studied on the well characterized materials described in the previous section, i.e., *hsa* and *smoke* MgO. As it will see in the following, the data obtained on MgO are also helpful to elucidate the HCN chemistry on Mg-silicates, being the materials considered highly attractive in prebiotic concerns.

3.6.3 The HCN/MgO interaction at 150 K: experimental results and discussion

The IR spectra of increasing doses of HCN adsorbed at 150 K on a *hsa* MgO previously outgassed at 1073 K under high vacuum are reported in *Figure 63* (top panels) and compared in the same figure with those obtained by subsequent HCN desorption (bottom panels).

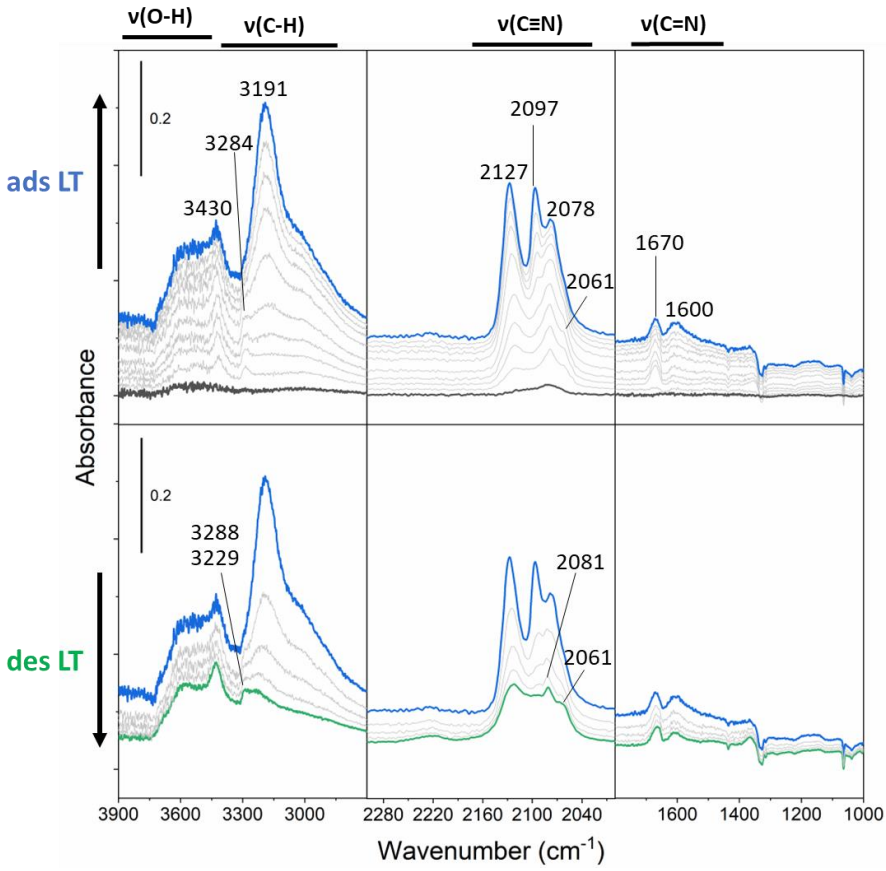

Figure 63. Top panels: IR spectra of increasing doses of HCN (from the dark grey to the blue curve) adsorbed at 150 K on hsa MgO outgassed 1073 K. The last spectrum was obtained at HCN equilibrium pressure of 5 mbar. Bottom panels: effect of reducing the HCN equilibrium pressure (from the blue to the green curve). All the spectra are background subtracted, i.e. obtained after subtraction of the spectrum of the pure MgO sample.

It is immediately evident in the upper part of *Figure 63* that the interaction of HCN with MgO results in the appearance of a broad absorption in the 3750-3450 cm^{-1} region.

On SiO_2 (paragraph *3.3.3*), TiO_2 (paragraph *3.4.4*) and Al_2O_3 (paragraph *3.5.3*), similar manifestations due to the formation of OH···NCH hydrogen bonding adducts between HCN and the residual OH groups (with some contribution in the alumina case due to HCN dissociative chemisorption) are observed. This assignment cannot be considered valid on MgO sample outgassed at 1073 K, because the number of residual OH groups is actually vanishingly low (as demonstrated by the absence in the IR spectrum of pure material of any absorption in the OH stretching region (results not shown for sake of brevity). On this basis, the progressive growth in *Figure 63* of the $\nu_{(OH)}$ manifestations at 3750-3450 cm^{-1} upon increasing the HCN coverage can be explained only if the possibility of a deprotonation reaction between the acid HCN molecule and the surface *cus* O^{2-} basic sites is hypothesized. The parallel growth of the band at 2080 cm^{-1} (upper part of *Figure 63)*, at a frequency close to that of homogeneous Mg-N≡C isocyanide species,[82] reinforces this view and allow to conclude that already at 150 K an HCN heterolytic chemisorption process occurs on surface $Mg^{2+}O^{2-}$ pairs following the scheme:

$$-Mg^{2+}_{cus}-O^{2-}_{cus}- + HCN \longrightarrow \begin{matrix} & CN^- & H^+ \\ & | & | \\ -Mg^{2+}_{cus}- & & O^{2-}_{cus}- \end{matrix}$$

The spectroscopic manifestations due to the fragments:

i) appear immediately already at the lowest HCN surface coverages (upper panels in *Figure 63*), which suggests that HCN splitting occurs on the more reactive portions, conceivably on the more coordinatively unsaturated sites, of the MgO surface;

ii) are little sensitive to outgassing (lower panels in *Figure 63*), which suggests that HCN is chemisorbed irreversibly.

As shown from *Figure 63* (upper part) a relatively narrow band also develops at 3430 cm^{-1}. It can be assumed that this absorption is still related to OH groups formed by HCN splitting, but on sites different from those responsible for the 3750-3450 cm^{-1} doublet. Indeed, the frequency and the narrow character of this feature closely resemble those of the $(O^{2-})_3H^+$ OH groups formed by H_2 heterolytic splitting on tricoordinated positive pseudo-vacancies located at inverse corners, as described in structure II of paragraph *3.6.1*. By analogy with the H_2 case, it can be therefore hypothesized that the HCN splitting on these inversed defects leads to surface species like those shown in the scheme below:

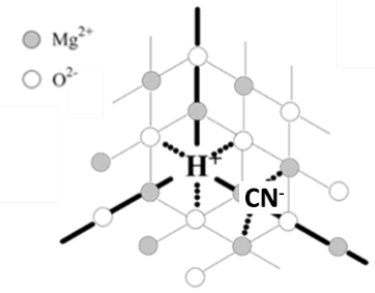

Some more, beside the well accounting for the 3430 cm^{-1} band, the double bridged $Mg^{2+}-(CN^-)-Mg^{2+}$ cyanides species covered by this

model can well explain the low frequency bands growing in the 1700-1550 cm^{-1} region, compatible with C=N double bonds.

Again, in analogy with the H_2 case, it cannot be excluded the formation also of HCN splitting products involving oxygen (structure V) and Mg^{2+} vacancies (structure VI) at monoatomic steps.

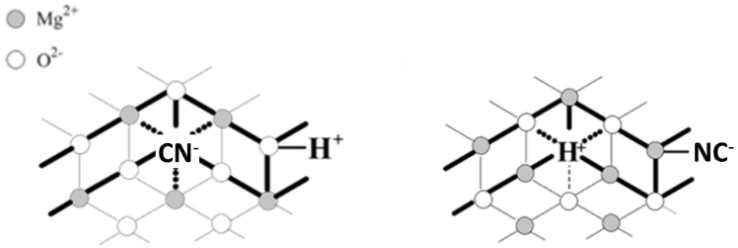

V **VI**

Hence both V and VI models could well account for the $\nu_{(OH)}$ broad band in the 3750-3450 cm^{-1} region (which at a closer inspection of the spectra in the upper part of *Figure 63* indeed looks the superposition of at least two components). Notice that: i) the triple bridged $(O^{2-})_3\cdots(CN^-)$ species provided by scheme V could account for the lowest component (1600 cm^{-1}) of the $\nu_{(C=N)}$ doublet in the 1700-1550 cm^{-1} region (being that at 1670 cm^{-1} subsequently assignable to double bridged cyanides like in scheme IV); ii) the linear Mg^2-NC^- species of scheme VI could account for the 2080 cm^{-1} absorption in the $\nu_{(C\equiv N)}$ region (*Figure 63*).

Notice that all the above species result to be irreversible adsorbed at the surface, as their manifestations do not disappear upon reducing the HCN equilibrium pressure (bottom part of *Figure 63*).

The previous assignments have a speculative character and will hopefully benefit of the ongoing computational studies performed by a Theoretical Chemistry group in our department.

It is however worth recalling that the tendency to form Mg^{2+}-(CO)-$Mg^{2+}$and $(Mg^{2+})_2CO$ bridged species on stepped portions of the MgO surface has been observed also for the CO molecule (see paragraph *3.6.1*), isoelectronic with CN^- anion.

The previously discussed features are not the only ones observed in the spectra of the HCN/MgO system at 150 K. Other bands whose intensity is much more pressure dependent, and hence related to more weakly, reversibly adsorbed species are also observed in the $\nu_{(CH)}$ region at 3191 cm^{-1} (broad and strong), accompanied by a broad shoulder on the low frequency side at *ca.* 3000 cm^{-1}, and in the $\nu_{(C\equiv N)}$ region at 2127 cm^{-1} and 2097 cm^{-1}. A weak feature at *ca*. 3284 cm^{-1} is also present already at the lowest HCN coverages and then seems to disappear on increasing coverages (with the opposite behaviour on decreasing the equilibrium pressure). Also, by comparison with the spectra of the HCN/TiO_2 and the HCN/Al_2O_3 systems, it is possible to assign these manifestations to HCN adsorption in molecular form on surface sites more coordinatively unsaturated with respect to those discussed above. More in detail, the tricoordinated Mg^{2+} and O^{2-} ions exposed at the regular corners of the MgO nanostructures or the tetracoordinated ones at their edges, tentatively (and without entering into excessive details) account for the 3284/2127 cm^{-1} doublet due to Mg^{2+}···NCH complexes and the 3250-3000/2097 cm^{-1} features due to the O^{2-}···HCN interaction. A contribution to the above IR manifestations of hydrogen bonded OH···NCH complexes formed by HCN

physisorption on the OH groups formed by the chemisorption paths is also conceivable.

Finally, some results concerning the HCN adsorption on *smoke* MgO are reported. Due to the wide dimension of the particles, the *smoke* sample is a strong scatterer of the IR radiation in the 3800-2800 cm^{-1} interval and the spectrum in this region appears therefore too noisy to give any spectroscopic information. For this reason, the spectra of HCN on *smoke* and *hsa* are compared in *Figure 64* only in the v(CN) region (2300-2000 cm^{-1}). It is immediately evident that the spectra at maximum HCN coverage at 150 K, despite the dramatically different overall intensities certainly related to the different surface area (*ca*. 10 m^2g^{-1} for *smoke* and *ca*. 200 m^2g^{-1} for *hsa* MgO), show the same absorptions with similar intensity ratios. This suggests that the HCN chemistry, described in the previous part, is not (or very little) associated with the (100) faces (largely predominant on *smoke* MgO) but rather with defective situations.

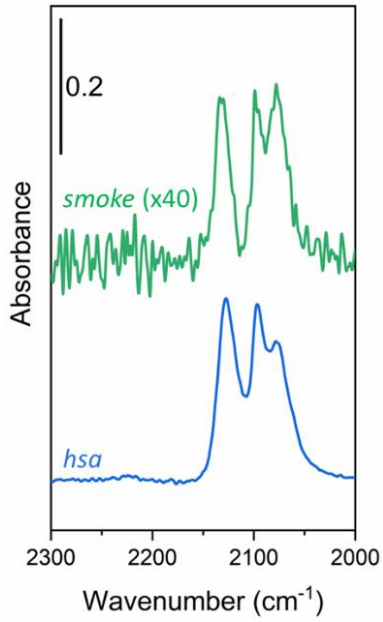

Figure 64: IR spectra of HCN (5 mbar equilibrium pressure) adsorbed at ca. 150 K on smoke (enlarged 40 times) and hsa MgO.

Based on the discussed results, it can be concluded that the HCN interaction at 150 K with the complex and morphologically heterogeneous MgO surface is characterized by the prevalent formation of chemisorbed species formed by HCN splitting on $Mg^{2+}O^{2-}$ acid-base pair, mainly controlled by the strong Lewis base properties of the surface *cus* O^{2-} species. However, the simultaneous occurring of molecularly adsorbed species, which are structurally and spectroscopically similar to that of the other oxides (silica, titania and alumina), must be highlighted.

1. Chadwick, B. M.; Edwards, H. G. M., *Vibrational and vibrational-rotational spectroscopy of the cyanide ion, the cyano-radical, the cyanogen molecules, and the triatomic cyanides XCN (X=H, F, Cl, Br, and I).* In Molecular Spectroscopy: Volume 1, Barrow, R. F.; Long, D. A.; Millen, D. J., Eds. The Royal Society of Chemistry: **1973**; Vol. 1, pp 446-522.
2. Mino, L.; Pellegrino, F.; Rades, S.; Radnik, J.; Hodoroaba, V.-D.; Spoto, G.; Maurino, V.; Martra, G., *Beyond Shape Engineering of TiO_2 Nanoparticles: Post-Synthesis Treatment Dependence of Surface Hydration, Hydroxylation, Lewis Acidity and Photocatalytic Activity of TiO_2 Anatase Nanoparticles with Dominant {001} or {101} Facets*. ACS Applied Nano Materials **2018,** 1 (9), 5355-5365.
3. Brinker, C. J.; Butler, K. S.; Garofalini, S. H., *Are nearly free silanols a unifying structural determinant of silica particle toxicity?* Proceedings of the National Academy of Sciences **2020,** 117 (48), 30006-30008.
4. Zhuravlev, L. T., The surface chemistry of amorphous silica. Zhuravlev model. Colloids and Surfaces A: Physicochemical and Engineering Aspects **2000,** 173 (1), 1-38.
5. Bunker, B. C.; Haaland, D. M.; Michalske, T. A.; Smith, W. L., *Kinetics of dissociative chemisorption on strained edge-shared surface defects on dehydroxylated silica*. Surface Science **1989,** 222 (1), 95-118.
6. Hadjiivanov, K., Chapter Two - *Identification and Characterization of Surface Hydroxyl Groups by Infrared Spectroscopy.* In Advances in Catalysis, Jentoft, F. C., Ed. Academic Press: **2014**; Vol. 57, pp 99-318.
7. Bordiga, S.; Roggero, I.; Ugliengo, P.; Zecchina, A.; Bolis, V.; Artioli, G.; Buzzoni, R.; Marra, G.; Rivetti, F.; Spanò, G.; Lamberti, C., *Characterisation of defective silicalites*. Journal of the Chemical Society, Dalton Transactions **2000,** (21), 3921-3929.
8. Armandi, M.; Bolis, V.; Bonelli, B.; Otero Areán, C.; Ugliengo, P.; Garrone, E., *Silanol-Related and Unspecific Adsorption of Molecular Ammonia on Highly Dehydrated Silica*. The Journal of Physical Chemistry C **2011,** 115 (47), 23344-23353.
9. Storozhev, P. Y.; Otero Areán, C.; Garrone, E.; Ugliengo, P.; Ermoshin, V. A.; Tsyganenko, A. A., *FTIR spectroscopic and ab initio evidence for an amphipathic character of CO bonding with silanol groups*. Chemical Physics Letters **2003,** 374 (5), 439-445.
10. Gierada, M.; De Proft, F.; Sulpizi, M.; Tielens, F., *Understanding the Acidic Properties of the Amorphous Hydroxylated Silica Surface.* The Journal of Physical Chemistry C **2019,** 123 (28), 17343-17352.
11. Zecchina, A.; Scarano, D.; Bordiga, S.; Spoto, G.; Lamberti, C., *Surface structures of oxides and halides and their relationships to catalytic properties.* In Advances in Catalysis, Academic Press: **2001**; Vol. 46, pp 265-397.
12. Rimola, A.; Costa, D.; Sodupe, M.; Lambert, J.-F.; Ugliengo, P., Silica Surface Features and *Their Role in the Adsorption of Biomolecules: Computational Modeling and Experiments*. Chemical Reviews **2013,** 113 (6), 4216-4313.

13. Akouche, M.; Jaber, M.; Maurel, M. C.; Lambert, J. F.; Georgelin, T., Phosphoribosyl Pyrophosphate: *A Molecular Vestige of the Origin of Life on Minerals*. Angew Chem Int Ed Engl **2017,** 56 (27), 7920-7923.
14. Martra, G.; Deiana C Fau - Sakhno, Y.; Sakhno Y Fau - Barberis, I.; Barberis I Fau - Fabbiani, M.; Fabbiani M Fau - Pazzi, M.; Pazzi M Fau - Vincenti, M.; Vincenti, M., *The formation and self-assembly of long prebiotic oligomers produced by the condensation of unactivated amino acids on oxide surfaces.* Angew Chem Int Ed Engl **2014,** 53 (18), 4671-4.
15. Rimola, A.; Fabbiani, M.; Sodupe, M.; Ugliengo, P.; Martra, G., *How does Silica Catalyze the Amide Bond Formation in Dry Conditions? Role of Specific Surface Silanol Pairs*. ACS Catalysis **2018,** 8 (5), 4558-4568.
16. Signorile, M.; Pantaleone, S.; Balucani, N.; Bonino, F.; Martra, G.; Ugliengo, P., *Monitoring the reactivity of formamide on amorphous SiO_2 by in-situ UV-Raman spectroscopy and DFT modeling*. Molecules **2020,** 25 (10), 9-12.
17. *Adsorption on Silica Surfaces*. Surfactant Science Series. Volume 90 Edited by Eugène Papirer (Institute de Chimie des Surfaces et Interfaces, Mulhouse, France). Marcel Dekker: New York. . American Chemical Society: **2001**; Vol. 123, p 2468-2468.
18. Davydov, V. Y.; Kiselev, A. V.; Zhuravlev, L. T., *Study of the surface and bulk hydroxyl groups of silica by infra-red spectra and D_2O-exchange.* Transactions of the Faraday Society **1964,** 60 (0), 2254-2264.
19. Zecchina, A.; Spoto, G.; Bordiga, S., *Vibrational Spectroscopy of Zeolites*. In Handbook of Vibrational Spectroscopy, Griffiths, J. M. C. a. P. R., Ed. **2006**; Vol. 4, pp 3043-3071.
20. Tsyganenko, A. A.; Chizhik, A. M.; Chizhik, A. I., A FTIR search for linkage isomerism of CN− ions adsorbed on oxides and zeolites. Physical Chemistry Chemical Physics **2010**, 12 (24), 6387-6395.
21. Kim, S.; Sorescu, D. C.; Yates, J. T., *Infrared Spectroscopic Study of the Adsorption of HCN by γ-Al_2O_3: Competition with Triethylenediamine for Adsorption Sites*. The Journal of Physical Chemistry C **2007,** 111 (14), 5416-5425.
22. Morrow, B. A.; Cody, I. A., *Infra-red studies of reactions on oxide surfaces. Part 3.—HCN and C_2N_2 on silica.* Journal of the Chemical Society, Faraday Transactions 1: Physical Chemistry in Condensed Phases **1975,** 71 (0), 1021-1032.
23. Raskó, J.; Bánsági, T.; Solymosi, F., *HCN adsorption on silica and titania supported Rh catalysts studied by FTIR.* Physical Chemistry Chemical Physics **2002,** 4 (14), 3509-3513.
24. Zhang, H.; Banfield, J. F., *Structural characteristics and mechanical and thermodynamic properties of nanocrystalline TiO_2.* Chem Rev **2014,** 114 (19), 9613-44.
25. Srivastava, A. K.; Deepa, M.; Bhandari, S.; Fuess, H., Tunable, *Nanostructures and Crystal Structures in Titanium Oxide Films.* Nanoscale Res Lett **2009,** 4 (1), 54-62.
26. Diebold, U.; Ruzycki, N.; Herman, G. S.; Selloni, A., *One step towards bridging the materials gap: surface studies of TiO_2 anatase.* Catalysis Today **2003,** 85 (2-4), 93-100.
27. Wen, C. Z.; Jiang, H. B.; Qiao, S. Z.; Yang, H. G.; Lu, G. Q., *Synthesis of high-reactive facets dominated anatase TiO_2*. Journal of Materials Chemistry **2011,** 21 (20).

28. Bourikas, K.; Kordulis, C.; Lycourghiotis, A., *Titanium dioxide (Anatase and Rutile): Surface chemistry, liquid-solid interface chemistry, and scientific synthesis of supported catalysts.* Chemical Reviews **2014,** 114 (19), 9754-9823.
29. Ho, S.-W., *Surface Hydroxyls and Chemisorbed Hydrogen on Titania and Titania Supported Cobalt.* Journal of the Chinese Chemical Society **1996,** 43 (2), 155-163.
30. Hadjiivanov, K. I.; Klissurski, D. G., *Surface chemistry of titania (anatase) and titania-supported catalysts*. Chemical Society Reviews **1996,** 25 (1), 61-69.
31. Busca, G.; Saussey, H.; Saur, O.; Lavalley, J. C.; Lorenzelli, V., *FT-IR characterization of the surface acidity of different titanium dioxide anatase preparations.* Applied Catalysis **1985,** 14, 245-260.
32. Tsyganenko, A. A.; Filimonov, V. N., *Infrared Spectra of Surface Hydroxyl Groups and Crystalline Structure of Oxides.* Spectroscopy Letters **1972,** 5 (12), 477-487.
33. Primet, M.; Pichat, P.; Mathieu, M. V., *Infrared study of the surface of titanium dioxides. I. Hydroxyl groups.* The Journal of Physical Chemistry **1971,** 75 (9), 1216-1220.
34. Hashimoto, K.; Irie, H.; Fujishima, A., *TiO_2 Photocatalysis: A Historical Overview and Future Prospects.* Japanese Journal of Applied Physics **2005,** 44 (12), 8269-8285.
35. Jain, S. M.; Biedrzycki, J. J.; Maurino, V.; Zecchina, A.; Mino, L.; Spoto, G., *Acetylene oligomerization on the surface of TiO_2: a step forward in the in situ synthesis of nanostructured carbonaceous structures on the surface of photoactive oxides.* Journal of Materials Chemistry A **2014,** 2 (31), 12247-12254.
36. Biedrzycki, J. J.; Livraghi, S.; Corazzari, I.; Mino, L.; Spoto, G.; Giamello, E., *On the Redox Mechanism Operating along C_2H_2 Self-Assembly at the Surface of TiO_2.* Langmuir **2015,** 31 (1), 569-577.
37. Mino, L.; Cesano, F.; Scarano, D.; Spoto, G.; Martra, G., *Molecules and heterostructures at TiO_2 surface: the cases of H_2O, CO_2, and organic and inorganic sensitizers*. Research on Chemical Intermediates **2019,** 45 (12), 5801-5829.
38. Volokh, M.; Peng, G.; Barrio, J.; Shalom, M., *Carbon Nitride Materials for Water Splitting Photoelectrochemical Cells.* Angewandte Chemie International Edition **2019,** 58 (19), 6138-6151.
39. Hazen, R. M.; Papineau, D.; Bleeker, W.; Downs, R. T.; Ferry, J. M.; McCoy, T. J.; Sverjensky, D. A.; Yang, H., *Mineral evolution*. American Mineralogist **2008,** 93 (11-12), 1693-1720.
40. ZüRcher, L.; Kring, D. A., *Hydrothermal alteration in the core of the Yaxcopoil-1 borehole, Chicxulub impact structure, Mexico*. Meteoritics & Planetary Science **2004,** 39 (7), 1199-1221.
41. Wang, A.; Kuebler, K.; Jolliff, B.; Haskin, L. A., *Mineralogy of a Martian meteorite as determined by Raman spectroscopy.* Journal of Raman Spectroscopy **2004,** 35 (6), 504-514.
42. Han, J.; Brearley, A., *Formation of TiO_2 Nanoparticles in a CAI-Like Object from an AOA in the ALHA 77307 CO3.0 Carbonaceous Chondrite*. Meteoritics and Planetary Science Supplement **2011,** 46.
43. Cleaves, H. J., 2nd; Jonsson, C. M.; Jonsson, C. L.; Sverjensky, D. A.; Hazen, R. M., *Adsorption of nucleic acid components on rutile (TiO_2) surfaces.* Astrobiology **2010,** 10 (3), 311-23.

44. Leyton, P.; Saladino, R.; Crestini, C.; Campos-Vallette, M.; Paipa, C.; Berríos, A.; Fuentes, S.; Zárate, R. A., *Influence of TiO_2 on prebiotic thermal synthesis of the Gly-Gln polymer*. Amino Acids **2012,** 42 (6), 2079-2088.
45. Rimola, A.; Sodupe, M.; Ugliengo, P., *Role of Mineral Surfaces in Prebiotic Chemical Evolution. In Silico Quantum Mechanical Studies.* Life (Basel) **2019,** 9 (1).
46. Deiana, C.; Sakhno, Y.; Fabbiani, M.; Pazzi, M.; Vincenti, M.; Martra, G., *Direct Synthesis of Amides from Carboxylic Acids and Amines by Using Heterogeneous Catalysts: Evidence of Surface Carboxylates as Activated Electrophilic Species.* ChemCatChem **2013,** 5 (10), 2832-2834.
47. Martra, G.; Deiana, C.; Sakhno, Y.; Barberis, I.; Fabbiani, M.; Pazzi, M.; Vincenti, M., *The formation and self-assembly of long prebiotic oligomers produced by the condensation of unactivated amino acids on oxide surfaces.* Angew Chem Int Ed Engl **2014,** 53 (18), 4671-4.
48. Pantaleone, S.; Rimola, A.; Sodupe, M., Canonical, *Deprotonated, or Zwitterionic? A Computational Study on Amino Acid Interaction with the TiO_2 (101) Anatase Surface*. The Journal of Physical Chemistry C **2017,** 121 (26), 14156-14165.
49. Pantaleone, S.; Ugliengo, P.; Sodupe, M.; Rimola, A., *When the Surface Matters: Prebiotic Peptide-Bond Formation on the TiO_2 (101) Anatase Surface through Periodic DFT-D2 Simulations.* Chemistry - A European Journal **2018,** 24 (61), 16292-16301.
50. Saladino, R.; Ciambecchini, U.; Crestini, C.; Costanzo, G.; Negri, R.; Di Mauro, E., *One-pot TiO_2-catalyzed synthesis of nucleic bases and acyclonucleosides from formamide: implications for the origin of life.* Chembiochem **2003,** 4 (6), 514-21.
51. Civis, S.; Szabla, R.; Szyja, B. M.; Smykowski, D.; Ivanek, O.; Knizek, A.; Kubelik, P.; Sponer, J.; Ferus, M.; Sponer, J. E., *TiO_2-catalyzed synthesis of sugars from formaldehyde in extraterrestrial impacts on the early Earth.* Sci Rep **2016,** 6, 23199.
52. Mino, L.; Spoto, G.; Bordiga, S.; Zecchina, A., *Particles morphology and surface properties as investigated by HRTEM, FTIR, and periodic DFT calculations: From pyrogenic TiO_2 (P25) to nanoanatase.* Journal of Physical Chemistry C **2012,** 116 (32), 17008-17018.
53. Nakamoto, K., *Infrared and Raman Spectra of Inorganic and Coordination Compounds_ Part B_* Applications in Coordination, Organometallic, and Bioinorganic Chemistry. **2009**.
54. Busca, G., *Structural, Surface, and Catalytic Properties of Aluminas*. **2014**; pp 319-404.
55. Prins, R., On the structure of γ-Al_2O_3. Journal of Catalysis **2020,** 392, 336-346.
56. Trueba, M.; Trasatti, S. P., *γ-Alumina as a Support for Catalysts: A Review of Fundamental Aspects*. European Journal of Inorganic Chemistry **2005,** 2005 (17), 3393-3403.
57. Gribov, E. N.; Zavorotynska, O.; Agostini, G.; Vitillo, J. G.; Ricchiardi, G.; Spoto, G.; Zecchina, A., *FTIR spectroscopy and thermodynamics of CO and H_2 adsorbed on γ-, δ- and α-Al_2O_3.* Physical Chemistry Chemical Physics **2010,** 12 (24), 6474-6482.
58. Digne, M., *Use of DFT to achieve a rational understanding of acid?basic properties of ?-alumina surfaces*. Journal of Catalysis **2004,** 226 (1), 54-68.

59. Wischert, R.; Laurent, P.; Coperet, C.; Delbecq, F.; Sautet, P., *Gamma-Alumina: the essential and unexpected role of water for the structure, stability, and reactivity of "defect" sites*. J Am Chem Soc **2012,** 134 (35), 14430-49.
60. Joubert, J.; Salameh, A.; Krakoviack, V.; Delbecq, F.; Sautet, P.; Copéret, C.; Basset, J. M., *Heterolytic Splitting of H_2 and CH_4 on γ-Alumina as a Structural Probe for Defect Sites*. The Journal of Physical Chemistry B **2006,** 110 (47), 23944-23950.
61. Morterra, M., *A case study: surface chemistry and surface structure of catalytic aluminas, as studied by vibrational spectroscopy of adsorbed species*. **1996**.
62. Knözinger, H.; Ratnasamy, P., *Catalytic Aluminas: Surface Models and Characterization of Surface Sites.* Catalysis Reviews **1978,** 17 (1), 31-70.
63. Arora, A. K.; Kamaluddin, *Role of metal oxides in chemical evolution: interaction of ribose nucleotides with alumina.* Astrobiology **2009,** 9 (2), 165-71.
64. Nittler, L. R.; Alexander, C. M. O. D.; Wang, J.; Gao, X., *Meteoritic oxide grain from supernova found.* Nature **1998**, 393 (6682), 222-222.
65. Nittler, L.; Alexander, C.; Gallino, R.; Hoppe, P.; Nguyen, A.; Stadermann, F.; Zinner, A., *Aluminum-, Calcium- And Titanium-Rich Oxide Stardust In Ordinary Chondrite Meteorites*. The Astrophysical Journal **2008,** 682, 1450.
66. Basiuk, V. A.; Sainz-Rojas, J., *Catalysis of peptide formation by inorganic oxides: High efficiency of alumina under mild conditions on the earth-like planets*. Advances in Space Research **2001,** 27 (2), 225-230.
67. Bujdák, J.; Rode, B. M., *Activated alumina as an energy source for peptide bond formation: Consequences for mineral-mediated prebiotic processes*. Amino Acids **2001,** 21 (3), 281-291.
68. Bujdák, J.; Rode, B. M., *Preferential amino acid sequences in alumina-catalyzed peptide bond formation.* Journal of Inorganic Biochemistry **2002,** 90 (1), 1-7.
69. Bujdák, J.; Rode, B. M., *Alumina catalyzed reactions of amino acids. Journal of Thermal Analysis and Calorimetry* **2003,** 73 (3), 797-805.
70. Saladino, R.; Crestini, C.; Costanzo, G.; Negri, R.; Di Mauro, E., *A possible prebiotic synthesis of purine, adenine, cytosine, and 4(3H)-pyrimidinone from formamide: implications for the origin of life.* Bioorg Med Chem **2001,** 9 (5), 1249-53.
71. Low, M. J. D.; Ramamurthy, P., *Infrared study of HCN polymer on alumina*. Journal of the research institute for catalysis Hokkaido university **1968,** 16 (2), 535-542.
72. Spoto, G.; Gribov, E. N.; Ricchiardi, G.; Damin, A.; Scarano, D.; Bordiga, S.; Lamberti, C.; Zecchina, A., *Carbon monoxide MgO from dispersed solids to single crystals: A review and new advances.* Progress in Surface Science **2004,** 76 (3-5), 71-146.
73. Spoto, G.; Gribov, E.; Damin, A.; Ricchiardi, G.; Zecchina, A., *The IR spectra of Mg_{5c}^{2+}(CO) complexes on the (001) surfaces of polycrystalline and single crystal MgO*. Surface Science **2003,** 540 (2), L605-L610.
74. Gribov, E. N.; Bertarione, S.; Scarano, D.; Lamberti, C.; Spoto, G.; Zecchina, A., *Vibrational and Thermodynamic Properties of H_2 Adsorbed on MgO in the 300−20 K Interval.* The Journal of Physical Chemistry B **2004,** 108 (41), 16174-16186.

75. Chizallet, C.; Costentin, G.; Che, M.; Delbecq, F.; Sautet, P., *Revisiting Acido-basicity of the MgO Surface by Periodic Density Functional Theory Calculations: Role of Surface Topology and Ion Coordination on Water Dissociation.* The Journal of Physical Chemistry B **2006,** 110 (32), 15878-15886.
76. Spoto, G.; Bordiga, S.; Zecchina, A.; Cocina, D.; Gribov, E. N.; Regli, L.; Groppo, E.; Lamberti, C., *New frontier in transmission IR spectroscopy of molecules adsorbed on high surface area solids: Experiments below liquid nitrogen temperature.* Catalysis Today **2006,** 113 (1), 65-80.
77. Pilchova, I.; Klačanová, K.; Tatarkova, Z.; Kaplan, P.; Racay, P., *The Involvement of Mg^{2+} in Regulation of Cellular and Mitochondrial Functions.* Oxidative Medicine and Cellular Longevity 2017, 2017, 1-8.
78. Fornaro, T.; Brucato, J. R.; Branciamore, S.; Pucci, A., *Adsorption of nucleic acid bases on magnesium oxide (MgO).* International Journal of Astrobiology **2012,** 12 (1), 78-86.
79. Yuasa S., Orò J., *Role of weak bases on the prebiotic formation of heterocyclic compounds*. In Cosmochemical Evolution and the Origins of Life, Springer, D., Ed. **1974**; pp 295-299.
80. Yuasa, S.; Ishigami, M., *Geochemically possible condensation of hydrogen cyanide in the presence of divalent metal compounds*. GEOCHEMICAL JOURNAL **1977**, 11 (4), 247-252.
81. Xiong, Y.; Wang, X.; Zhang, L.; Hu, Z.; Niu, Y.; Tan, H., *Conversion mechanism of toxic hydrogen cyanide by magnesium oxide at high temperatures*. Asian Journal of Chemistry **2014,** 26 (2), 495-498.
82. Ballmann, G.; Elsen, H.; Harder, S., *Magnesium Cyanide or Isocyanide?* Angew Chem Int Ed Engl **2019,** 58 (44), 15736-15741.

Chapter 4

IR investigation of the HCN adsorption at 150 K on amorphous and crystalline Mg_2SiO_4 as models of cosmic dust grains

4.1 Amorphous and Crystalline (Forsterite) Magnesium Silicate

4.1.1 Mg_2SiO_4 surface structure and chemical properties

As already mentioned, silicates are the constituents of the Earth rocks but they are also widespread throughout the solar system. Silicate dust particles mainly having the $(Mg^{2+},Fe^{2+})_2SiO_4$ composition typical of olivines have been detected as well in deep space environments like ISM (interstellar medium), protoplanetary disks and debris and even in distant objects like quasars.[1]

The Mg-rich member *forsterite* (Mg_2SiO_4) has deserved special attention as it is thought that grains of this mineral could have played a role in the adsorption and the reaction of simple chemical precursors to give prebiotic molecules (see for instance ref.[2]).

Forsterite has an orthorhombic structure composed by an ordered distribution of negatively charged SiO_4 tetrahedra intercalated in 1:2 molar ratio by Mg^{2+} cations occupying two different octahedral sites (M_1 and M_2 in *Figure 65*).[3]

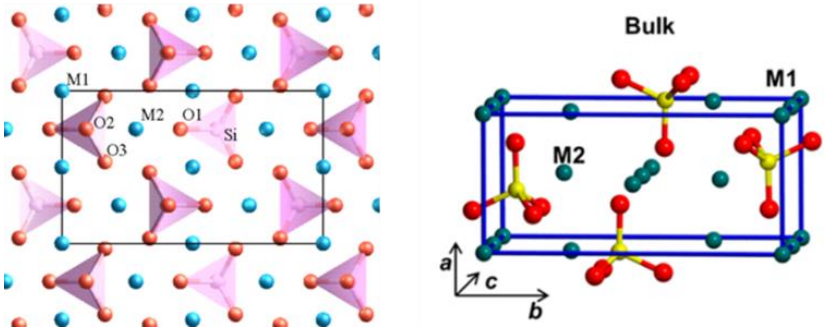

Figure 65. Forsterite bulk structure (on the left, from [4]) and unit cell (on the right, from ref. [3]). The tetrahedral units have SiO_4 composition. M_1 and M_2 indicate the two different octahedral sites occupied by the Mg^{2+} cations.

The Wullf's reconstruction of a forsterite crystal and the simulation of the structure of the most stable surface terminations of are shown in *Figure 66*.

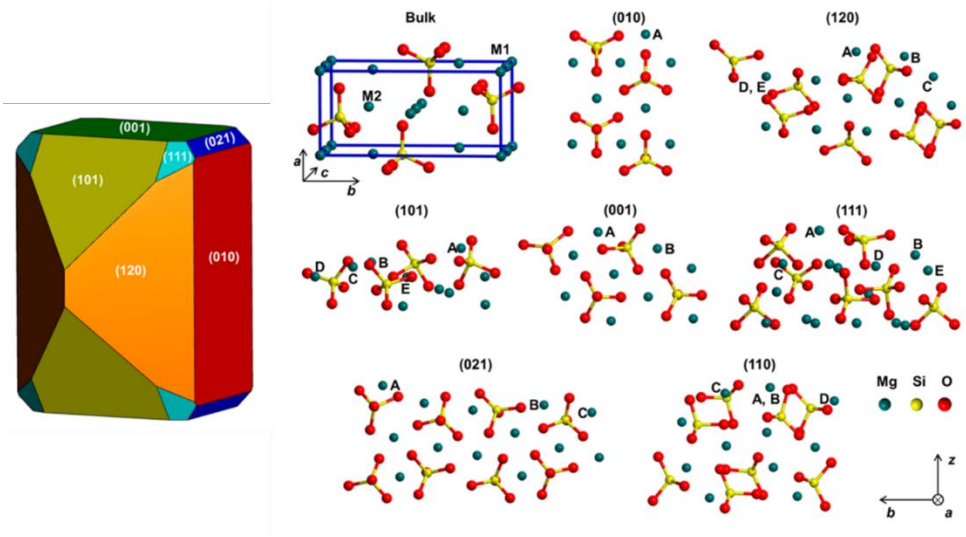

Figure 66. Wullf's construction (on the left) and simulated surface structure (on the right) of the most stable terminations of forsterite crystal (surface energy increasing in the order (010) → (110)). The capital letters indicate coordinatively unsaturated Mg^{2+} Lewis acid sites in different local environment, from the most (A) to the less (E) exposed on the termination surface. From ref. [3]

Focusing the attention on the surface Mg^{2+} cations, it is noticeable in *Figure 67* the variety of possible local structures they can assume, going from situations where they are highly exposed (A sites) to situations where they are more hidden (like in E) through a variety of intermediate possibilities. The only exception is the (010) termination where only one family (A) of protruding Mg^{2+} ions is present.

The electrostatic potential maps at the surface of the (010) and of the (120) terminations (the latter one assumed as representative of faces with highly heterogeneous population of Mg^{2+} sites) are shown in *Figure 67*. As it is possible to see, on the thermodynamically most stable (010) surface the exposed Mg^{2+} cations (all belonging to the same A family) lie in between significative positive regions, while on the (120) surface the most exposed A sites lie on positive regions and those less exposed (B-E sites) occupy more neutral or even negative portions.

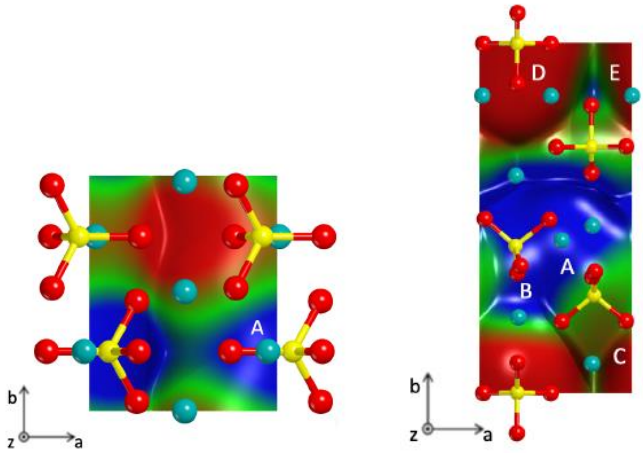

Figure 67. Map (red = negative, blue = positive, green = neutral) of the electrostatic potential (EPS) at the (010) (left) and (111) (right) forsterite terminations (top view). Adapted from ref. [5]

Crystalline forsterite is the common form when the mineral is produced in hot environments (like those leading to formation of ultramafic and igneous rocks on our planet or close to stars in the outer space); on the contrary in the dust grains of the cold ISM it is predominantly (*ca.* 98%) present in amorphous form.[1] Similar composition is found in primitive meteorites, comets, and interplanetary dust particles (IDPs).[6] As shown in *Figure 68* the bulk and the surface structure of amorphous forsterite (AMS) and of the crystalline form (CMS) are dramatically different.

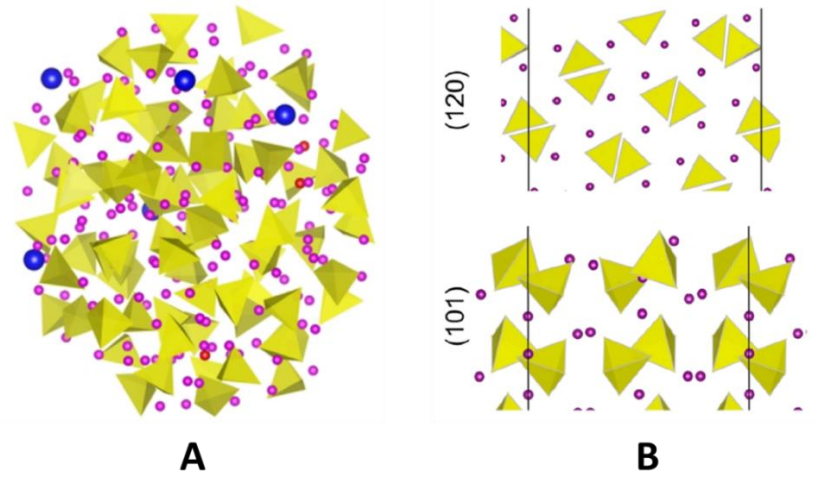

Figure 68. Computer simulations of an amorphous Mg_2SiO_4 cluster (A) and of a lateral view of the (120) and (101) terminations of crystalline forsterite (CMS). The blue dots in (A) represents defective O sites not belonging to SiO_4 tetrahedra (in yellow) and not present in the crystalline form (B). The purple dots represent Mg sites. Adapted from Signorile et al. [7]

Concerning the bulk, the regular distribution of SiO_4 tetrahedra and intercalated Mg^{2+} cations typical of CMS is lost in AMS, whose structure has been rather described as a mixture of $(MgO)_x$ polymers and monomeric SiO_4 or dimeric Si_2O_7 species (*Figure 69*).[8,9]

Concerning the surface, beside portions where the regular distribution of SiO_4 tetrahedra and isolated Mg^{2+} of CMS is maintained, defective situations are now present leading to formation of Si-O-Si bridges, similar to those found on silica, and of $-O^{2-}Mg^{2+}O^{2-}Mg^{2+}-$ chains or more complex structures (like MgO clusters made of few atoms) containing $Mg^{2+}O^{2-}$ acid/base couples (absent in the CMS ideal framework). Furthermore, in presence of H_2O it is also expected the formation of surface OH groups to occur, following the hydration mechanisms schematized in *Figure 69*.

In conclusion, the AMS surface is expected to be much more heterogeneous than that of CMS from the structural point of view and possibly also for the chemical properties.

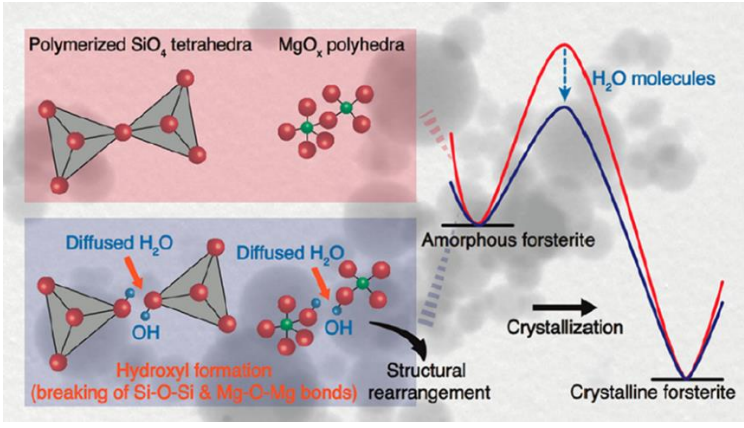

Figure 69. Schematic representation of polymerized SiO_4 tetrahedra and MgO_x polyhedral structures forming the (completely dehydrate) AMS phase (upper scheme on the left). In the bottom scheme on the left is shown the effect of chemical adsorption of water, resulting in the formation Si-OH (surface silanols) and Mg-OH defective groups. In the right part of the figure, it is illustrated the thermodynamic role of adsorbed water in the AMS → CMS crystallization process.[10]

Different surface properties due to different surface structures are already revealed by the IR spectra of the two materials in air (hydrated form) and after outgassing at high temperature (dehydrated form) (*Figure 70*).[10] Notice that, both hydrated AMS and CMS show manifestations due to adsorbed water molecules in reciprocal hydrogen bonding interaction in the 3700-2200 cm^{-1} region ($\nu_{OH\cdots O}$) and at 1640 cm^{-1} (δ_{OHO}), but their intensity on CMS is definitely lower (curves a and b in *Figure 70*) despite the comparable surface area. This suggests that the not (or little, *vide infra*) defective surface of CMS is definitely less hydrophilic. The larger hydrophilicity of the amorphous sample is indeed compatible with the presence of Brønsted acid OH groups like those in *Figure 70*.

Another characteristic of AMS is the presence of strong absorptions in the 1600-1330 cm^{-1} region associated with monodentate carbonates, almost totally absent on CSM. Their presence is in agreement with the enhanced surface Lewis basicity conferred to the AMS surface by the *cus* O^{2-} (and OH^-) species of MgO-like surface portions.

After outgassing at high temperature (curves a" and b" in *Figure 70*), most of the above manifestations disappear and only residual narrow OH bands are observed in the 3700-3500 cm^{-1} interval.

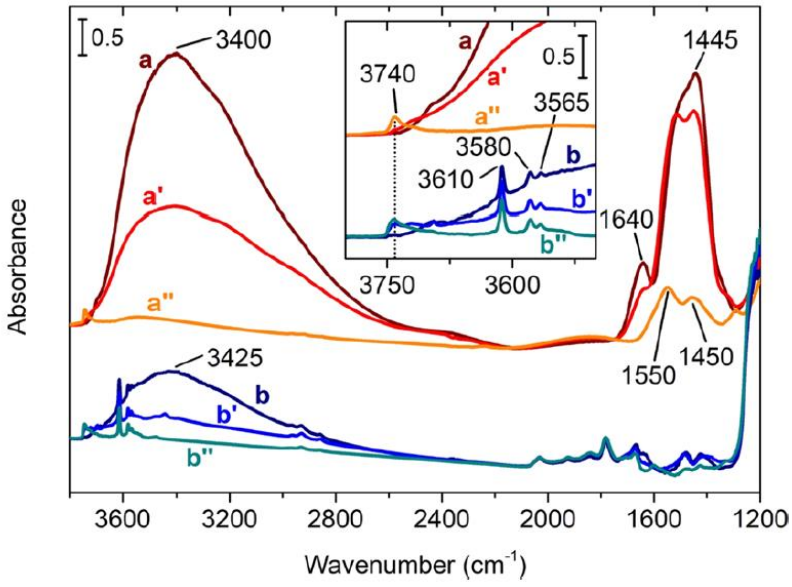

Figure 70. IR spectra of AMS (upper part) and CMS (lower part) samples exposed to air (curves a and b), outgassed at RT (a' and b') and outgassed at 673 K (a" and b").[7]

Their unexpected presence on CSM is conceivable to be due to the existence even on the crystalline material of small still amorphous residual areas as a consequence of not complete crystallization. The existence of these areas has been indeed proven by High Resolution Transmission Electron Microscopy.[7]

Signorile et al.[7] have investigated the surface properties of the two materials also in terms of Brønsted acidity (due to OH groups), Lewis basicity (related to O^{2-}/OH^{-} species) and Lewis acidity (due to Mg^{2+} species) by IR spectroscopy of adsorbed CD_3CN, CO_2 and CO. For the scope of the thesis, we will shortly summarize only the results obtained with the CN-containing molecule. The spectra obtained by dosing CD_3CN at RT on AMS and CMS samples previously outgassed at high temperature, then at decreasing gas pressure are shown in the $\nu_{(C\equiv N)}$ stretching region in *Figure 71*; they allow to conclude that:

i. the isolated Mg^{2+} species present on both the samples are able to form $CD_3C{\equiv}N{\cdots}Mg^{2+}$ molecular adducts giving rise to the $\nu_{(C{\equiv}N)}$ absorption at 2300 cm^{-1} in *Figure 71*. Only a fraction of them is reversible upon outgassing, thus evidencing some heterogeneity as far their Lewis acidity is concerned.

ii. Both samples form fully reversible $CD_3C{\equiv}N{\cdots}H$-O-Si hydrogen bonded species by interaction of the molecule with Brønsted acid silanol groups, as testified by the $\nu_{(C{\equiv}N)}$ band at 2266 cm^{-1}.

iii. Unlike CMS, AMS possesses unique properties due to the presence on its surface of strongly basic O^{2-} or OH^- species, absent (nearly) on CMS. These sites are responsible for acetonitrile irreversible chemisorption through proton transfer from the molecule to the surface and formation of CD_2CN^- adsorbed species (responsible for the $\nu_{(C{\equiv}N)}$ band in the 2250-2075 cm^{-1} interval in the upper part of *Figure 71*).

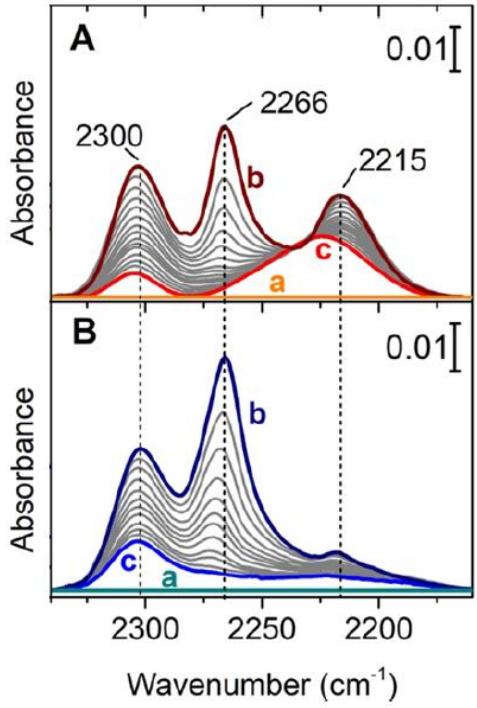

Figure 71. IR spectra of CD3CN adsorbed at RT at decreasing equilibrium pressure (from the most intense to the less intense curve) on AMS (panel A) and CMS (panel B) samples previously outgassed at 673 K (adapted from ref. [7]).

These observations (together with those concerning the CMS and AMS interaction with CO and CO_2) allow the authors to draw some important conclusions: "*Remarkably, the amorphous and crystalline form of Mg_2SiO_4 characterized here present identical composition but a different surface reactivity. In the framework of the complex network of reaction occurring on the surface of dust grains in the cosmic environment, this implies that the atomic structure of the grain strongly determines its interaction with the molecules adsorbed on it, possibly promoting completely different reaction paths".*[7]

4.1.2 Silicates and prebiotic chemistry

The possible role of silicates as heterogeneous catalysts for prebiotic chemical processes has been the subject of several theoretical and experimental investigations.[2] Among them here only mention those devoted to the surface chemistry of Mg-silicates toward more simple (H_2O, H, H_2, O_2 and NH_3)[3, 11-24] and more complex organic molecules (alcohols, aldehydes, carboxylic acids, hydrocarbons, amines, amides, glycine, phosphonic and sulfonic acids, nucleobases, etc.)[7, 25-32] detected in the interstellar medium and on extraterrestrial bodies.

In this thesis the investigation has been extended to HCN, whose interaction with AMS and CSM has been studied by *in situ* IR spectroscopy in the 150-300 K temperature interval, as for the solids described in the previous sections.

4.2 Experimental details

Materials

- ✓ **Amorphous magnesium silicate (hereafter AMS):** was produced by mixing the precursors $Mg(OH)_2$ and SiO_2 in a high temperature plasma (~10,000 K) and subsequent quenching; SSA = 37 m^2/g (more details in ref. [33]).
- ✓ **Crystalline magnesium silicate or forsterite (hereafter CMS):** was obtained by heating the amorphous material prepared as above at 1073 K for 24 h in air. SSA = 26 m^2/g; (more details in ref. [33])

Before HCN dosage, the AMS and CMS samples were outgassed at 673 K for 1 hours under high vacuum (residual pressure $5x10^{-4}$ mbar) to obtain a dehydrated/dehydroxylated surface.
More information about the properties of the two materials are available in ref. [7]

Methods

As described in *Chapter 3*, paragraph *3.2*.

4.3 The HCN/Mg_2SiO_4 interaction at 150 K: experimental results and discussion

The IR spectra obtained at 150 K at increasing HCN equilibrium pressure on two CMS and AMS samples outgassed at 673 K are compared in *Figure 72*.

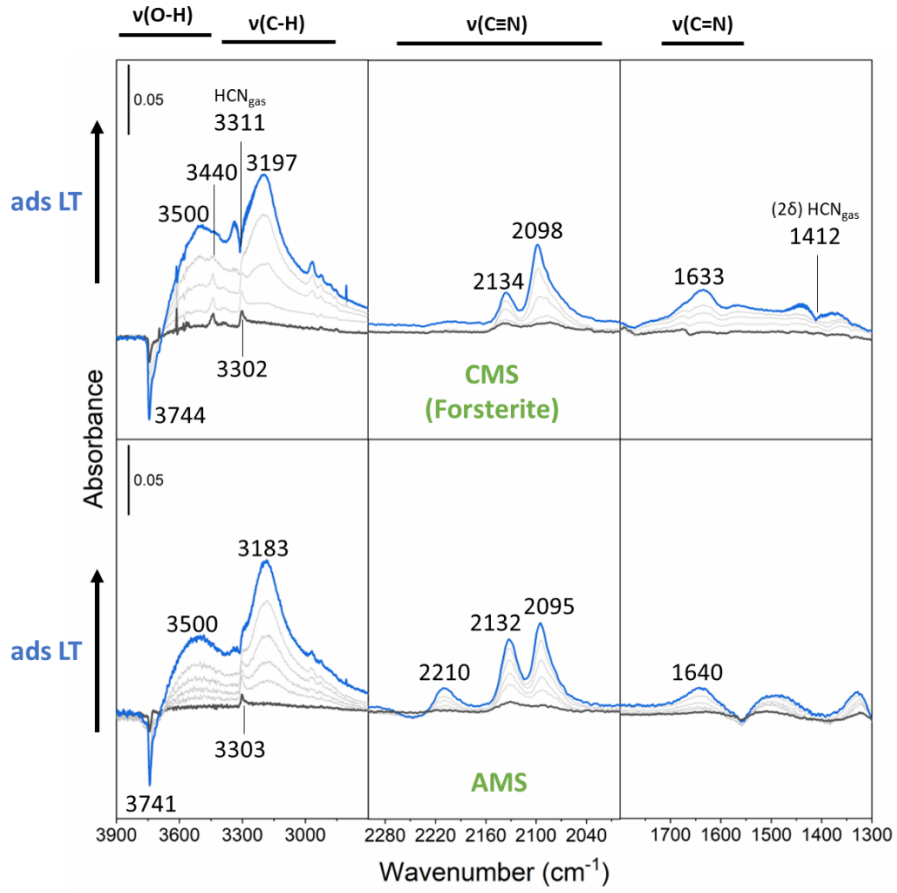

Figure 72. Background subtracted IR spectra of HCN adsorbed at 150 K on Mg-silicates in amorphous (AMS) and crystalline (CMS) form previously outgassed at 673 K. The series shows the effect of gradually increasing the HCN equilibrium up to 5 mbar (blue spectrum).

Already at a first inspection, the spectral patterns appear quite similar to those of the HCN/metal oxide systems discussed in the previous Chapter and their assignment can therefore benefit of most of the conclusions already drawn there. Moreover, SiO_2 and MgO can be assumed as close references materials for the Mg-silicates (especially AMS) because of the chemical composition and of the structural analogies (presence of OH groups, of Mg^{2+} and O^{2-} sites, of $Mg^{2+}O^{2-}$ couples, etc.). For this reason, the spectra obtained at maximum HCN coverage at 150 K on the Mg-silicate samples are compared in *Figure 73* with those on SiO_2 and MgO.

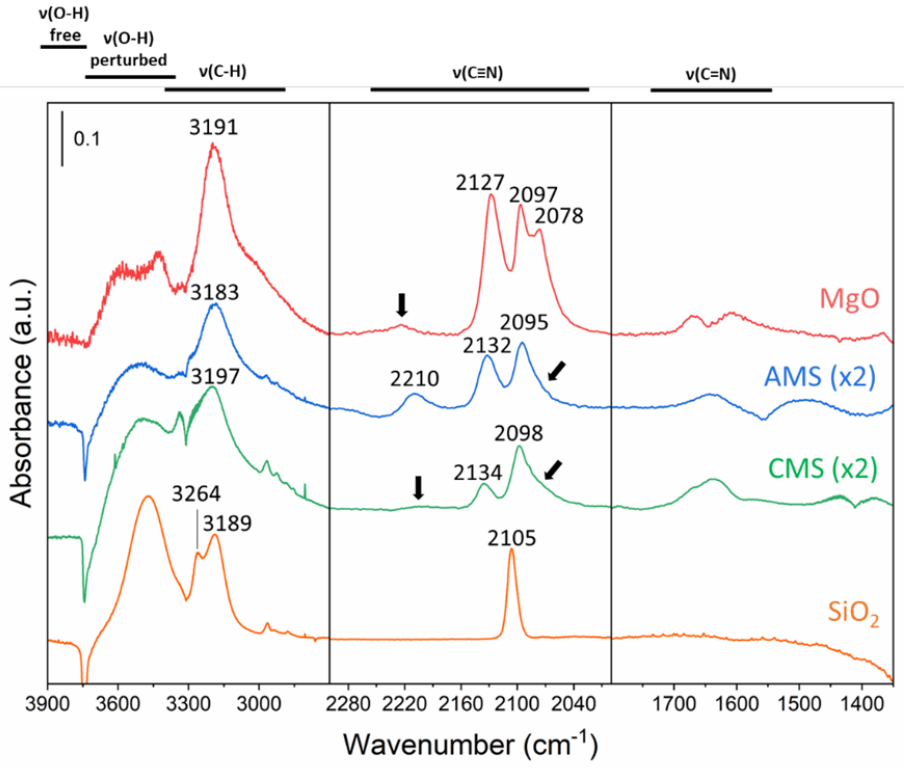

Figure 73. Comparison of the spectra of HCN adsorbed at 150 K and maximum coverage on AMS and CMS and on the SiO_2 and MgO as reference materials.

Upon HCN dosage on both CSM and ASM the progressive erosion of the band at *ca*. 3740 cm^{-1} can be observed with the parallel growth of two broad absorptions at *ca*. 3500 cm^{-1} and 3190 cm^{-1} (*Figure 72*). The transformation is accompanied by the appearance of a clear isosbestic point at ca. 3690 cm^{-1}. Comparison with the spectra of the HCN/SiO_2 system (see paragraph 3.3.3 and *Figure 73*) allows to explain this behaviour with the formation of Si-OH···NCH adducts involving the silanol groups which are present in the disordered AMS structure as well as on the not completely crystallized portions of the CMS sample (see paragraph *4.1.1*). By comparison again with the HCN/SiO_2 system (*Figure 73*) it is straightforward to conclude that the $\nu_{(C\equiv N)}$ mode of these hydrogen bonded adducts contribute to the absorption at 2098-2095 cm^{-1} in the spectra of CMS and AMS and the $\nu_{(CH)}$ one to that at 3197-3183 cm^{-1}. As discussed in the paragraph devoted to HCN/SiO_2 it is not possible to distinguish between the signals due to Si-OH···NCH adducts from those of ···HCN···HCN··· clusters eventually formed at the highest coverages because they are falling in the same spectral regions.

Most of the other absorptions of the HCN/CMS and HCN/AMS systems are in common with those of HCN/MgO (see chapter *3.6.3* and *Figure 72* and *Figure 73*) and can by analogy assigned to:

(i) Mg^{2+}···NCH adducts involving the Mg^{2+} ions present in the structure of both AMS and CMS: $\nu_{(C\equiv N)}$ mode at *ca.* 2130 cm^{-1} and $\nu_{(C-H)}$ at *ca.* 3300 cm^{-1}, the latter one more visible at low coverages in *Figure 72*);

(ii) η^2(C,N)-HCN bridged species: $\nu_{(C=N)}$ band at ca. 1630 cm^{-1}. Notice that the formation of bridged species requires the

presence of clustered $Mg^{2+}O^{2-}$ moieties which, if expected on AMS, should not be present in perfectly crystalline CMS. This again confirm that our CMS samples contain crystalline domains as well as still amorphized portions;

(iii) $Mg^{2+}NC^-$ species formed by HCN heterolytic splitting (*i.e.*, a $\nu_{(C\equiv N)}$ absorption appearing as a weak shoulder at ca. 2080 cm^{-1} and a $\nu_{(OH)}$ feature appearing as a weak shoulder at *ca*. 3600 cm^{-1} of the 3500 cm^{-1} Si-O-H band). As previously described, also these species require $Mg^{2+}O^{2-}$ defective structures to be formed.

Special attention must be paid to the peak at ca. 2210 cm^{-1}, which is relatively strong on AMS and barely visible on CMS (as well as on MgO) (*Figure 72* and *Figure 73*). The frequency of this band is compatible with the $\nu_{(C\equiv N)}$ vibration of the HCN dimer iminoacetonitrile (IAN):

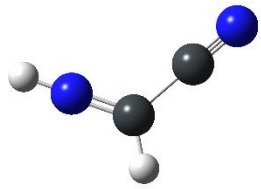

The fact that its manifestation at 2210 cm^{-1} appears immediately at the first HCN doses (*i.e.,* at HCN equilibrium pressure of the order of 10^{-2} mbar or lower) and already at 150 K is a clear evidence that the AMS surface catalyses its formation (*i.e.,* HCN dimerization). It is assumed that the key steps of the dimerization reaction are the formation of CN^- anions as described above at point (iii) and their

nucleophilic attack of incoming gaseous HCN molecules, to give the IAN product plausibly chemically adsorbed at the AMS surface as in the following scheme:

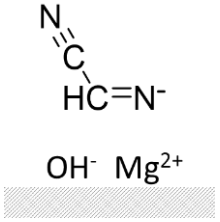

Some results discussed in the master thesis of N. Bancone[5] of the Theoretical Chemistry Group of our Department confirmed this view. Bancone has actually investigated the HCN dimerization on the forsterite (101), (120), and (111) extended surfaces by computational methods aiming to localize transition state (TS) of the dimerization reaction with respect to the reagents and the products. Among the calculated potential barriers, the greatest stabilization was obtained for the anionic IAN adsorbed on the more exposed Mg^{2+} sites at the (101) face (the most extended of forsterite) (*Figure 74*). The anionic IAN formed on this site could be a short-lived intermediate for further oligomerization steps. The calculated reaction rates resulted to vary from a few minutes to 10^{-7} seconds in the 150-300 K temperature range, being these values fully compatible with our spectroscopic results.

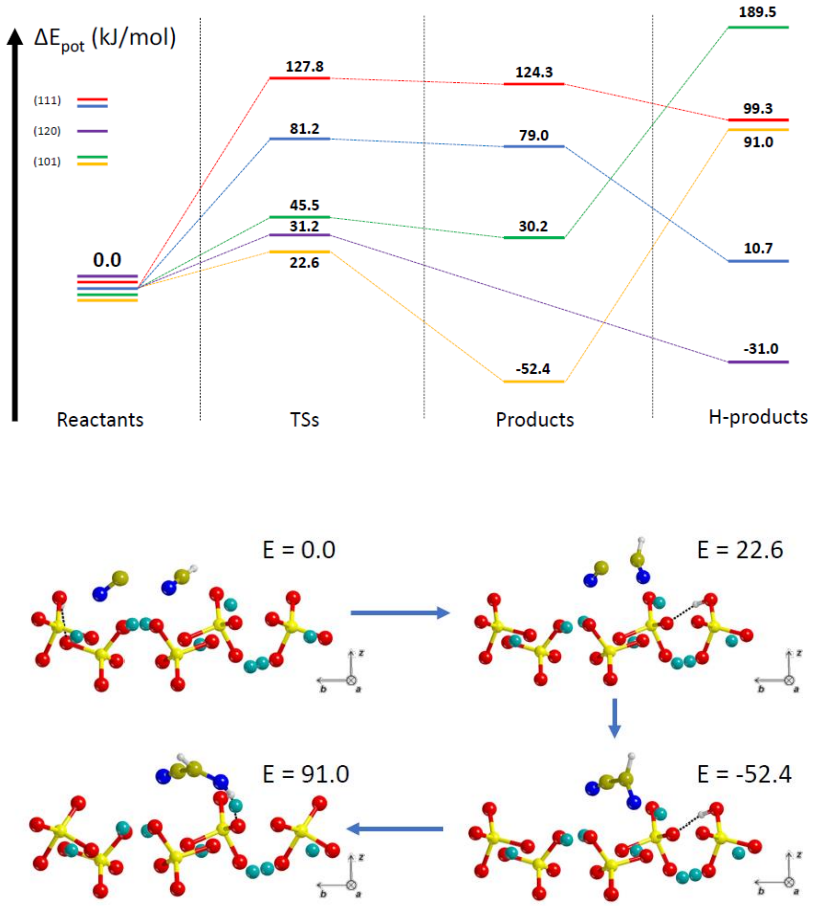

Figure 74. In the upper part, the PBE-D(N) energy profiles for five dimerizations on (111), (101), and (120) surfaces. The bottom part shows the side view of the dimerization on (101) surface. Adapted from. ref [5]*

Based on these findings, it is possible to conclude that for both AMS and CMS the interaction with HCN at 150 K leads to the formation of adsorbed species similar to that found on silica and magnesium oxide, which therefore represent good reference structural models. In particular, the presence of surface Mg^{2+}-O^{2-} moieties, especially on amorphous samples, is crucial to promote the HCN dissociation and the subsequent dimerization already at 150 K.

1. Henning, T., *Cosmic Silicates*. Annual Review of Astronomy and Astrophysics, 21-46 (2010) **2010,** 48.
2. Rimola, A.; Sodupe, M.; Ugliengo, P., *Role of Mineral Surfaces in Prebiotic Chemical Evolution. In Silico Quantum Mechanical Studies.* Life (Basel) **2019,** 9 (1).
3. Zamirri, L.; Corno, M.; Rimola, A.; Ugliengo, P., *Forsterite Surfaces as Models of Interstellar Core Dust Grains: Computational Study of Carbon Monoxide Adsorption*. ACS Earth and Space Chemistry **2017,** 1 (7), 384-398.
4. Wikipedia contributors. *Forsterite*. In Wikipedia, The Free Encyclopedia. https://en.wikipedia.org/w/index.php?title=Forsterite&oldid=1071645469.
5. Bancone, N. *HCN adsorption and reactivity on crystalline forsterite surfaces: a quantum-mechanical study*. University of Turin, Turin, 2022.
6. Hanner, M. S. In *The Silicate Material in Comets, Composition and Origin of Cometary Materials, Dordrecht*; Altwegg, K.; Ehrenfreund, P.; Geiss, J.; Huebner, W. F., Eds. Springer Netherlands: Dordrecht, **1999**; pp 99-108.
7. Signorile, M.; Zamirri, L.; Tsuchiyama, A.; Ugliengo, P.; Bonino, F.; Martra, G., *On the Surface Acid–Base Properties of Amorphous and Crystalline Mg_2SiO_4 as Probed by Adsorbed CO, CO_2, and CD_3CN.* ACS Earth and Space Chemistry **2020,** 4 (3), 345-354.
8. Kohara, S.; Suzuya, K.; Takeuchi, K.; Loong, C. K.; Grimsditch, M.; Weber, J. K. R.; Tangeman, J. A.; Key, T. S., *Glass Formation at the Limit of Insufficient Network Formers*. Science **2004**, 303 (5664), 1649-1652.
9. Kohara, S.; Akola, J.; Morita, H.; Suzuya, K.; Weber, J. K. R.; Wilding, M. C.; Benmore, C. J., *Relationship between topological order and glass forming ability in densely packed enstatite and forsterite composition glasses*. Proceedings of the National Academy of Sciences **2011**, 108 (36), 14780-14785.
10. Yamamoto, D.; Tachibana, S., *Water Vapor Pressure Dependence of Crystallization Kinetics of Amorphous Forsterite.* ACS Earth and Space Chemistry **2018,** 2 (8), 778-786.
11. Navarro-Ruiz, J.; Sodupe, M.; Ugliengo, P.; Rimola, A., *Interstellar H adsorption and H2 formation on the crystalline (010) forsterite surface: a B3LYP-D2* periodic study*. Physical Chemistry Chemical Physics **2014,** 16 (33), 17447-17457.
12. Navarro-Ruiz, J.; Martinez-Gonzalez, J.; Sodupe, M.; Ugliengo, P.; Rimola, A., *Relevance of silicate surface morphology in interstellar H_2 formation. Insights from quantum chemical calculations*. Monthly Notices of the Royal Astronomical Society **2015,** 453, 914-924.
13. Garcia-Gil, S.; Teillet-Billy, D.; Rougeau, N.; Sidis, V., *H Atom Adsorption on a Silicate Surface: The (010) Surface of Forsterite.* The Journal of Physical Chemistry C **2013,** 117 (24), 12612-12621.
14. Suhasaria, T.; Thrower, J.; Zacharias, H., *Thermal desorption of astrophysically relevant molecules from forsterite (010)*. Monthly Notices of the Royal Astronomical Society **2017,** 472.

15. Molpeceres de Diego, G.; Rimola, A.; Ceccarelli, C.; Kästner, J.; Ugliengo, P.; Maté, B., *Silicate-mediated interstellar water formation: A theoretical study.* Monthly Notices of the Royal Astronomical Society **2018**, 482, 5389-5400.
16. Liu, T.; Gautam, S. S.; Daemen, L. L.; Kolesnikov, A. I.; Anovitz, L. M.; Hartl, M.; Cole, D. R., *Vibrational Behavior of Water Adsorbed on Forsterite (Mg_2SiO_4) Surfaces*. ACS Earth and Space Chemistry **2020,** 4 (7), 1050-1063.
17. Smith, R. S.; Li, Z.; Dohnálek, Z.; Kay, B. D., *Adsorption, Desorption, and Displacement Kinetics of H_2O and CO_2 on Forsterite, Mg_2SiO_4 (011).* The Journal of Physical Chemistry C **2014,** 118 (50), 29091-29100.
18. King, H. E.; Stimpfl, M.; Deymier, P.; Drake, M. J.; Catlow, C. R. A.; Putnis, A.; de Leeuw, N. H., *Computer simulations of water interactions with low-coordinated forsterite surface sites: Implications for the origin of water in the inner solar system.* Earth and Planetary Science Letters **2010,** 300 (1), 11-18.
19. Goumans, T. P. M.; Catlow, C. R. A.; Brown, W. A.; Kästner, J.; Sherwood, P., *An embedded cluster study of the formation of water on interstellar dust grains.* Physical Chemistry Chemical Physics **2009,** 11 (26), 5431-5436.
20. De Leeuw, N. H.; Parker, S. C.; Catlow, C. R. A.; Price, G. D., *Modelling the effect of water on the surface structure and stability of forsterite.* Physics and Chemistry of Minerals **2000,** 27 (5), 332-341.
21. Muralidharan, K.; Deymier, P.; Stimpfl, M.; de Leeuw, N. H.; Drake, M. J., *Origin of water in the inner Solar System: A kinetic Monte Carlo study of water adsorption on forsterite*. Icarus **2008,** 198 (2), 400-407.
22. Zamirri, L.; Pantaleone, S.; Ugliengo, P., *Carbon monoxide adsorption at forsterite surfaces as models of interstellar dust grains: An unexpected bathochromic (red) shift of the CO stretching frequency*. J Chem Phys **2019,** 150 (6), 064702.
23. Escamilla-Roa, E.; Sainz-Díaz, C. I., *Amorphous Ammonia–Water Ice Deposited onto Silicate Grain: Effect on Growth of Mantles Ice on Interstellar and Interplanetary Dust*. The Journal of Physical Chemistry C **2014,** 118 (7), 3554-3563.
24. Suhasaria, T.; Thrower, J.; Zacharias, H., *Thermal desorption of ammonia from crystalline forsterite surfaces.* Monthly Notices of the Royal Astronomical Society **2015,** 454, 3317-3327.
25. Rimola, A.; Trigo-Rodríguez, J. M.; Martins, Z., *Interaction of organic compounds with chondritic silicate surfaces. Atomistic insights from quantum chemical periodic simulations*. Physical Chemistry Chemical Physics **2017,** 19 (28), 18217-18231.
26. Fornaro, T.; Brucato, J. R.; Pace, E.; Guidi, M. C.; Branciamore, S.; Pucci, A., *Infrared spectral investigations of UV irradiated nucleobases adsorbed on mineral surfaces.* Icarus **2013,** 226 (1), 1068-1085.
27. Asaduzzaman, A. M.; Zega, T. J.; Laref, S.; Runge, K.; Deymier, P. A.; Muralidharan, K., *A computational investigation of adsorption of organics on mineral surfaces: Implications for organics delivery in the early solar system*. Earth and Planetary Science Letters **2014,** 408, 355-361.

28. Corazzi, M. A.; Fedele, D.; Poggiali, G.; Brucato, J. R*., Photoprocessing of formamide ice: route towards prebiotic chemistry in space.* Astron. Astrophys. **2020,** 636.
29. Escamilla-Roa, E.; Moreno, F., *Adsorption of glycine by cometary dust: Astrobiological implications*. Planetary and Space Science **2012,** 70 (1), 1-9.
30. Escamilla-Roa, E.; Moreno, F., *Adsorption of glycine on cometary dust grains: II—Effect of amorphous water ice.* Planetary and Space Science **2013,** 75, 1-10.
31. Escamilla-Roa, E.; Sainz-Díaz, C. I., *Effect of Amorphous Ammonia–Water Ice onto Adsorption of Glycine on Cometary Dust Grain and IR Spectroscopy*. The Journal of Physical Chemistry C **2014,** 118 (45), 26080-26090.
32. Saladino, R.; Crestini, C.; Neri, V.; Brucato, J. R.; Colangeli, L.; Ciciriello, F.; Di Mauro, E.; Costanzo, G., *Synthesis and degradation of nucleic Acid components by formamide and cosmic dust analogues*. Chembiochem **2005,** 6 (8), 1368-74.
33. Koike, C.; Imai, Y.; Chihara, H.; Suto, H.; Murata, K.; Tsuchiyama, A.; Tachibana, S.; Ohara, S., *Effects of forsterite grain shape on infrared spectra*. The Astrophysical Journal **2010,** 709 (2), 983-992.

Chapter 5

IR investigation of the HCN reactivity on TiO_2, Al_2O_3, MgO and Mg_2SiO_4 at 150-300 K

5.1 The HCN/solids interaction at 150-300 K: experimental results and discussion

It has been already shown in section *3.3.3* that the interaction of HCN with SiO_2 at 150 K results in the formation of Si-OH···HCN hydrogen bonded adducts only and that there is no evidence of chemisorption or chemical reactivity upon increasing the temperature up to 300 K interval. On the contrary, the spectra of HCN adsorbed on TiO_2, Al_2O_3, MgO and Mg_2SiO_4 show a complex evolution in the 150-300 K range, which is due to HCN surface activation, caused by a complex surface chemistry. This will be discussed hereafter and in the next *Chapter 6*. The evolution of the IR spectra of the different HCN/solid systems, upon gradually increasing the temperature from 150 to 300 K, at constant HCN pressure, is shown in *Figure 75*; in all panels the blue curve is related to HCN adsorbed at 150 K (already discussed in *Chapter 3* and

Chapter 4), the grey lines are corresponding to the spectra collected at nearly constant time intervals by increasing the temperature and finally the red curve depicts the spectrum obtained after one hour at 300 K. From the spectral series in *Figure 75*, it is immediately evident that all the signals due to HCN adsorbed in molecular and dissociated forms at 150 K gradually disappear in favour of a complex set of absorptions which can be ascribed to the formation of oligomeric and more complex reaction products.

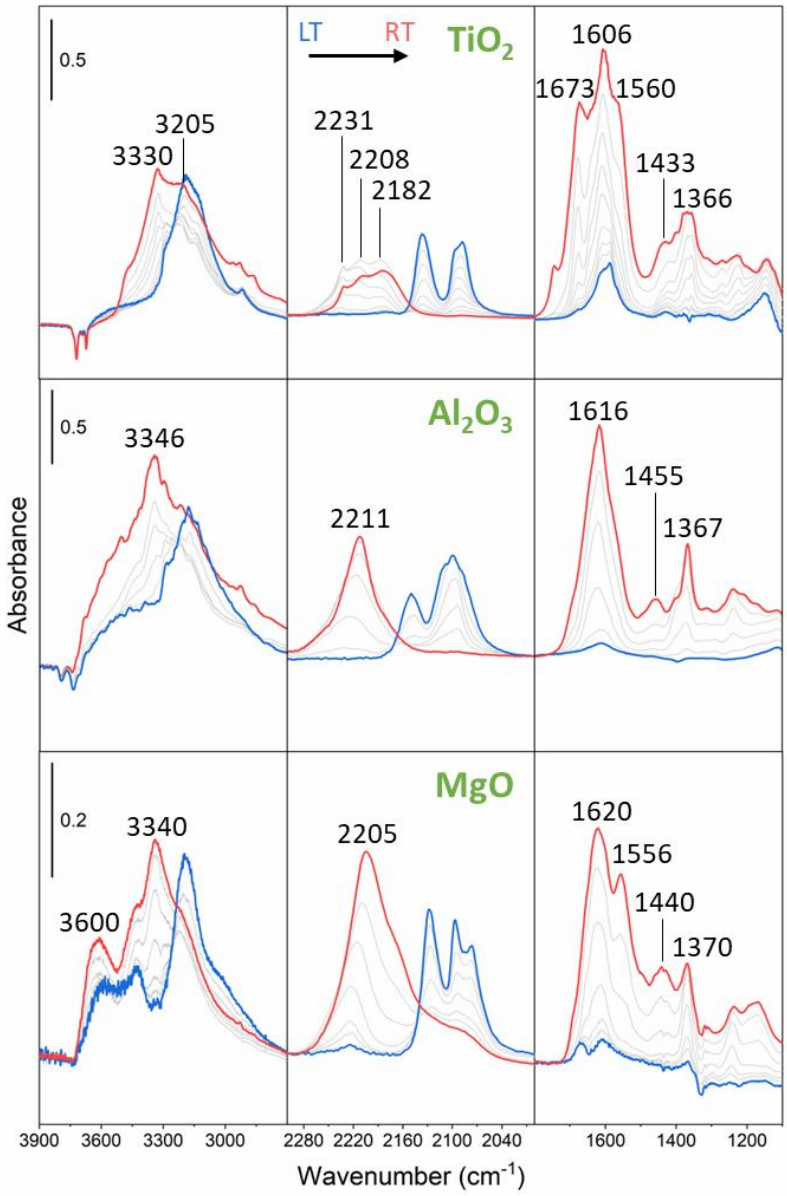
LT
RT
TiO2
0.5
3205
3330
2231
2208
2182
1606
1673
1560
1433
1366
Al2O3
0.5
3346
2211
1616
1455
1367
MgO
0.2
3340
3600
2205
1620
1556
1440
1370
Absorbance
3900 3600 3300 3000
2280 2220 2160 2100 2040
1600 1400 1200
Wavenumber (cm-1)

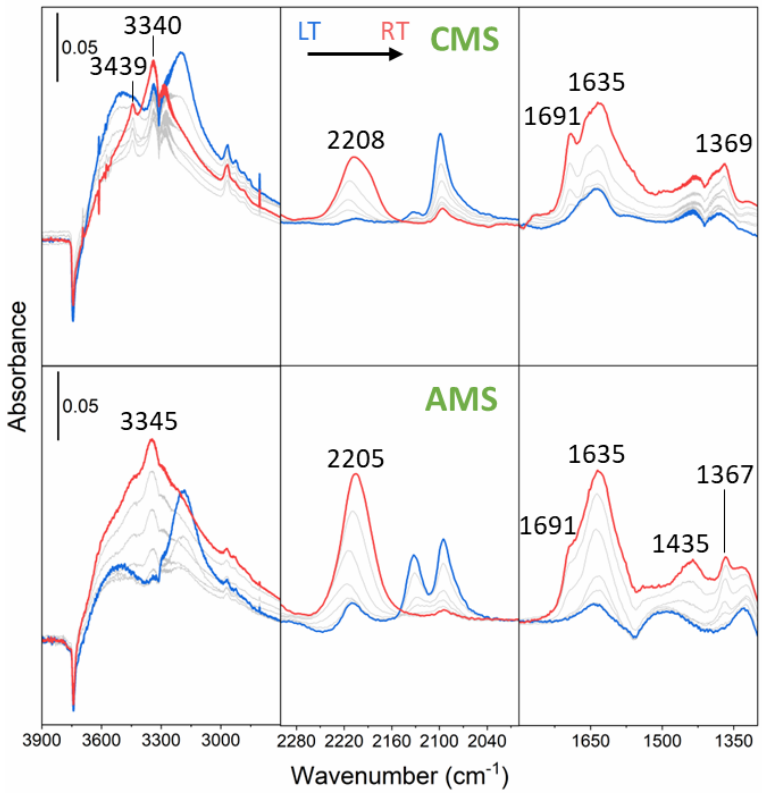

Figure 75. Background subtracted IR spectra of the HCN interaction with TiO_2, Al_2O_3, MgO (on the top) and Mg_2SiO_4 (on the bottom) samples in the range 150-300 K (from the blue to the red curve). The blue curves are the spectra at 150 K already discussed in Chapter 3 and

Chapter 4. The grey curves were obtained by increasing the temperature up to 300 K. The red curves were obtained after 1 hr of contact with HCN (equilibrium pressure of 5 mbar) at 300 K.

More in detail the following can be highlighted:

i) on all the samples the manifestations of the $\nu_{(CH)}$ mode of adsorbed HCN (*ca*. 3300-2700 cm^{-1}) decrease in intensity while new absorptions develop in the *ca*. 3330-3350 cm^{-1} interval. On the basis of the literature concerning the HCN chemistry in homogeneous and heterogeneous conditions it is reasonable to assign these features to the $\nu_{(NH)}$ stretching modes of NH or NH_2 newly formed groups.[1-8] The fate of the signals due to the perturbed OH groups by interaction with HCN at 150 K (*ca.* 3800-3400 cm^{-1}) is less clear due to the fact that the spectra in this region are the superposition of many broad components, but nevertheless their intensity seems to decrease on CMS and AMS.

ii) The spectral changes described above are paralleled on all samples by remarkable changes in the $\nu_{(C\equiv N)}$ stretching region (2300-2000 cm^{-1}), where the bands due to HCN adsorbed in molecular and dissociated forms (2160-2030 cm^{-1}, blue curves) disappear in favour of features at higher frequencies (2250-2200 cm^{-1}, red curves). The presence of a clear isosbestic point at *ca*. 2150 cm^{-1} visible in all the series proves without any doubt that the direct transformation of the adsorbed HCN and CN^- species into products responsible for the manifestations at higher frequency take places. The reader is referred to the spectra acquired at 150 K on AMS (paragraph *4.3*), where it was already emphasized to the presence of a band at *ca*. 2205 cm^{-1} (see also *Figure 72*), which

was assigned the $\nu_{(C\equiv N)}$ mode of the HCN dimer (HN=CH-C≡N), namely IAN (IminoAcetoNitrile).[9]

iii) It is a matter of facts that such a compound justifies the $\nu_{(C\equiv N)}$ manifestation at 2205 cm^{-1} but can also account for the $\nu_{(NH)}$ absorptions quoted in (i) and for $\nu_{(C=N)}$ modes which could contribute to the manifestation growing in the 1700−1600 cm^{-1} region of *Figure 75*. It is most noticeable in *Figure 75* that the 2205 cm^{-1} band in the spectra of HCN/AMS increase in intensity with the temperature, becoming also tailed on the low frequency side, as do the features in the 1700−1600 cm^{-1}, which by growing in intensity become more complex. As it will be better discussed in the following and in *Chapter 6*, this behaviour implies the formation of larger HCN oligomers together their evolution to more complexes surface products. The spectra of the other HCN/solid systems in *Figure 75*, show that reactions similar to that on AMS are occurring, although some differences concerning the overall intensity and the number of spectral components on the different surfaces have to be highlighted.

iv) The absorptions in the 1800−1300 cm^{-1} interval are difficult to be precisely assigned because of the numerous/overlapped features and of their complicated behaviour during their evolution (especially on TiO_2, MgO and silicates). The contribution in this region could come by several different functional groups, like C=N and C=C (stretching modes), NH_2 (bending), C-C and C-N (stretching) and CH/CH_2 (bending). Nevertheless, the clear development in the TiO_2, CMS and AMS spectra of *Figure 75* of some absorption at frequencies as high as 1700−1670 cm^{-1}

deserves some comment. This frequency range is in fact compatible with the C=O stretching mode of carbonylic groups. Notice that a weak component in this range is also present in the first spectra of MgO and then rapidly submerged by the strong absorption growing at lower wavenumber. Since all the experiments were conducted under controlled experimental conditions able to ensure the absence of contaminant H_2O, it follows that the presence of oxygenated species can be explained with the transfer of surface O^{2-}/OH^- species to the HCN reaction products. In this respect it is worth recalling the tendency of *hsa* MgO to form CO_2^{2-} species by reaction at RT with CO due to highly coordinatively unsaturated surface O^{2-}(3C) sites (see paragraph *3.6.1*). The presence of oxygenated products is indeed confirmed by chemical analysis (see *Chapter 6*).

v) All the absorptions discussed above do not disappear upon outgassing at room temperature, suggesting that the HCN reaction products are irreversibly formed and that they are strongly adsorbed at the solids surface.

Another important experimental evidence is the change of the colour of all the samples from white to reddish-brown or even black (*Figure 76*) during the experiments described above. In fact, this suggests that at least some of the HCN reaction products contain networks of unsaturated bonds, as expected in the case of HCN extensive oligomerization.

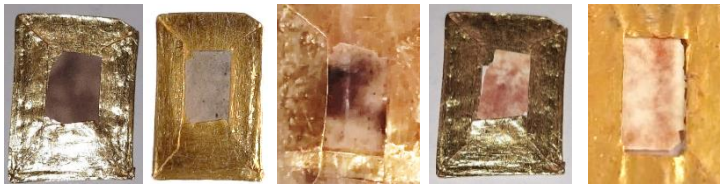

Figure 76. Images of some of the samples' pellets after the interaction with HCN in the range 150 - 300 K.

As discussed in *Chapter 1* (see section *1.3.3*) the tendency of HCN in homogeneous conditions to form a variety of polymerization products and derivates is well known. These formed chemical species contain functional groups like alkyls, cyanides, amines and imines, and assume a large variety of linear or cyclic structures like those of polyimines, polyamines, polyaminoimidazoles, polyiminopyrroles, polyaminopyrazines and polyamides.[6] In addition, important biomolecules have also been identified among the products, as described in section *1.3.3*.

This large variety of products is formed through many different reaction paths which however have common precursors, such as the aminomalononitrile (AMN) HCN trimer and the diaminomaleonitrile (DAMN) HCN tetramer, formed according to the following scheme:

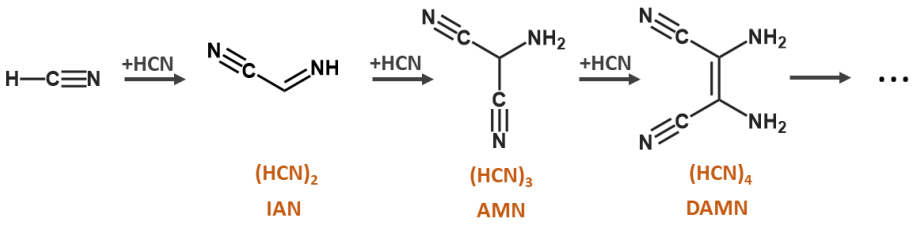

The HCN oligomerization in homogeneous conditions requires the presence of ammonia as catalyst (see section *1.3.3*). The role of NH_3

is to form nucleophilic CN^- species by HCN deprotonation which initiate the oligomerization chain (*Figure 10*). Yuasa et al.[10, 11] have also reported that Mg-containing minerals like MgO (periclase) and $MgCO_3$ (magnesite) can play the same role of ammonia in catalysing the HCN oligomerization at liquid/solid interphases.

Based on this, it is thought that a similar mechanism can operate in heterogeneous conditions at the gas/surface interphase on the oxides investigated here, at least on those that exhibit some surface basic properties.

The reaction path leading on these surfaces to the HCN trimer and tetramer species, which, as said before, are supposed to be the precursors in the formation of further HCN reaction products, can be schematized as follows:

As already pointed out above, the experimental spectra of *Figure 75* are too complicated to identify single products such as the HCN trimer (AMN) or tetramer (DAMN). Nevertheless, by comparison the spectra of all samples (outgassed at r.t after 1 hr of contact with HCN) with that of pure DAMN, it is possible to recognize many similar vibrational manifestations.

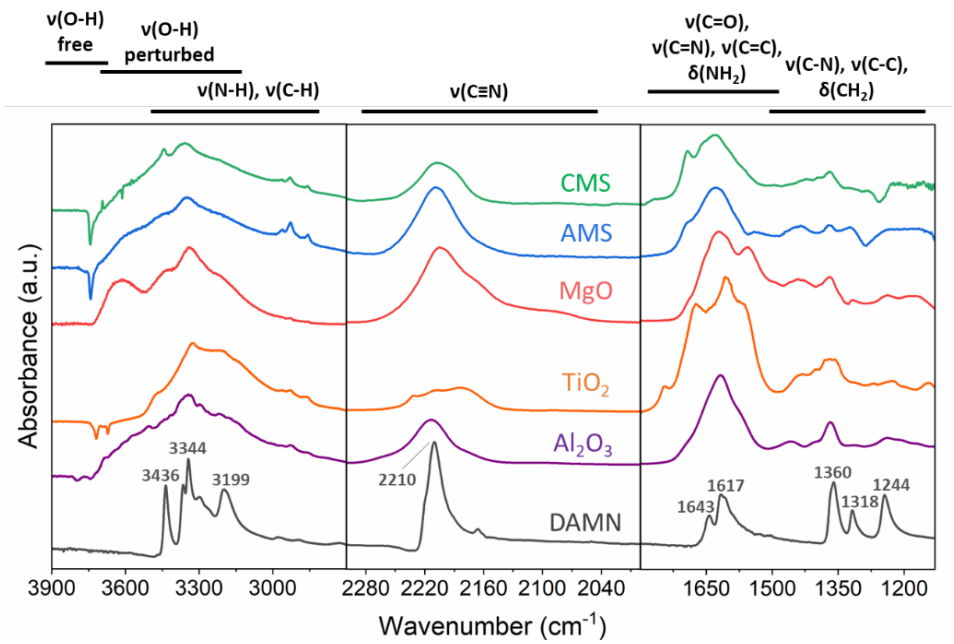

Figure 77. Comparison between the spectra of the HCN/solid systems studied in this work and that of the pure DAMN HCN tetramer.

It is finally worth recalling that beside weakly adsorbed and dissociated species containing the -C≡N group, a variety of bridged species where the bond order is reduced to two (-C=N-) was already detected at 150 K (see

Chapter 4). These species could in principle have enhanced chemical activity with respect to HCN and therefore could heavily contribute to the HCN surface chemistry. This could explain the activity of TiO_2, a material where dissociative chemisorption of HCN to give the CN^- precursor was not revealed at 150 K by IR data discussed in paragraph *3.4.4*.

In conclusion, the complex evolution of the IR spectra of the HCN/solid systems and the presence of many superimposed components, while revealing the occurrence of a complex surface chemistry involving the HCN absorbed species formed at 150 K, do not allow to unambiguously individuate the reaction products. The elucidation of their nature will be the subject of the next chapter, where the results of their chemical analysis by high resolution mass spectroscopy will be illustrated.

1. Low, M. J. D.; Ramamurthy, P., *Infrared study of HCN polymer on alumina*. Journal of the research institute for catalysis Hokkaido university **1968,** 16 (2), 535-542.
2. Vuitton, V.; Bonnet, J. Y.; Frisari, M.; Thissen, R.; Quirico, E.; Dutuit, O.; Schmitt, B.; Le Roy, L.; Fray, N.; Cottin, H.; Sciamma-O'Brien, E.; Carrasco, N.; Szopa, C., *Very high resolution mass spectrometry of HCN polymers and tholins.* Faraday Discuss **2010,** 147, 495-508; discussion 527-52.
3. de la Fuente, J. L.; Ruiz-Bermejo, M.; Nna-Mvondo, D.; Minard, R. D., *Further progress into the thermal characterization of HCN polymers*. Polymer Degradation and Stability **2014,** 110, 241-251.
4. Fernandez, A.; Ruiz-Bermejo, M.; de la Fuente, J. L., *Modelling the kinetics and structural property evolution of a versatile reaction: aqueous HCN polymerization*. Phys Chem Chem Phys **2018,** 20 (25), 17353-17366.
5. Ruiz-Bermejo, M.; de la Fuente, J. L.; Carretero-Gonzalez, J.; Garcia-Fernandez, L.; Aguilar, M. R., A *Comparative Study on HCN Polymers Synthesized by Polymerization of NH_4CN or Diaminomaleonitrile in Aqueous Media: New Perspectives for Prebiotic Chemistry and Materials Science.* Chemistry **2019,** 25 (49), 11437-11455.
6. Ruiz-Bermejo, M.; de la Fuente, J. L.; Pérez-Fernández, C.; Mateo-Martí, E., *A Comprehensive Review of HCN-Derived Polymers.* Processes **2021,** 9 (4).
7. Villafane-Barajas, S. A.; Ruiz-Bermejo, M.; Rayo-Pizarroso, P.; Galvez-Martinez, S.; Mateo-Marti, E.; Colin-Garcia, M., *A Lizardite-HCN Interaction Leading the Increasing of Molecular Complexity in an Alkaline Hydrothermal Scenario: Implications for Origin of Life Studies*. Life (Basel) **2021,** 11 (7).
8. Ruiz-Bermejo, M.; García-Armada, P.; Mateo-Martí, E.; de la Fuente, J. L., *HCN-derived polymers from thermally induced polymerization of diaminomaleonitrile: A non-enzymatic peroxide sensor based on prebiotic chemistry.* European Polymer Journal **2022,** 162.
9. Benallou, A., *Understanding the most favourable dimer of HCN for the oligomerization process in the gas phase of interstellar clouds*. Computational and Theoretical Chemistry **2016,** 1097, 79-82.
10. Yuasa S., Orò J., *Role of weak bases on the prebiotic formation of heterocyclic compounds*. In Cosmochemical Evolution and the Origins of Life, Springer, D., Ed. **1974**; pp 295-299.
11. Yuasa, S.; Ishigami, M., *Geochemically possible condensation of hydrogen cyanide in the presence of divalent metal compounds*. GEOCHEMICAL JOURNAL **1977**, 11 (4), 247-252.

Chapter 6

Investigation of the HCN/solids reaction products by direct-infusion HR-MS

The IR investigation provided information about the HCN/solids interaction, thus allowing to identify some of the functional groups belonging to the reaction products, but it was not able to establish the exact nature of the formed species. To overcome this limitation, the extraction of the reaction products with methanol was carried out and the extracted fraction was analysed by Direct Infusion High Resolution Mass Spectrometry (DI-HRMS).

High resolution mass spectrometry, by combining high resolution and high mass accuracy, is a powerful tool for the analysis of complex organic mixtures, for the determination of elemental compositions and for the identification of unknown molecules. The high resolving power of the mass analyser allows to distinguish between compounds with the same nominal mass, thus obtaining an unambiguous assignment of the underlying chemical formulas. Coupling of HR-MS with separation techniques, such as liquid or gas chromatography, can further increase the sensitivity in terms of the attainable qualitative and quantitative information but often at the expenses of complexes sample preparation procedures.

Since the nature of the species formed on the HCN/solids systems was not known *a priori*, here it was decided to perform a first screening of the surface products by means of the direct infusion (DI) method,

without any preventive separation, to obtain in a few minutes an overview of the species present in the samples under investigation. However, DI technique has an important limitation in that it does not allow to distinguish among isomers having the same m/z ratio. To try to overcome this problem, some detected species (actually those giving the most intense signals in the MS spectra), were investigated in deeper detail by using the MS/MS fragmentation technique (data reported in Appendix). Without entering into excessive details outside the scope of this thesis, the basic principles of the MS/MS technique can be summarized in *Figure 78* : once the sample has been ionized by a proper source, a first mass analyser allows to isolate a given ion with a specific m/z ratio; this "precursor ion" (MS^1) is then fragmented by Collision Induced Fragmentation (CID, *i.e.* by impact with an inert molecular target) to give "product ions" (or fragments, MS^2) which are analysed by a second mass analyser.[1]

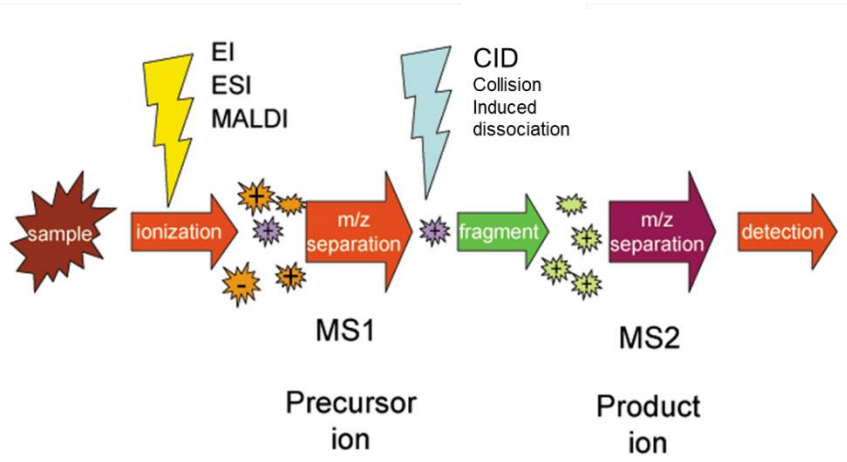

Figure 78. Schematic MS/MS spectrometry. From ref. [1]

Since the number and nature of the MS^2 fragments is strongly related to the composition and the structure of the precursor ion, MS/MS analysis provides valuable information for the identification of unknown species.

Another limitation of the DI-HRMS technique is that, unless the products are previously separated and standards are used, it is not possible to obtain quantitative information. This because the relative abundance of the different species (as measured by the instrument) is inevitably dependent on their ionizability (i.e., capability of protonation or deprotonation, *vide infra*) which in turn depends on their chemical nature as well as on the experimental conditions. In other words, the number of ions of a given species counted by the mass analyser is not univocally dependent on the concentration of that species.

A further limitation of the quantitative significance of the relative abundances measured in the mass spectra arises in our case from the peculiar nature of the samples, where the HCN reaction products are anchored or adsorbed at the surface of the investigated solids. In these conditions the relative abundances are also related to the fraction of each compound which is extracted by methanol and transferred to the solution used to get the MS spectrum. This fraction not only depends on the solubility of the different species in methanol, but also on the solid/liquid transfer equilibrium of the adsorbed phases. The latter is, in turn, controlled by their adsorption strength at the surface, which can dramatically vary going from a product to the other on a given surface, as well as for a given product moving from one solid to the other.

For these reasons in the following the results of the HRMS experiments will be discussed mainly as far as the qualitative point of view is concerned, with little attention to the quantitative aspects.
The results concerning MgO and the CMS and AMS silicates have already been published in a recent paper[2]. Here, those concerning TiO_2 and Al_2O_3 are also presented and discussed and some general conclusions about the HCN chemistry on all the investigated solids drawn.

6.1 Experimental part

6.1.1 Products extraction and Mass Spectrometry analysis

At the end of the IR spectroscopic experiments the samples were extracted from the measurement cell, grounded, and suspended in 1 mL of methanol. The suspensions were sonicated for 30 min and then centrifuged for 10 min at 10000 rpm. The liquid phase was finally separated and analyzed by DI-HRMS technique using an electrospray ionization (ESI) source. Electrospray ionization is a "soft" ionization method (i.e., uses little amounts of energy to ionize the sample) which strips molecules from their solutions into the gas phase as protonated (positively charged) or deprotonated (negatively charged) species depending on the sign of the applied electrical field. Basically (see *Figure 79*), a high positive (ESI +) or negative (ESI-) voltage (0.5-5 kV) is applied between a capillary and a counter electrode. The generated electric field causes a charge separation at the surface of the liquid, thus the ions of interest migrate out of the capillary tip

forming "Taylor cone". As the charge accumulates, the Taylor cone releases droplets that contain an excess of positive or negative charge. Evaporation of the droplets forces the charged analytes closer together until the Rayleigh limit is reached and the droplet breaks apart in what is termed a "Coulombic explosion". This process continues until no solvent remains, after which the charged analytes are accelerated towards the opposite charge of the counter electrode and into the mass spectrometer. In this study, the mass spectra were acquired both in positive (ESI +) and negative mode (ESI −). Nevertheless, in the following only the ESI- data will be reported and discussed, as this mode ensured a better signal to noise ratio and high sensitivity.[3]

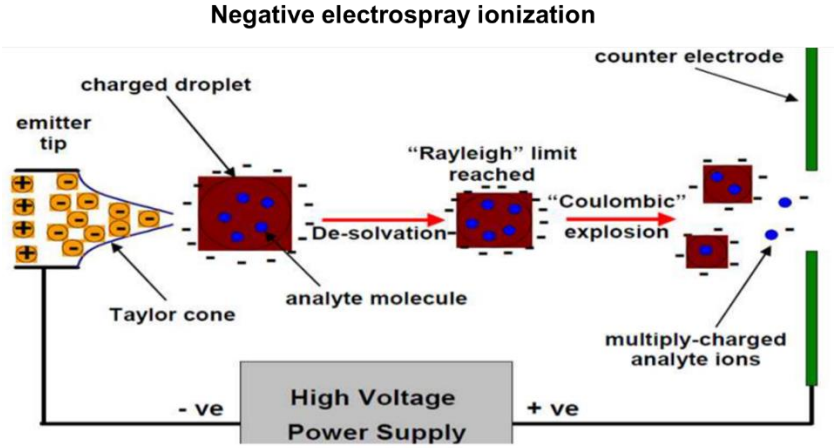

Figure 79 The electrospray ionization process in negative mode. Adapted from ref. [3]

HR-MS analyses were performed using an LTQ Orbitrap mass spectrometer (Thermo Scientific). Samples were delivered directly to the mass spectrometer via a Hamilton microliter syringe at constant flow (10 µl/min). The capillary, magnetic lenses, and collimating multipole voltages were optimized and the collision energy used for the

CID- MS/MS measurements is reported in *Table 14* (see *Appendix*). Data acquisition and processing was performed using the Xcalibur 3.6 software (Thermo Fisher Scientific). Accurate m/z values (< 5 ppm) and isotopic abundance in full mass scan were used to identify elemental composition, whereas MS/MS fragmentation and RDB (ring double bond) were used to hypothesize the structures. All mass spectra were acquired with resolution of 30,000 in full mass range between 50 and 500 m/z. Because of the great uncertainty in assigning signals at high m/z (where a great number of complex molecular structures can fit the same m/z value), the analysis was restricted to m/z values in the 70-200 m/z range.

6.2 ESI-HRMS data

The mass spectra of the fractions extracted from all the solids of interest after the interaction with HCN are shown in *Figure 80*.

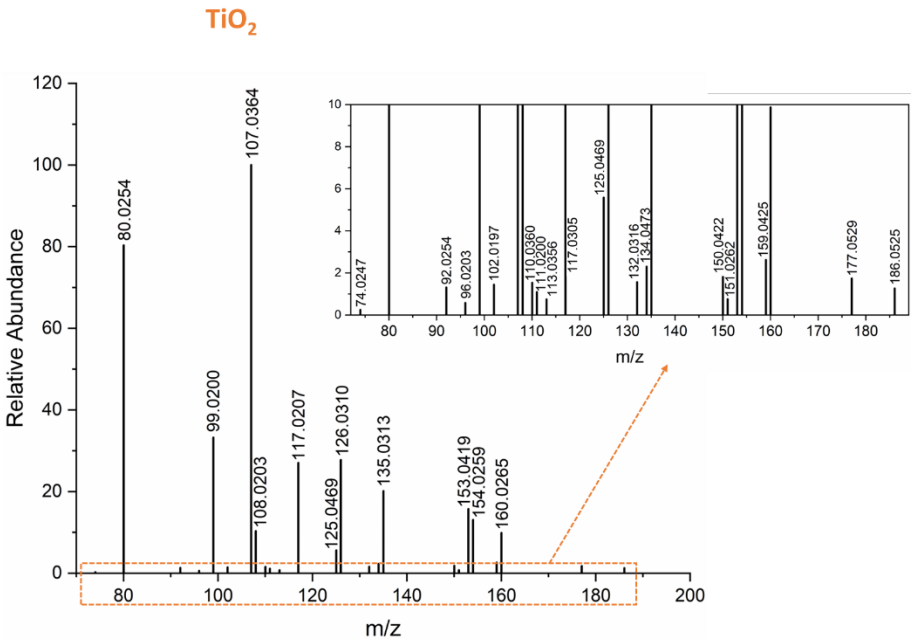

Al_2O_3

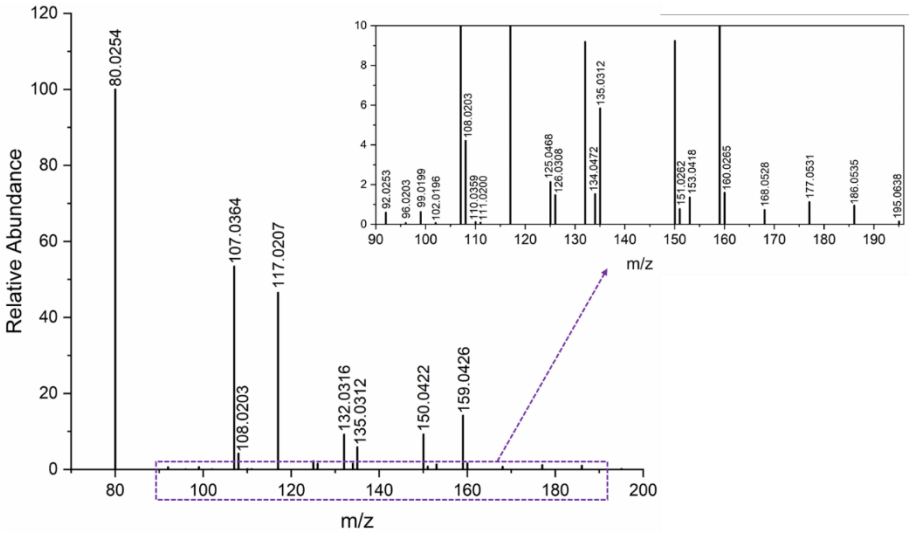
Relative Abundance
m/z
80.0254
107.0364
108.0203
117.0207
132.0316
135.0312
150.0422
159.0426
92.0253
96.0203
99.0199
102.0196
108.0203
110.0359
111.0200
125.0468
126.0308
134.0472
135.0312
151.0262
153.0418
160.0265
168.0528
177.0531
186.0535
195.0638

MgO

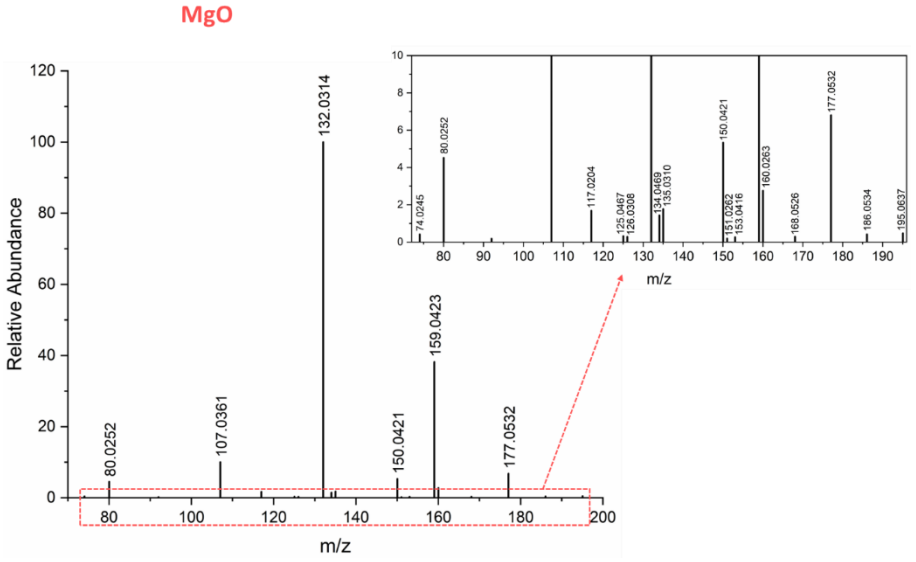
Relative Abundance
m/z
132.0314
159.0423
80.0252
107.0361
150.0421
177.0532
74.0245
80.0252
117.0204
125.0467
126.0306
134.0469
135.0310
150.0421
151.0262
153.0416
160.0263
168.0526
177.0532
186.0534
195.0637

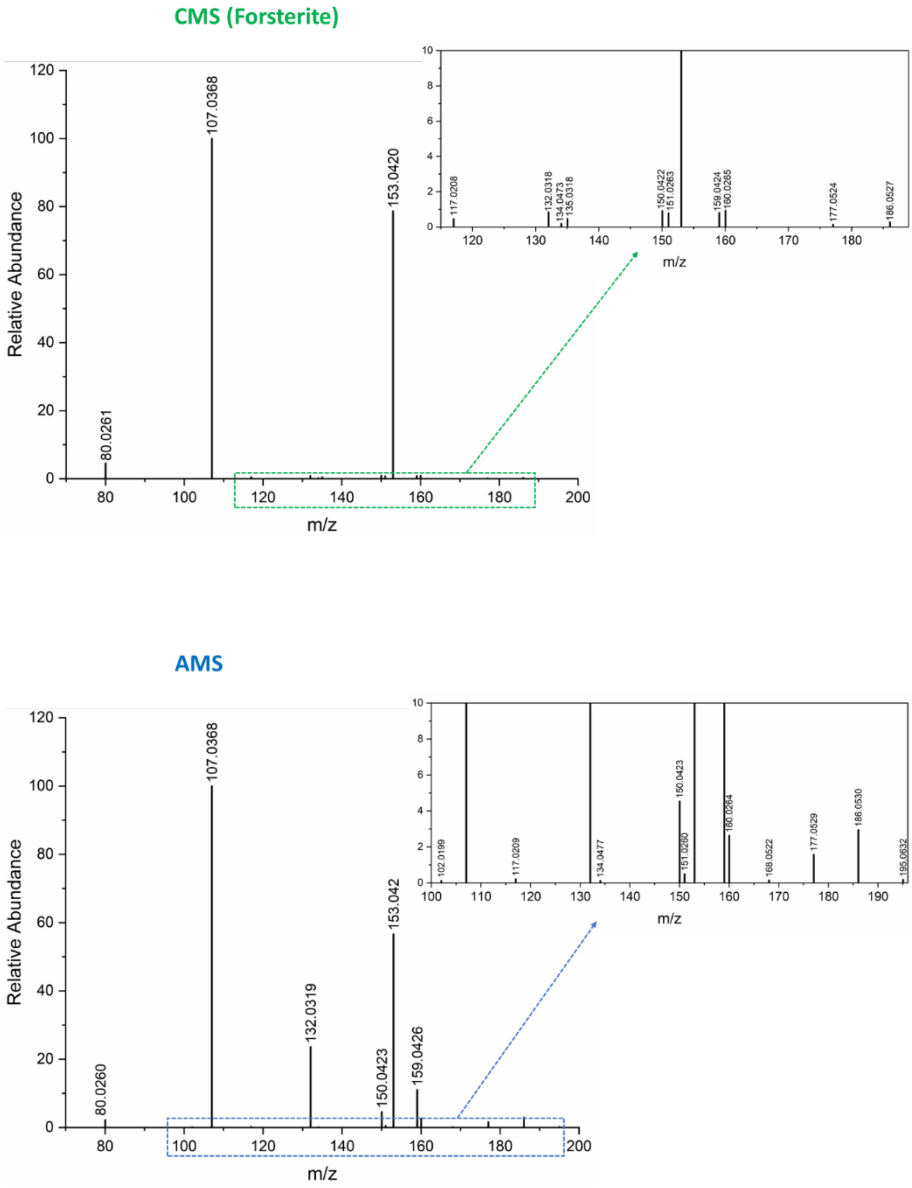

Figure 80. Direct infusion ESI-HRMS spectra (acquired in negative ion mode in the 70 ≤ m/z ≤ 200 range) of the solutions obtained by extraction with methanol of the reaction products formed after HCN interaction with TiO_2, Al_2O_3, MgO, CMS and AMS (as described in Chapter 3 and

Chapter 4). The peaks of interest are labelled with their m/z values. See also Table 13 and Figure 81.

The list of the possible compounds compatible with the observed m/z values on the various samples (compiled taking also into account the literature data concerning the HCN chemistry in homogeneous conditions)[4-7] is reported in *Table 13*. To facilitate the discussion, each compound is labelled with a number which is used as reference in the text.

Table 13. Chemical species compatible with the m/z ratios of the ions identified in the HR-MS spectra of Figure 80. The smaller deviation (Δppm) between the experimental mass m/z and the theoretical mass of the chemical formula attributed at the experimental m/z is reported. Couples of isomers are marked with a letter (a-f).

	Chemical formula [M]	Theoretical m/z $[M-H]^-$	Δppm				
			TiO_2	Al_2O_3	MgO	CMS	AMS
HCN oligomers and related compounds							
1	$H_3C_3N_3$	80.0254	0.131	0.381	2.630	4.491	3.992
2a	$H_4C_4N_4$	107.0363	0.659	0.472	1.770	4.863	4.676
3	$H_3C_3N_3O$	96.0203	0.157	0.157	-	-	-
4	$H_3C_4N_3O$	108.0203	0.139	0.695	-	-	-
Glycine and related compounds							
5	$H_5C_2NO_2$	74.0248	1.374	-	3.671	-	-
6	$H_5C_3NO_3$	102.0197	0.062	0.160	-	-	2.291
7	$H_6C_3N_2O_3$	117.0306	0.217	-	-	-	-
8	$H_4C_3N_2O_2$	99.0200	0.007	0.916	-	-	-
Imidazole compounds							
9	$H_3C_4N_3$	92.0254	0.440	1.200	3.374	-	-
10a	$H_4C_4N_4$	107.0363					
11	$H_2C_5N_4$	117.0207	0.347	0.518	2.302	1.116	1.714
12	$H_3C_5N_5$	132.0316	0.390	0.012	1.579	1.526	2.663

13b	$H_4C_6N_6$	159.0425	0.079	0.582	0.802	0.424	0.833
14	$H_5C_7N_7$	186.0534	4.550	0.449	0.126	3.636	1.862
15	$H_6C_4N_4O$	125.0469	0.127	0.593	1.873	-	-
16	$H_6C_5N_4O_2$	153.0418	0.466	0.057	1.299	1.380	1.184
17c	$H_4C_5N_4O$	135.0312	0.488	0.327	1.579	3.969	-
18d	$H_5C_5N_5O$	150.0421	0.579	0.179	0.421	0.712	1.112
19	$H_3C_6N_5O$	160.0265	0.356	0.043	1.394	0.082	0.707
20e	$H_6C_6N_6O$	177.0530	0.803	0.327	0.722	3.570	0.633
21	$H_7C_5N_5O_2$	168.0527	-	0.370	0.582	-	3.141
22	$H_8C_6N_6O_2$	195.0636	-	1.042	0.375	-	1.932
16	$H_5C_4N_3O_2$	126.0309	0.399	0.553	0.871	-	-
Purine and pyrimidine compounds							
23	$H_5C_5N_5$	134.0472	0.533	0.287	2.302	0.384	3.443
24b	$H_4C_6N_6$	159.0425					
25e	$H_6C_6N_6O$	177.0530					
26c	$H_4C_5N_4O$	135.0312					
27	$H_4C_5N_4O_2$	151.0262	0.671	0.340	0.141	0.869	1.051
28d	$H_5C_5N_5O$	150.0421					
29	$H_5C_4N_3O$	110.0360	0.228	0.955	-	-	-
30	$H_6C_4N_4O$	125.0469	0.127	0.593	1.873	-	-
31f	$H_5C_4N_3O_2$	126.0309					
32	$H_5C_5N_3O_3$	154.0258	0.426	-	-	-	-
33	$H_4C_4N_2O_2$	111.0200	0.006	0.174	-	-	-
34f	$H_5C_4N_3O_2$	126.0309					
35	$H_4C_4N_2O_3$	127.0149	0.116	-	-	-	-
36	$H_6C_4N_2O_2$	113.0357	0.095	-	-	-	-

In *Figure 81* the structure and the name of the supposed compounds are also reported. For sake of clarity these compounds are divided into different groups, thus distinguishing among not oxygenated and oxygenated species and their chemical nature. It is possible to note that for some of the listed species the same chemical formula was

assigned to different structures (marked with a letter (a-f)). The proposed structural isomers are all species related to the chemistry of HCN, therefore they could be simultaneously present in the mixture, maybe as intermediates of the same reaction pathway (for instance, DAMN (**2a**) and AICN (**10a**) *vedi infra*).

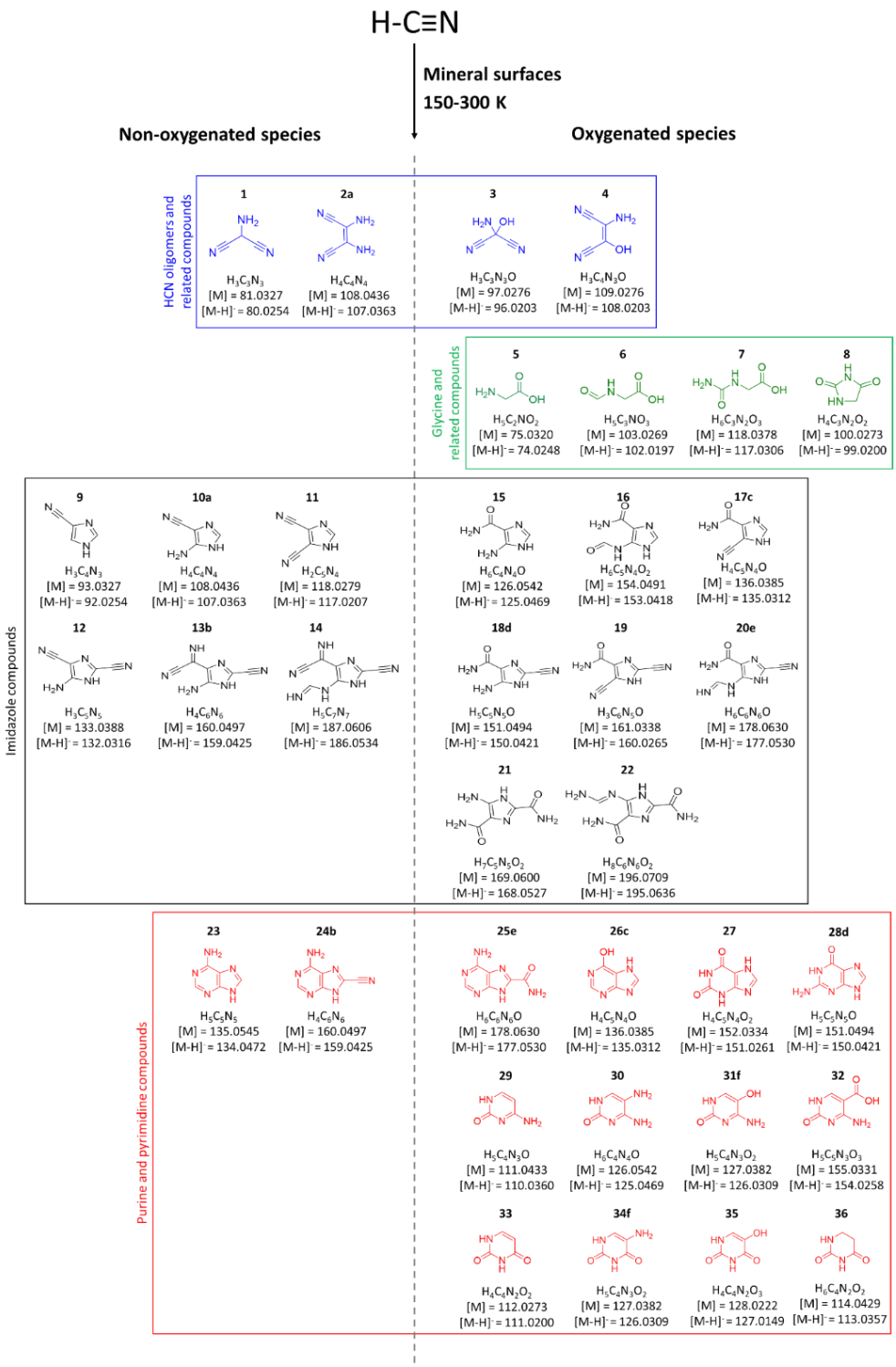
H-C≡N
Mineral surfaces
150-300 K
Non-oxygenated species
Oxygenated species
HCN oligomers and related compounds
1
H3C3N3
[M] = 81.0327
[M-H]- = 80.0254
2a
H4C4N4
[M] = 108.0436
[M-H]- = 107.0363
3
H3C3N3O
[M] = 97.0276
[M-H]- = 96.0203
4
H3C4N3O
[M] = 109.0276
[M-H]- = 108.0203
Glycine and related compounds
5
H5C2NO2
[M] = 75.0320
[M-H]- = 74.0248
6
H5C3NO3
[M] = 103.0269
[M-H]- = 102.0197
7
H6C3N2O3
[M] = 118.0378
[M-H]- = 117.0306
8
H4C3N2O2
[M] = 100.0273
[M-H]- = 99.0200
Imidazole compounds
9
H3C4N3
[M] = 93.0327
[M-H]- = 92.0254
10a
H4C4N4
[M] = 108.0436
[M-H]- = 107.0363
11
H2C5N4
[M] = 118.0279
[M-H]- = 117.0207
12
H3C5N5
[M] = 133.0388
[M-H]- = 132.0316
13b
H4C6N6
[M] = 160.0497
[M-H]- = 159.0425
14
H5C7N7
[M] = 187.0606
[M-H]- = 186.0534
15
H6C4N4O
[M] = 126.0542
[M-H]- = 125.0469
16
H6C5N4O2
[M] = 154.0491
[M-H]- = 153.0418
17c
H4C5N4O
[M] = 136.0385
[M-H]- = 135.0312
18d
H5C5N5O
[M] = 151.0494
[M-H]- = 150.0421
19
H3C6N5O
[M] = 161.0338
[M-H]- = 160.0265
20e
H6C6N6O
[M] = 178.0630
[M-H]- = 177.0530
21
H7C5N5O2
[M] = 169.0600
[M-H]- = 168.0527
22
H8C6N6O2
[M] = 196.0709
[M-H]- = 195.0636
Purine and pyrimidine compounds
23
H5C5N5
[M] = 135.0545
[M-H] = 134.0472
24b
H4C6N6
[M] = 160.0497
[M-H]- = 159.0425
25e
H5C6N5O
[M] = 178.0630
[M-H]- = 177.0530
26c
H4C5N4O
[M] = 136.0385
[M-H]- = 135.0312
27
H4C5N4O2
[M] = 152.0334
[M-H]- = 151.0261
28d
H5C5N5O
[M] = 151.0494
[M-H]- = 150.0421
29
H5C4N3O
[M] = 111.0433
[M-H]- = 110.0360
30
H6C4N4O
[M] = 126.0542
[M-H]- = 125.0469
31f
H5C4N3O2
[M] = 127.0382
[M-H]- = 126.0309
32
H5C5N3O3
[M] = 155.0331
[M-H]- = 154.0258
33
H4C4N2O2
[M] = 112.0273
[M-H]- = 111.0200
34f
H5C4N3O2
[M] = 127.0382
[M-H]- = 126.0309
35
H4C4N2O3
[M] = 128.0222
[M-H]- = 127.0149
36
H6C4N2O2
[M] = 114.0429
[M-H]- = 113.0357

Figure 81. Structures of the possible reaction products obtained from HCN/solid interaction: ***1.*** *aminomalononitrile (**AMN**);* ***2a.*** *diaminomaleonitrile (**DAMN**);* ***3.*** *2-amino-2-hydroxymalononitrile;* ***4.*** *2-amino-3-hydroxymaleonitrile;* ***5.*** *glycine;* ***6.*** *N-formylglycine;* ***7.*** *N-carbamoylglycine (hydantoic acid);* ***8.*** *hydantoin;* ***9.*** *1H-imidazole-4-carbonitrile;* ***10a.*** *5-amino-1H-imidazole-4-carbonitrile (**AICN**);* ***11.*** *1H-imidazole-4,5-dicarbonitrile;* ***12.*** *5-amino-1H-imidazole-2,4-dicarbonitrile;* ***13b****. 5-amino-2-cyano-1H-imidazole-4-carbimidoyl cyanide;* ***14.*** *2-cyano-5-formimidamido-1H-imidazole-4-carbimidoyl cyanide;* ***15.*** *5-amino-1H-imidazole-4-carboxamide (**AICA**);* ***16.*** *5-formamido-1H-imidazole-4-carboxamide (**fAICA**);* ***17c****. 5-cyano-1H-imidazole-4-carboxamide;* ***18d.*** *5-amino-2-cyano-1H-imidazole-4-carboxamide;* ***19.*** *2,5-dicyano-1H-imidazole-4-carboxamide;* ***20e.*** *2-cyano-5-formimidamido-1H-imidazole-4-carboxamide;* ***21.*** *5-amino-1H-imidazole-2,4-dicarboxamide;* ***22.*** *(E)-5-((aminomethylene)amino)-1H-imidazole-2,4-dicarboxamide;* ***23.*** *adenine;* ***24b.*** *6-amino-9H-purine-8-carbonitrile;* ***25e.*** *6-amino-9H-purine-8-carboxamide;* ***26c.*** *hypoxanthine;* ***27.*** *xanthine;* ***28d.*** *guanine;* ***29.*** *cytosine;* ***30.*** *5-amino-cytosine;* ***31f.*** *5-hydroxy-cytosine;* ***32.*** *cytosine-5-carboxylic acid;* ***33.*** *uracil;* ***34f.*** *5-amino-uracil;* ***35.*** *5-hydroxy-uracil;* ***36.*** *dihydrouracil.*

Among the detected species (*Table 13* and *Figure 81*), those which are known to be among the most stable HCN oligomers, i.e. the trimer (AMN (**1**), m/z = 80) and the tetramer (DAMN (**2a**), m/z = 107) are found in all the samples. It is worth recalling that in homogeneous conditions AMN and DAMN are considered as the key intermediates for the growth of larger HCN polymers and of a variety of complex molecules which include prebiotic species (section *1.3.3.2* in *Chapter 1*). It is assumed that they could play a similar role also on our heterogeneous systems, since a variety of complex molecules similar to those reported for the polymerisation of HCN in aqueous solution (*Figure 10* in *Chapter 1*) is observed as well. These include (*Figure 81*) (i) AMN and DAMN oxygenated derivatives (**3-4**), (ii) glycine and related compounds (**5-8**), (iii) imidazolic species (**9-22**) and (iv) purine and pyrimidine compounds (**23-36**).

The presence among the products of oxygenated species is intriguing. If the formation of oxygenated species is not unexpected in homogeneous conditions due to the presence of H_2O as solvent (and of OH^- in NH_3 solutions), this is somehow surprising in our heterogeneous experiments which, at least during the IR investigation, are performed in rigorous anhydrous conditions. Nevertheless, it is already outlined the presence on the IR spectra of HCN/solid systems of an absorption at ca. 1700 cm-1 (*Figure 75* in *Chapter 5*) which suggests the formation of compounds containing carbonyl groups. This evidence strongly allows to hypothesize that the oxygen incorporation in the first formed HCN surface species can already occur through the participation of surface O^{2-}/OH^- species. Of course, it cannot be excluded that the formation of further oxygenated species can also occur when the samples are exposed to air after the IR measurements and during the surface products extraction with methanol prior to the HR-MS analysis. This point deserves further investigation, but it is however evident, from the IR results, that the surface plays a key catalytic role in initiating the oxygen transfer mechanisms and in sustaining it in presence of moisture to give a variety of molecules including prebiotic species.

A brief description of the classes of identified compounds (*Figure 81*) and of their potential synthesis pathways in the prebiotic scenarios are provided below.

Glycine and related compounds (5-8). The formation of glycine (**5**) on some of the analyzed systems is suggested by the HRMS signal at m/z 74.0248 (*Table 13*). Interesting is also the presence of signals

due to glycine-related products, like its N-formylated form (**6**) (m/z 102.0197) and N-carbamoylglycine (hydantoic acid) (**7**) (m/z 117.0306). In addition, the hydantoin compound (**8**), proposed in literature as possible precursor of glycine in prebiotic scenarios (*Figure 82*),[8, 9] can be recognized at m/z 99.0200.

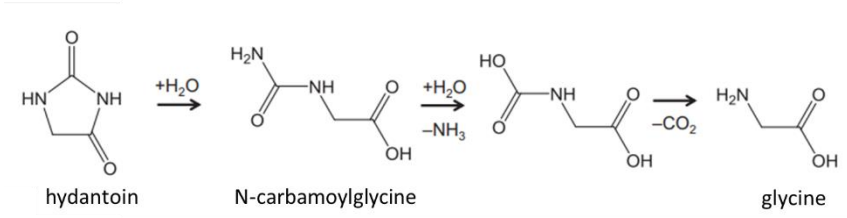

Figure 82. Reaction mechanism of the formation of glycine by the hydrolysis of hydantoin. Adapted from ref.[8]

Imidazolic compounds (9-22). Numerous species containing the imidazole ring can be identified among the detected products in the HRMS spectra. Among them, the masses at m/z 125.0469 and m/z 153.0418 can be plausibly assigned to AICA (**15**) and f-AICA (**16**) compounds which are typical oxygenated reaction products of the chemistry of HCN and its derivatives (i.e., AMN, DAMN as well as formamide) in homogeneous phases.[10]

Assuming the presence of such compounds, it is reasonable to think that the m/z 107, already assigned above to DAMN (**2a**), can also refers to its cyclic isomer AICN (**10a**), since it is the precursor of AICA (**15**). This hypothesis is in agreement with the results of previous literature data[11-15] which indicate that AMN, DAMN, AICN and AICA are all key intermediates in the synthesis of purines, via HCN

polymerization in acqueous solution, following the reaction paths reported in *Figure 83*.

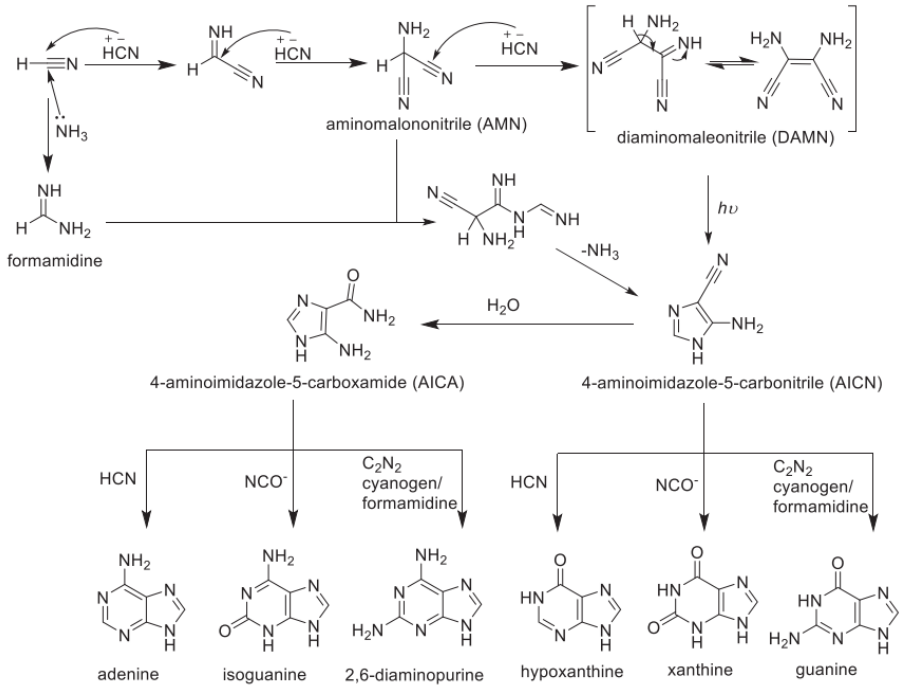

Figure 83. Mechanism of purine synthesis postulated by Orò and later modified by Ferris and Orgel. From ref. [7]

According to this mechanism, AICN (4-aminoimidazole-5-carbonitrile) can be formed by reaction of AMN with formamidine (H_2N-CH-NH) or through photochemical rearrangement of the DAMN. AICA (4-aminoimidazole-5-carboxamide) is the hydrated form of AICN and both are involved in the synthesis of purine derivatives (including adenine, diaminopurine, isoguanine, guanine, hypoxanthine and xanthine) by reaction with other carbon sources as HCN, C_2N_2 (cyanogen) or cyanate.

Although this is the most widely known mechanism for purine synthesis from HCN, many other pathways of formation have been reported in the literature.[7]

As far as fAICA (**16**) (m/z 153.0418) is concerned, i.e., the N-formylated form of AICA (**15**), it has been mainly detected in experiment involving formamide. Its relevance comes from the fact that, together with AICA, is a crucial intermediate (actually their ribosyl derivatives) in the biosynthesis of inosine-5'-monophosphate (IMP) that is the main route to form purine nucleotides in living cells (*Figure 84*).[16] Thus, they represent an important example of the "chemomimesis" concept developed by Eschenmoser,[17] whereby "*chemical compounds and processes characterizing biological phenomena often have purely abiotic precedents: something is copied and used that already existed*."[18]

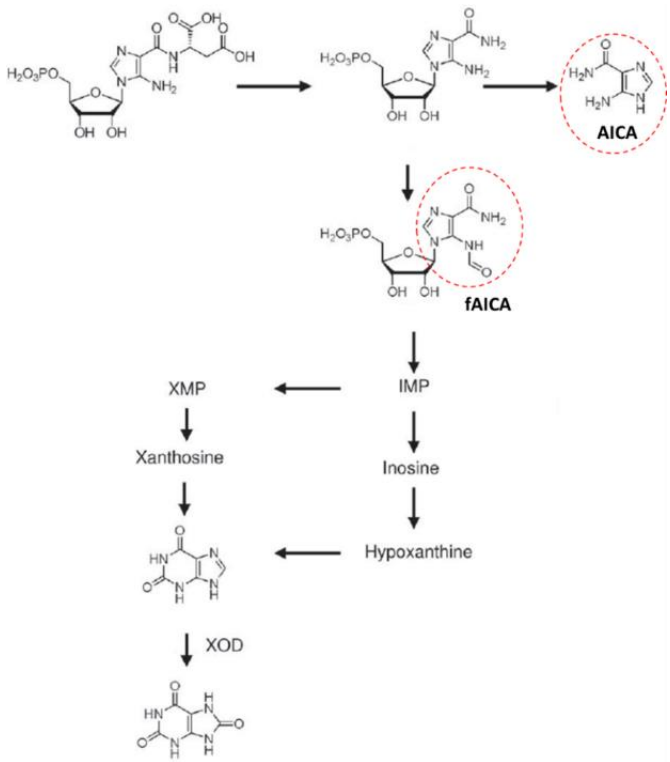

Figure 84. Purine metabolic pathway in animals, plants and microorganisms. Adapted from ref. [16]

Other imidazole compounds can be recognized among our products at m/z 132.0316 (**12**), 159.0425 (**13b**), 186.0534 (**14**), 150.0421 (**18d**), 168.0527 (**21**), and 195.0636 (**22**). These masses (and, as it will be seen in the follow, those also of some (**24b**, **25e**, **23**) identified purinic species) are perfectly in agreement with those of the species proposed by Voet and Schwartz as intermediates in the synthesis of adenine in HCN solution.[19, 20] The authors suggested a mechanism (*Figure 85*) alternative to that proposed by Orò, Ferris, and Orgel (see *Figure 83*), which does not imply the formation of AICN.

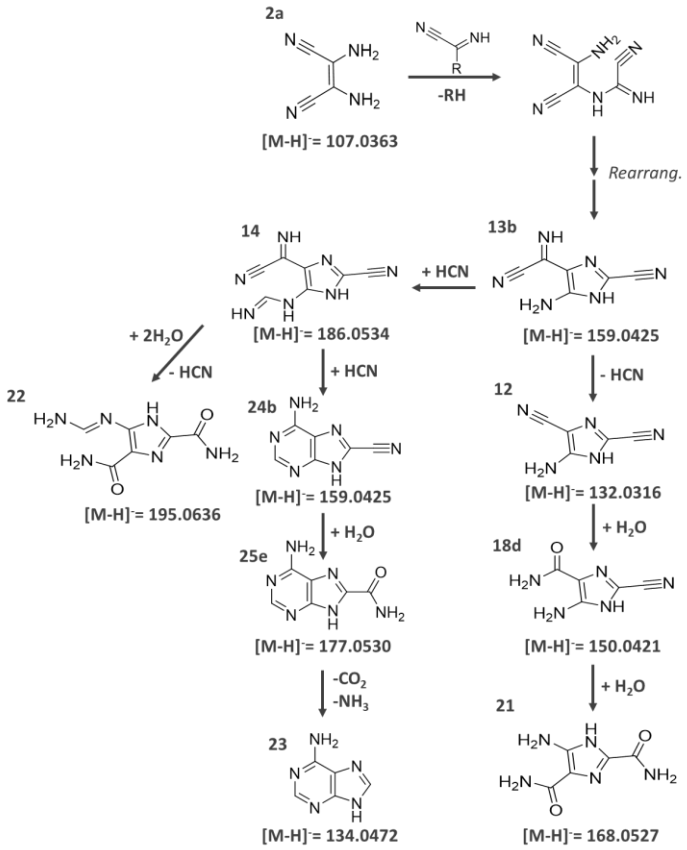

Figure 85. Pathway for the synthesis of adenine from HCN as suggested by Voet and Schwartz (adapted from ref. [20]). The mass exact of the deprotonated species are also reported.

Following this mechanism, by reaction of DAMN (**2a**) with an HCN cyanoimino derivate (like the iminoacetonitrile, IAN, HCN dimer or the DISN, diiminosuccinonitrile, DAMN oxidation product), a key intermediate (**13b**) is formed which, after a series of rearrangements, can initiate different reactive pathways. One leads to formation of 5-amino-1H-imidazole-2,4-dicarbonitrile (**12**) and its hydrated form (**18d**). The other, after the formation of compound (**14**) by addition of a HCN molecule to the species (**24b**), leads to the synthesis of

adenine (**23**), which directly occurs from decarboxamidation of the adenine-8-carboxamide (**25e**) precursor.

Our MS/MS fragmentations experiments performed on some of the extracted products (see the spectra reported in the *Appendix* at the end of this part) gave results compatible with the presence on our samples of most of the species hypothesized in the Voet's mechanism, which could hence give explanation for the formation of purine, including adenine, on the HCN/solid systems.

Purine and pyrimidine (23-36). As already anticipated, the purinic species involved in the Voet's mechanism are assigned to m/z 134.0472 (**23**), 159.0425 (**24b**), and 177.0530 (**25e**). The first is the nucleobase adenine and the other two are its 8-substituted derivatives. In addition to these, there are several exact masses which may be attributed to other purine and pyrimidine derivatives. Among the purines, it is assumed the presence of hypoxanthine (**26c**), xanthine (**27**) and guanine (**28d**) at m/z 135.0312, 151.0261, and 150.0421, respectively. In the case of pyrimidine compounds, the m/z values at 110.0360, 125.0469, 126.0309, 154.0258, 111.0200, 126.0309, 127.0149, and 113.0357 suggest the presence of cytosine (**29**) and of three its 5-substituted derivatives (**30, 31f, 32**), as well as of uracil (**33**) and of three its 5-substituted derivatives (**34f, 35, 36**). However, some of these m/z values also correspond to other structural isomers of the imidazole type, but without MS/MS data they cannot be unequivocally attributed.

The two main mechanisms of formation of purine are already reported in *Figure 83* and *Figure 84*, while for pyrimidine the main route of synthesis, starting from HCN solution, is that formulated by Ferris et al.,[21] which leads to the formation of 4,5-dihydroxypyrimidine, 5-hydroxyuracil (**35**) and orotic acid (*Figure 86*). In addition, many studies in homogeneous phase performed under a variety of experimental conditions have shown that also the hydrolysis of the HCN polymers leads to the formation of pyrimidine and purine species (*Figure 87*).[22-24]

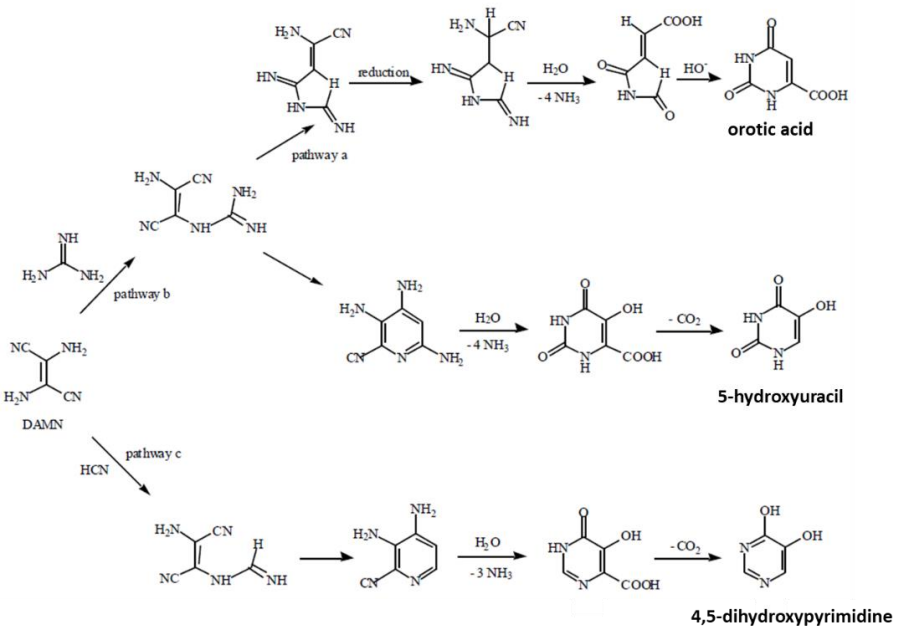

Figure 86. Reaction pathway for the conversion of diaminomaleonitrile (DAMN) to orotic acid, 5-hydroxyuracil and 4,5dihydroxypyrimidine. Adapted from ref. [25]

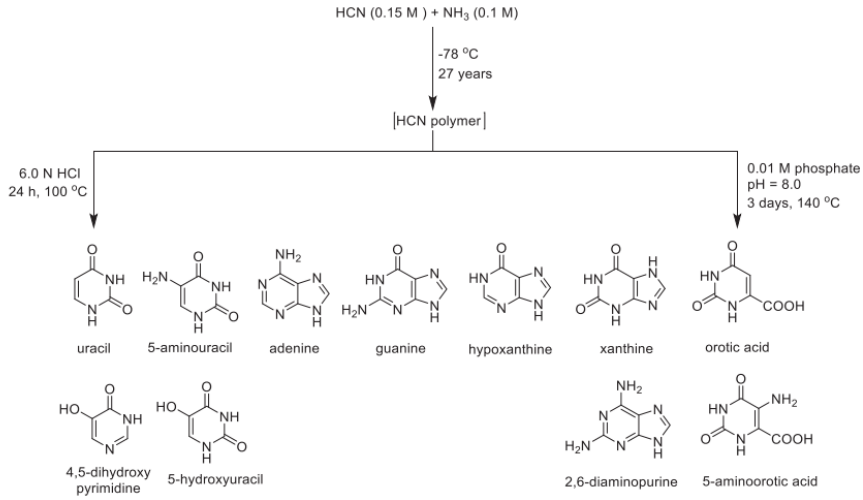

Figure 87. Different purines and pyrimidines obtained from HCN polymer under acidic and basic hydrolysis by Lowe and Ferris. Adapted from ref. [7]

The above discussed classes of compounds are very interesting in term of prebiotic molecular synthesis, since they are common reaction products in numerous experiments aiming to simulate prebiotic terrestrial and extraterrestrial environments.[26]

Some of reported species have been found in astrochemical environments like meteorites (i.e., amino acids, hydantoins, nucleobases and related compounds),[27-32] while glycine (the simplest amino acid) has recently also been detected in the coma of comets, such as Wild 2 and 67P/Churymov-Gerasimenko.[33, 34]

Although more research needs to be done, especially on the reaction mechanisms, the obtained results are very promising because, they show for the first time that the complex chemistry of hydrogen cyanide, leading to prebiotic molecules in solution or at solid/liquid interphases, can be reproduced at the gas/solid interphase under very mild temperature and pressure conditions, without external energy sources

(UV irradiation or electrical discharges). It is also worth underlining that, despite differences in the nature of the final products and plausibly in the reaction mechanisms, the catalytic activity toward HCN seems to be common to the investigated solids.

MS/MS fragmentation spectra of some reaction products.

Further information on the nature of the detected products comes from the ESI-MS/MS direct infusion data. The obtained products ions are summarized in *Table 14* while the MS/MS spectra with the related fragments structures are reported in *Figure 88*.

Table 14. Collision-induced dissociation MS/MS data of main ions identified for all samples (see Figure 80). The related fragmentation spectra (MS/MS) are shown in Figure 88.

Chemical formula	Precursor ion m/z	Product ions m/z (*base peak)	CID-MS^2 (eV)
$[C_5H_2N_5]^-$	132.0313	117.0041 105.0204* 78.0095	30
$[C_5H_4N_5]^-$	134.0469	107.0360 92.0251 80.0251*	35
$[C_5H_4ON_5]^-$	150.0421	132.0313 123.0310* 107.0360 80.0251	30
$[C_6H_3N_6]^-$	159.0424	132.0310* 107.0357 80.0249	30
$[C_6H_5ON_6]^-$	177.0532	134.0469*	30
$[C_7H_4N_7]^-$	186.0534	159.0419* 132.0310	25

The fragmentation profiles indicate that the species are closely related to each other. The fragmentation profiles (MS/MS) reveal that the selected species mainly dissociate by the loss of HCN (-27) or its dimer, iminoacetonitrile ($H_2C_2N_2$, -54). In addition, fragments produced by loss of cyanogen (C_2N_2, -52), carbodiimide (HNCNH, -42) and/or cyanamide (NH_2CN, -42), DAMN ($H_4C_4N_4$, -108), methylamine (CH_3NH_2, -31), and methyleneimine (H_2CNH, -29) have been found. Some more, losses of water (H_2O, -18) or isocyanic acid (HNCO, -43) have been detected, due to the dissociation of oxygenated species (m/z 150 and 177).

Figure 88. Product ions ESI(-)-MS/MS spectra via CID for the precursor ions at m/z, 132.0313, 159.0424, 150.0421, 186.0534, 177.0532, and 134.0469. Possible structures of the deprotonated fragments are reported.

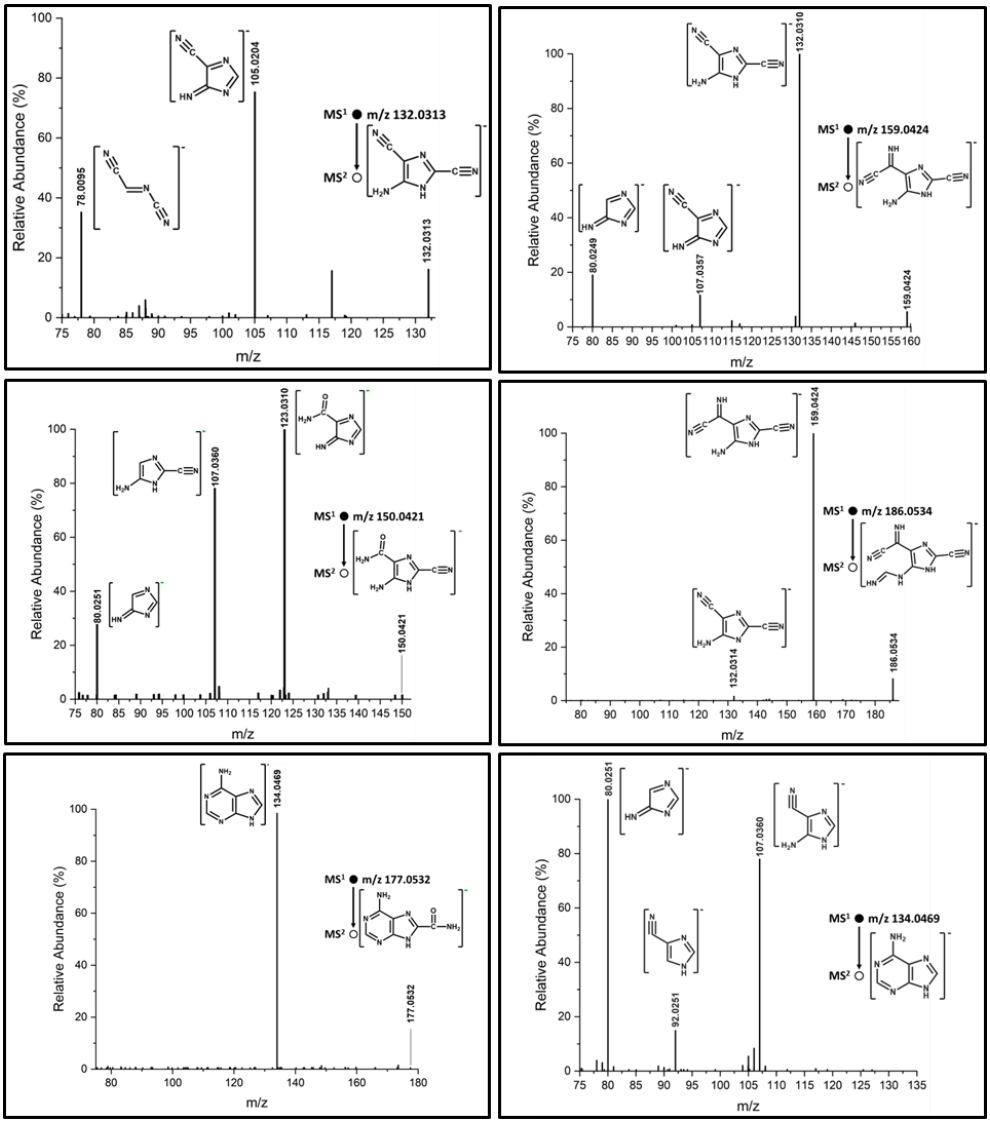

1. Wikipedia contributors. *Tandem_mass spectrometry*. In Wikipedia, The Free Encyclopedia. https://en.wikipedia.org/w/index.php?title=Tandem_mass_spectrometry&oldid=1075938839.
2. Santalucia, R.; Pazzi, M.; Bonino, F.; Signorile, M.; Scarano, D.; Ugliengo, P.; Spoto, G.; Mino, L., *From gaseous HCN to nucleobases at the cosmic silicate dust surface: an experimental insight into the onset of prebiotic chemistry in space.* Physical Chemistry Chemical Physics **2022**, 24 (12), 7224-7230
3. Ghosh, S.; Challamalla, P.; Banji, D., *Negative ion mode mass spectrometry- an overview*. Journal of Chemical, Biological and Physical Sciences **2012**, 2, 1462-1471.
4. J. P. Ferris, J. D. W., T. J. Ryan, A. P. Lobo, D. B. Donner, *Biomolecules from HCN*. Orig. Life Evol. Biosph. **1974**, 5, 153-7.
5. Ruiz-Bermejo, M.; Zorzano, M. P.; Osuna-Esteban, S., *Simple Organics and Biomonomers Identified in HCN Polymers: An Overview*. Life (Basel) **2013**, 3 (3), 421-48.
6. Ruiz-Bermejo, M.; de la Fuente, J. L.; Pérez-Fernández, C.; Mateo-Martí, E., *A Comprehensive Review of HCN-Derived Polymers*. Processes **2021**, 9 (4).
7. Yadav, M.; Kumar, R.; Krishnamurthy, R., *Chemistry of Abiotic Nucleotide Synthesis*. Chem Rev **2020**, 120 (11), 4766-4805.
8. Kayanuma, M.; Kidachi, K.; Shoji, M.; Komatsu, Y.; Sato, A.; Shigeta, Y.; Aikawa, Y.; Umemura, M., *A theoretical study of the formation of glycine via hydantoin intermediate in outer space environment*. Chemical Physics Letters **2017**, 687, 178-183.
9. Pascal, R.; Boiteau, L.; Commeyras, A., *From the Prebiotic Synthesis of α-Amino Acids Towards a Primitive Translation Apparatus for the Synthesis of Peptides*. In Prebiotic Chemistry, **2005**; pp 69-122.
10. Saladino, R.; Crestini, C.; Costanzo, G.; Di Mauro, E., *On the Prebiotic Synthesis of Nucleobases, Nucleotides, Oligonucleotides, Pre-RNA and Pre-DNA Molecules*. In Prebiotic Chemistry, **2005**; pp 29-68.
11. Oró, J., *Mechanism of Synthesis of Adenine from Hydrogen Cyanide under Possible Primitive Earth Conditions.* Nature **1961**, 191 (4794), 1193-1194.
12. Oró, J.; Kimball, A. P., *Synthesis of purines under possible primitive earth conditions: II. Purine intermediates from hydrogen cyanide*. Archives of Biochemistry and Biophysics **1962**, 96 (2), 293-313.
13. Ferris, J. P.; Orgel, L. E., *Aminomalononitrile and 4-Amino-5-cyanoimidazole in Hydrogen Cyanide Polymerization and Adenine Synthesis*. Journal of the American Chemical Society **1965**, 87 (21), 4976-4977.
14. Ferris, J. P.; Orgel, L. E., *Studies in Prebiotic Synthesis. I. Aminomalononitrile and 4-Amino-5-cyanoimidazole*. Journal of the American Chemical Society **1966**, 88 (16), 3829-3831.
15. Ferris, J. P.; Orgel, L. E., *An Unusual Photochemical Rearrangement in the Synthesis of Adenine from Hydrogen Cyanide.* Journal of the American Chemical Society **1966**, 88 (5), 1074-1074.

16. Choi, J.-H.; Ohnishi, T.; Yamakawa, Y.; Takeda, S.; Sekiguchi, S.; Maruyama, W.; Yamashita, K.; Suzuki, T.; Morita, A.; Ikka, T.; Motohashi, R.; Kiriiwa, Y.; Tobina, H.; Asai, T.; Tokuyama, S.; Hirai, H.; Yasuda, N.; Noguchi, K.; Asakawa, T.; Sugiyama, S.; Kan, T.; Kawagishi, H., *The Source of "Fairy Rings": 2-Azahypoxanthine and its Metabolite Found in a Novel Purine Metabolic Pathway in Plants*. Angewandte Chemie International Edition **2014**, 53 (6), 1552-1555.
17. Eschenmoser, A.; Loewenthal, E., *Chemistry of potentially prebiological natural products.* Chemical Society Reviews **1992**, 21 (1), 1-16.
18. Saladino, R.; Sponer, J.; Šponer, J.; Costanzo, G.; Pino, S.; Di Mauro, E., *Chemomimesis and Molecular Darwinism in Action: From Abiotic Generation of Nucleobases to Nucleosides and RNA*. Life 2018, 8, 24.
19. Voet, A. B.; Schwartz, A. W. *In HCN Oligomerization - Isolation and Preliminary Characterization of a New Precursor of Adenine*, Origin of Life, Dordrecht; Wolman, Y., Ed. Springer Netherlands: Dordrecht, **1981**; pp 217-223.
20. Voet, A. B.; Schwartz, A. W., *Prebiotic adenine synthesis from HCN—Evidence for a newly discovered major pathway.* Bioorganic Chemistry **1983**, 12 (1), 8-17.
21. Ferris, J. P.; Joshi, P. C.; Lawless, J. G., *Chemical evolution XXIX. Pyrimidines from hydrogen cyanide.* Biosystems **1977**, 9 (2), 81-86.
22. Lowe, C. U.; Rees, M. W.; Markham, R*., Synthesis of Complex Organic Compounds from Simple Precursors: Formation of Amino-Acids, Amino-Acid Polymers, Fatty Acids and Purines from Ammonium Cyanide.* Nature **1963**, 199 (4890), 219-222.
23. Ferris, J. P.; Joshi, P. C.; Edelson, E. H.; Lawless, J. G., *HCN: A plausible source of purines, pyrimidines and amino acids on the primitive earth.* Journal of Molecular Evolution **1978**, 11 (4), 293-311.
24. Ferris, J. P.; Hagan, W. J., *HCN and chemical evolution: The possible role of cyano compounds in prebiotic synthesis.* Tetrahedron **1984**, 40 (7), 1093-1120.
25. Saladino, R.; Crestini, C.; Costanzo, G.; DiMauro, E., *Advances in the Prebiotic Synthesis of Nucleic Acids Bases: Implications for the Origin of Life*. Current Organic Chemistry **2004**, 8, 1425-1443.
26. Kitadai, N.; Maruyama, S., *Origins of building blocks of life: A review*. Geoscience Frontiers 2018, 9 (4), 1117-1153.
27. Ehrenfreund, P.; Charnley, S. B., Organic Molecules in the Interstellar Medium, Comets, and Meteorites: A *Voyage from Dark Clouds to the Early Earth.* Annual Review of Astronomy and Astrophysics **2000**, 38 (1), 427-483.
28. Martins, Z.; Botta, O.; Fogel, M. L.; Sephton, M. A.; Glavin, D. P.; Watson, J. S.; Dworkin, J. P.; Schwartz, A. W.; Ehrenfreund, P., *Extraterrestrial nucleobases in the Murchison meteorite*. Earth and Planetary Science Letters **2008**, 270 (1-2), 130-136.
29. Martins, Z., *Organic Chemistry of Carbonaceous Meteorites*. Elements **2011**, 7 (1), 35-40.
30. Martins, Z., *The Nitrogen Heterocycle Content of Meteorites and Their Significance for the Origin of Life*. Life (Basel) **2018**, 8 (3).

31. Rodriguez, L. E.; House, C. H.; Smith, K. E.; Roberts, M. R.; Callahan, M. P., *Nitrogen heterocycles form peptide nucleic acid precursors in complex prebiotic mixtures.* Scientific Reports **2019**, 9 (1), 9281.
32. Oba, Y.; Takano, Y.; Furukawa, Y.; Koga, T.; Glavin, D. P.; Dworkin, J. P.; Naraoka, H., *Identifying the wide diversity of extraterrestrial purine and pyrimidine nucleobases in carbonaceous meteorites*. Nature Communications **2022**, 13 (1), 2008.
33. Rimola, A.; Sodupe, M.; Ugliengo, P., *CHAPTER 13 The Birth and Fate of Glycine: From the Interstellar Medium to Primitive Earth.* In Prebiotic Photochemistry: From Urey–Miller-like Experiments to Recent Findings, The Royal Society of Chemistry: **2021**; pp 265-287.
34. Hadraoui, K.; Cottin, H.; Ivanovski, S. L.; Zapf, P.; Altwegg, K.; Benilan, Y.; Biver, N.; Della Corte, V.; Fray, N.; Lasue, J.; Merouane, S.; Rotundi, A.; Zakharov, V., *Distributed glycine in comet 67P/Churyumov-Gerasimenko.* A&A **2019**, 630.

Chapter 7

Summary, Conclusions and Perspectives

7.1 Summary and Conclusions

The aim of this PhD project was a systematic investigation of the adsorption and the reactivity of gaseous HCN at the surface of some oxides (SiO_2, TiO_2, Al_2O_3, MgO) and Mg-silicates (amorphous and crystalline Mg_2SiO_4) by *in situ* infrared spectroscopy at variable temperature (150−300 K) and mass spectrometry.

The expected outcomes of the research were detailed information about the HCN heterogeneous chemistry (a topic covered in the literature by a few papers only) which are thought to be useful in many fields, including environmental protection (in view of pollutant HCN removal by adsorption), materials science (in view of the use of HCN as precursor for the surface heterogenization of catalytic and photocatalytic solids) and, mainly, prebiotic chemistry and astrochemistry (because of the role assigned nowadays to HCN as ingredient for the synthesis of prebiotic molecules).

A decisive preliminary step of the research work, which took up a relevant fraction of the first Ph.D. year, was the setup of an innovative safe and clean method for the *in situ* production of high purity HCN gas by reduction of AuCN with H_2 in presence of noble metal particles as catalyst (*Chapter* 2). To this scope, many efforts were devoted to

individuate the best operative conditions in terms of reduction temperature and H_2 pressure, along with gas composition checking by IR and mass spectroscopies.

The IR investigation of the HCN interaction at the surface of oxides and Mg-silicates of interest, in the 150-300 K temperature range, allowed to roughly distinguish two steps: (a) HCN adsorption in molecular and/or dissociative forms, prevalently occurring at *ca*. 150 K and (b) reactions at increasing temperatures of the adsorbed species with excess HCN to give a variety of complex reaction products (*Chapter 3* and *Chapter 4*).

To shortly resume the obtained results, a comparison of the IR spectra obtained at maximum HCN coverage at 150 K is reported in *Figure 89*.

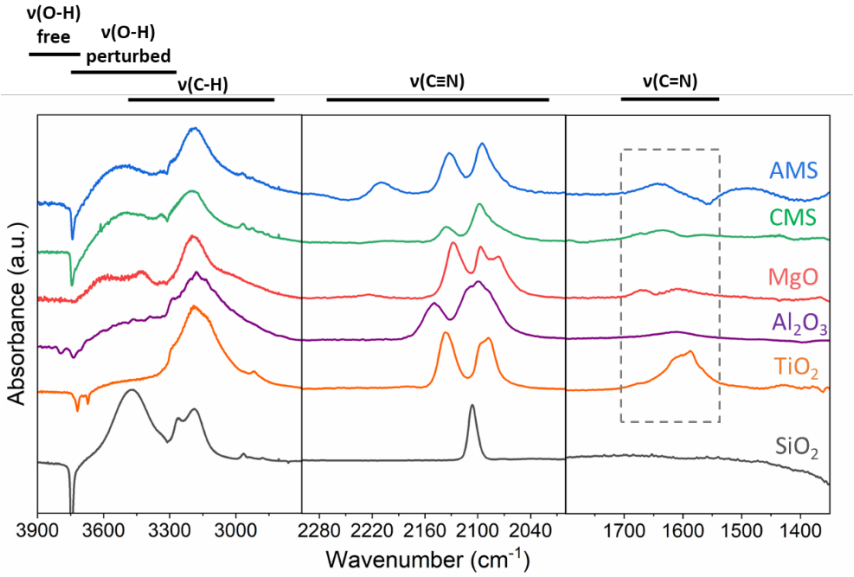

Figure 89. Comparison of the IR spectra (background subtracted) of the HCN adsorbed species at the surface of the investigated solids at 150 K and 5 mbar equilibrium pressure.

The plausible HCN surface species, that have been taken into consideration, to explain the observed features are shown in *Figure 90*, while the given assignments are summarized in *Table 15*.

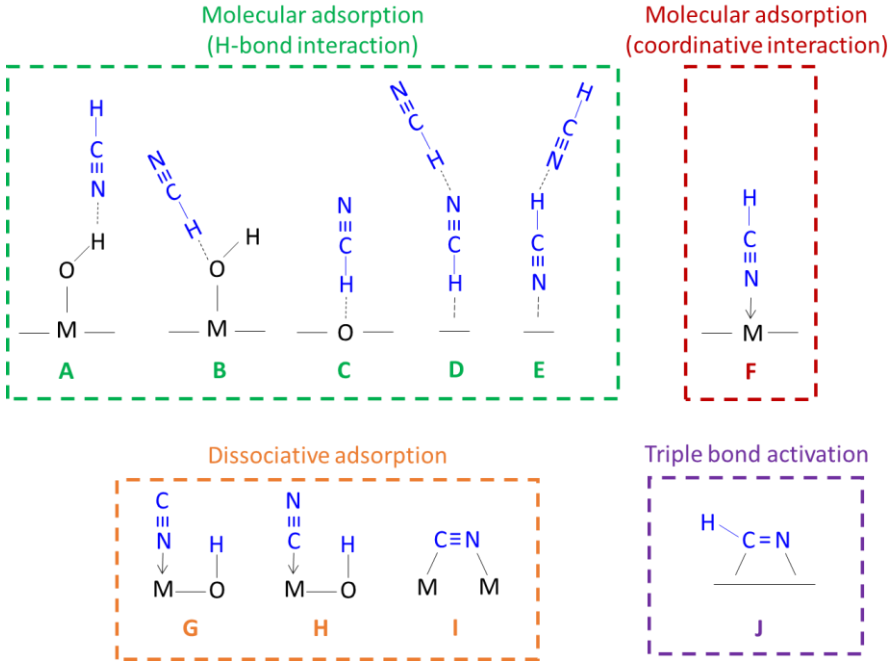

Figure 90. Possible ways of HCN interaction with the oxide surfaces. The corresponding vibration frequencies are reported in Table 15.

Table 15. Main absorption bands (in cm^{-1}) observed in the spectra reported in Figure 89 and their assignments with reference to the species reported in Figure 90.

Sample	ν(O-H)	ν(C-H)	ν(C≡N)	ν(C=N)
SiO_2	3700-3350	3261 3189	2106 **(A, B, D, E)**	-
TiO_2	3650-3350	3301	2137 **(F)**	1700-1500 **(J)**
		3250-3000 (3177)	2097 **(A, D, E)**	
		3100-2800	2087 **(B, C)**	
Al_2O_3	3650-3350	3300	2150 **(F)**	1700-1500 **(J)**
		-	2109 **(G, I)**	
		3250-3000 (3181)	2099 **(A, D, E)**	
		3150-2800	2087 **(B, C)**	
MgO	3650-3350	3284 3288-3229*	2127 **(F)**	1700-1500 **(J)**
		3250-3000 (3191)	2097 **(A, D, E)**	
		3100-2800	2090-2060 **(B, C)**	
		-	2090-2080 **(G, I)**	
CMS	3650-3350	3302	2134 **(F)**	1700-1500 **(J)**
		3250-3000 (3197)	2098 **(A, D, E)**	
		3100-2800	2090-2060 **(B, C)**	
		-	2090-2060 **(G, I)**	
AMS	3650-3350	-	2210 (anionic dimer IAN)	1700-1500 **(J)**
		3303	2132 **(F)**	
		3250-3000 (3183)	2095 **(A, D, E)**	
		3100-2800	2090-2060 **(B, C)**	
		-	2090-2060 **(G, I)**	

Based on the spectra of HCN adsorbed at 150 K, the following conclusions can be summerized (see also *Table 15*):

i. HCN is reversibly adsorbed on amorphous SiO_2 by weak hydrogen bonding interaction with residual surface silanols groups (Si-OH) to form Si-OH····(HCN) adducts, without any evidence (at 150 K as well as at higher temperature) of HCN chemisorption.

ii. The formation of weakly adsorbed hydrogen bonded complexes also occurs on the residual OH groups at the TiO_2 surface. However, on this solid the prevailing adsorption mechanism is mainly through HCN coordination in molecular form on the coordinatively unsaturated Lewis acid (Ti^{4+}) and basic (O^{2-}) surface sites (structures **C** and **F** in *Table 15* and *Figure 90*). Although, there is no evidence of dissociative adsorption via HCN heterolytic splitting to form Ti-cyanides and OH groups, a broad feature in the 1700-1500 cm^{-1} interval suggests the formation of species containing C=N double bonds compatible with η^2(C,N)-HCN moieties (structure **J** in *Table 15*). This fact is relevant, as it suggests that some surface sites are able to "activate" the HCN molecule by reducing the CN bond order.

iii. γ-Al_2O_3 behaves in a way similar to TiO_2 as for the molecular adsorption of HCN on the residual OH Brønsted sites and on Al^{3+}, O^{2-}Lewis sites. However, it also shows the ability to heterolytically split HCN already at 150 K to form surface cyanides (structures **G** and **I** in *Table 15* and *Figure 90*). It is hypothesized that this ability is due to Al^{3+}–O^{2-} pairs located in

highly defective positions, which may be responsible for the splitting of the much harsher H_2 and CH_4 molecules.

iv. The ability to dissociate HCN at 150 K is shown also by MgO, as well as its ability to adsorb it in molecular form on coordinatively unsaturated Mg^{2+} and O^{2-} sites. Notice that the as outgassed oxide is free from residual OH groups, which are however formed due to HCN splitting and then immediately engaged in hydrogen bonded interaction with excess HCN. Comparison of the spectra of the HCN/MgO and H_2/MgO systems allow to hypothesize that the sites responsible for the HCN chemisorption are the same able to heterolytically split H_2, *i.e.,* tri-coordinated pseudo-vacancies located at inverse corners, defects commonly encountered at the surface of high surface area MgO and more rare on other oxides.

The results obtained on the simpler oxides discussed above (and especially those on SiO_2 and MgO) were used as reference for investigation of the interaction HCN with amorphous and crystalline (forsterite) Mg_2SiO_4, *i.e.* with solids assumed as laboratory models for the composition of interstellar dust grains (

Chapter 4). The amorphous sample (AMS) showed spectral features closely resembling that of SiO_2 and MgO. This behaviour is not surprising, based on the literature which assign to AMS a structure made of randomly intercalated SiO_4 tetrahedra and Mg^{2+} ions, with defective portions where clustered $(SiO_4)_n$ (resembling the silica structure) and $(Mg^{2+}O^{2-})_x$ species (resembling the MgO structure) are formed. The presence of similar features on forsterite (CMS), whose structure is expected to consist of a regular distribution of SiO_4 tetrahedra intercalated by a regular distribution of Mg^{2+} ions, was a little surprising but seems to confirm the hypothesis already advanced in the literature of an incomplete crystallization. The presence in the spectra of the HCN/AMS system at 150 K of a band ascribable to $(HC_2N_2)^-$ anionic dimers (IAN), together with the manifestation of CN^- fragments (as on MgO), is noteworthy. This highlights, already at 150 K, the onset of a HCN surface chemistry which is initiated by the HCN splitting on $Mg^{2+}O^{2-}$ acid/base pairs and proceeds through the nucleophilic attack of the CN^- fragment on incoming (or nearby adsorbed) HCN molecules. Similar reactions in homogeneous conditions are the starting point of a complex HCN chemistry, which finally leads to molecules of biological relevance. Based on our experiments in the 150–300 K temperature interval, we can state that this chemistry is reproduced at the surface of oxides and Mg-Silicates (*Chapter 5*).

The final spectra of the HCN/oxides and HCN/Mg-silicates after increasing the temperature up to 300 K are compared in *Figure 91*.

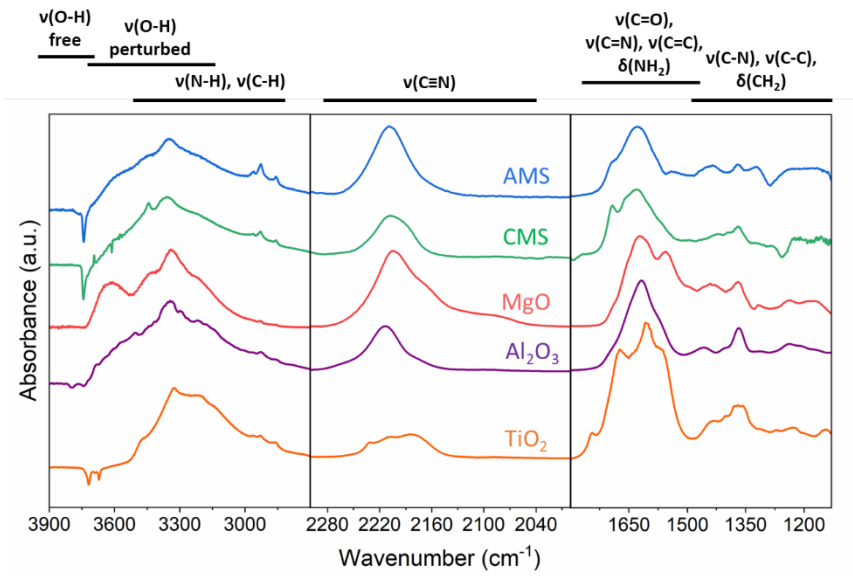

Figure 91. Comparison of the IR spectra of all the investigated HCN/systems collected at 300 K in presence of HCN gas (5 mbar equilibrium pressure).

These spectra are dramatically different with respect to those obtained at 150 K (*Figure 89*), thus suggesting the formation of a mixture of surface products containing the functional groups listed in the top part of the figure.

The identification of the products was performed by DI-HR-MS after their extraction with methanol (*Chapter 6*). Beside HCN oligomers (trimer and tetramer), the formation of glycine and derivatives, families of imidazole, purine and pyrimidine compounds have been evidenced (some of these products are shown in *Figure 92*).

The presence of oxygenated species among the detected products is explained with the direct involvement of surface oxygen species.

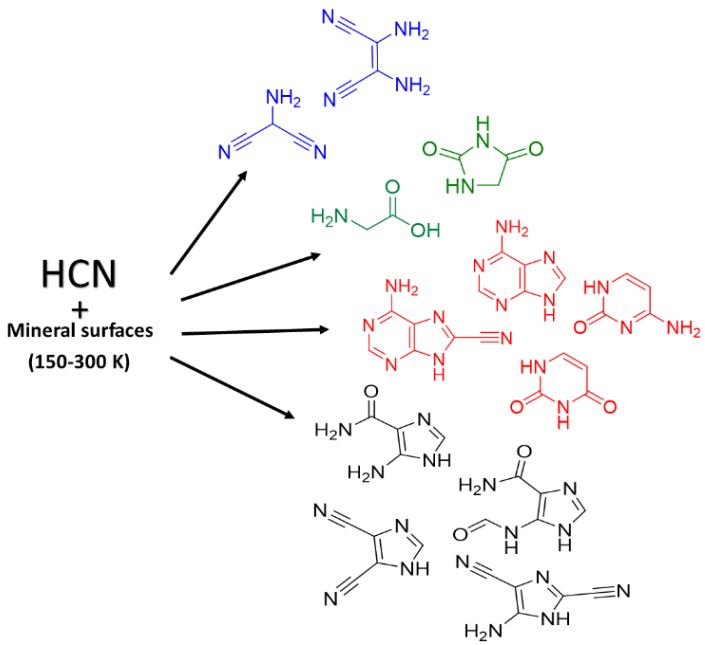

Figure 92. Some species identified among the many products obtained by the HCN/solid interaction in the range 150-300 K.

The obtained results are, in our opinion, of special interest, as they represent the first evidence of the formation of complex molecules of prebiotic interest directly from HCN in heterogeneous conditions, at low temperature and in absence of external energy sources.

Significance and implications in the field of prebiotic chemistry in the astrophysical context are self-evident. Indeed, the experiments performed during the thesis are compatible (also from the point of view of the temperature conditions) with a primordial scenario in which gaseous HCN came directly in contact with the surface of the minerals abundant in the core of the interstellar medium particles as well as on comets. Therefore, it can be stated that HCN contributed as an ingredient to form molecules that are among the building blocks of the chemistry of life.

7.2 Future Perspectives

The work done so far has allowed to reach some important results, but nevertheless some important questions remain still unresolved and deserve further investigation. In particular:

- ✓ The need exists to individuate all the reaction products and to advance reasonable hypotheses about the mechanisms underlying their formation with respect to the peculiar surface properties of the various solids. The mechanisms illustrated here are those proposed for the HCN reactivity in homogeneous conditions, and it is questionable if they can satisfactory reproduce those occurring at the solid surfaces. In this respect we think that quantum mechanical calculations could make a significant contribution for both the interpretation of the experimental data and the control of the key steps of the reaction paths.

- ✓ The IR results evidenced differences in the HCN reactivity among the various solids and the DI-HRMS data a different distribution of the products. In this respect, it could be useful to combine chromatographic separation techniques with HR-MS to significantly quantify the products distribution. The dependence of the HCN reactivity on parameters including the contact time, the pressure of the HCN gas, the temperature, and the degree of hydration of the materials also deserves a more detailed investigation. Finally, different conditions for the extraction of the surface products should be attempted (solvents other than

methanol, extraction in inert atmosphere, etc.) to exclude possible unwanted contributions to the formation of the products revealed by the HRMS analysis.

- ✓ In the field of prebiotic chemistry, it is believed that molecules like the DAMN (detected among the reaction products) or formamide ($HCONH_2$, *i.e.,* basically, hydrated HCN), are key intermediates in the abiotic formation of biomolecules. A study of the direct interaction of these molecules with the investigated solids in the same conditions used for HCN could add important knowledge to the formation mechanisms of products in heterogeneous conditions.

- ✓ Once completed the study of the interaction of individual molecules (HCN, DAMN and $HCONH_2$), it could be interesting to investigate their reactivity in mixture with of other simple species of prebiotic interest, like CH_4, C_2H_2, H_2O, CO, NH_3, H_2S etc.

- ✓ Finally, it could be remarkable to explore the possible effects of an external energy source on the behavior of these solids towards HCN. For example, evaluating the HCN/solid interaction at temperatures above 300 K or under UV irradiation (condition of special interest when dealing with a photo-active substrate like TiO_2).

List of publications

1. Pavan, C.; **Santalucia, R**.; Leinardi, R.; Fabbiani, M.; Yakoub, Y.; Uwambayinema, F.; Ugliengo, P.; Tomatis, M.; Martra, G.; Turci, F.; Lison, D.; Fubini, B., *Nearly free surface silanols are the critical molecular moieties that initiate the toxicity of silica particles*. Proceedings of the National Academy of Sciences **2020**, 117 (45), 27836-27846. https://doi.org/10.1073/pnas.2008006117

2. Mino, L.; Negri, C.; **Santalucia, R**.; Cerrato, G.; Spoto, G.; Martra, G., *Morphology, Surface Structure and Water Adsorption Properties of TiO_2 Nanoparticles: A Comparison of Different Commercial Samples*. Molecules **2020**, 25 (20). https://doi.org/10.3390/molecules25204605

3. **Santalucia, R**.; Mino, L.; Cesano, F.; Scarano, D.; Spoto, G.; Martra, G., Surface *Processes in Photocatalytic Reduction of CO_2 on TiO_2-based Materials.* Journal of Photocatalysis **2021**, 2 (1), 10-24. DOI: 10.2174/2665976X01999201022142435

4. **Santalucia, R**.; Vacca, T.; Cesano, F.; Martra, G.; Pellegrino, F.; Scarano, D., *Few-Layered MoS_2 Nanoparticles Covering Anatase TiO_2 Nanosheets: Comparison between Ex Situ and In Situ Synthesis Approaches*. Applied Sciences **2021**, 11 (1). https://doi.org/10.3390/app11010143

5. **Santalucia, R**.; Spoto, G.; Mino, L., *Probing Molybdenum Active Sites during In Situ Photoreduction of the Mo^{6+}/SiO_2 Catalyst*. Molecules **2021**, 26 (6). https://doi.org/10.3390/molecules26061700

6. **Santalucia, R**.; Pazzi, M.; Bonino, F.; Signorile, M.; Scarano, D.; Ugliengo, P.; Spoto, G.; Mino, L., *From gaseous HCN to nucleobases at the cosmic silicate dust surface: an experimental insight into the onset of prebiotic chemistry in space*. Physical Chemistry Chemical Physics **2022**, 24 (12), 7224-7230. https://doi.org/10.1039/D1CP05407D